

ABSTRACT

BASCIANO, CHRISTOPHER ANTHONY. Computational Particle-Hemodynamics Analysis Applied to an Abdominal Aortic Aneurysm with Thrombus and Microsphere-Targeting of Liver Tumors. (Under the direction of Professor Clement Kleinstreuer).

Human blood is a suspension of cells, i.e., primarily erythrocytes, leukocytes, and platelets, in plasma. In some pathological cases, e.g., abdominal aortic aneurysms, adverse particle-hemodynamics may lead to intraluminal thrombus formation. In a very different application of particle-hemodynamics, particles may be injected into the blood stream that are measurably larger than the cellular components of blood; for example, Yttrium-90 microspheres for the treatment of liver tumors. The transport of both biological and clinically induced particles can be modeled using a deductive research approach, implementing the same fluid-particle transport theory.

After a review of abdominal aortic aneurysms with intraluminal thrombus, Yttrium-90 radioembolization of liver tumors and the theory describing fluid-particle transport, the particle-hemodynamics of an abdominal aortic aneurysm and Yttrium-90 microsphere transport in the hepatic arteries have been analyzed. Original contributions to the scientific field from the completed analysis are: i) the relation of an abdominal aortic aneurysm's particle-hemodynamics with future intraluminal thrombus development; ii) quantification of particle shear stress exposure in an abdominal aortic aneurysm sac; iii) improved characterization of the transient hemodynamics in the hepatic arteries; iv) the illustration of Yttrium-90 microsphere transport to specific downstream locations through the selection of appropriate temporal and spatial release positions; and v) identification of primary hemodynamic influences on microsphere transport in the hepatic arteries.

In summary, particle-hemodynamics modeling and simulation has been applied to new subject areas and new knowledge has been generated that can improve current and future clinical therapies treating abdominal aortic aneurysms and liver tumors.

© Copyright 2010 Christopher Anthony Basciano

All Rights Reserved

Computational Particle-Hemodynamics Analysis Applied to an
Abdominal Aortic Aneurysm with Thrombus
and Microsphere-Targeting of Liver Tumors

by
Christopher Anthony Basciano

A dissertation submitted to the Graduate Faculty of
North Carolina State University
in partial fulfillment of the
requirements for the degree of
Doctor of Philosophy

Mechanical Engineering

Raleigh, North Carolina

2010

APPROVED BY:

James W. Leach

Mark Farber, M.D.

Tarek Echehki

Andrew Kennedy, M.D., FACRO

Greg Buckner

Clement Kleinstreuer
Chair of Advisory Committee

DEDICATION

To all those who sacrificed and worked hard
to give me the opportunities I enjoy today

BIOGRAPHY

Christopher Anthony Basciano was born on May 10, 1983 in Teaneck, NJ. He is the son of Frank and Judy Basciano and is third generation Italian-American. The author's family moved to Spring Hill, FL shortly after he was born. While in Florida, the author's younger brother and sister were born while the author went through grade, middle, and high-school, eventually graduating from Hernando Christian Academy located in Brooksville, FL in May 2001.

He then attended Mercer University in Macon, GA where he met his wife, Amanda Basciano neé Chappell, and in May 2005, earned a Bachelor of Science in Engineering with a specialization in Biomedical Engineering and a minor in Business Administration. While at Mercer, Christopher had many wonderful experiences. One of them was being mentored by Dr. Sinjae Hyun, who sparked his interest in computational research within the field of biomedical engineering. In August 2005, the author continued to pursue biomedical computational research and began work on this dissertation under the direction of Dr. Clement Kleinstreuer within the Department of Mechanical and Aerospace Engineering at North Carolina State University.

Christopher married Amanda Chappell on June 30, 2007 in Raleigh, NC. They are looking forward to starting a family in the future and both have a sustained interest in biomedical research.

ACKNOWLEDGMENTS

My research has richly benefited from multiple collaborations and the enthusiastic support of many different sources, sometimes a simple “thank-you” appears very inadequate, but I will do my best to extend my heartfelt gratitude. I wish to acknowledge the effort and time that my committee chair, Dr. C. Kleinstreuer exerts for all his graduate students. His guidance, ideas, and encouragement have been an invaluable source of inspiration and direction throughout this study. Thank-you Dr. Kleinstreuer for the opportunity to work in your lab and for the time you invested in developing my research potential. I wish to also thank my other committee members Dr. J.W. Leach, Dr. T. Echeikki, Dr. G. Buckner, A. Kennedy, MD, FACRO, and M. Farber, MD who have exerted significant amounts of time and energy throughout my research ventures. Their support has been invaluable and I deeply appreciate all the conversations, recommendations, research data, and encouragement they so willingly provided. I wish to also acknowledge the assistance of Dr. Brooke Steele (Department of Biomedical Engineering, North Carolina State University) in giving her time and comments on the Windkessel model implementation in MATLAB and Dr. Sinjae Hyun (Department of Biomedical Engineering, Mercer University, Macon, GA) in converting a patient’s CT-scan DICOM files into a usable mesh file. His support enabled the hepatic research to move beyond the population averaged, representative domains.

The aneurysm study would not be possible without the data set of a single patient’s abdominal aortic aneurysm development provided by Dr. Ender Finol (Institute for Complex Engineered Systems, Departments of Biomedical and Mechanical Engineering, Carnegie

Melon University, Pittsburgh, PA) and his former student Ms. Julie H.Y. Ng (Departments of Biomedical and Mechanical Engineering, Carnegie Melon University, Pittsburgh, PA). Their willingness to collaborate and support my research is readily acknowledged and will hopefully spur on continued research collaborations. Thank-you very much to you both, I wish you the best in your future endeavors.

My fellow colleagues in the Computational Multi-Physics Lab have provided invaluable suggestions, comments, and discussions throughout my research. I would like to acknowledge these individuals as Mr. Yu Feng, Ms. Emily Childress, Dr. Jie Li, and Dr. Zhe Zhang. Dr. Jie Li deserves specific mention for creating the computational meshes used in the smart micro-catheter geometries and allowing me to use his meshes for my research. I also gratefully acknowledge the use of ANSYS software (ICEM CFD, ANSYS CFX, and ANSYS Mechanical) for the computational research studies, which was provided by ANSYS Inc., Canonsburg, PA. The technical support of Dr. Kurt Svihla (Senior Technical Services Manager, ANSYS Inc.) and his team of code developers is gratefully acknowledged for their assistance in developing a custom solution to writing transient fluid-particle variables to the particle results file, which were required for the force calculations in the aneurysm particle-hemodynamics simulations. The financial support of SirTex Medical (LaneCove, Australia) is greatly appreciated and duly acknowledged. I hope my work will inspire continued support of applied research.

The support and encouragement from my parents and family has inspired me to strive for excellence in all things. Thank-you for the faith and love you so willingly poured into my life and your understanding throughout my many years in school. I would also like to extend

a special thanks to my new parents Mark and Cindy Chappell for welcoming me into your family and encouraging my research. I look forward to holidays and times with everyone when I'm not "still in school."

To my wife Amanda: Your devotion and support through the many facets and experiences of graduate student life is nothing short of amazing. I cannot begin to thank you enough and will spend the rest of my life attempting to make your dreams come true. Your love and encouragement is priceless to me and as our next chapter in life is just over the horizon, I am so looking forward to traversing its paths with you by my side. I love you.

Finally, I wish to thank my Lord and savior, Jesus Christ. I am amazed at the opportunities He has given me and I hope to be a wise steward of whatever He brings my way. Thank-you for guiding my path and the gracious love you so richly bestow, which I still struggle to fully grasp. I pray that the work and research ultimately glorifies You.

TABLE OF CONTENTS

| | |
|--|----------|
| LIST OF TABLES | xii |
| LIST OF FIGURES | xiv |
| NOTATION AND SYMBOLS | xxiii |
| CHAPTER 1: Research Motivation, Research Objectives, and Background Information | 1 |
| 1.1 Research Motivation | 1 |
| 1.1.1 Abdominal Aortic Aneurysms and Intraluminal Thrombus Development | 1 |
| 1.1.2 Yttrium-90 Microsphere Transport and Liver Targeting | 2 |
| 1.2 Research Objectives | 4 |
| 1.2.1 Abdominal Aortic Aneurysms and Intraluminal Thrombus Development | 4 |
| 1.2.2 Yttrium-90 Microsphere Transport and Liver Targeting | 5 |
| 1.3 Primary Cellular Components of Whole Blood | 6 |
| 1.4 Platelet Plug Formation, Blood Coagulation, and Thrombosis | 7 |
| 1.5 Abdominal Aortic Aneurysms and Intraluminal Thrombus | 9 |
| 1.5.1 General Information on Abdominal Aortic Aneurysms | 9 |
| 1.5.2 Composition and Mechanical Behavior of the Intraluminal Thrombus | 11 |
| 1.5.3 Influence of the Intraluminal Thrombus on the Abdominal Aortic Aneurysm Wall | 14 |
| 1.5.4 Theories of Intraluminal Thrombus Development in Abdominal Aortic Aneurysms | 17 |
| 1.5.5 Previous Investigations of Particle Transport in Abdominal Aortic Aneurysms | 19 |

| | |
|---|-----------|
| 1.6 Liver Tumors and Yttrium-90 Radioembolization | 21 |
| 1.6.1 General Information on Liver Tumors | 21 |
| 1.6.2 Yttrium-90 Radioembolization of Liver Tumors | 27 |
| 1.7 Chapter Outlook | 35 |
| CHAPTER 2: Fluid-Particle Transport Theory, Numerical Solution Method, and Model Validations | 36 |
| 2.1 Introduction | 36 |
| 2.2 Fluid Transport | 37 |
| 2.3 Particle Transport | 39 |
| 2.4 Solution Method | 44 |
| 2.5 Model Validations | 45 |
| 2.5.1 Velocity Profiles | 46 |
| 2.5.2 Recirculation Lengths | 47 |
| 2.5.3 Particle Transport | 51 |
| 2.5.4 Particle Deposition | 53 |
| 2.6 Conclusions | 59 |
| CHAPTER 3: Computational Domain Construction and Mesh Generation of Arterial System Morphologies | 60 |
| 3.1 Introduction | 60 |
| 3.2 Patient-Specific Infrarenal Abdominal Aortic Aneurysm (AAA) Geometry | 61 |
| 3.2.1 Patient-Specific Computational Domain | 61 |
| 3.2.2 Mesh Generation | 64 |
| 3.3 Hepatic Arterial System and Stationary Smart Micro-Catheter Geometries | 69 |
| 3.3.1 Hepatic Arterial System Anatomy and Representative Computational Domain | 69 |
| 3.3.2 Hepatic Arterial System Mesh Generation | 74 |

| | |
|---|------------|
| 3.3.3 Stationary Smart Micro-Catheter Computational Domain | 77 |
| 3.3.4 Smart Micro-Catheter Mesh Generation | 79 |
| 3.4 Patient-Inspired Replaced Common Hepatic Arterial Geometry | 80 |
| 3.4.1 Patient-Inspired Computational Domain | 80 |
| 3.4.2 Mesh Generation | 82 |
| 3.5 Conclusions | 85 |
| | |
| CHAPTER 4: Derivation and Implementation of Numerical Inlet/Outlet Conditions | 86 |
| 4.1 Introduction | 86 |
| 4.2 Derivation of Transient, Physiologically Relevant Boundary Conditions for Abdominal Aortic Aneurysms | 87 |
| 4.2.1 Abdominal Aortic Aneurysm Hemodynamics | 87 |
| 4.2.2 Selected Inlet/Outlet Conditions | 88 |
| 4.3 Derivation of Transient, Clinically-Inspired Inlet/Outlet Conditions for the Hepatic Arterial System | 90 |
| 4.3.1 Hepatic Arterial System General Physiology and Hemodynamics | 90 |
| 4.3.2 Blood Supply to Liver Tumors | 102 |
| 4.3.3 Processing Transient <i>in-vivo</i> Clinical Data | 105 |
| 4.3.4 Windkessel Models Utilized to Construct Additional Inflow and Outflow Waveforms | 123 |
| 4.4 Implementation of Derived Boundary Conditions | 136 |
| 4.5 Conclusions | 137 |
| | |
| CHAPTER 5: Transient Particle-Hemodynamics of an Abdominal Aortic Aneurysm | 138 |
| 5.1 Computational Simulation Parameters | 138 |
| 5.2 Transient Particle-Hemodynamics of a Patient's Abdominal Aortic Aneurysm | 143 |
| 5.2.1 Transient Flow Fields | 143 |

| | |
|---|------------|
| 5.2.2 Particle Transport and Mechanical Loading of Particles | 157 |
| 5.2.3 Fluid-Particle Entrapment and Transit Time | 171 |
| 5.3 Potential Regions of Intraluminal Thrombus Development in Relation to Particle Transport and Entrapment | 176 |
| 5.4 Conclusions | 179 |
| | |
| CHAPTER 6: Steady and Transient Particle-Hemodynamics of Hepatic Arterial Systems | 180 |
| 6.1 Computational Simulation Parameters | 180 |
| 6.2 Steady-State Particle-Hemodynamics of a Representative Hepatic Artery System | 184 |
| 6.2.1 Flow Distribution and Local Flow Fields | 184 |
| 6.2.2 Particle Transport and Specific Daughter Vessel Targeting | 187 |
| 6.3 Transient Particle-Hemodynamics of a Representative Hepatic Artery System using the WK2 Inflow Waveform | 193 |
| 6.3.1 Flow Fields and Patterns | 193 |
| 6.3.2 Particle Transport and Specific Daughter Vessel Targeting | 197 |
| 6.3.3 Influence of Micro-Catheter and its Position on Flow Fields and Particle Transport | 209 |
| 6.3.4 Steady Flow Approximation of Transient Particle- Hemodynamics | 217 |
| 6.3.5 Influence of Particle Injection Velocity on Microsphere Transport and Daughter Vessel Targeting | 220 |
| 6.4 Transient Particle-Hemodynamics Using a Patient-Inspired, Replaced Common Hepatic Geometry Comparing Clinical, WK2, and WK4s Inflow/Outflow Waveforms | 228 |
| 6.4.1 Transient Flow Fields for Different Inflow/Outflow Waveforms | 228 |
| 6.4.2 Microsphere Transport considering Different Inflow/Outflow Waveforms | 232 |
| 6.5 Yttrium-90 Microsphere Injection Conditions Recommended for Liver Targeting | 234 |
| 6.6 Conclusions | 235 |

| | |
|---|------------|
| CHAPTER 7: Research Summary, Conclusions, and Future Work | 236 |
| 7.1 Research Summary | 236 |
| 7.2 Conclusions | 237 |
| 7.3 Future Work | 238 |
| REFERENCES | 249 |
| APPENDICES | 259 |
| APPENDIX I: Select Clinical Trials of Yttrium-90 Radioembolization of Primary and Metastatic Liver Malignancies | 260 |
| APPENDIX II: Custom MATLAB Code Used to Process Clinical Hemodynamics Data from Hepatic Arteries | 263 |
| APPENDIX III: Custom MATLAB Code Used to Construct Population- Averaged Windkessel Flow Waveforms | 270 |
| APPENDIX IV: Discrete Data of Derived Inlet/Outlet Transient Waveforms Based on <i>in-vivo</i> Hemodynamics Data | 283 |
| APPENDIX V: Steady Particle-Hemodynamics of an Abdominal Aortic Aneurysm | 291 |
| APPENDIX VI: Custom ANSYS CFD Post v12.1 Perl Scripts and MATLAB Functions for AAA Particle Post-Processing | 308 |
| APPENDIX VII: Custom ANSYS CFD Post v12.1 Perl Scripts for Hepatic Post-Processing | 337 |
| APPENDIX VIII: Copyright Permissions | 345 |

LIST OF TABLES

| | | |
|------------|--|-----|
| Table 1.1: | Properties of particles suspended in whole blood..... | 7 |
| Table 1.2: | Clotting times of particles in ILT layers..... | 19 |
| Table 1.3: | Tumor vascular morphology | 26 |
| Table 1.3: | Physical characteristics of clinically available Y ⁹⁰ microspheres ... | 30 |
| Table 1.4: | Indications for 90Y radioembolization | 33 |
| Table 2.1: | Quemada model parameter values | 38 |
| Table 3.1: | Computational AAA Meshes Tested for Solution Independence ... | 65 |
| Table 3.2: | Percentages of different anatomic configurations of the hepatic arterial system | 70 |
| Table 3.3: | Geometric features of representative hepatic arterial geometry | 73 |
| Table 3.4: | Mesh parameters used in the current study | 75 |
| Table 3.5: | Mesh characteristics of the SMC domain | 80 |
| Table 3.6: | Computational meshes of the patient-inspired hepatic artery system | 82 |
| Table 4.1: | Blood flow measurements in the celiac artery | 92 |
| Table 4.2: | Blood flow measurements in the splenic artery | 93 |
| Table 4.3: | Blood flow measurements in the common hepatic artery | 95 |
| Table 4.4: | Blood flow measurements in the proper hepatic artery | 97 |
| Table 4.5: | Blood flow measurements in the right hepatic artery | 99 |
| Table 4.6: | Blood flow measurements in the superior mesenteric artery | 100 |

| | | |
|-------------|--|-----|
| Table 4.7: | Weighted average blood flow measurements of each artery and flow percentages of various parent vessels | 101 |
| Table 4.8: | Blood flow measurements in patients with liver tumors | 103 |
| Table 4.9: | Representative mean Reynolds numbers in the hepatic arterial system | 105 |
| Table 4.10: | Variables used in the flowchart diagrams | 115 |
| Table 4.11: | Physical interpretations of each electrical circuit component | 123 |
| Table 4.12: | Optimization constraints of each Windkessel model | 128 |
| Table 4.13: | Parameters of the different Windkessel models | 132 |
| Table 4.14: | Time delay between systolic pressure and max. flow in the RHA waveforms | 134 |
| Table 5.1: | Particle shear-stress calculations for Stokes flow | 171 |
| Table 6.1: | Catheter flows and their relation to the arterial velocity | 221 |
| Table A4.1: | Maximum particle Reynolds numbers in the AAA sac | 301 |

LIST OF FIGURES

| | | |
|--------------|---|----|
| Figure 1.1: | Primary cells in whole blood..... | 6 |
| Figure 1.2: | Flowchart describing simplified thrombosis pathway..... | 9 |
| Figure 1.3: | (a) Medical diagram of healthy vs. aneurysmal abdominal aorta and (b) A patient-specific AAA geometry | 10 |
| Figure 1.4: | (a) Three layers of ILT and their structure and (b) ILT identified in a patient's CT-scan | 12 |
| Figure 1.5: | Liver with widespread presence of pancreatic metastatic tumors..... | 22 |
| Figure 1.6: | (a) Increasing size of tumor with its different layers of activity and (b) Laird (1964) Gomertzian tumor growth function with different proliferation rate constants..... | 23 |
| Figure 1.7: | (a) Illustration of hypervascular liver tumor with necrotic core and (b) Association of tumor blood vessel morphology with characteristics of local blood flow in the tumor vessels after Tanaka et al. (1990)..... | 25 |
| Figure 1.8: | Illustration of ⁹⁰ Y-microsphere delivery and transport to liver tumors | 28 |
| Figure 1.9: | Vials of ⁹⁰ Y-microspheres and their corresponding delivery apparatuses | 29 |
| Figure 1.10: | Treatment flowchart of Y90-microsphere brachytherapy | 32 |
| Figure 2.1: | Apparent viscosity vs. shear rate curve of the Quemada model | 38 |
| Figure 2.2: | (a) Symmetric, single bifurcation computational domain with locations of velocity profile measurement and (b) Numerical velocity profiles calculated by ANSYS CFX and experimental velocity profiles of Zhao and Lieber (1994) | 46 |
| Figure 2.3: | Two-dimensional computational domain of a rectangular backstep . | 47 |

| | | |
|--------------|---|----|
| Figure 2.4: | Comparison between 2D numerical calculations and 3D experimental data of recirculation lengths of a rectangular backward facing step..... | 48 |
| Figure 2.5: | Annular geometries of ^(a) an axisymmetric outward expansion and ^(b) an axisymmetric inward expansion..... | 49 |
| Figure 2.6: | Comparison between ANSYS CFX and published calculations of recirculation lengths of axisymmetric ^(a) outward annular expansions and ^(b) inward annular expansions | 50 |
| Figure 2.11: | Computational geometry and dimensions to represent the physical experiment of Bushi et al. (2005)..... | 51 |
| Figure 2.12: | Comparison between the numerical and Bushi et al. (2005) exit fractions of 0.6 [mm] particles exiting the single bifurcation domain | 53 |
| Figure 2.7: | Computational geometry and dimensions used in particle deposition validation | 55 |
| Figure 2.8: | Numerical deposition efficiency of present model predictions compared against the experimental results of Piu et al. (1987) | 56 |
| Figure 2.9: | Computational geometry and geometric parameters used in double-bifurcation particle deposition validation | 57 |
| Figure 2.10: | Comparison between numerical and experimental deposition efficiencies of the Kim and Fisher (1999) double bifurcation geometry | 58 |
| Figure 3.1: | Patient's AAA volume history and accompanying geometries | 63 |
| Figure 3.2: | Wall shear stress vectors with and without inlet boundary extension | 64 |
| Figure 3.3: | Primary and secondary flow fields of AAA meshes | 66 |
| Figure 3.4: | Velocity profiles of all meshes in one AAA plane | 67 |
| Figure 3.5: | Anatomic configurations of the hepatic arterial system | 71 |

| | | |
|--------------|---|-----|
| Figure 3.6: | Artist rendering of Type 1 hepatic arterial system and symmetric, representative hepatic artery geometry | 72 |
| Figure 3.7: | Core features of hepatic arterial system mesh | 74 |
| Figure 3.8: | Location of geometric points where solution values of each mesh are compared | 75 |
| Figure 3.9: | Qualitative comparison of velocity field magnitudes along symmetry plane | 76 |
| Figure 3.10: | ^(a) SMC domain connected to representative CHA domain and ^(b) Detailed sketches of the SCM computational domain | 78 |
| Figure 3.11: | Computational mesh of the SMC domain | 79 |
| Figure 3.12: | Patient-inspired hepatic arterial system geometry | 81 |
| Figure 3.13: | Velocity profile data at lines one and two in the patient-inspired hepatic artery geometry from the different meshes | 83 |
| Figure 3.14: | Velocity profile data at lines three and four in the patient-inspired hepatic artery geometry from the different meshes | 84 |
| Figure 4.1: | Inflow and outlet pressure waveforms used in the AAA study | 89 |
| Figure 4.2: | Macro and micro anatomy of the human liver | 91 |
| Figure 4.3: | Raw pressure data from the Radi PressureWire® | 107 |
| Figure 4.4: | Waveform spectra and color Doppler images in the patient's hepatic arteries | 107 |
| Figure 4.5: | Raw pressure data from zero to five seconds | 108 |
| Figure 4.6: | Smoothing response using an eleven-point moving average filter ... | 110 |
| Figure 4.7: | ^(a) Filter response and ^(b) effect on frequency power spectrum of 2 nd Derivative Data | 112 |
| Figure 4.8: | Raw and filtered data of downstream pressure waveforms from zero to three seconds | 112 |

| | | |
|--------------|---|-----|
| Figure 4.9: | Flowchart of algorithm used to track individual waveforms and periods | 116 |
| Figure 4.10: | Flowchart of algorithm used to isolate individual waveforms | 117 |
| Figure 4.11: | Representative mean pressure waveforms with one standard deviation and range of values | 119 |
| Figure 4.12: | Mean velocity waveforms from ultrasound spectra | 119 |
| Figure 4.13: | Histograms of the pressure waveforms' periods | 120 |
| Figure 4.14: | Scatter plots of the periods from each pressure waveform | 121 |
| Figure 4.15: | Patient-inspired flow rate waveforms and corresponding equations . | 122 |
| Figure 4.16: | ^(a) Physical sketch of Windkessel reservoir and ^(b) Electrical circuits of the utilized Windkessel models | 123 |
| Figure 4.17: | Flowchart of custom MATLAB Windkessel algorithm and population averaged SMA inflow waveform calculation | 130 |
| Figure 4.18: | Validation of Fourier transforms and frequency-based computational algorithm of Windkessel flow waveform calculation | 131 |
| Figure 4.19: | Impedance modulus and phase angle vs. nondimensional frequency (Hz.* = 1 / nondimensional time unit) | 132 |
| Figure 4.20: | RHA flow waveforms of population average Windkessel models and patient-specific data sets | 133 |
| Figure 4.21: | SMA inflow and outflow waveforms from the patient and population-averaged Windkessel data sets | 134 |
| Figure 4.22: | LHA flow waveforms of patient and population-averaged Windkessel data sets | 135 |
| Figure 5.1: | AAA domain with inlet/outlet extensions and waveforms | 139 |
| Figure 5.2: | Velocity profile at the terminal end of the AAA inlet extension | 144 |
| Figure 5.3: | Velocity streamlines in the AAA throughout the arterial pulse | 146 |
| Figure 5.4: | Transient velocity vectors on axial plane of AAA sac | 147 |

| | | |
|--------------|--|-----|
| Figure 5.5: | Transient secondary flow fields in the AAA sac | 148 |
| Figure 5.6: | Transient cross-sectional plots of dynamic viscosity in the AAA sac | 150 |
| Figure 5.7: | Transient contours of dynamic viscosity along the AAA sac wall ... | 151 |
| Figure 5.8: | Magnitudes of time-averaged velocity vector components | 153 |
| Figure 5.9: | Time-averaged viscosity inside the AAA sac and along the AAA wall | 153 |
| Figure 5.10: | Magnitude of the time-averaged WSS vector components | 154 |
| Figure 5.11: | OSI contours along the AAA wall | 156 |
| Figure 5.12: | Transient mean exiting flow distribution, particle exit fractions, and particle injection fractions | 158 |
| Figure 5.13: | Particle depositions along the AAA sac wall | 159 |
| Figure 5.14: | Transient particle trajectories that exit the AAA domain | 160 |
| Figure 5.15: | Transient particle trajectories that remain in the AAA sac | 160 |
| Figure 5.16: | Spatial regions of the AAA sac with their numbering system | 162 |
| Figure 5.27: | Cross-sectional and three dimensional views of the AAA near-wall region | 163 |
| Figure 5.18: | Number of particles in each near-wall region at 2.4, 3.6, 4.8, and 6.0 seconds (error bars = $\pm 5\%$) | 164 |
| Figure 5.19: | Near-wall particle distribution throughout the AAA sac at 2.4, 3.6, 4.8, and 6.0 seconds | 165 |
| Figure 5.20: | Shear stress on the PLTs and WBCs in the AAA sac from 2.4 to 6.0 seconds | 167 |
| Figure 5.21: | Time-averaged particle shear stress magnitudes in the near-wall regions of the AAA lumen | 169 |
| Figure 5.22: | Fluid residence time distribution in AAA lumen along AAA wall after five periods of pulsatile flow | 172 |
| Figure 5.23: | Relative near-wall residence time derived from OSI | 173 |

| | | |
|--------------|--|-----|
| Figure 5.24: | Regional distribution of particle near-wall residence times for PLTs, RBCs, and WBCs | 175 |
| Figure 5.25: | (a) History of AAA and ILT development and (b) Qualitative correlation between future ILT presence and previous AAA particle-hemodynamics | 178 |
| Figure 6.1: | (a) Representative common hepatic artery domain with implemented waveforms, (b) Patient-inspired replaced common hepatic artery domain with implemented waveforms, and (c) Representative common hepatic artery domain with SMC attachment and implemented waveforms | 181 |
| Figure 6.2: | (a) Flow distributions and (b) Symmetry-plane velocity fields at steady Reynolds number of 1150 | 185 |
| Figure 6.3: | Global and local flow distributions under steady physiologic inflow magnitudes | 186 |
| Figure 6.4: | Particle global exit fractions of those injected at the domain inlet and past the bifurcation | 187 |
| Figure 6.5: | Particle release maps of different injection planes under steady flow | 188 |
| Figure 6.6: | Particle release maps at the inlet injection plane for different branch vessel pressures | 189 |
| Figure 6.7: | Particle release maps of varying density particles and gravity directions | 190 |
| Figure 6.8: | (a) Daughter vessel one targeting by selecting appropriate particle release position and (b) Targeting other daughter vessels with different cross sectional positions | 192 |
| Figure 6.9: | Transient flow fields in the symmetric CHA domain | 193 |
| Figure 6.10: | Time-averaged velocity profiles in the symmetric CHA domain | 194 |
| Figure 6.11: | Streamlines at recirculation regions in daughter vessels two and three | 195 |
| Figure 6.12: | Primary non-dimensional recirculation lengths over physiologic pulse (Error bars are arbitrarily set at $\pm 3\%$ and D_o is the outlet diameter) | 196 |

| | | |
|--------------|--|-----|
| Figure 6.13: | (a) Flow rate and pressure waveforms through each outlet and (b) Mean, max., and min. flow rates through each vessel outlet | 197 |
| Figure 6.14: | (a) Temporal particle release zones during the inflow waveform and (b) cross-sectional particle release position | 198 |
| Figure 6.15: | Influence of release time on particle trajectories (Red = SIR-Spheres®, Blue – TheraSpheres®) | 199 |
| Figure 6.16: | Magnified trajectories of ⁹⁰ Y particles injected in the deceleration phase exiting through daughter vessel two | 201 |
| Figure 6.17: | Magnified trajectories of ⁹⁰ Y particles injected in the deceleration phase exiting through daughter vessel three | 202 |
| Figure 6.18: | (a) Particle inlet percentages through each outlet and (b) maximum traveling times through each outlet for a single pulse (Error bars are ±3% of graph value) | 204 |
| Figure 6.19: | Particle release maps of SIR-Spheres® and TheraSpheres® for each time-zone (Red = Daughter 1 , Blue = Daughter 2 , Green = Daughter 3 , Orange = Daughter 4) | 205 |
| Figure 6.20: | (a) SIR-Spheres® particle release map of accelerating injection time-zone (b) TheraSpheres® particle release map of the accelerating time-injection zone (Light grey spheres represent particles that do not exit after one pulse) | 207 |
| Figure 6.21: | Spatial release position and particle trajectories for (a)transient simulation targeting daughter vessel two and (b)transient simulation targeting daughter vessel four | 208 |
| Figure 6.23: | Velocity profiles at terminal end of SMC | 211 |
| Figure 6.24: | Transient flow recirculation at the terminal end of the SMC | 212 |
| Figure 6.25: | Transient flow fields in the SMC domain at plane y = 0 | 213 |
| Figure 6.26: | Particle trajectories altered by flow recirculation near the SMC | 214 |
| Figure 6.27: | Particle release maps with and without the SMC | 215 |
| Figure 6.28: | Global exit fractions of all transient fluid-particle simulations in representative CHA domains | 216 |

| | | |
|--------------|--|-----|
| Figure 6.29: | ^(a) Velocity vector field at the $y = 0$ plane and ^(b) global flow distribution of steady flow representing transient flow | 218 |
| Figure 6.30: | Steady particle release maps and global exit fractions | 219 |
| Figure 6.31: | Flow fields near SMC under the different SMC outflow magnitudes | 221 |
| Figure 6.32: | General CHA flow fields under the different SMC outflow magnitudes for the 45° SMC-orientation | 222 |
| Figure 6.33: | Global flow distribution under different SMC outflow magnitudes .. | 223 |
| Figure 6.34: | ^(a) Particle trajectories and ^(b) Global exit fractions under different SMC outflow magnitudes | 224 |
| Figure 6.35: | Velocity field at midpoint of accelerating region of the inflow waveform for the forty-five degree SMC-CHA domain | 226 |
| Figure 6.36: | ^(a) Particle trajectories and ^(b) Global particle exit fractions for transient SMC delivery of particles | 227 |
| Figure 6.37: | Cross-sectional planes in patient-inspired geometry | 229 |
| Figure 6.38: | Velocity magnitudes at RHA and LHA planes for each inlet waveform's systolic velocity | 230 |
| Figure 6.39: | Velocity magnitudes at the CHA planes for different time points and each inlet waveform | 231 |
| Figure 6.40: | Inflow waveform influence on particle release maps | 232 |
| Figure 6.41: | ^(a) Global particle exit fractions and ^(b) global flow distribution of each inflow waveform | 233 |
| Figure A4.1: | Streamline plots of steady flow through an AAA | 292 |
| Figure A4.2: | Secondary velocity vector plots in the AAA sac | 293 |
| Figure A4.3: | Non-Newtonian viscosity ratio contours throughout the AAA | 295 |
| Figure A4.4: | WSS contours and vector field on the AAA wall | 296 |
| Figure A4.5: | Steady flow distribution, particle exit fractions, and particle injection fractions | 298 |

| | | |
|---------------|---|-----|
| Figure A4.6: | ^(a) Deposition efficiency in the AAA vs. particle Stokes Number and ^(b) Injection fraction of particles left in AAA domain | 300 |
| Figure A4.7: | Particle trajectories under the different steady flow fields | 302 |
| Figure A4.8: | Residence time distribution in the AAA sac | 303 |
| Figure A4.9: | Contours of residence time distribution along the AAA wall | 304 |
| Figure A4.10: | Particle trajectory maps in the AAA domain | 305 |
| Figure A4.11: | Particle release maps at the particle injection plane | 306 |

NOTATION AND SYMBOLS

Abbreviations

| | |
|-----------------|------------------------------|
| AAA | Abdominal Aortic Aneurysm |
| ILT | Intraluminal Thrombus |
| RBC | Red Blood Cell (Erythrocyte) |
| WBC | White Blood Cell (Leukocyte) |
| PLT | Platelet |
| HCC | Hepatocellular Carcinoma |
| SMC | Smart Micro-Catheter |
| WK | Windkessel |
| CHA | Common Hepatic Artery |
| PHA | Proper Hepatic Artery |
| RHA | Right Hepatic Artery |
| LHA | Left Hepatic Artery |
| SMA | Superior Mesenteric Artery |
| GDA | Gastroduodenal Artery |
| ^{90}Y | Yttrium-90 |

Chapter 1:

Research Motivation, Research Objectives, and Background Information

1.1 Research Motivation

1.1.1 Abdominal Aortic Aneurysms and Intraluminal Thrombus Development

Aneurysm rupture is the 13th most common cause of death in the Western World where abdominal aortic aneurysm (AAA) rupture has been reported as the tenth leading cause of death in the United States (Choke et al., 2005; Silverberg et al., 1990). Furthermore the frequency of AAA rupture has not decreased over several years, revealing the pathological condition has the potential to be a long-term presence in the medical field (Hans et al., 2005). The physico-biochemical causes of AAA rupture are not fully understood (Vorp, 2007; Vorp et al., 2005; Kleinstreuer and Li, 2006; among others). Often associated with aneurysms is a

layer of intraluminal thrombus (ILT) that forms along the luminal side of aneurysm wall and is present in approximately 75% of all AAAs (Vorp et al., 2001). The ILT has been repeatedly shown to be a source of proteolytic activity; condensed inflammatory response; site of local wall thinning, weakening, and hypoxia; and a factor in the overall risk of aneurysm rupture and development (Houard et al., 2007; Vande Geest et al., 2006a; Swedenborg and Eriksson, 2006; Houard et al., 2006; Kazi et al., 2003; Vorp et al., 2001; Vorp et al., 1996). Despite the established influence of ILT on general AAA pathology, there have been few studies that can test hypotheses and theories of ILT development over time. Biological experiments are difficult to utilize in answering such questions since many studies require the biopsied ILT samples, which cannot be easily obtained from an AAA patient's ILT over the development of the AAA and corresponding ILT. The current study seeks to increase the overall understanding of AAA pathology and conduct pioneering computational analyses that test the hypothesis that the primary cellular components of blood (erythrocytes, leukocytes, and platelets) become activated and/or entrapped in general regions of future ILT development, where their ultimate fate is to attach to the AAA luminal wall or existing ILT.

1.1.2 Yttrium-90 Microsphere Transport and Liver Targeting

Hepatocellular carcinoma is the third leading cause of cancer-related death and the most frequent form of primary liver cancer (Bruix and Sherman, 2005; Cabibbo et al., 2009; Kennedy et al., 2004). In recent years the number of reported cases has been steadily increasing in developed Western nations (Befeler and Di Bisceglie, 2002). Additionally, primary liver tumors are the fifth most common cause of cancer related death and metastatic tumors are the most common locations of spreading colorectal cancer, with about 50% of

such patients developing metastatic liver tumors (Bosch et al., 1999; Liu et al., 2003). Despite the high prevalence of primary and metastatic liver tumors, they are among the more challenging medical situations that oncologists face due to the complex arterial vessel morphology and wide range of anatomic configurations. A rising therapy for liver tumor cell treatment is the local delivery of Yttrium-90 (^{90}Y) radiation via the injection of radiation equipped microspheres into the hepatic arteries, where they are hopefully delivered preferentially to the tumor cells due to enhanced arterial vessel density around tumor cells. The ^{90}Y microspheres have sufficient potency to both partially embolize the very small arterial vessels supplying the tumor and deliver intense radiation locally to destroy the tumor cells. The ultimate treatment goal is to deliver potent radiation to tumor cells via the enhanced arterial blood supply of the tumor, thereby causing minimal damage to the surrounding healthy liver tissue and negligible microsphere migration to other organs. While theoretically ^{90}Y microsphere therapy should be the prevalent treatment of liver tumors after surgery, the use of ^{90}Y microspheres is often a “last-resort” therapy. The main reason is that its efficacy to selectively target the tumor cells with minimal damage to healthy tissue has not been demonstrated in expansive clinical trials. The current study seeks to investigate ^{90}Y -microsphere transport via computational simulations of particle-hemodynamics in the hepatic arteries with the intention of identifying primary influences on particle transport and providing parameters needed for targeting specific arterial vessels connected to tumors for ^{90}Y -microsphere delivery. Such information will hopefully enhance oncologists’ ability to effectively treat liver tumors and improve the current technique of ^{90}Y -microsphere radioembolization.

1.2 Research Objectives

Computational particle-hemodynamics analyses utilizing a one-way coupled Eulerian-Lagrangian particle transport model were implemented to investigate high-risk sites of future ILT development in AAAs and the transport of ^{90}Y -microspheres in the hepatic arteries. The same theory and particle transport model were employed to consider two distinct biological conditions, each with a high level of severity that warrants in-depth analyses to provide further understanding of the pathological condition and potentially improve medical treatments.

1.2.1 Abdominal Aortic Aneurysms and Intraluminal Thrombus Development

Specifically, the particle-hemodynamics analyses will investigate potential relationships between blood-particle trajectories, local residence times, and shear/drag force exposure histories and regions of future ILT development. Additional variables such as an Eulerian regional time distribution will also be used to determine the regions of elevated particle residence times. A representative AAA pre-treatment geometry of a patient tracked over almost two years, was utilized for this study. The aforementioned parameters of particle-hemodynamics are calculated in the AAA lumen at a time point with little thrombus and compared with regions of measurable ILT development throughout the patient's AAA development.

The primary goal of the study is to test the hypothesis that critical particle-hemodynamics contributes to ILT formation. Specifically, blood particles are entrapped within zones of flow separation, clotting mechanisms are activated by critical shear forces, and blood particles aggregate in those regions close to the AAA wall where they may affix,

forming the ILT. Outcomes from the study are aimed at furthering the understanding of ILT development along with providing new information to medical practitioners identifying patients at risk and improving their treatment of AAAs.

1.2.2 Yttrium-90 Microsphere Transport and Liver Targeting

Currently, there has been little published research to model the trajectories of ^{90}Y -microspheres once they are injected into the hepatic arteries. With the aforementioned statistics on liver tumor prevalence and rise in frequency, research studies seeking to improve current clinical methods are crucial to advancing radiation oncologists' ability to effectively treat the increasing number of patients afflicted with liver tumors. The implemented particle-hemodynamics simulations provide, detailed insight to the primary influences affecting the injected particles' trajectories and exit locations. The focus will be given to identifying parameters that enable a new degree of ^{90}Y -microsphere control, and provide radiation oncologists with the ability to direct the injected particles toward specified daughter vessels and/or avoid specific vessels that support healthy organs.

Primary outcomes of the study include novel quantification of the transient hemodynamics in the hepatic arterial system, the identification of hemodynamic parameters that will aid oncologists in ^{90}Y -microsphere treatment planning, and provide novel parameters for targeting specific daughter vessels of the liver hepatic arteries. Additional research goals are to provide justification for increased clinical research aimed at further quantifying the transient hemodynamics of the hepatic arteries on a wide range of patients and determining ^{90}Y -microsphere brachytherapy's efficacy as a liver tumor treatment after surgery.

1.3 Primary Cellular Components of Whole Blood

Human blood contains four primary components: plasma, erythrocytes/red blood cells (RBCs), leukocytes/white blood cells (WBCs), and platelets (Marieb, 1998; Kleinstreuer, 2006). Plasma is the liquid phase of blood and on average makes up approximately 55% of a given volume of blood, whereas RBCs make up approximately 44-45%, and WBCs and platelets make up approximately 0.7% (Marieb, 1998). The concentration of RBCs within whole blood has been labeled the Hematocrit (Ht) and is often used to discern the severity of chronic pathological conditions (i.e., diabetes). The suspended cells within the blood plasma are responsible for the shear-thinning behavior exhibited by whole blood (Buchanan et al., 2001; Nichols and O'Rourke, 2005; Kleinstreuer, 2006).

RBCs have a biconcave shape with a diameter of about $8\mu\text{m}$ and are responsible for transporting nutrients to the body organs and tissue. WBCs are the “workhorse” cells of the immune system that attack foreign objects in the body and have a spherical shape with a diameter of $10\text{--}15\mu\text{m}$. Platelets are the smallest cells with a diameter of about $2\mu\text{m}$ and are actively involved in the clotting abilities and thrombus formation of blood (Hochmuth, 1986; Schmid-Schoenbein, 1986).

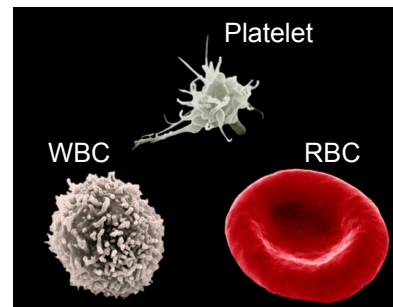


Figure 1.1: Primary cells in whole blood

After: <http://c.photoshelter.com/img-get/I0000bD6Ylr5NRqQ/s/600>

Figure 1 illustrates the three primary cells suspended in the blood plasma whereas Table 1.1 lists common ranges of the cells' physical characteristics.

Table 1.1: Properties of particles suspended in whole blood

| <u>Property</u> | <u>RBCs</u> | <u>WBCs</u> | <u>Platelets</u> |
|------------------------------|-------------|-------------|------------------|
| Density [kg/m ³] | 1093-1100 | 1065-1090 | 1040 |
| Diameter [μm] | ≈ 8.0 | 10-15 | 2.0 |

1.4 Platelet Plug Formation, Blood Coagulation, and Thrombosis

Platelets are the first response cells to damage signals emitted by the arterial cellular components. They normally do not stick to each other or the endothelial cells that line that arterial wall. However, when platelets contact exposed collagen fibers, they begin to rapidly adhere to the collagen molecules, degranulate into cellular components losing their individual identity and release phospholipids (such as adenosine diphosphate (ADP)), which are powerful aggregating agents that attract and collect more platelets to cover the exposed collagen. After sufficient platelets have been recruited to the area and sealed the damaged region, a platelet plug begins to form and the blood coagulation process in the area surrounding the plug begins. Blood coagulation is a normal physiological process that transforms the blood near the platelet plug from a liquid to a gel or viscoelastic solid. The body initiates the chemical pathways when blood vessel cellular constituents (primarily smooth muscle cells, collagen fibers, and endothelial cells) are damaged and express chemical signals that combine with the recruited platelets and react with the native components of blood plasma (e.g., Calcium, phospholipids, etc.) to produce prothrombin activator. The complex substance converts the plasma protein prothrombin into the enzyme thrombin, which catalyzes soluble fibrinogen molecules already in the blood plasma into an

insoluble fibrin mesh. After sufficient time the thrombin reacts with local Calcium ions to synthesize fibrin stabilizing factor that binds the fibrin mesh together yielding a cross-linked fibrin polymer that may be capable of bearing mechanical loads. Amidst the fibrin mesh generation, the cross-linked polymer attracts and traps surrounding cellular components of blood regardless of their activation state and hence RBCs, WBCs, also can become part of cross-linked polymer structure. In normal physiological function, platelet activation is limited to the distinct region(s) of interest due to the endothelial cell production of prostacyclin, which is a powerful inhibitor of platelet activation, and prevents platelets from adhering to undesired locations along the arterial wall. The entire process is a complex positive feedback loop that relies on rapid activation and deactivation to effectively respond to injury and disengage once the damaged cells have been sealed (Marieb, 1998).

When the feedback mechanism malfunctions or if the coagulation and clotting mechanism are initiated in undesirable situations, a clot can form in unbroken blood vessels. Thrombosis is defined as the formation of a blood clot (thrombus) inside an artery or vein that has been shown to persist over a period of time. Platelets, RBCs, glycoproteins (GPs) and in some cases cross-linked fibrin polymer molecules are present in thrombi, with platelets being the prominent component. In addition to the biochemical pathways of the normal clotting and coagulation mechanism, the local hemodynamic shear forces (both low and high) combined with elevated collisions with the arterial wall activate the platelets to adhere to the arterial wall by attaching to local GPs and/or aggregate that can form a platelet plug (Kleinstreuer, 2006). Figure 1.2 illustrates the simplified thrombosis pathway through a visual flowchart.

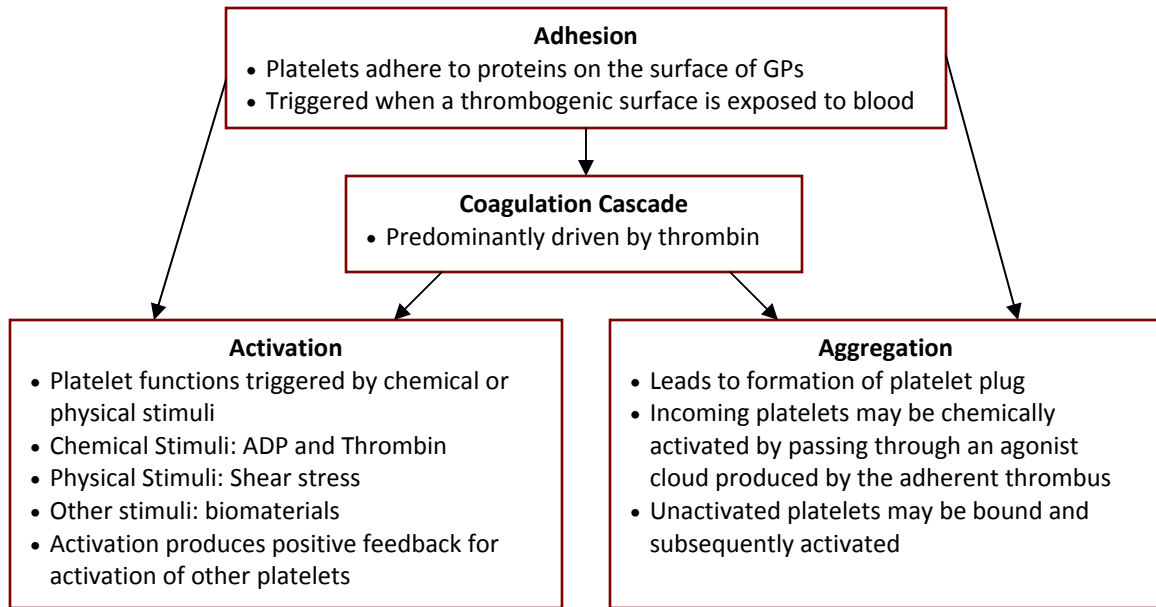


Figure 1.2: Flowchart describing simplified thrombosis pathway
After: Longest, 2002

1.5 Abdominal Aortic Aneurysms and Intraluminal Thrombus

1.5.1 General Information on Abdominal Aortic Aneurysms

Abdominal aortic aneurysms (AAAs) are permanent local ballooning of the abdominal aorta that result in irreversible changes to the arterial wall and an elevated risk of mortality due to potential aneurysm rupture. The pathological conditions of AAAs invoke multifaceted biological changes of varying scales that are seen in matrix metalloproteinase, proteolytic, and other biochemical imbalances; local sites of increased inflammation; irregular hemodynamics with massive flow separation; increased vessel tortuosity; loss of vessel wall elasticity with local calcifications, increased anisotropy, and reduced wall strength; degradation of arterial wall cellular components, and the presence/development of mural thrombi along the luminal side of arterial wall named the intraluminal thrombus (ILT)

(Urbonavicius et al., 2009; Basciano and Kleinstreuer, 2009; Vorp, 2007; Basciano, 2007; Kleinstreuer and Li, 2006; Vande Geest et al., 2006a, 2006b; Choke et al., 2005; Vorp and Van de Geest, 2005; Vallabhaneni et al., 2004; Thubrikar et al., 2001; Vorp et al., 1996; He and Roach, 1994). Figures 1.3a,b illustrate a medical diagram of a healthy abdominal aorta vs. an abdominal aorta with an aneurysm and a patient-specific geometry of an AAA with a substantial ILT volume.

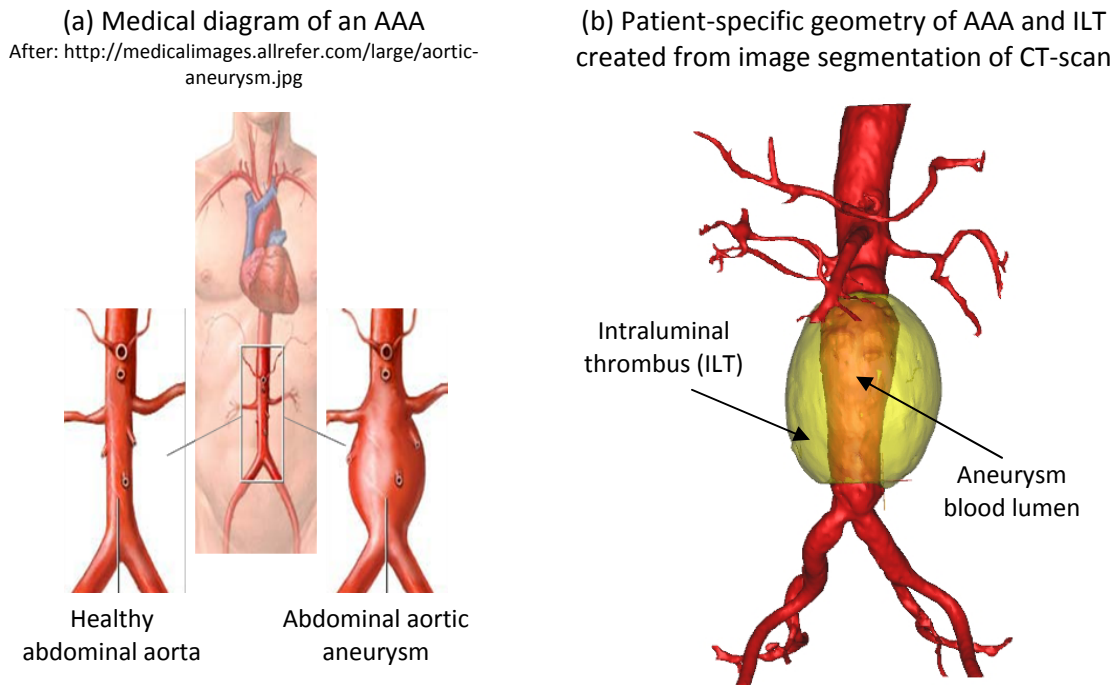


Figure 1.3: ^(a) Medical diagram of healthy vs. aneurysmal abdominal aorta and ^(b) A patient-specific AAA geometry

AAAs are treated using two main clinical techniques of open surgical repair/replacement of the abdominal aorta, and endovascular repair where a stent-graft is inserted inside the AAA lumen forming a synthetic blood vessel that shields the AAA wall from the pulsatile arterial blood pressure. Groundbreaking computational analyses by Li and Kleinstreuer (2005) revealed that successful deployment of a stent-graft can reduce the

pressure acting on the aneurysm wall by a factor of ten and the maximum wall stress by a factor of twenty. Recent investigations by Moloni et al. (2009) extended the pioneering work of Li and Kleinstreuer (2005) by conducting fluid-structure interaction analyses on pre- and post- endovascular treated patient-specific AAA geometries and reported reductions in the AAA wall pressure load and maximum wall stress of similar magnitudes. Despite the computationally demonstrated benefit of successful endovascular treatment of aneurysms, several post-treatment complications exist and require extensive routine follow-up examinations. Specifically, stent-graft migration, fatigue fracture, and endoleaks are among the most common complications and remain current issues in stent-graft design and clinical therapy (Kleinstreuer et al., 2007).

1.5.2 Composition and Mechanical Behavior of the Intraluminal Thrombus

The ILT is present in a large majority of AAA patients and has been shown by Adolph et al. (1997) and Harter et al. (1982) to be a fibrin structure composed of the cellular components of blood (RBCs, WBCs, and platelets); specific immune cells (macrophages, T-cells, neutrophils, and lymphocytes), and additional blood-borne proteins with random cellular debris. Wang et al. (2001) revealed the ILT is a heterogeneous structure composed of three distinct layers: luminal, medial, and abluminal. The luminal layer of the ILT is in contact with the flowing blood through the AAA and generally has a red color; whereas the structural integrity of the remaining ILT layers degrades with decreasing distance between the ILT the AAA wall (Ashton et al., 2009; Gasser et al., 2008; Wang et al., 2001). Figures 1.4a,b illustrate the ILT's different layers appearance and microstructure with regional identification of the ILT from a patient's CT-scan.

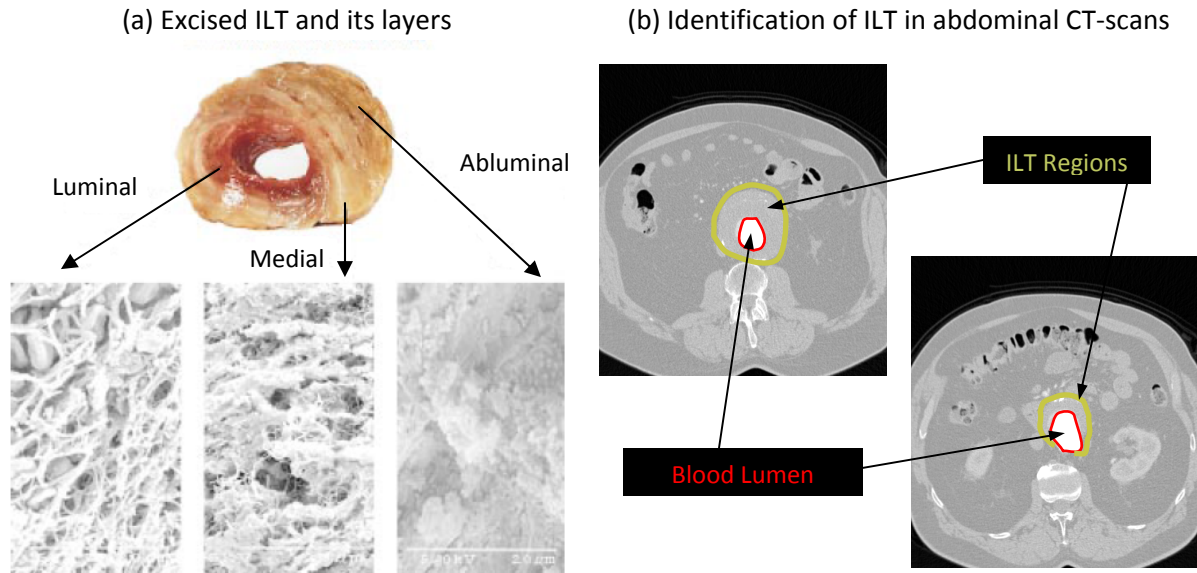


Figure 1.4: ^(a) Three layers of ILT and their structure and ^(b) ILT identified in a patient's CT-scan
 (ILT images in Fig. 1.3a used with permission from Wang et al. 2001 published by ASME)

The microstructure of the ILT layers shown in Fig. 1.4a reveal a complex network of fibrin molecules, entrapped cellular components of blood and a complex network of interconnected canniculi (Wang et al., 2001). Touat et al. (2006) and Houard et al. (2006, 2009) performed histological staining of the ILT layers and found that the luminal layer has localized regions of RBCs and/or fibrin, with widespread presence of neutrophil WBCs entrapped in regions of elevated fibrin caused by platelet accumulation; but no endothelial cells were present in the luminal layer. Their study also showed no RBCs in the medial layer, but a lessened fraction of neutrophil WBCs in a fibrin network still existed. The abluminal layer is thought to have the longest presence in the AAA, hence the its fibrin network exhibits the most degradation and Adolph et al., (1998), Touat et al. (2006), and Houard et al. (2006) found its structure

being largely acellular or its constituents were degraded to such a high degree that no cellular components could be identified.

Ex-vivo tensile tests by Gasser et al. (2008), Vande Geest et al. (2006c), Wang et al. (2001), and Di Martino et al. (1998) showed that the collective ILT structure and each individual ILT layer is capable of bearing mechanical tensile loads. Gasser et al. (2008) was the first to test the cyclic/pulsatile tensile behavior of the ILT layers, and revealed that under cyclic loads, the ILT layers failed at a load level of 60% of the layer's ultimate strength. Conversely, the ILT layers were able to sustain cyclic tensile loads that were 40% of their ultimate strength for 13.9 hours. Therefore, the ILT is susceptible to fatigue failure, which may be a key piece to predicting the onset of AAA rupture. In conjunction to the tensile data, Ashton et al. (2009), Boschetti et al., (2007), and Hinnen et al. (2007) tested the compressive behavior of the ILT structure and its individual layers using *ex-vivo* compression tests. Each study reported different levels of stiffness magnitudes, but a common trend between Ashton et al. (2009) and Boschetti et al. (2007) reported heterogeneous properties of the ILT, with the compressive modulus increasing from the luminal to abluminal layers (e.g., abluminal layer had the largest compressive stiffness). Ashton et al. (2009) also reported the highest amount of water content being present in the abluminal layer, revealing a direct relationship between the compressive stiffness and water content.

The previous studies' collective data enables the ILT to be classified as a nearly volume-conserving, nonlinear, and isotropic material. Hyperelastic theory calls the volume-conserving as incompressible, but the term is merely a mathematical formulation and does not imply that the structure cannot be compressed. For example, Truijers et al. (2009) further

characterized the ILT mechanical behavior by using dynamic CT angiography to measure the *in-vivo* compressibility of seventeen patients. Their results showed a large amount of interpatient variability in ILT compressibility during the cardiac cycle with a range of 0.4% to 43.6% compression of the overall ILT volume. The study also showed that ILT compression was inversely related to the AAA lumen's expansion, with changes in the total aneurysm volume being less than the changes in the lumen and thrombus volume. Moreover, there were no correlations with ILT compressibility and AAA size, total ILT volume, or pulse pressure; revealing that a patient's *in-vivo* ILT compressibility is most likely caused by its intrinsic biomechanical properties and constituents.

1.5.3 Influence of the Intraluminal Thrombus on the Abdominal Aortic Aneurysm Wall

The high prevalence of ILT in AAAs has inspired numerous studies investigating the influence of the ILT on the surrounding AAA wall. Analytical calculations by Vorp et al. (1998) gave initial support to the hypothesis that the ILT prevents ample oxygen diffusion to AAA wall, significantly hindering the wall's nutrient supply and eventually decreasing the wall's ultimate strength. Vorp et al. (2001) conducted an experimental study which confirmed that the ILT reduces oxygen transport to the AAA wall. Specifically, AAA walls adjacent to regions of ILT greater than 4mm in thickness exhibited greater amounts of localized hypoxia with a 60% reduction in normalized oxygen pressure at the AAA wall. Furthermore, the mean ultimate strength of AAA walls adjacent to ILT greater than 4mm thick was reduced by 36% from the strength of the aneurysm wall adjacent to no thrombus and/or ILT less than 4mm thick. Kazi et al. (2003) continued revealing biomechanical influences of the ILT on the AAA wall when showing the AAA wall completely covered in

thrombus were thinner and contained fewer, more fragmented elastin fibers than the AAA wall exposed to flowing blood. Additionally, smooth muscle cells and the extracellular matrix of the AAA wall covered in ILT were more degraded, apoptotic, and necrotic than the smooth muscle cells in the AAA wall exposed to flowing blood. Speelman et al. (2010) conducted a patient specific analysis of wall stress, thrombus volume, AAA growth rate, and AAA size finding that ILT volume is correlated with AAA growth rate supporting the claims that AAA growth rate is attributed to local wall weakening caused by the ILT.

The ILT has also been shown to be a local site of elevated inflammatory response and biochemical imbalance that aids in the AAA wall degradation. Kazi et al. (2003) showed in, that addition to thinner walls, AAA walls covered with ILT had an increased presence of inflammatory cells near or in the arterial wall compared AAA walls exposed to flowing blood. Vorp and Vande Geest (2005) reviewed that when macrophages are exposed to the hypoxic conditions of the AAA wall with large deposits of ILT, they elevate their expression of matrix metalloproteinase (MMP)-7, elastase (which degrades elastin) and cytokines. The ILT has also been reported to contain high amounts of MMP-9 with an increased presence in the luminal ILT layer, which is also shown to degrade the components of the AAA wall (Basciano, 2007; Fontaine et al., 2002; Sakalihasan et al., 1996). Panek et al. (2004) also showed that the ILT contains chemical evidence of collagenolytic activity, which is linked to AAA wall weakening and rupture. Swedenborg and Eriksson (2006) also presented evidence MMP-9 molecules in the ILT were bound in various amounts to one molecule of neutrophil gelatinase associated lipocalin, which prevents MMP deregulation and could be one of the causes for the proteolytic imbalance of the ILT. Houard et al. (2006) provided strong

evidence that the ILT (particularly the luminal layer) is biologically active and undergoes consistent renewal and fibrinolysis. The immunohistological staining of Fontaine et al. (2004) and Houard et al. (2007) provided further support of the ILT luminal layer's biological activity by revealing more plasmin α_2 -antiplasmin complexes (a fibrinolytic agent) than the other ILT layers and AAA wall coinciding with the elastase from neutrophils entrapped in the luminal ILT layer prevents recolonization of the ILT by smooth muscle cells. Previously, Lindholt et al. (2001) revealed that plasmin α_2 -antiplasmin is predictive of AAA expansion, particular in small aneurysms. In short, the ILT is not an unstructured collection of dead cells, but rather the ILT is a dynamic biologically active and responsive assortment of constituents that is being increasingly correlated with the general pathology of AAAs.

The load bearing nature of the complete ILT structure has led to multiple studies investigating whether the ILT reduces the blood pressure loads of arterial flow on the AAA wall. Primarily computational investigations using isotropic hyperelastic or incompressible linear elastic models have reported that the ILT shields the AAA wall from a portion of the arterial blood pressure (Di Martino et al., 1998; Wang et al., 2002; Georgakarakos et al., 2009; Speelman et al., 2010). However, clinical and experimental studies by Schurink et al. (2000) and Thubrikar et al. (2003) revealed that pressure readings in the AAA lumen had little difference with pressure readings between the ILT and AAA wall, inferring that the ILT does not reduce the pressure load experienced by the AAA wall. Such conflicting studies have continued to spark different theories over the influence of ILT on the load experienced by the AAA wall. Recent results and discussions by Speelman et al. (2010) and Truijers et al.

(2009) have shown a large intersubject dependence on ILT behavior and its potential influence on the ILT's load-bearing and cushioning capabilities. Other recent ventures of AAA and ILT research are investigating potential correlations between geometric and morphologic properties of the AAA lumen and the ILT, where AAA wall stress has been correlated centerline tortuosity, ILT volume, and asymmetry (Georgakarakos et al., 2010; Doyle et al., 2009; Pappu et al., 2008).

1.5.4 Theories of Intraluminal Thrombus Development in Abdominal Aortic Aneurysms

Like most pathological processes, the development of ILT is believed to be a multifaceted process. Many parallels exist between the progression of atherosclerotic plaque (atherogenesis) and the development of mural ILT in AAAs (e.g., inflammation conditions, thrombin presence, thrombosis, disturbed hemodynamics, activated platelets, etc.). A primary differentiating factor is the limited role of endothelial cells in mural ILT development compared to the atherosclerotic development observed in carotid and/or coronary arteries. Steinman et al. (2003) reviewed several studies that have shown links between disturbed hemodynamics and atherosclerosis, but also linked atherogenesis with increased permeability of the endothelial wall. Conversely, Adolph et al. (1997) showed no presence of endothelial deposition in the ILT from AAAs, which is found in many atherosclerotic plaques. Furthermore, larger aneurysms are believed to not show endothelialization and their endothelial cells on the luminal side of their arterial walls are believed to not respond to biomechanical stimuli (e.g., shear forces) that have been correlated with atherosclerotic conditions (Biasseti, et al. 2010). Plausible hypotheses regarding the ILT genesis that include

endothelial response still exist by postulating that the ILT is a result of atherosclerotic plaque rupture through the endothelial arterial layer.

A more widely accepted hypothesis is that ILT genesis is an ongoing process that involves a myriad of hemodynamic and biochemical stimuli, primarily including the activation, coagulation, and clotting of platelets. Evidence for such behavior is seen in the direct relationship between ILT and AAA volume and the reported simultaneous increase in the ILT volume as the AAA increases in volume (Speelman et al., 2010; Truijers et al., 2009; Swedengorg and Eriksson, 2006; Hans et al., 2005; Wolf et al., 1994). Furthermore, the growth rate of ILT has been shown to be an indication of elevated risk of AAA rupture (Stenbaek et al., 2000). Further support of continual ILT development during the expanding AAA is seen in the general hemodynamics of the expanding AAA geometry. Salsac et al. (2004, 2006) and Lasheras (2007) illustrated the large amounts of flow separation that is present throughout the pulsatile hemodynamics in progressively enlarging AAA geometries. Similar transient patterns of flow separation in the downstream expanding region of a stenosed vessel were shown by Raz et al. (2007) to entrap platelets and activate their clotting mechanism revealed by the direct relationship between recirculation time and platelet acetylated thrombin generation. Steady experimental and computational studies of AAA hemodynamics have shown the geometries' recirculation regions to be associated with increased platelet density and deposition along the vessel wall (Bluestein et al., 1997; Bluestein et al., 1996; Schoepfoerster et al., 1993). Yamazumi et al. (1998) also showed that AAA hemodynamics exhibit an activated state of coagulation and fibrinolysis that is correlated with the aneurysm morphology (neck angle, tortuosity, and size). Contributing to

the activated state of coagulation, Houard et al. (2006, 2007) showed elevated amounts of blood-borne proteases and fibrinolytic enzymes that are retained in the aneurysm lumen entrapped in the local patterns of flow recirculation. Touat et al. (2006) illustrated the enhanced coagulation properties of blood particles in ILT by measuring their clotting time compared against a control state of enriched media. Table 1.2 reveals the statistically significant differences in clotting time between the ILT layers and the control.

Table 1.2: Clotting times of particles in ILT layers
(From: Touat et al., 2006)

| <u>Particle Origin</u> | <u>Clotting time [s]</u> |
|------------------------|--------------------------|
| Luminal ILT | 62 ± 6 |
| Medial ILT | 120 ± 20 |
| Abluminal ILT | 110 ± 16 |
| Control | 270 |

Interestingly, the particles from the luminal ILT layer had the shortest clotting time and thus exhibited the highest degree of fibrin generation coinciding with the enhanced presence of fibrin in the luminal ILT layer mentioned in Section 1.5.2. The elevated activation level of platelets in AAAs was further illustrated by Dai et al. (2009) when by inhibiting platelet clotting, they found fewer leukocytes infiltrate the ILT and the AAA wall retained a higher degree of mechanical integrity in experimental AAAs.

1.5.5 Previous Investigations of Particle Transport in Abdominal Aortic Aneurysms

To date there have been a few studies modeling blood particle trajectories in patient-specific AAAs. However, in axisymmetric expansions representing AAAs, Schoepfoerster et al. (1993) and Bluestein et al. (1996) showed an elevated amount of platelet deposition along

the AAA wall under steady flows and correlated the enhanced deposition with circular fluid streamlines convecting the platelets towards the lumen walls. In most cases, they reported higher platelet depositions in the distal portion of the AAA sac. Basciano et al. (2009) analyzed steady flow patterns influencing particle entrapment in a patient-specific AAA with elevated particle residence times and future ILT development. Salsac et al. (2009b) used an Eulerian-Lagrangian fluid-particle methodology to model the trajectories of particles in AAAs and further confirmed that AAA hemodynamics moves platelet-like particles towards the aneurysm wall. Biasetti et al. (2010) analyzed the hemodynamics inside AAAs and showed elevated flow separation and recirculation when compared to the flow fields of a healthy abdominal aorta. That indicates, AAAs possess the necessary hemodynamic conditions coinciding with biological trends of elevated coagulation and activation of the platelet clotting mechanism. They further postulated that platelets are activated as they enter into the aneurysm bulge, and when later entrapped in the recirculation zones they preferentially attach to the already existing ILT or the AAA wall in distal regions of the vessel. Their postulate is somewhat confirmed by multiple anatomic studies showing eccentric volume distributions of ILT with some prevalence being seen in the distal anterior region of the AAA (Guimarães et al., 2008; Vega de Céniga et al. 2008; Hans et al., 2005; Muraki, 1983). The current study seeks to further investigate blood particle trajectories in AAAs and investigate potential correlations of local particle accumulation and stress-induced activation with future ILT development.

1.6 Liver Tumors and Yttrium-90 Radioembolization

1.6.1 General Information on Liver Tumors

The multiple physiologic functions of the liver (blood toxin removal, bile production, endocrine homeostasis, etc.) and the extensive network of lymph, vascular, and bile vessels throughout the liver parenchyma involve many different types of cells. Such diverse functions and interactions provide an environment that can develop a wide array of abnormalities, which is seen in the multiple types of tumors that can develop in the liver. Primary liver tumors describe malignant neoplasms that originate in the liver. The most common being hepatocellular carcinoma (HCC), which makes up 85% to 90% of all primary liver tumors and is the fifth most common form of cancer worldwide. A more rare form of primary liver tumors is cholangiocarcinoma which form malignant neoplasms along hepatobiliary vessels and in a great majority of patients is considered an incurable disease. In addition to malignant primary tumors, the liver's involvement with multiple organ systems make it the most prevalent site of metastatic malignancies, where some autopsy studies have shown existence of liver metastases up to 100% with certain forms of malignant tumors. Several benign liver tumors also exist, with the most common being hemangiomas (Jakobs, 2008; Rodrigues et al., 2008; El-Serag and Rudolph, 2007; Nakeeb et al., 1996). Figure 1.5 depicts a liver heavily inflicted with pancreatic metastatic tumors.



Image From: http://upload.wikimedia.org/wikipedia/commons/5/53/Secondary_tumor_deposits_in_the_liver_from_a_primary_cancer_of_the_pancreas.jpg

Figure 1.5: Liver with widespread presence of pancreatic metastatic tumors

Tumor growth begins with uncontrolled proliferation of cells that result in an abnormal mass of tissue. Benign tumors often show slow proliferation rates and they have a small but localized influence on the body's healthy tissue. Malignant tumors exhibit rapid proliferation and have the potential to spread its cells to other locations of the body. If left unchecked, they will kill healthy tissue by absorbing the body's nutrients (Marieb, 1998). In most tumors, only the outer shell of the tumor exhibits active growth and proliferation. In the early stages of tumor development, the entire tumor tends to exhibit an exponential growth rate, but mature tumors have been shown to exhibit a linear growth rate due to the decreasing volume of the tumor's proliferating outer shell as the overall tumor expands. Large tumors are expected to have a necrotic core that is devoid of nutrient (primarily oxygen) supply with surrounding circular layers of more active cells towards the tumor periphery (Araujo and

McElwain, 2004). Early attempts of modeling tumor growth were made by Laird (1964) who constructed a Gompertzian growth function shown in Eq. (1.1):

$$X(t) = X_f \exp\left(\ln\left(\frac{X_0}{X_f}\right) \cdot \exp(-\beta t)\right) \quad (1.1)$$

where $X(t)$, X_f , X_0 , β , and t represents the time-dependent tumor size, final tumor size, initial tumor size, constant related to tumor cell proliferation rate and time, respectively. In general $X_f > X_0$ unless the model is being used to model decrease in tumor size subsequent to clinical treatment. Figures 1.6a,b illustrate the layers of activity inside the tumor periphery as the tumor increases in size aside plots of the Gompertzian growth function (Laird, 1964). It is important to notice the exponential increase seen in the function's behavior when the tumor is small and the decreasing slope seen as the function approaches the final tumor size.

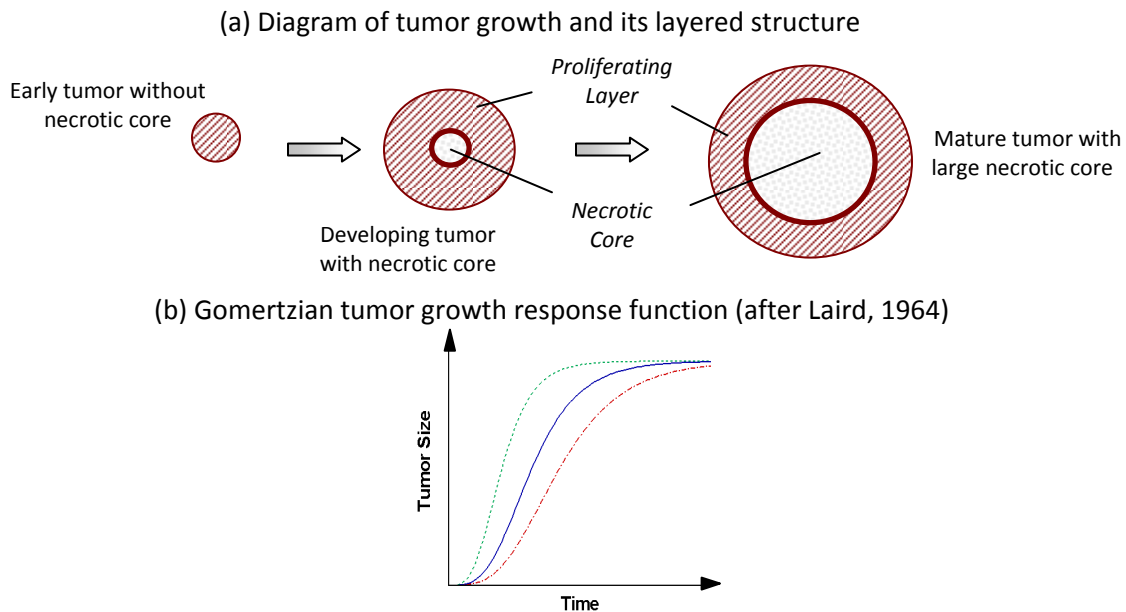
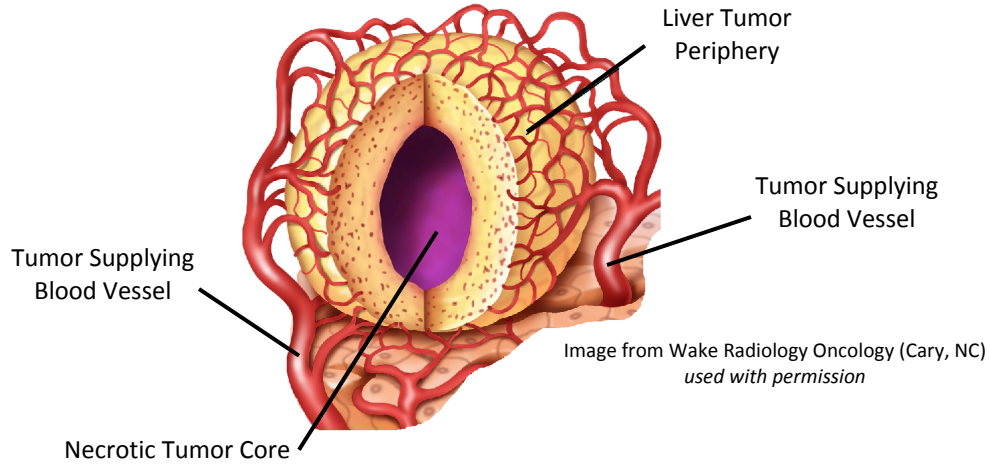


Figure 1.6: (a) Increasing size of tumor with its different layers of activity and
 (b) Laird (1964) Gompertzian tumor growth function with different proliferation rate constants

As the tumor expands, the proliferating cells require nutrients to fuel their potentially rapid growth. Tumors exhibit varying degrees of angiogenesis, which constructs new blood vessels to supply the proliferating cells with essential nutrients for their survival and continued growth (Araujo and McElwain, 2004). If local neovascularization occurs at elevated levels to create an abnormal increase in local blood vessel density to surrounding tissue density, the tumor is considered to be hypervascular. Due to the high baseline degree of vascularization present in the liver without the presence of tumor cells, most liver tumors exhibit hypervascular behavior. This can be utilized for specific methods of liver tumor treatment (e.g., embolization or intra-arterial drug-delivery therapies). Tanaka et al. (1990) used color Doppler flow imaging to ascertain the flow patterns in blood vessels supply the tumors with nutrients and found preferred correlations between local vessel morphology and the transient nature of the flow inside the tumor vessels. Figure 1.7a depicts a hypervascular liver tumor with necrotic core via a medical diagram while Figure 1.7b illustrates the vessel morphologies and associated transient flow patterns reported in Tanaka et al. (1990).

[See next page for Fig. 1.7]

(a) Medical illustration of hypervascular liver tumor with necrotic core



(b) Vessel morphology and transient flow in tumor supplying blood vessels

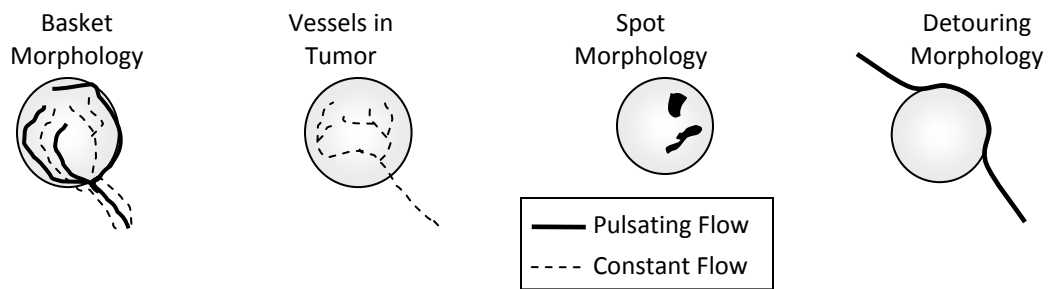


Figure 1.7: (a) Illustration of hypervascular liver tumor with necrotic core and (b) Association of tumor blood vessel morphology with characteristics of local blood flow in the tumor vessels after Tanaka et al. (1990)

Ackerman et al. (1969) analyzed to which vascular system (arterial vs. venous) tumor angiogenesis constructed the most supplying vessels, and found that metastatic tumors greater than 3mm had 80% to 100% of their blood flow supplied by arterial connections. Lien and Ackerman (1970) supplemented the previous study with experimental analyses of healthy and tumor arteriole and capillary morphology in the liver and found that tumors had

the potential to profoundly impact the vascular morphology. Table 1.3 lists the ranges of their experimental results.

Table 1.3: Tumor vascular morphology

After Lien and Ackerman (1970)

| <u>Vessel Characteristic</u> | <u>Normal</u> | <u>Tumor</u> |
|--------------------------------------|---------------|--------------|
| Arteriole Diameter [μm] | 20-30 | 25-75 |
| Capillary Diameter [μm] | 8 | 8-50 |
| Vessel Density | NA | 3 to 200x |

Narrowing the diameter range, Kennedy et al. (2004) asserted that distal tumor capillaries are expected to have diameters between 8-10 μm , revealing a noticeable variation in tumor vessel diameters around the tumor.

In addition to their proliferating characteristics, liver tumors exhibit much higher tolerance to radiation than healthy liver tissue. A quantitative measure of patient absorbed radiation dose is specified in terms of energy per unit mass called grays (Gy), where 1Gy = 1 J/kg. Dawson et al. (2000) showed that the radiation dose required to destroy solid tumors was ≥ 70 Gy which is far greater than the liver tolerance dose of 35 Gy delivered to the whole liver in 1.8 Gy/d fractions. Higher doses of radiation have been recommended by Lau et al. (1994) who showed that patient survival from HCC was increased if the tumors received ≥ 120 Gy. Thus, tumor treatment using system-wide radiation introduces significant challenges of sparing healthy liver tissue while administering sufficient radiation to kill the targeted liver tumor cells.

1.6.2 Yttrium-90 Radioembolization of Liver Tumors

A rising medical treatment that holds promise for improving liver tumor healthcare is ^{90}Y -radioembolization, a form of intra-arterial brachytherapy that attempts to locally deliver intense doses of ^{90}Y -radiation to the proliferating tumor cells while sparing the healthy liver tissue. In short, micron-size particles containing the ^{90}Y -radioisotope (termed ^{90}Y -microspheres) are injected into the supplying arteries of the liver via an intravascular catheter. Currently relying on enhanced blood flow through the tumor supply vessels, the expectation is that most of the ^{90}Y -microspheres become preferentially and permanently embedded in and around the tumor. Once the ^{90}Y -microspheres have reached their terminal locations, the ^{90}Y -radioisotope delivers local radiation as it decays, killing the surrounding tumor cells.

Yttrium-90 radiation emitted by the microspheres is composed solely of beta waves and decays to stable zirconium-90 with a half-life of 64.2 hours, making the radiation from the treatment 99% decayed in less than three weeks. The emitted beta rays enable localized radiation with most of the radiation delivered within 2-4mm of the source, a tissue penetration of approximately 2.5mm, and a maximum range of influence approximately 11mm. While their narrow regions of influence make beta waves ideal for brachytherapy applications, they also introduce new challenges of imaging resolution since nuclear medicine detectors are currently unable to readily image pure beta sources (Kennedy and Salem, 2010; Kennedy, 2010). Figures 1.8 illustrates the injection and transport of ^{90}Y -microspheres to a liver tumor and the radiation cloud that envelopes the tumor periphery upon successful implantation of ^{90}Y -microspheres.

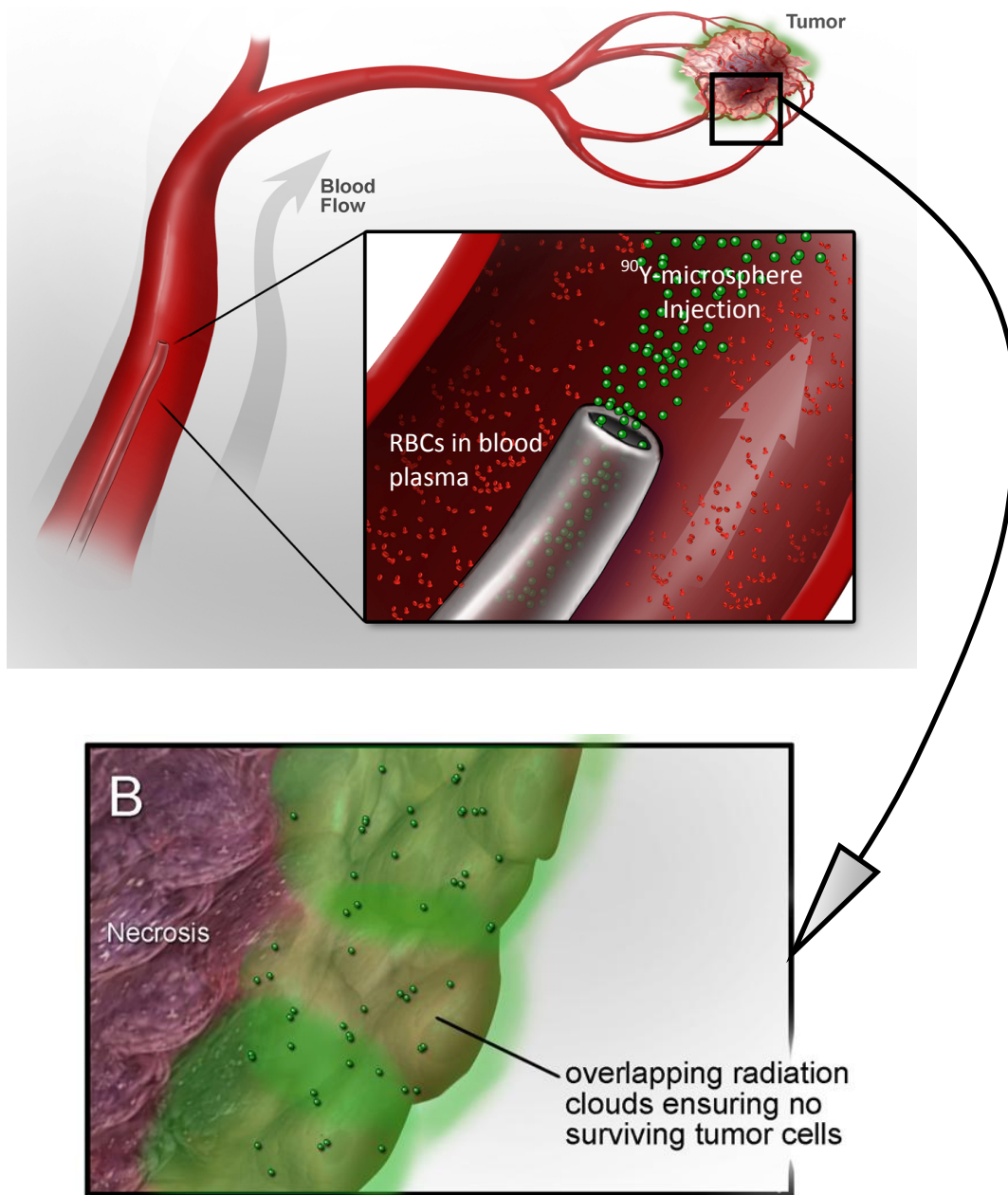


Figure 1.8: Illustration of ⁹⁰Y-microsphere delivery and transport to liver tumors
 Images from Wake Radiology Oncology (Cary, NC), *Used with permission*

Interestingly, while ⁹⁰Y-radioembolization has become an increasingly popular therapy with the consistent rise of liver tumors worldwide, the delivery of radio-isotopes using

microparticles injected into the arteries dates back to the 1940s. Moreover, the first clinical trials that injected ^{90}Y -microspheres for the treatment of cancer took place in the early 1960s, where by the late 1980s and 1990s, clinical research studies established the safety of ^{90}Y -radiation and ^{90}Y -microspheres for hepatic malignancies (Kennedy and Salem, 2010; Kennedy et al., 2008a). Currently, two commercially available ^{90}Y -microspheres are used in clinical treatment of liver tumors: SIR-Spheres® (Sirtex Medical Limited, Lane Cove, Australia) and TheraSpheres® (MDS Norion Inc., Ontario, Canada). Figure 1.9 shows vials and the delivery apparatus of both clinically available ^{90}Y -microspheres and Table 1.3 lists the physical and radiological characteristics of both clinically available ^{90}Y -microspheres.

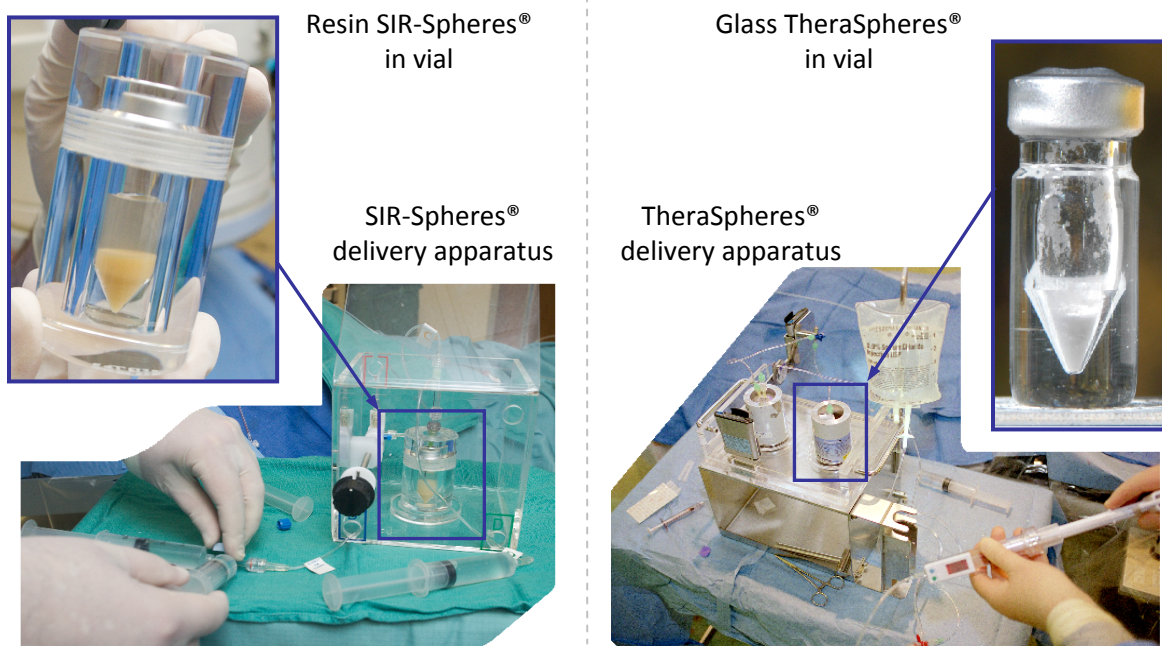


Figure 1.9: Vials of ^{90}Y -microspheres and their corresponding delivery apparatuses
Images from Wake Radiology Oncology (Cary, NC), *used with permission*

Table 1.3: Physical characteristics of clinically available ^{90}Y microspheres (Kennedy et al., 2006; Kennedy et al., 2007;)

| <u>Microsphere Characteristic</u> | <u>SIR-Spheres®</u> | <u>TheraSpheres®</u> |
|---|---|---|
| Manufacturer | Sirtex Medical (Lane Cove, Australia) | MDS Nordion (Ontario, Canada) |
| Material | Resin | Glass |
| Yttrium Source | Bound to spheres | Embedded in sphere matrix |
| Sphere Diameter (Mean \pm Std. Dev.) | Range: 20 - 60 [μm] 32 \pm 10 [μm] | Range: 20 - 30 [μm] 25 \pm 10 [μm] |
| Specific Gravity (Density) | 1.6 (1600 [kg m^{-3}]) | 3.6 (3600 [kg m^{-3}]) |
| Number of Microspheres per 3 GBq vial | 40-80 $\times 10^6$ | 1.2 $\times 10^6$ |
| Nuclear activity per particle | 50 Bq | 2500 Bq |

The radiation activity of ^{90}Y -microspheres is reported in units of GBq, where one Bq is the decay of one nucleus per second. The data in Table 1.3 reveals that TheraSpheres® exhibit a much larger amount of radiation activity per particle than SIR-Spheres®, but SIR-Spheres® include almost forty to eighty times the number of TheraSphere® particles per vial, resulting in SIR-Spheres® having greater embolizing tendency. Relating the administered radiation activity of ^{90}Y -microspheres in GBq to a patient's absorbed radiation dose in Gy is an area of active investigation. The enhanced vessel density surrounding liver tumors, sole emission of beta waves from ^{90}Y , and heterogeneous distribution of injected particles in the liver reported in multiple studies (Kennedy et al., 2004; Campbell et al., 2000; Robertson et al., 1992; Meade et al., 1987), make calculating a relation between the radiation

activity of ^{90}Y -microspheres and the radiation absorbed by liver tumors a much more complicated task than calculated absorbed radiation from systemic or external beam radiation therapies. Currently, no software or clinical trial data exists that accurately calculates a recommended radiation activity that would maximize radiation absorption by tumor cells and minimize damage to normal liver tissue. An important note is that similar difficulties hold for computing the exact ^{90}Y -microsphere deposition efficiencies around the tumor vs. healthy tissue. Common methods of estimating a radiation dose include custom formulas provided by SirTex Medical (Lane Cove, Australia) and MDS Norion Inc. (Ontario, Canada) that are dependent on patient-specific characteristics such as body surface area, mass of liver tumor(s), mass of healthy liver tissue, quantitative index of hepatic-lung shunting, and metabolic activity of tumor vs. healthy tissue (Kennedy et al., 2008b; Murthy et al., 2005).

Recommended treatment practices of ^{90}Y radioembolization have begun to take shape due to reports on ^{90}Y -microsphere successes, complications, and technical practices (Kennedy and Salem, 2010; Riaz et al., 2009; Kennedy et al., 2007; Murthy et al., 2005). Typical treatment policies involve extensive pre-microsphere-delivery steps such as: blood vessel imaging and potential embolization of extrahepatic vessels, quantification of hepatic-lung shunting, tumor volume and metabolic activity calculations, dosing calculations and, ultimately, catheter position for best microsphere release. Figure 1.10 illustrates a recommended treatment process and potential window where computational fluid-particle dynamics simulations could assist the medical team in determining the optimal location of microsphere release. An important note is that prior to extensive and rigorous validation of the computer models, they should be used as a *post-treatment* evaluation step to ascertain the

validity of the computational model and determine its efficacy in providing information that readily assists medical practitioners in planning ^{90}Y -microsphere therapy.

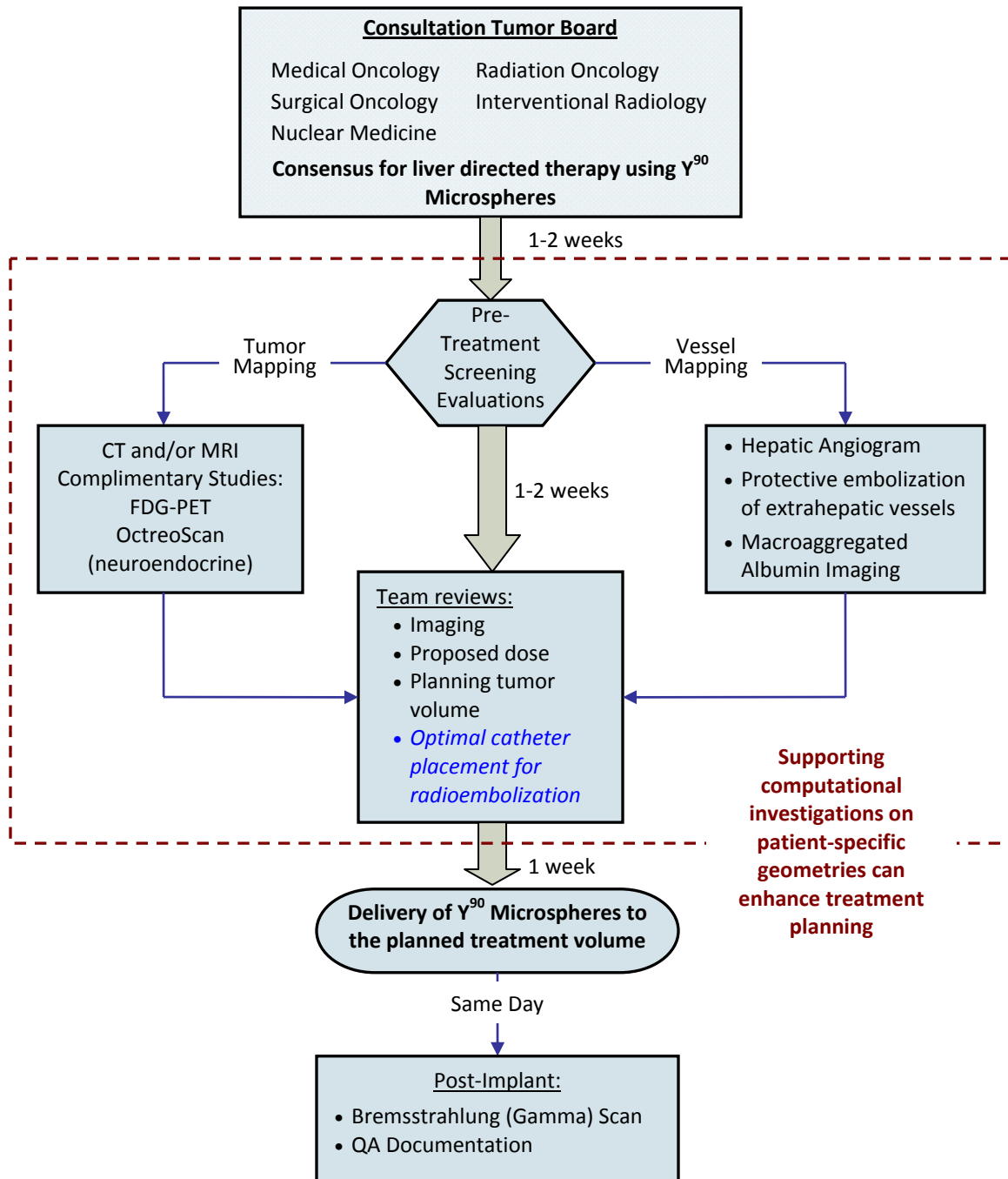


Figure 1.10: Treatment flowchart of ^{90}Y -microsphere brachytherapy
After: Kennedy et al., 2007

Unfortunately, current medical technology does not enable all patients to be candidates for ⁹⁰Y-radioembolization and some patients develop serious complications from the therapy. Patients selected for ⁹⁰Y-radioembolization must meet multiple criteria related to liver function, additional treatment options, and the patient's general health. Table 1.4 outlines the primary criteria that clinicians believe support the use of ⁹⁰Y-radioembolization on a patient.

Table 1.4: Indications for ⁹⁰Y radioembolization
After: Hoffman et al. (2008) and Salem and Thurston (2006)

| <u>Positive Patient Selection Criteria</u> | | |
|---|--|---------------------------------------|
| ✓ | Primary or secondary tumors confined to the liver | |
| ✓ | Surgical options not available: <ul style="list-style-type: none"> • Due to lesion size • Due to inoperability | |
| ✓ | Thermal ablation therapy not possible | |
| ✓ | Standard chemotherapies not viable treatment <ul style="list-style-type: none"> • Tumors resistant to chemotherapy • Treatment produces intolerable side effects | |
| ✓ | Preserved liver function with existing tumors <ul style="list-style-type: none"> • Bilirubin less than 2mg/dl • Alanine and Aspartate transaminase ≤ 5x normal levels • Normal blood coagulation parameters • Albumin ≥ 3mg/dl | |
| ✓ | ECOG status of 0 – 2 | |
| ✓ | Karnofsky index ≥ 60% | |
| <u>Eastern Cooperative Oncology Group (ECOG) Status</u> | | <u>Equivalent Karnofsky Score (%)</u> |
| 0 | Asymptomatic and fully active | 100 |
| 1 | Symptomatic, fully ambulatory, restricted in physically strenuous activity | 80-90 |
| 2 | Symptomatic, ambulatory, capable of self-care, greater than 50% of waking hours are spent out of bed | 60-70 |
| 3 | Symptomatic, limited of self-care, greater than 50% of waking hours are spent in bed | 40-50 |
| 4 | Completely disabled, no self care, bed ridden | 20-30 |

Even if all the criteria listed in Table 1.4 are satisfied, a patient may still be disqualified from ⁹⁰Y-radioembolization due to blood flow distribution through the vessels of the liver. Murthy et al. (2005) reported two absolute criteria disqualifying patients from ⁹⁰Y-radioembolization are extensive hepatopulmonary (hepatic-lung) shunting and reflux of flow from the hepatic arteries into the splanchnic (digestive) arteries. Both flow distribution characteristics are analyzed in pre-treatment imaging using angiograms and macroaggregated albumin imaging, where if the lung is calculated to potentially absorb > 30Gy of radiation, microspheres administered into the liver would be transported into the lung and cause substantial damage to the pulmonary tissue (Salem and Kennedy, 2010). Riaz et al. (2009) reported several complications of radiation induced lesions in the gastrointestinal track, bile ducts, and the gallbladder. A common pre-treatment method used to reduce such side-effects is to use coil embolization or prophylactic embolizing agents to eliminate blood flow in vessels that attach to the hepatic arteries where ⁹⁰Y-microspheres will be released. Other post-treatment complications include portal hypertension, post radioembolization syndrome (usually mild not requiring hospital treatment), radiation induced liver disease (max. in 4% of patients and mostly connected with preexisting liver abnormalities), radiation pneumonitis, lymphopenia, and vascular injury (Riaz et al., 2009). The aforementioned side-effects occur in a minority of treated patients and are often corrected by medical practitioners. Salem and Kennedy (2010) reviewed several clinical trials that illustrate ⁹⁰Y-radioembolization caused minimal side effects while successfully diminishing tumor burden and extending the patients' overall life more than other available treatments (see Appendix I for more detailed information on select clinical trials). Additionally, many ongoing clinical trials are aimed at further

determining the efficacy of ^{90}Y -radioembolization as a first line treatment option and reducing adverse complications. Such goals are inspirations for the current research with the desire to make ^{90}Y -radioembolization available to more liver tumor patients.

1.7 Chapter Outlook

The previous sections provided the research motivation, research goals and needed background information to understand the medical topics of interest in this study. A deductive research approach utilizing the same theory was implemented to undertake the two (seemingly very different) projects. Chapter 2 describes in detail the conservation laws needed to model both projects. Chapters 3 and 4 describe the physical domains used in both projects, the computational mesh used to model physical space, and the project-specific inlet/outlet conditions with custom variables. One should note that the boundary conditions and custom variables are the only differentiating factors of the modeling theory used in each project. Chapter 5 presents the research data based on steady and transient particle-hemodynamics simulations for an AAA and their relation to ILT formation. Chapter 6 provides research data for the steady and transient particle-hemodynamics simulations of ^{90}Y -microsphere transport and targeting in hepatic artery systems. Chapter 7 concludes the research discussion by reviewing the novel aspects of the study and listing inherent model limitations. It also charts the course of future research in both projects. A large amount of supporting information has been placed in the Appendices (supporting simulation results, copyright permissions, custom MATLAB code, ANSYS CFD v.12.1 Post Perl scripts, etc.) in hopes of benefiting the general scientific and medical community.

Chapter 2:

Fluid-Particle Transport Theory, Numerical Solution Method, and Model Validations

2.1 Introduction

The particle-hemodynamics in abdominal aortic aneurysms and Yttrium-90 microsphere transport in the hepatic arteries were calculated by using a one-way coupled Eulerian-Lagrangian solution methodology. In the current chapter, the modeling theory and equations, all derivations and justifications, and the computational solution strategies are discussed. Following the documented theory and research methodology, several validation

studies are presented which ensures the computational model can reproduce known physical phenomena and can be used as a predictive tool for new research investigations.

2.2 Fluid Transport

Blood has been shown to be an incompressible, non-Newtonian fluid (Kleinstreuer, 2006). For the present research applications transient 3-D laminar, isothermal flow is assumed. Thus, the equations of continuity and conservation of linear momentum being used are (Kleinstreuer, 2010):

Continuity

$$\nabla_i v_i^f = 0 \quad (2.1)$$

Linear Momentum

$$\rho_f \frac{\partial v_i^f}{\partial t} + \nabla_j v_j^f v_i^f = -\nabla_i p + \nabla_j \tau_{ij} + F_{ig} \quad (2.2)$$

The quantities ρ_f , p , τ_{ij} , v_i^f , and F_{ig} are the fluid density, pressure, shear stress tensor, the fluid velocity vector, and the gravitation force vector, respectively. Blood density was set to a constant value of 1.06 [g/cm³] and the shear stress tensor was described by the relation between the apparent viscosity and the shear rate tensor:

$$\tau_{ij} = \eta(\dot{\gamma}) \left[\nabla_j v_i^f + \nabla_i v_j^f \right] \quad (2.3)$$

The simplified Quemada model presented in Buchanan et al. (2000) was used to define blood's apparent viscosity (η) and is a function of the scalar shear rate ($\dot{\gamma}$). Both relations are shown in Eqs. (2.4a,b).

$$\eta(\dot{\gamma}) = \max \left\{ \mu_0, \left(\sqrt{\eta_\infty} + \frac{\sqrt{\tau_0}}{\sqrt{\lambda + \sqrt{\dot{\gamma}}}} \right)^2 \right\} \quad (2.4a,b)$$

$$\dot{\gamma} = \left[\nabla_j v_i^f (\nabla_j v_i^f + \nabla_i v_j^f) \right]^{1/2}$$

The parameters μ_0 , η_∞ , τ_0 , and λ are constants that were determined by Buchanan et al. (2000) by fitting Eq. 2.4a to the experimental blood viscosity data of Merrill (1969). Table 2.1 lists each parameter and its corresponding value, where Fig. 2.1 depicts the viscosity vs. shear rate curve.

Table 2.1: Quemada model parameter values

| Parameter | Value |
|---------------|---|
| μ_0 | 0.03090 [g cm ⁻¹ s ⁻¹] |
| η_∞ | 0.02654 [g cm ⁻¹ s ⁻¹] |
| τ_0 | 0.04360 [g cm ⁻¹ s ⁻¹] |
| λ | 0.02181 [s ⁻¹] |

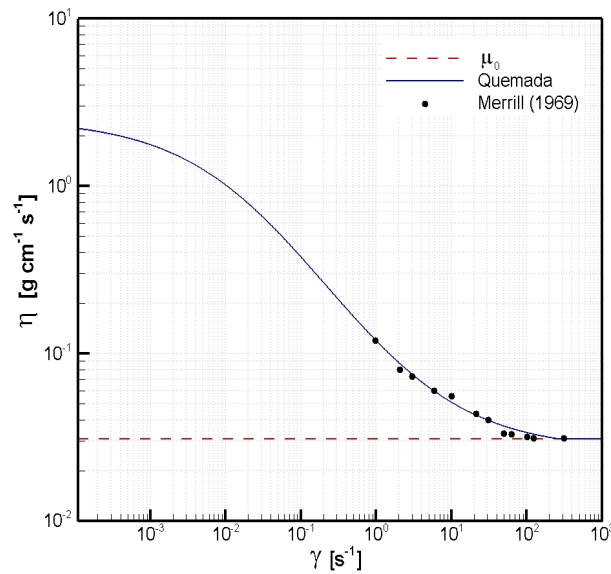


Figure 2.1: Apparent viscosity vs. shear rate curve of the Quemada model

2.3 Particle Transport

While the carrier fluid (blood) is solved based on the continuum assumption in an Eulerian framework, a Lagrangian framework is used to calculate the trajectories of dispersed particles through the computational domain. The Lagrangian approach tracks each injected particle independently as it moves throughout the computational domain. A one-way coupled Eulerian-Lagrangian particle transport model with non-interacting particles was employed to calculate each particle's trajectory after the carrier fluid's flow field has been determined at the node and element locations throughout the computational domain. Thus, particle-particle collisions are neglected and the particle motion does not influence the flow field of the carrier fluid. Such a model is a simplification of physical reality, but is plausible in situations where the dispersed particles form a dilute suspension, occupying a relatively small volume fraction of the local fluid elements (Kleinstreuer, 2006; 2003). An important note is that RBCs make up approximately 45% of total blood volume and seemingly violates the use of a dilute suspension model. However, the Quemada viscosity model captures the macroscale shear-thinning behavior of blood caused by the RBC transport and, when combined with a Lagrangian dispersed particle transport model, can provide reasonable predictions of individual RBC, WBC, and platelet trajectories through a continuum model of whole blood (Kleinstreuer, 2006; Hyun et al., 2004; Longest et al., 2004; Longest, 2002). Additionally, the analytical calculations shown in Kennedy et al. (2010) reveal that assumption of dilute suspension is a reasonable approach to model the trajectories of ^{90}Y -microspheres in computational domains mimicking the hepatic arteries.

Lagrangian particle transport of spherical particles was modeled using the conservation of momentum expressed as Newton's 2nd Law of Motion (Kleinstreuer, 2006; 2003; Longest et al., 2004). The model's governing equations of particle transport are derived from the equations of motion for a representative particle and express the fundamental relationship between the net forces acting on an object and the object's resulting acceleration. The derived equations assume that the time derivative following a moving particle can be approximated by a simple time differentiation and that all volumetric and surface forces are expressed as point forces. Equation (2.5) lists the derived equations:

$$m_p a_i^p = m_p \frac{dv_i^p}{dt} = m_p \frac{d^2 x_i^p}{dt^2} = \sum F_i \quad (2.5)$$

where m_p , a_i^p , v_i^p , x_i^p , and $\sum F_i$ represent the particle's mass, acceleration vector, velocity vector, position vector, and sum of forces acting on the particle, respectively. A multitude of forces are exerted on suspended particles that can result in their acceleration. Common forces include (but not limited to) drag, gravitational, virtual mass, pressure gradient, lift, Basset history, and interaction forces (equations quantifying each of these forces can be found in Kleinstreuer, 2006; 2003; and Buchanan, 2000). However, in many cases only a few forces have a pivotal impact on the particle trajectory calculation and a relatively good model of particle transport can be developed by including only these primary forces in the right hand side of Eq. (2.5).

Buchanan (2000) completed a detailed analytical analysis that revealed when a particle's relaxation time is much less than the transient system's period, the Basset history

force can be neglected. Equation (2.6) defines the relaxation time of a particle, which represents the time a particle requires to respond to changes in the surrounding fluid velocity.

$$\tau_p = \frac{\rho_p d_p^2}{18\eta} \quad (2.6)$$

Most arterial pulses have a period close to one second and when using even the largest possible diameter of the clinically available ^{90}Y -microspheres (see Table 1.3 in Ch.1), with the lowest possible apparent viscosity of the Quemada model, the maximum particle relaxation time is on the order of $1\text{e-}4$ [s], which is much less than a typical arterial period of 1 [s]. Thus, the Basset history force is not included in Eq. (2.5).

Longest et al. (2004) completed an experimental validation of his particle transport model used for arterial fluid-particle flows and showed that the virtual mass force had negligible impact on a single particle's trajectory captured within flow recirculation caused by an annular expansion. For the current study, a simulation of particle transport under pulsatile flow in a symmetric, representative hepatic artery geometry (see Chs. 3 and 6) were conducted with and without the virtual mass force included in the particle trajectory calculation. The resulting exit fractions from the simulation, revealed no numerical difference between the calculations that neglected and included the virtual mass force. Thus, the virtual mass force was not included in Eq. (2.5).

The Saffmann-type lift force is important for large rotating particles and in regions of high shear rate, which normally correlates with near-wall regions (Kleinstreuer, 2006; Longest et al., 2004). While the current study does involve flow fields that have near-wall and flow-separation regions of high shear, such regions will occupy only a very small portion

of the computational domain. Additionally, when modeling fine particles and the relative velocity between the particle and carrier fluid is small, the Saffman force is often negligible. Thus, the influence of the Saffman lift force on the overall particle trajectories is expected to be small in comparison to the drag force and is not included in Eq. (2.5).

The final force simplification comes from the simulation of a dilute suspension of particles, which enables the interaction of particles to be neglected. To reinforce the calculations of Kennedy et al. (2010) that justify the assumption of dilute particle suspension, Eqs. (E-2.2-4a,b) from Kleinstreuer et al. (2003) have been utilized to calculate the ratio between particle response time and particle collision time. Equations (2.7a-d) list the derived ratio between the characteristic times of a spherical particle:

$$\begin{aligned} \frac{\tau_p}{\tau_c} &= \frac{\bar{\rho}_p d_p v_p^r}{3\eta} \\ \bar{\rho}_p &= \left[\frac{4}{3} \pi \left(\frac{d_p}{2} \right)^2 \rho_p \right] \cdot n \\ n &\approx \frac{N}{\pi/4 d_r^2 d_p} \\ \frac{\tau_p}{\tau_c} &\approx N \frac{\rho_p d_p^3 v_p^r}{72 \eta d_r^2} \end{aligned} \tag{2.7a-d}$$

where: $\bar{\rho}_p$, v_p^r , d_r , n , and N is the particle bulk density, relative (slip) velocity of particle phase, particle release/injection zone diameter, particle number density, and total number of injected particles at a single point in time, respectively. When Eq. (2.7d) is less than unity, the fluid-particle flow can be considered a dilute suspension of the particulate/dispersed phase. A representative max. value of Eq. (2.7d) for ^{90}Y -microspheres using the mean

particle diameter and density, a parent vessel diameter of 5 [mm] as the particle release/injection zone diameter, a rather large slip velocity of 10 [cm/s], the lowest possible Quemada viscosity, and ten-thousand as the number of injected particles is approximately 4.27×10^{-2} and easily satisfies the conditions of a dilute suspension as described by Kleinstreuer (2003, 2010). An important note is that if the slip velocity is decreased by an order of magnitude, the number of injected particles at a single point in time can reach one million and the ^{90}Y microspheres would still satisfy the conditions of a dilute suspension.

To complete the derivation, any additional influences from particle diffusion effects are negligible compared with convection due to particle diameters. Thus, the primary forces in the governing equation needed for reasonably predicting the biological and clinical particles trajectories through the arterial flow fields of interest are the frictional and form drag, pressure gradient, and gravitational forces. Equations (2.8a-f) lists the resulting governing equation and the equations needed for the calculation of each force acting on a spherical particle:

$$m_p \frac{dv_i^p}{dt} = F_i^D + F_i^P + F_i^G \quad (2.8a)$$

where

$$\begin{aligned} F_i^D &= \frac{1}{8} \pi \rho_p d_p^2 C_d (v_i^f - v_i^p) |v_i^f - v_i^p| \\ F_i^P &= -d_p^3 \frac{\pi}{6} \nabla_i p \\ F_i^G &= \frac{\pi}{6} d_p^3 (\rho_p - \rho_f) g_i \\ C_d &= \frac{24}{\text{Re}_p} (1 + 0.15 \text{Re}_p^{0.687}) \\ \text{Re}_p &= \frac{\rho_f |v_i^f - v_i^p| d_p}{\mu_f} \end{aligned} \quad (2.8b-f)$$

Here, F_i^D , F_i^P , F_i^G , C_d , and Re_p are the drag force, pressure gradient force, gravity force, drag coefficient, and particle Reynolds number, respectively. The drag coefficient is specified with the Schiller-Naumann empirical relation that adjusts the coefficient in the transitional regions between viscous and inertial particle transport, while the particle Reynolds number is defined according to a single particle's slip velocity and diameter.

Particle interactions with the fluid domain's walls are modeled using fundamental collision principles that calculate the momentum and kinetic energy of each particle in directions normal and parallel to the wall. The model is primarily determined by a parallel and a perpendicular restitution coefficient. A coefficient value of 1.0 implies an ideal elastic collision (momentum and energy are conserved), whereas any value less than one indicates an inelastic collision (momentum but not energy is conserved) and a value of zero results in particle deposition on the wall ($v_2^p = -C_R v_1^p$ where v_2^p , C_R , v_1^p is the final particle velocity, restitution coefficient, and initial particle velocity, respectively). Using this model, the arterial wall is modeled as a smooth surface without any surface roughness.

2.4 Solution Method

The commercial finite-volume software ANSYS CFX v12 (ANSYS Inc., Canonsburg, PA) was used to solve the conservation equations. A high-resolution iterative upwind solution scheme was used to integrate the advection term in the governing fluid equations. The high-resolution scheme uses nonlinear blending factors at each node to lessen the smearing of high spatial gradients by a 1st-order upwind difference scheme while preventing

dispersive discretization errors of linear blend factors and/or central difference schemes in regions of high spatial gradients. An iterative, 2nd-order backwards Euler transient solution scheme continued until the specified mass and momentum maximum error residuals were less than the user-specified threshold value.

Each particle's position is calculated using forward Euler integration of the particle velocity with an integration timestep (δt) and is shown in Eq. (2.9):

$$x_i^{pN} = x_i^{p0} + v_i^{p0} \delta t \quad (2.9)$$

where: x_i^{pN} , x_i^{p0} , and v_i^{p0} are the new particle position at the end of the particle integration timestep (δt), initial particle position at the beginning of the particle integration timestep, and the velocity at the beginning of the particle integration timestep, respectively. At the end of the particle integration timestep, the new particle velocity is calculated through the analytical solution to Eq. (2.8a).

2.5 Model Validations

The numerical models described in the previous sections need to be compared against experimental results prior to using them as research tools for investigating problems without a known solution. Validations were divided into two broad categories of fluid flow and particle deposition/transport. An important note is that since the particle transport model is completely dependent on the calculated flow field, numerical particle transport calculations matching the experimental results also imply that the numerical flow field matches the experimental flow field.

2.5.1 Velocity Profiles

The experimental velocity profiles of steady flow through single, symmetric bifurcation from Zhao and Lieber (1994) were utilized to validate ANSYS CFX v.12 (ANSYS Inc., Canonsburg, PA) ability to accurately calculate the physics of internal flows through bifurcating domains. Figures 2.2a,b illustrate the computational domain, locations of velocity profile measurement, and the acceptable match between the experimental and numerical velocity profiles for an inlet Reynolds number of 518.

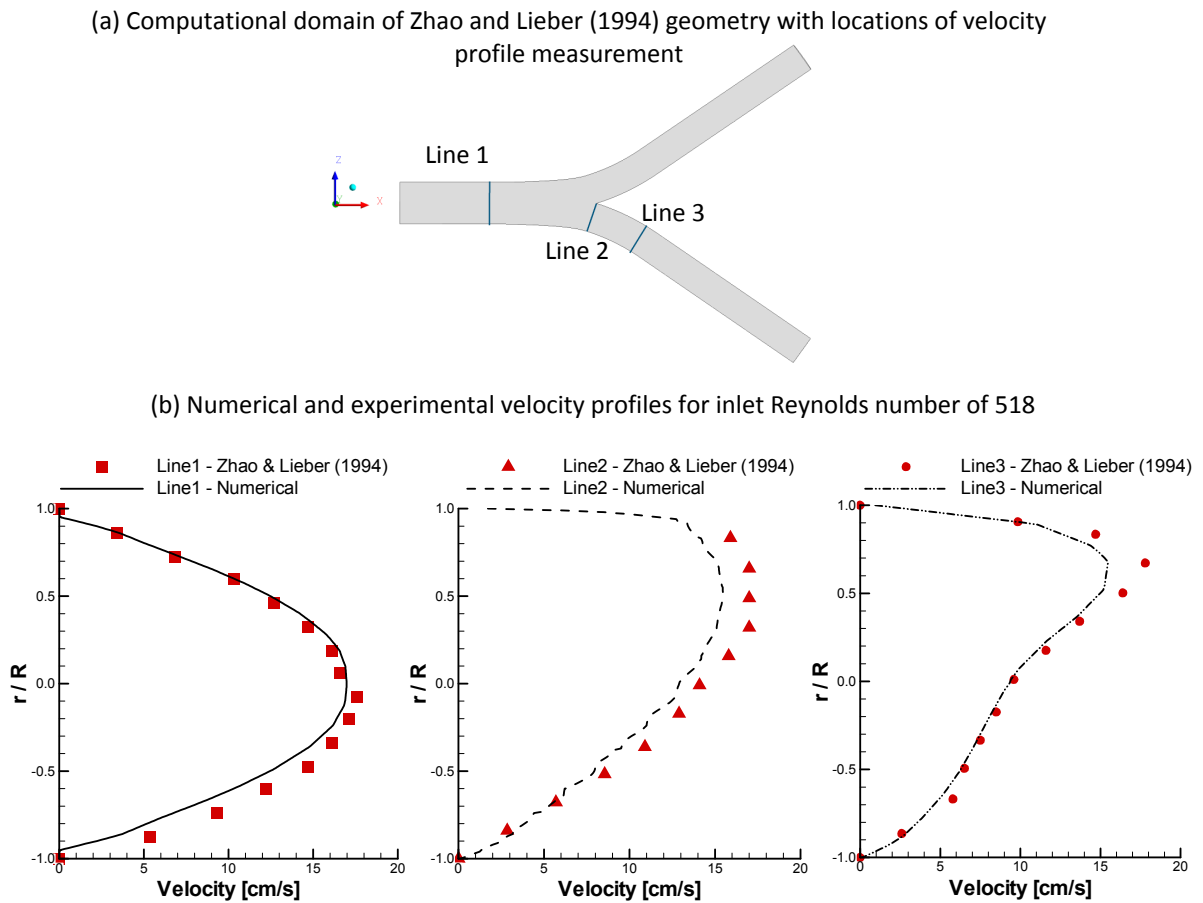


Figure 2.2: (a) Symmetric, single bifurcation computational domain with locations of velocity profile measurement and (b) Numerical velocity profiles calculated by ANSYS CFX and experimental velocity profiles of Zhao and Lieber (1994)

The source of misalignment between the computational and experimental profiles is believed to be due to experimental error, which is seen in the skewing of the experimental inlet profile towards the negative radial direction, which would direct additional flow towards the lower bifurcation branch (where the comparisons are made) and increase the maximum velocity magnitudes of the experimental profiles. Thus, the first validation shows good agreement between the ANSYS CFX flow solver and experimental velocity profiles of internal, bifurcating flow.

2.5.2 Recirculation Lengths

The geometric morphology of AAAs and endovascular devices such as catheters often result in complex flow fields with ample regions of recirculating flow. Therefore, verifying ANSYS CFX ability to accurately quantify a recirculation region's influence on the local flow field is an important step prior to analyzing the complex flow patterns present in AAAs or in tortuous arteries. Common geometries used to measure lengths of recirculation regions are outward and inward expansions which can be rectangular or annular. Figure 2.3 illustrates a 2D computational domain of a rectangular backstep and defines the important system lengths.

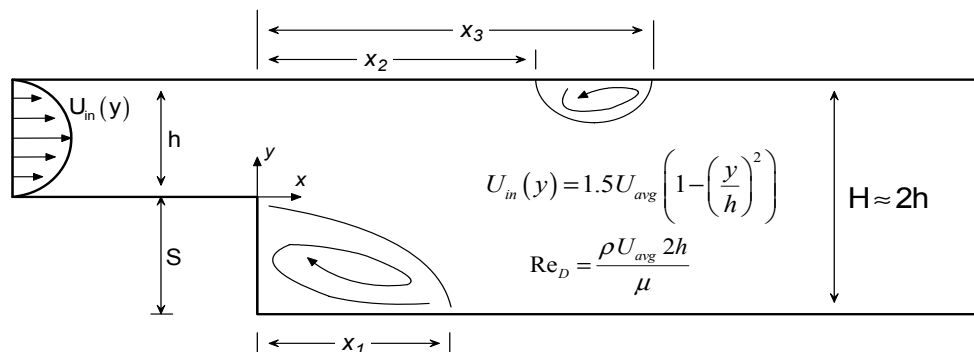


Figure 2.3: Two-dimensional computational domain of a rectangular backstep

All boundaries except the left and right vertical lines are treated as impermeable, stationary walls with a no-slip boundary condition. Despite the simple nature of the geometry, the 2D approximation fails to predict accurate recirculation lengths at Re_D values above 600, which is close to the point when the multiple recirculation regions illustrated in Fig. 2.3 begin to form. The aforementioned trends are illustrated in Fig. 2.4 below, where the recirculation lengths calculated by 2D computations are compared against experimental results of a 3D domain.

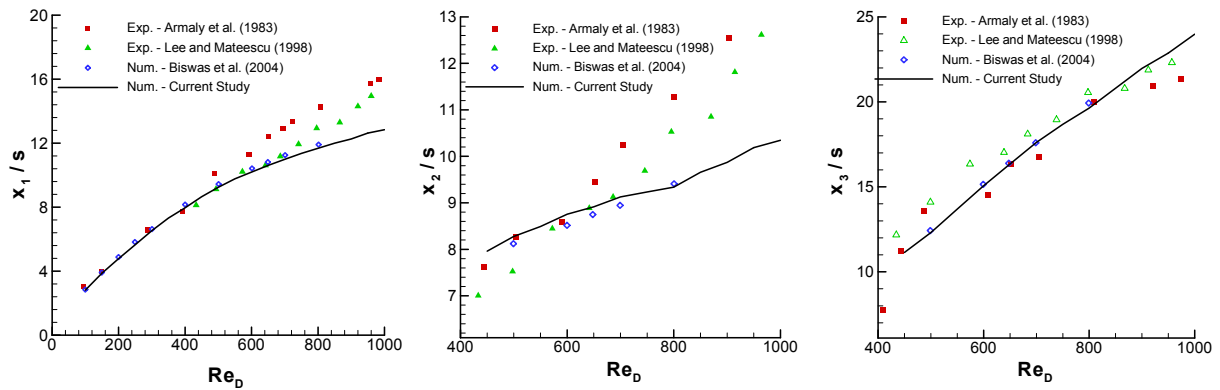


Figure 2.4: Comparison between 2D numerical calculations and 3D experimental data of recirculation lengths of a rectangular backward facing step

Biswas et al. (2004) also reported the inability of 2D simulations to report the recirculation lengths above the critical Re_D value and stated that the cause for the discrepancy is that the experimental results begin to be influenced by the vessel walls above the critical Re_D . Sheu and Rani (2006) reinforced their statements by showing out-of-plane streamline movement of the primary recirculation region above Re_D values of 600. Despite the discrepancy at the higher Re_D values, the close match between the experimental and numerical data when $Re_D < 600$ gives credibility to ANSYS CFX ability to accurately reproduce 2D recirculation

zones. However, AAAs and other arterial pathological conditions (i.e., stenoses) often produce 3D recirculation regions and warrants the validation of ANSYS CFX to accurately predict recirculation regions when using a 3D computational domain.

Axi-symmetric annular geometries are a better representation of the cylindrical shape of the arterial vessels than rectangular backward facing steps. Thus, inward and outward expansions of axi-symmetric geometries were used for the additional validation studies and are illustrated in Figs. 2.5a,b.

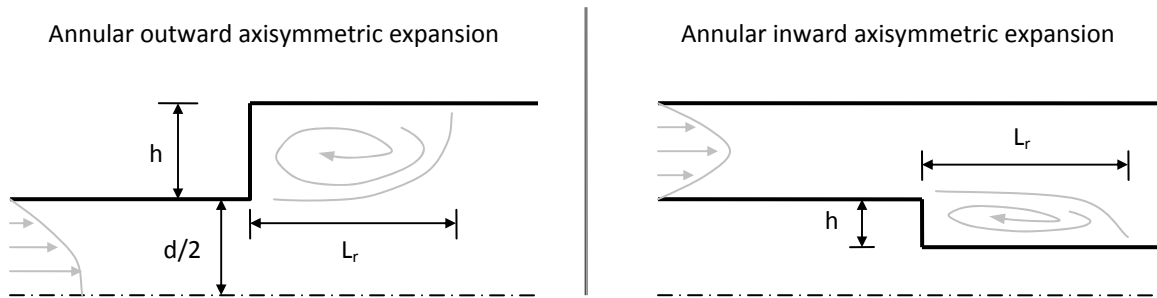


Figure 2.5: Annular geometries of ^(a)an axisymmetric outward expansion and ^(b)an axisymmetric inward expansion

The bold lines in Figs. 2.5a,b symbolize impermeable, stationary walls with no slip boundary conditions and the dashed-dotted lines represent the vessels' axis of symmetry. Inlet Reynolds numbers defined according to the inlet diameter (d) and the step height (h) produce different recirculation lengths (L_r). The experimental results of Karino and Goldsmith (1977) with a downstream to upstream diameter ratio (D_r) of approximately 3.338 were used to validate ANSYS CFX recirculation lengths of a similar outward annular expansion while the experimental results of Goharzadeh and Rogers (2009) and the numerical results of Nag and Datta (2007) with a downstream to upstream diameter ratio of approximately 1.500 were

used to validate ANSYS CFX recirculation lengths of a similar inward annular expansion. Figures 2.6a,b illustrate the close match between the results of ANSYS CFX and the published results of both inward and outward axisymmetric, annular expansions, where D_r represents the downstream to upstream vessel diameter ratio and Re_d and Re_h represents the inlet Reynolds number defined according to the inlet diameter (d) and step height (h), respectively.

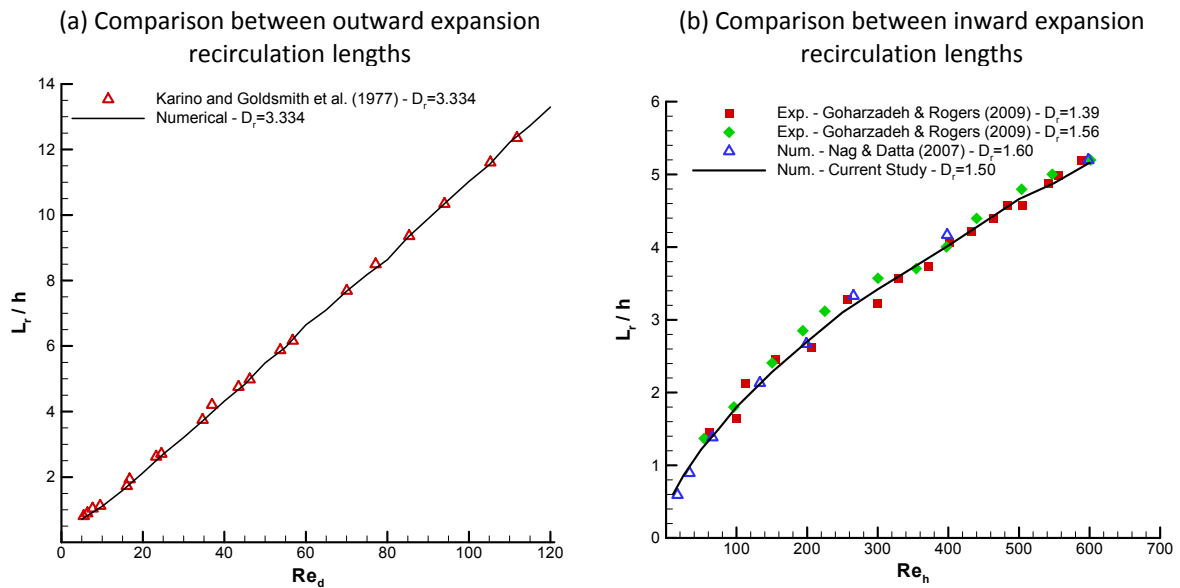


Figure 2.6: Comparison between ANSYS CFX and published calculations of recirculation lengths of axisymmetric ^(a)outward annular expansions and ^(b)inward annular expansions

An important difference between the recirculation length vs. Reynolds number data sets is the nonlinear relation present in the inward expansion and the linear relation present in the outward expansion. Such trends are important differentiating characteristics of each system, which ANSYS CFX (ANSYS Inc., Canonsburg, PA) accurately captures using the different

geometries and ensures the computational solver can accurately produce three-dimensional recirculation regions.

2.5.3 Particle Transport

Longest et al. (2004) and Kleinstreuer (2006) provide additional experimental validations of Eulerian-Lagrangian computational particle transport modeling, but many of the referenced studies involved additional particle deposition studies or a single particle's trajectory. To provide a validation of widespread particle behavior without wall deposition, (applicable to the ^{90}Y -microsphere study) a group of particles were tracked through a single-bifurcation with different daughter vessel diameters and the percentages of particles exiting the two daughter vessels from the bifurcation were compared with the experimental data of Bushi et al. (2005). Figure 2.11 illustrates the computational geometry used to represent the benchtop experiment.

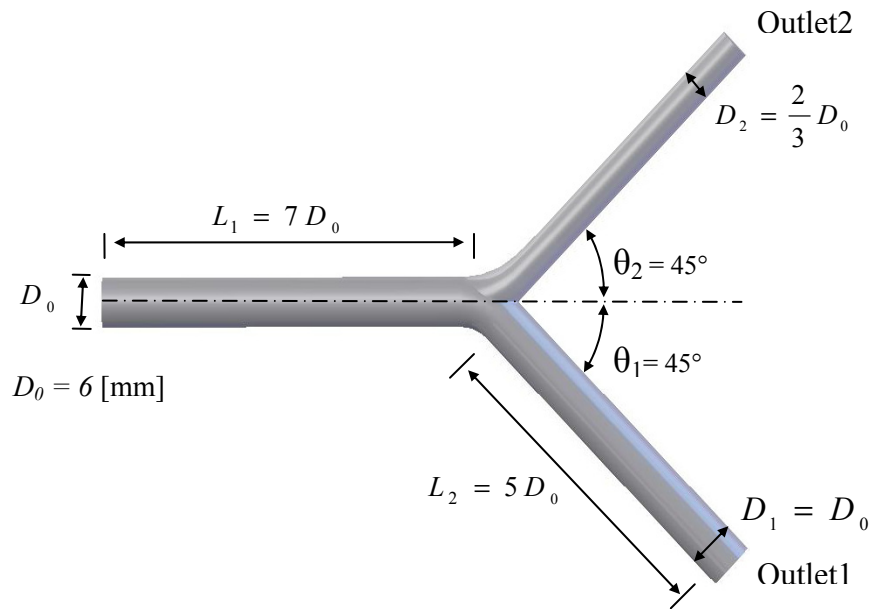


Figure 2.11: Computational geometry and dimensions to represent the physical experiment of Bushi et al. (2005)

The bifurcation angles with respect to the parent vessel centerline and all vessel diameters exactly matched the experimental conditions. The length of the parent tube prior to the bifurcation was seven times the inlet diameter and the daughter branch tubes were set to five times the inlet diameter. Meshes of the computational domain were generated using ICEM CFD with a significant amount of prism elements along the walls of the domain to accurately model high gradients of the velocity vector near the wall. A mesh independent analysis was conducted to ensure the velocity profiles prior to, within, and after the bifurcation did not change with refinements in mesh. The final mesh had a total of 374,097 elements, where 198,927 were prism elements. Steady flow of Reynolds number equal to 500 was prescribed at the parent tube while flow through the two daughter branches of the bifurcations was adjusted by adjusting the downstream resistance of each branch in the form of varying the static pressure at each outlet. Neutrally buoyant (particles had same density as carrier fluid) particles of diameters 0.6mm were introduced at the inlet in a parabolic distribution according to Eq. (2.10). The particles were injected with the same velocity as the carrier fluid and all error RMS residuals had to fall below $4.1E-6$ prior to completion of the simulation. Wall restitution coefficients were set to 1.0, which enabled no particles to deposit along the walls of the domain. The flow through outlets one and two were labeled Q1 and Q2 respectively, and the exit percentages of particles were compared for different flow ratios ($Q1/Q2$) to the experimental data of Bushi et al. (2005). Figure 2.12 illustrates the close match between the numerical and experimental data sets for the particle exit fractions.

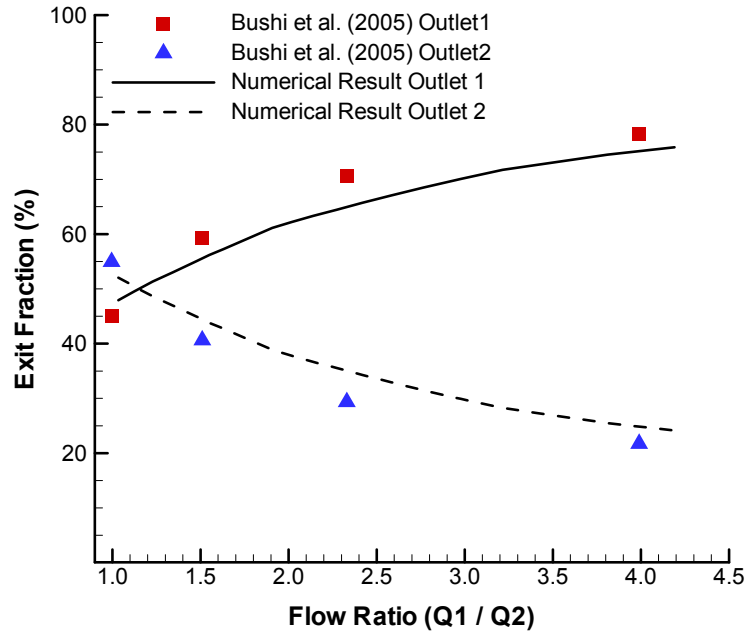


Figure 2.12: Comparison between the numerical and Bushi et al. (2005) exit fractions of 0.6 [mm] particles exiting the single bifurcation domain

2.5.4 Particle Deposition

In order to validate the particle transport model's ability to predict terminal locations of injected particle, the regional deposition efficiency (number of particles depositing in designated region of a larger system divided by the number of particles entering the system) of multiple geometries were calculated using the particle transport model previously described in Sections 2.3-2.4 and compared against published data of the same geometries. An important dimensionless parameter which provides a quantitative measure for the potential of particles to collide with vessel walls is the Stokes Number (St), which is the characteristic stopping distance of a particle divided by the vessel/obstacle's characteristic length. For situations of internal flow such as flow in the human airways or arteries, the Stokes number is defined according to Eq. (2.10):

$$St = \frac{\rho_p d_p^2 U}{18 \mu D_T} = \frac{1}{18} \left(\frac{\rho_p}{\rho_f} \right) \left(\frac{d_p}{D_T} \right)^2 Re \quad (2.10)$$

where U is the representative fluid velocity, Re is the fluid's accompanying Reynolds number, and D_T is the parent tube diameter. For many calculations a mean Stokes number is needed, based on the mean fluid velocity in the parent tube and the parent tube diameter. A probability density function was used to prescribe the spatial distribution of the spherical particles at the injection plane and is prescribed in Eq. (2.11):

$$PDF = \left[1 - \left(\frac{r}{R} \right)^2 \right] \quad (2.11)$$

where r is the local in-plane radial coordinate with the center of the tube as the origin and R is the tube radius.

Pui et al. (1987) conducted an experimental analysis of particle deposition carried by steady flow through a ninety-degree bend of circular cross-section. A long inlet tube length was implemented within the experimental study to ensure that a fully-developed velocity profile was achieved when the flow entered the ninety-degree bend. Figure 2.7 illustrates the computational geometry used to represent the physical experiment.

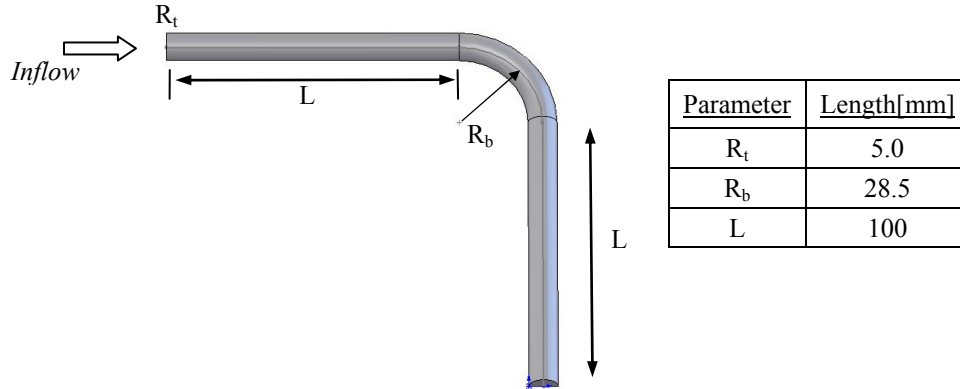


Figure 2.7: Computational geometry and dimensions used in particle deposition validation

The dimensions of the computational flow domain differed from the experimental geometry; but, the dimensionless groups which relate the two studies are identical (inverse curvature ratio $\{R_b/R_t\}$, bend angle $\{90^\circ\}$, and Reynolds number). A mesh of the computational domain was generated using ICEM CFD (ANSYS Inc., Canonsburg, PA) with a significant amount of prism elements along the walls of the domain to accurately model high gradients of the velocity vector near the wall. The computational mesh utilized a symmetry plane to reduce the total geometry by $\frac{1}{2}$, where the total number of elements was 577,655 of which 332,013 were prism elements. All simulations were conducted at a fluid Reynolds number of 1000 with particles having diameters in the range $4.6\mu m \leq d_p \leq 38.7\mu m$ and entering the system in a parabolic distribution according to Eq. (2.11). The carrier fluid was modeled as incompressible air at 25°C while the particles were modeled with the properties of water, implying a density ratio of $\rho_w/\rho_a \approx 841$. The particles were injected with the same velocity as the carrier fluid and the simulations were set to terminate when max. error residuals were below 1E-4. Wall restitution coefficients were set to zero, which forced particles to deposit

on walls whenever the particles contacted the wall. The computed deposition efficiency in the bend conservatively followed the experimental data points of Pui et al. (1987), and reflect the typical S-shaped deposition efficiency vs. Stokes Number curve seen in many particle deposition studies (Zhang et al., 2005; Kleinstreuer et al., 2008). Figure 2 illustrates the comparison between the numerical computations and the experimental data.

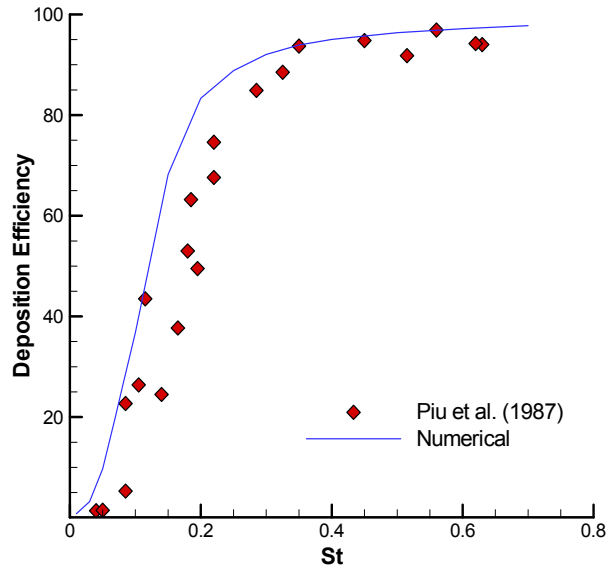


Figure 2.8: Numerical deposition efficiency of present model predictions compared against the experimental results of Piu et al. (1987)

Kim and Fisher (1999) conducted a similar experimental analysis of particle deposition in steady flow, but used a geometry that consisted of two sequential, symmetric bifurcations. In the experiment, a long inlet tube was used to ensure a fully developed velocity profile before the carrier fluid reached the first bifurcation. The computational domain did not include the full inlet tube and also extended the daughter branches of the second bifurcation to prevent the numerical boundary conditions from influencing the local flow field near the

second bifurcation. Figure 2.9 depicts the computational geometry along with important physical dimensions.

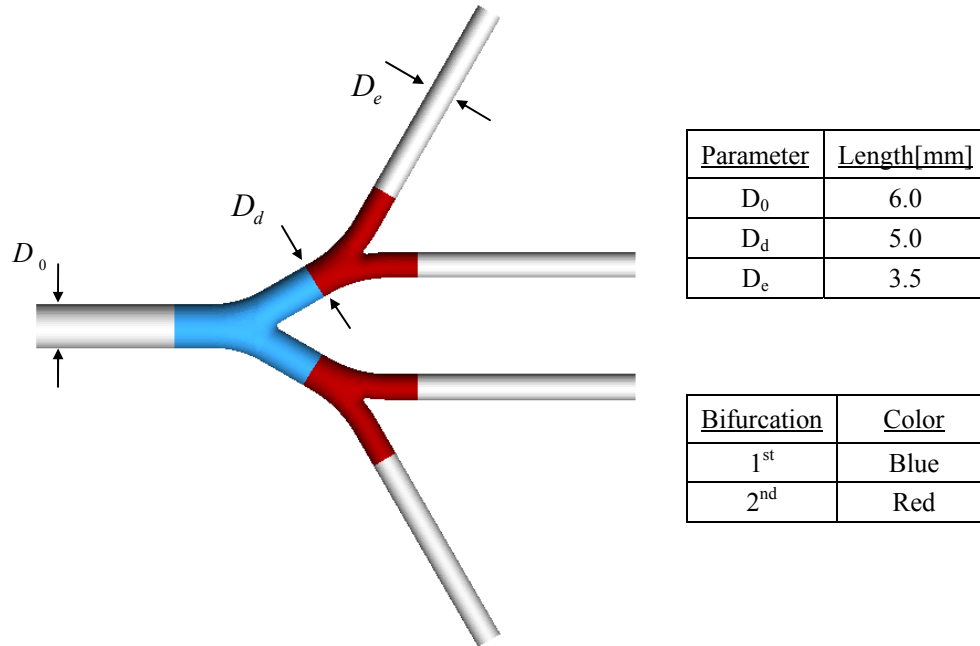


Figure 2.9: Computational geometry and geometric parameters used in double-bifurcation particle deposition validation

The computational mesh utilized a symmetry plane (i.e., $\frac{1}{2}$ the actual geometry) and contained 191,932 hexahedral elements that were organized in a structured “o-grid” orientation. Additional information regarding the computational geometry and mesh can be found in (Comer et al., 2001) All simulations were conducted at a Reynolds number of 1200 with the particles having diameters in the range $3.1\mu\text{m} \leq d_p \leq 8.4\mu\text{m}$ and entering the system at the inlet plane with a parabolic distribution according to Eq. (2.11). The carrier fluid was modeled as incompressible air at 25°C while the particles were modeled with the physical properties of water. The particles were injected with the same velocity as the carrier fluid and

the simulations were set to terminate when the max. error residuals were below 1E-4. Wall restitution coefficients were set to zero, which forced particles to deposit on walls whenever the particles contact the wall. The computed deposition efficiencies in the double bifurcation exhibited a good match to the data points of Kim and Fisher (1999), as illustrated in Fig. 2.10.

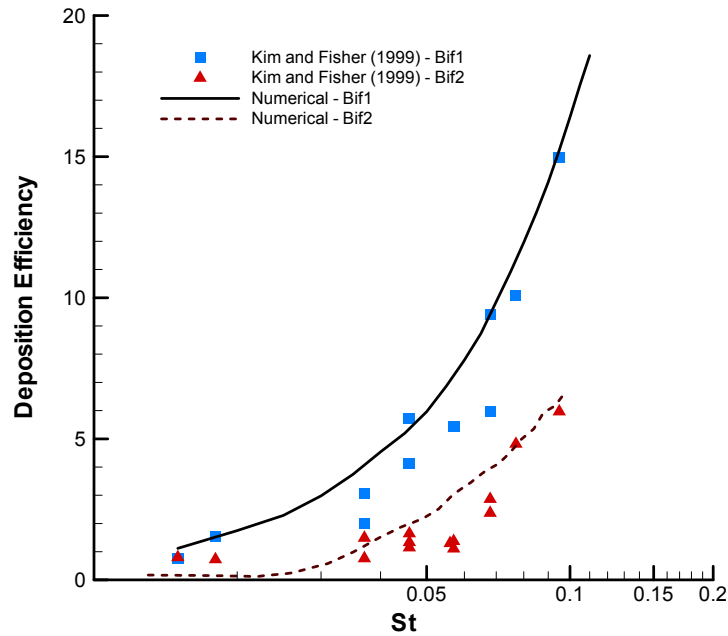


Figure 2.10: Comparison between numerical and experimental deposition efficiencies of the Kim and Fisher (1999) double bifurcation geometry

Figures 2.9 and 2.10 provide strong evidence that the employed particle transport model can reproduce known experimental trends of a wide range of Stokes Numbers and in multiple geometric types. Additionally, the ability of the model to accurately calculate regional deposition efficiencies enables the model to be used in other geometries (i.e., aneurysms) to predict regions of enhanced particle deposition in the computational domain.

2.6 Conclusions

The computational fluid and particle transport models have been described in Sections 2.2-2.4 and have been shown to accurately reproduce experimental results of: i) local flow fields, ii) recirculation lengths, iii) regional particle deposition efficiencies, and iv) particle exit fractions through the daughter vessels of a bifurcation. Thus, the simplifications made to the particle transport model have been shown to have a negligible influence on the model's ability to reproduce experimental data sets and are reasonable approximations of the physical reality. In conclusion, present computer simulation models can be used as a predictive tool to investigate the behavior of more complicated systems with relatively unknown behavior that include the same primary physical phenomena (e.g., laminar, incompressible fluid-flow and drag-dominated spherical particle transport in a dilute suspension).

Chapter 3:

Computational Domain Construction and Mesh Generation of Arterial System Morphologies

3.1 Introduction

The governing equations in Ch.2 are solved at prescribed locations across a computational domain representing a flow region. A mesh of the computational domain creates a spatial discretization and specifies the locations where governing equations are numerically solved. Prior to utilizing a computational mesh in widespread applications, the solution of the governing equations should be shown to be independent of further refinements to the spatial discretization.

The physical regions modeled in the current study were: the blood lumen of a patient-specific AAA, the blood lumen of a representative hepatic artery system, fluid domain around a positional microcatheter in a straight tube, and a patient-inspired geometry of a replaced common hepatic geometry stemming from the superior mesenteric artery (See section 3.3.1 for explanation of “replaced hepatic artery” description). In the current chapter, the individual domains will be introduced and a computational mesh of suitable discretization will be determined and presented. The meshes were then used to carry out the computational analyses of the physical regions’s particle-hemodynamics.

3.2 Patient-Specific Infrarenal Abdominal Aortic Aneurysm (AAA) Geometry

3.2.1 Patient-Specific Computational Domain

As illustrated in Fig. 1.2a,b an AAA is a focal dilation of the abdominal aorta. Typical classification of an AAA is when the outer diameter of the expanded vessel is at least one-and-a-half times the outer diameter of the healthy vessel. The morphology and geometric appearance of the AAA has been widely investigated and is an ongoing area of research. To test the continual intraluminal thrombus (ILT) formation process presented in Section 1.5.4, a single patient’s history of AAA and ILT development was sought. Dr. Ender Finol (Institute for Complex Engineered Systems, Departments of Biomedical and Mechanical Engineering, Carnegie Mellon University, Pittsburgh, PA) and his former student Ms. Julie H.Y. Ng (Departments of Biomedical and Mechanical Engineering, Carnegie Mellon University, Pittsburgh, PA) had recorded such a data set and completed the necessary image segmentation to construct a three-dimensional (3-D) geometry of the AAA blood lumen, ILT,

and AAA-wall at each point of the patient's timeline. They provided the single patient's multiple AAA geometries for current computational study.

Their process of geometry creation began with a retrospective review of records that followed a protocol approved by Allegheny General Hospital's IRB. From this review, the CT images of an electively repaired AAA were acquired and segmented using an in-house code following a procedure described in Martufi et al. (2009). The 3D anatomical geometry was obtained via reconstruction of the segmented images with subsequent surface meshing, using Simpleware (Simpleware Ltd., Exeter, UK). In addition, the lumen of the geometry was truncated at the infrarenal aorta and common iliac artery locations to be normal to the centerline flow direction. CAD software Rhino was used to create the normal boundary profiles.

After receiving the geometry files, ICEM CFD (ANSYS Inc., Canonsburg, PA.) and SolidWorks were used to refine the normal plane at the geometries boundaries and calculate the volumes of the AAA Lumen and the ILT. Interestingly, a rapid increase in ILT volumetric growth was seen at a specific time in between the patient's diagnostic exams. Figure 3.1 plots the patient's AAA volume history with accompany geometric shapes (red domain is the blood lumen and tan is the ILT) at specific times, where the AAA-Sac volume was calculated as the sum of the AAA-lumen and ILT volumes.

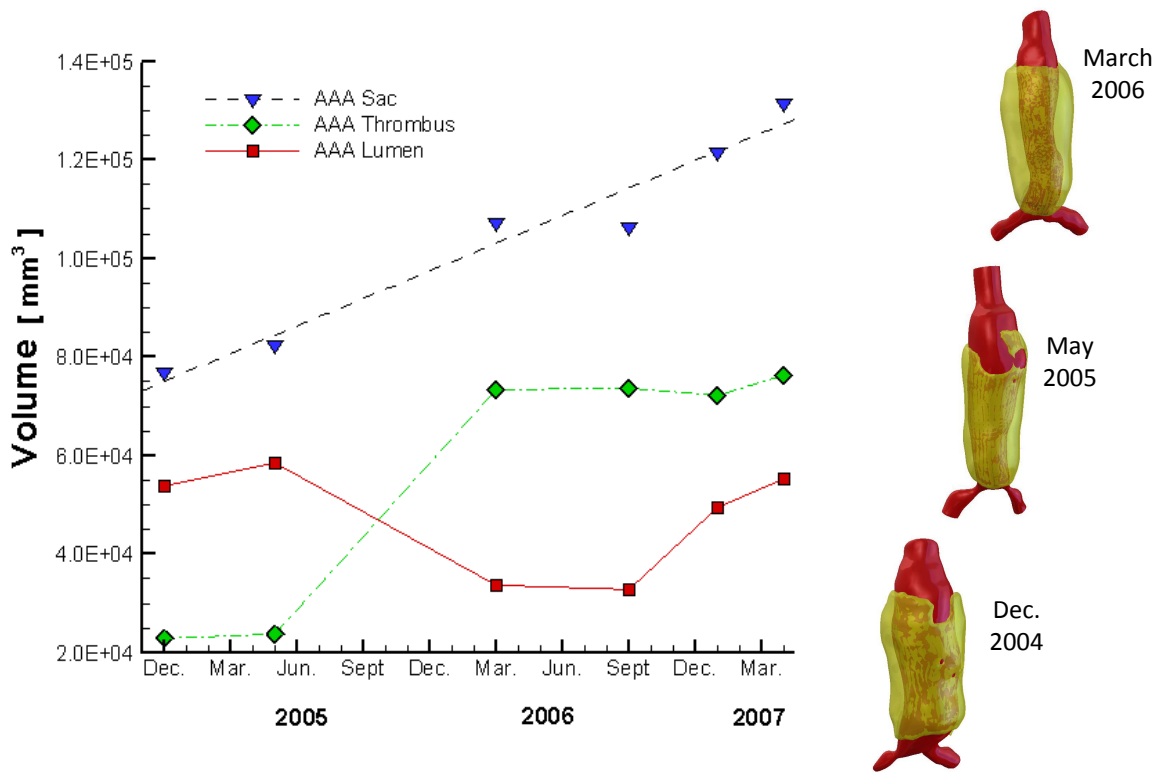


Figure 3.1: Patient's AAA volume history and accompanying geometries

Special attention should be directed to the rapid increase in ILT volume (represented in Fig. 3.1 by the green AAA Thrombus curve) mainly between May 2005 and March 2006. However, while the AAA-lumen volume of May 2005 may be slightly larger than then Dec. 2004 lumen volume, the Dec. 2004 geometry has more luminal bulges and a more severe neck angle. Thus, to investigate ILT formation and test if any bulges correlate with potential particle entrapment and deposition, the Dec. 2004 lumen geometry was used as the computational domain for the AAA particle-hemodynamics analysis.

3.2.2 Mesh Generation

ICEM CFD was used to generate a mesh of the patient-specific computational AAA lumen domain. The lumen wall was divided into multiple sections and prism elements of varying heights were generated across the wall boundaries to accurately capture the high gradients of near-wall velocity flow. Variable prism heights were used to ensure they did not overtake the smaller diameters of the common iliac arteries, where the AAA region had a max. prism height of 1.5mm and the iliac regions had a maximum prism height of 0.8mm. The maximum distance from the no-slip wall to the nearest node was prescribed to be 0.25mm in the AAA region and 0.13mm in the iliac zones, with a total of six prism layers from the nearest node at the wall. Extensions equivalent to three times the vessel diameter of the inlet and outlet boundaries were inserted to reduce the inaccurate influence of local boundary conditions and presence of unnatural wall shear stress (WSS) vectors at the AAA region proximal location. Figure 3.2 illustrates the unnatural WSS vectors at the proximal AAA region and the correction achieved by using the boundary extensions.

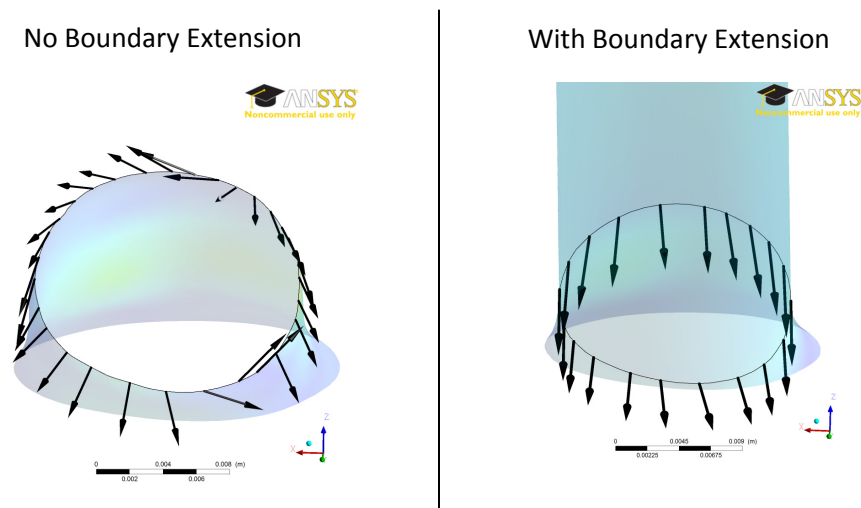


Figure 3.2: Wall shear stress vectors with and without inlet boundary extension

A mesh independence test was performed using steady flow simulations with an inlet Reynolds number of 1400, outlet boundary conditions of 100mmHg, and a specified solver root mean square (RMS) residual of 1×10^{-5} . The simulations were performed on a single Processor of a Dell Precision T7400 Workstation with two quad-core processors and 16GB of RAM. Table 3.1 illustrates the multiple mesh densities tested.

Table 3.1: Computational AAA Meshes Tested for Solution Independence

| <u>Mesh No.</u> | <u>No. of Elements</u> | <u>No. of Nodes</u> | <u>Simulation Time [hrs.]</u> |
|-----------------|--|---------------------|-------------------------------|
| 1 | 246,890 (128,762 Tetrahedrals ; 118,128 Prisms) | 86,085 | 1.133 |
| 2 | 800,475 (514,305 Tetrahedrals ; 286,170 Prisms) | 242,310 | 0.733 |
| 3 | 1,609,696 (669,664 Tetrahedrals ; 940,032 Prisms) | 662,393 | 1.133 |
| 4 | 4,072,360 (3,206,608 Tetrahedrals ; 865,752 Prisms) | 995,644 | 1.233 |
| 5 | 4,349,716 (3,212,716 Tetrahedrals ; 1,137,000 Prisms) | 1,133,697 | 1.333 |
| 6 | 5,635,988 (4,205,808 Tetrahedrals ; 1,430,180 Prisms) | 1,453,276 | 1.817 |

The primary and secondary velocity fields were recorded at multiple planes in the AAA sac and the quantitative velocity profiles of each velocity component were recorded at two lines through one plane in the AAA sac. Figure 3.3 depicts the different flow fields of specific meshes two through four and Figure 3.4 plots the velocity profiles of each mesh at the illustrated lines (Note that the current simulation results and all that follow relating to the AAA study used the boundary extensions, but they have been removed in the solution plots).

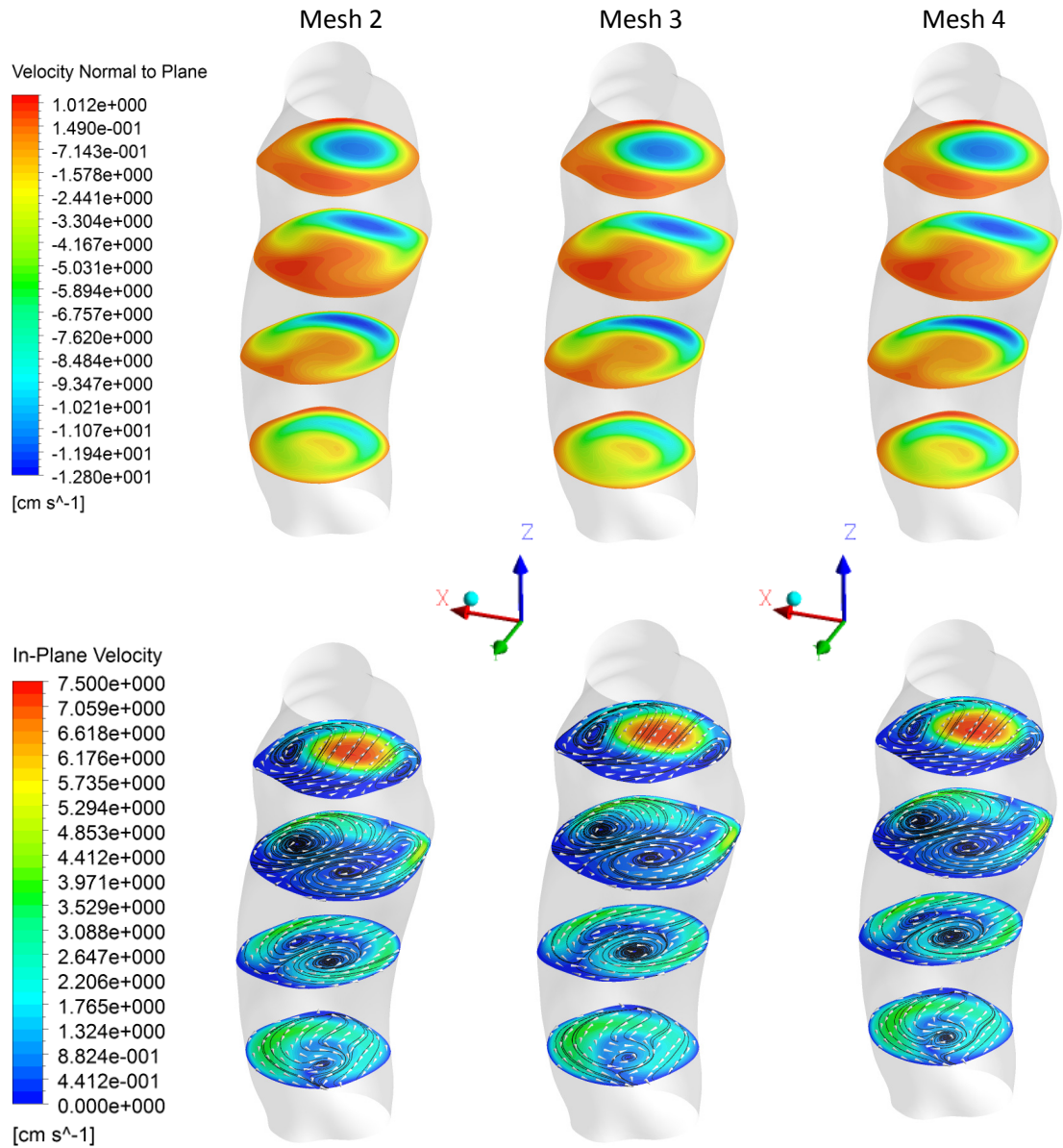
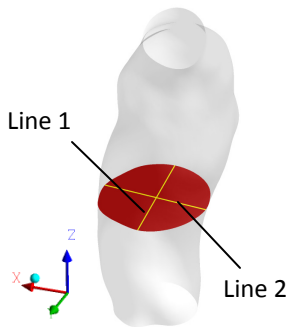
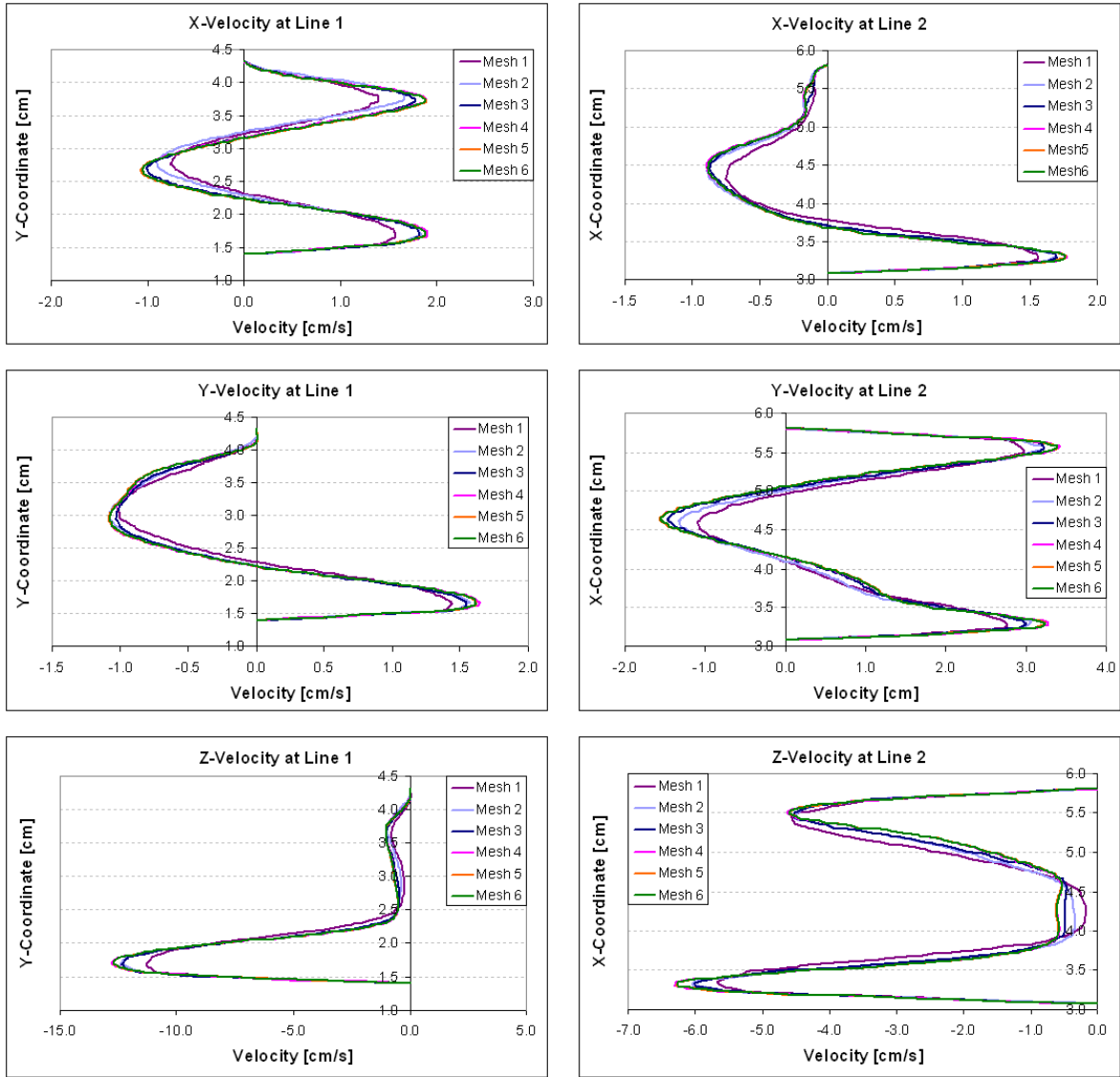


Figure 3.3: Primary and secondary flow fields of AAA meshes

Meshes five and six exhibited velocity contours that appeared indistinguishable from the velocity fields of mesh four; hence, they were not included in Fig. 3.3.



NOTE: A negative z-velocity corresponds to the downward (distal) direction

Figure 3.4: Velocity profiles of all meshes in one AAA plane

A comparison of the data in Fig. 3.3 show that the flow field structures in the different planes are almost indistinguishable for each mesh employed. However, the velocity profiles in Fig. 3.4 reveal a more noticeable quantitative difference between the meshes, where mesh 3 generated velocity profiles less than 4% of those when using mesh six. Moreover, mesh 4 had velocity profiles that were nearly indistinguishable from mesh 6. WSS distributions were then analyzed and an upper spatial discretization limit was encountered due to the triangular distance of the patient-specific geometry files which were in the STL data format. Mesh 4 produced unreasonable WSS distributions by recording stress concentrations in the STL triangular faces. Thus, a hybrid mesh between mesh 3 and 4 was constructed and produced reasonable WSS distributions with differences in max. WSS magnitudes less than 2%. The final hybrid mesh, being independent of further refinements, had 712,304 nodes and 1,937,461 elements (1,031,125 tetras. and 906,336 prisms). An important note is that the total element density is much less than those reported by Les et al. (2010a), but their domains are also much larger and their geometry files have been converted to smooth surfaces (B-spline or NURBS) that are not represented by triangulated faces and allow for more extensive refinement capabilities. For the current study, the mesh refinement analysis has shown sufficient independence, yet also exceeds the spatial discretization refinement reported by many other AAA computational studies including those that reproduced experimental flow fields (e.g., Boutsianis et al., 2009 and Frauenfelder et al., 2006).

3.3 Hepatic Arterial System and Stationary Smart Micro-Catheter Geometries

3.3.1 Hepatic Arterial System Anatomy and Representative Computational Domain

The hepatic arterial system is part of a larger cardiovascular sub-system called the splanchnic arteries, which deliver blood to the digestive and endocrine organs. All vessels of the splanchnic system originate from the abdominal aorta and in most cases stem from three main arteries: the celiac artery (CA), the superior mesenteric artery (SMA) and the inferior mesenteric artery (IMA). While the other arteries in the splanchnic system supply organs which decompose ingested food, the hepatic arteries deliver oxygenated blood to the liver, which assists the kidneys in purifying and filtering the blood itself.

The hepatic arterial system is highly variable from patient to patient and includes many different configurations. Vessels tend to have high degree of curvature and elevated levels of tortuosity when compared to other arteries in the cardiovascular system. Michels (1966) conducted one of the first studies of hepatic arterial anatomy by tabulating different configurations of the hepatic arterial system in 200 cadavers. The study introduced ten different configurations of the arteries, which are differentiated by the origin of the different vessels of the hepatic artery. Hiatt et al. (1994) conducted a more expansive study on 1000 patients and found similar anatomic configurations as Michels (1966) data. A recent study by Koops et al. (2004) identified sixteen unique configurations in 604 patients.

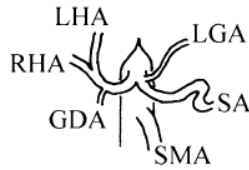
The most common anatomic configuration existed in approximately 74.6% of the combined population of the three previously reference anatomic studies (n = 1804). Such a configuration has the common hepatic artery (CHA) extending from the celiac artery (CA) distal to the splenic artery (SA) and the left gastric artery (LGA). In the normal

configuration, the CHA bifurcates into the gastroduodenal artery (GDA) and the proper hepatic artery (PHA), which then bifurcates into the right hepatic artery (RHA) and the left hepatic artery (LHA) which supply the right and left lobes of the liver respectively. The remaining 25.4% of the population is composed of different anatomic variations which have the RHA, LHA, or CHA originating from the superior mesenteric artery (SMA) or the LGA. Hiatt et al.'s (1994) classification enables all three studies to be compared using the same classification. Table 3.2 lists the percentage of the population contained in each classification while Figure 3.5 illustrates the primary anatomical configurations of the hepatic arterial system with sketches from Koops et al. (2004). An important note is that over 2% of the total population size is unclassified using the Hiatt et al. (1994) classification method, and further reveals the amount of patient-specific variation seen in the hepatic arterial system.

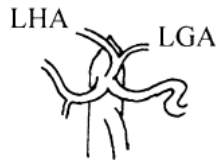
Table 3.2: Percentages of different anatomic configurations of the hepatic arterial system

| Type | Description | Percentage (n = 1804) |
|--------------|---|-----------------------|
| 1 | Traditional | 74.6% |
| 2 | a) Replaced LHA from LGA b) Accessory LHA from LGA | 7.5% |
| 3 | a) Replaced RHA from SMA b) Accessory RHA from SMA | 11.9% |
| 4 | a) Combination of 2a and 3a b) Combination of 2b and 3b c) Combination of 2b and 3a | 2.1% |
| 5 | CHA from SMA | 1.3% |
| 6 | CHA from abdominal aorta | 0.2% |
| Unclassified | | 2.4% |

Type 1: Traditional



Type 2a: Replaced LHA from LGA



Type 2b: Accessory LHA from LGA



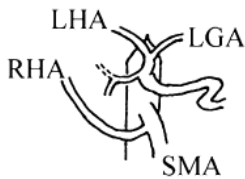
Type 3a: Replaced RHA from SMA



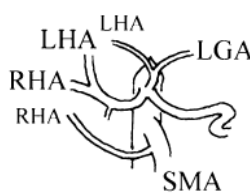
Type 3b: Accessory RHA from SMA



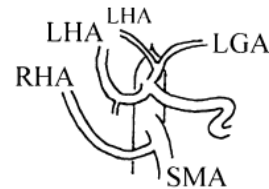
**Type 4a: Replaced RHA
and replaced LHA**



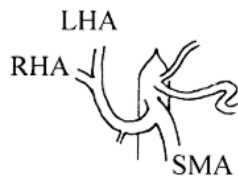
**Type 4b: Accessory RHA
and accessory LHA**



**Type 4c: Replaced RHA
and accessory LHA**



Type 5: Replaced CHA from SMA



Type 6: CHA from abdominal aorta



Figure 3.5: Anatomic configurations of the hepatic arterial system

Images used with kind permission from Springer Science and Business Media: *Surgical and Radiologic Anatomy*, "Anatomic variations of the hepatic arteries in 604 selective celiac and superior mesenteric angiographies," 26, 2004, 241, A. Koops, B. Wojciechowski, D.C. Broering, G. Adam, G. Krupski-Berdien, Figure 1

The measurably different anatomies identified in Fig. 3.5 support the need to obtain additional morphological data and move towards patient-specific morphologic classification.

A representative computational domain of the hepatic arterial system was created to mimic the most common anatomical configuration of the hepatic vasculature listed in Table 3.2 and is depicted in Fig. 3.6 alongside a clinical illustration of the primary hepatic arterial system with liver tumors and the right gastric artery (RGA) depicted near the GDA (Note: the right gastric artery was not included in the computational geometry because all relevant published anatomic studies do not include that arterial vessel).

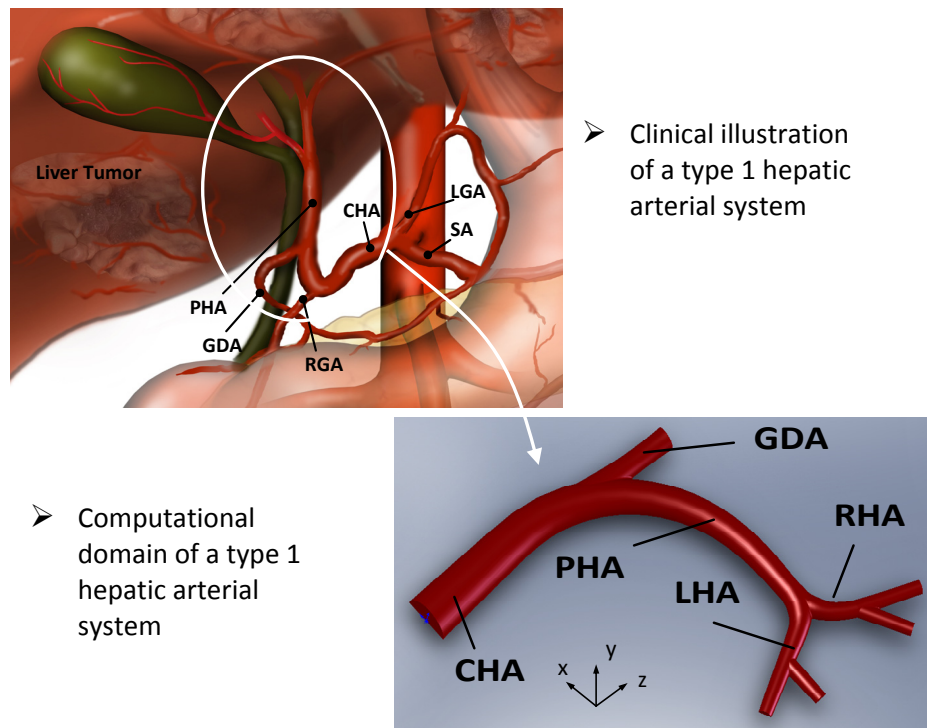


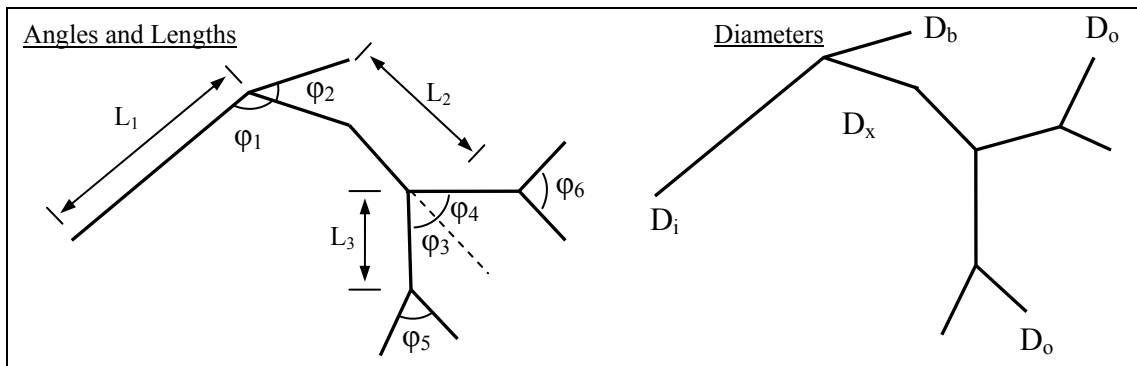
Figure 3.6: Artist rendering of Type 1 hepatic arterial system and symmetric, representative hepatic artery geometry

Image from Wake Radiology Oncology (Cary, NC), *used with permission*

Vessel diameters were based on published data from Ishigami et al. (2002) who recorded the mean diameter of the CHA ($6.3 \pm 0.9\text{mm}$) after the splenic bifurcation but prior to the GDA

bifurcation, Carlisle et al. (1992) who measured the common and proper hepatic diameters (6mm and 4mm respectively) and Han et al. (2002) who recorded the RHA diameter (2.68 ± 0.69 mm). Additionally, the cross-sectional area of the model's 6mm CHA inlet plane is within $\pm 7.5\%$ of the common hepatic artery lumen area measured by Jin et al. (2009) breath-hold MRI data. Remaining arteries such as the GDA and bifurcating branches of the RHA and LHA were approximated to represent reasonable values. Table 3.3 documents the lengths and bifurcation angles of each segment which were selected to represent anatomic illustrations, but are not based on patient data.

Table 3.3: Geometric features of representative hepatic arterial geometry



| <u>Feature</u> | <u>Value</u> | <u>Feature</u> | <u>Value</u> |
|----------------|--------------|----------------|--------------|
| L_1 | 2.80 [cm] | D_i | 0.6 [cm] |
| L_2 | 2.70 [cm] | D_b | 0.3 [cm] |
| L_3 | 0.67 [cm] | D_x | 0.44 [cm] |
| ϕ_1 | 135° | D_o | 0.17 [cm] |
| ϕ_2 | 35.6° | ϕ_5 | 65.2° |
| ϕ_3 | 65.7° | ϕ_6 | 38.8° |
| ϕ_4 | 67.2° | | |

3.3.2 Hepatic Arterial System Mesh Generation

ICEM CFD v.12 (ANSYS Inc., Canonsburg, PA) was used to generate unstructured tetrahedral meshes that are $\frac{1}{2}$ of the physical domain. Anisotropic distributions of element sizes were selected such that the element length is only on the order of 0.01 times the vessel diameter. Elevated element densities were implemented in regions of high curvature, such as vessel bifurcations. Prism/wedge elements were employed in near-wall regions to increase element density in regions of high velocity gradients. The first layer of elements in the computational domain has a maximum distance from the wall of 0.0133mm and a minimum distance of 0.0089mm. Figure 3.7 illustrates the core features of the computational mesh.

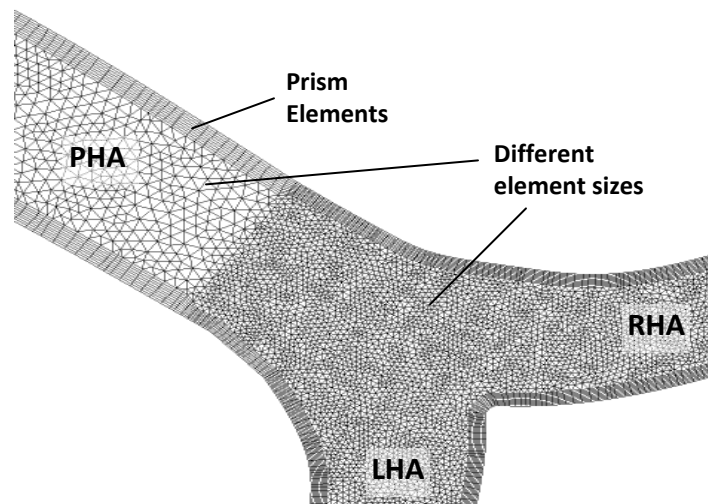


Figure 3.7: Core features of hepatic arterial system mesh

A mesh refinement study was conducted by comparing the results of three meshes for a steady inlet Reynolds number of 977, where the iterative solution process continued until the mass and momentum RMS residuals were less than 1×10^{-6} . Table 3.4 lists the characteristics of each mesh.

Table 3.4: Mesh parameters used in the current study

| <u>Parameter</u> | <u>Mesh 1</u> | <u>Mesh 2</u> | <u>Mesh 3</u> |
|--------------------------|--|--|--|
| Total Number of Elements | 484,775 (256,508 Tetrahedrals, 228,267 Prisms) | 973,210 (510,223 Tetrahedrals, 462,987 Prisms) | 1,734,058 (1,009,468 Tetrahedrals, 724,590 Prisms) |
| Total Number of Nodes | 170,700 | 384,113 | 569,122 |
| Max. Element Length | 0.500 [mm] | 0.365 [mm] | 0.300 [mm] |
| Min. Element Length | 0.150 [mm] | 0.135 [mm] | 0.100 [mm] |

The pressure and velocity vector components of each solution were measured at geometric locations (independent of mesh node locations) throughout the computational domain. A cloud of 50 equally-spaced points were distributed across the symmetry plane, where the velocity components and pressure were measured for each mesh. Additionally, the pressure and velocity components were recorded at discrete points 0.005mm apart along four planes throughout the computational domain. Figure 3 illustrates the locations of the geometric measuring points.

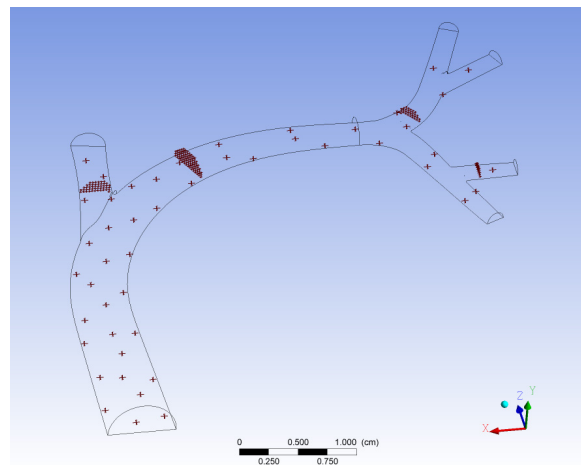


Figure 3.8: Location of geometric points were solution values of each mesh are compared

The maximum RMS-percent difference of the solution locations was less than 1.45% between all meshes, while a visual comparison revealed that mesh 2 produced smooth

velocity contours of higher quality than mesh 1. Figure 3.9 clearly depicts the smooth contours of mesh two versus the more jagged contours of mesh one.

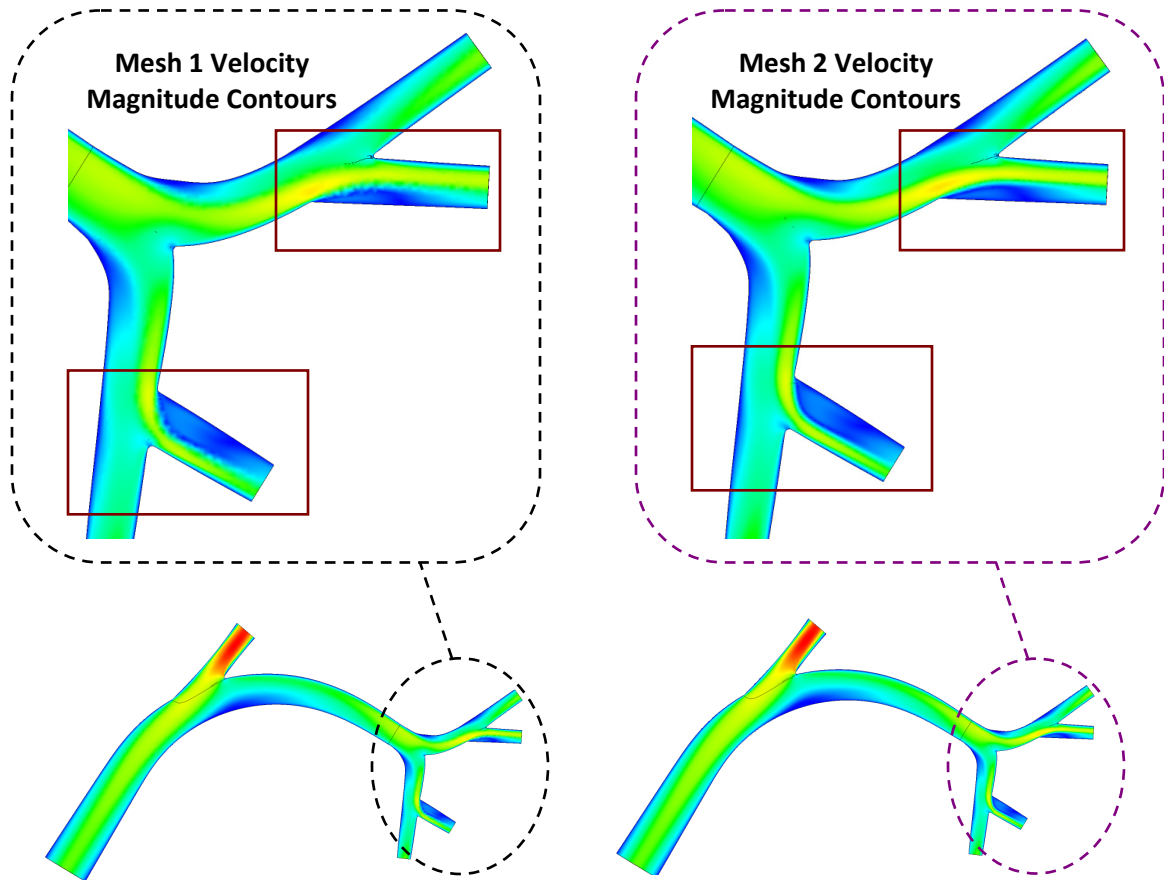


Figure 3.9: Qualitative comparison of velocity field magnitudes along symmetry plane

The velocity profiles at multiple locations were also compared of inferior meshes than those listed in Table 3.5 and exhibited differences in the profile data less than 2%. Thus, combining the direct data of meshes one through three and the indirect data of meshes not listed in Table 3.4, the mesh 2 solutions were deemed sufficiently independent of further mesh refinements and hence mesh 2 was utilized for the computational analysis.

3.3.3 Stationary Smart Micro-Catheter Computational Domain

To investigate the influence of a ^{90}Y -microsphere delivery catheter has on the local fluid flow and particle trajectories, a computational domain of the fluid surrounding the catheter and its fixation beams was created. The artery vessel containing the catheter had an outer diameter of 6mm to match the inlet vessel diameter of the representative CHA domain. A catheter diameter of 1mm was used to model a 3 F (F = French) catheter, which is representative of the catheter size currently used in ^{90}Y -microsphere delivery (Murthy et al., 2005). The catheter wall was modeled as an ideal, massless structure, neglecting the wall's physical thickness. Reinforcement beams connecting the catheter and arterial walls were added to the domain as a representation of a cross-sectional positioning system that would be available on a novel smart micro-catheter (SMC). The SMC would provide clinicians with a new degree of positional control by enabling the selection of a precise cross-sectional position inside the artery for optimal injection locations of various therapeutic agents (Kleinstreuer, 2009).

A single radial position with the catheter wall having a distance of 1mm from the vessel axial coordinate axis was chosen for this initial study. The total length of the SMC was approximately 13 times the catheter diameter. Reinforcement beams, placed at two axial locations of the catheter (5mm apart), were modeled as square structures with a uniform thickness of 0.08mm, and were arranged at equidistant angular positions 120° apart. Thus, a total of six reinforcement beams were present in the domain with three beams at each axial location. An illustration and detailed sketches of the SMC computational domain can be

found in Figs 3.10a and 3.10b, where the SMC-CHA interface is located at the topmost line of the axial view in Fig. 3.10b.

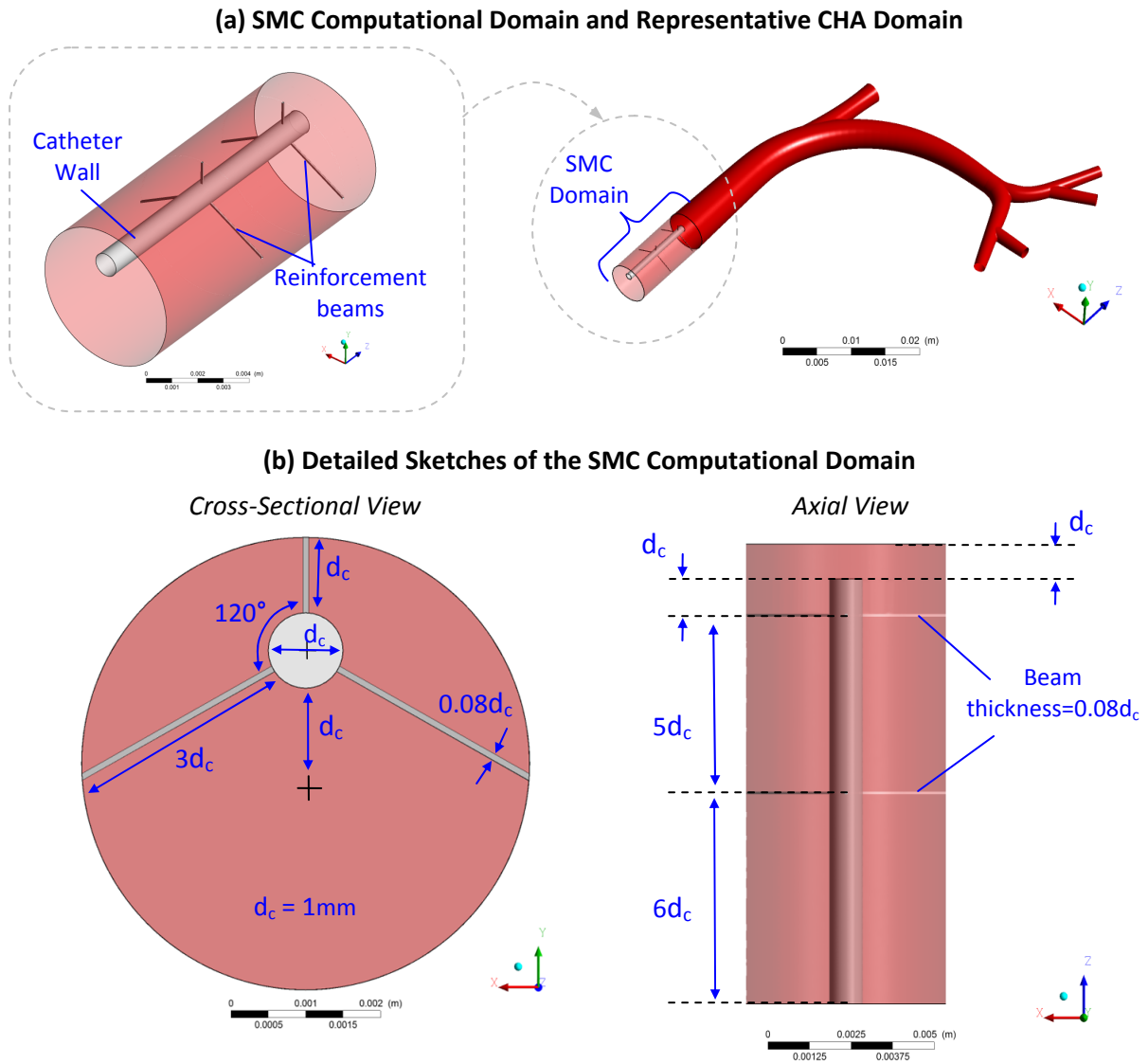


Figure 3.10: (a) SMC domain connected to representative CHA domain and (b) Detailed sketches of the SCM computational domain

3.3.4 Smart Micro-Catheter Mesh Generation

Multiple mesh files with different element densities were created to correlate regions of elevated mesh density with high gradients and local flow disturbances. Dr. Jie Li CM-P Lab team member, constructed a total of six mesh files that were integrated to form the SMC computational domain using ICEM CFD v12.0. The mesh files captured the regions of fluid flow only. Thus, the reinforcement beams volumes were not meshed and hence only the surfaces of fluid-solid interfaces are included in the fluid mesh. A mesh refinement analysis was conducted by comparing the velocity contours and velocity profiles at random locations in the domain. The mesh was continually refined until the velocity contours and profiles were indistinguishable. Figure 3.11 illustrates the mesh at the different regions of the SMC domain and Table 3.5 lists the mesh characteristics of each region.

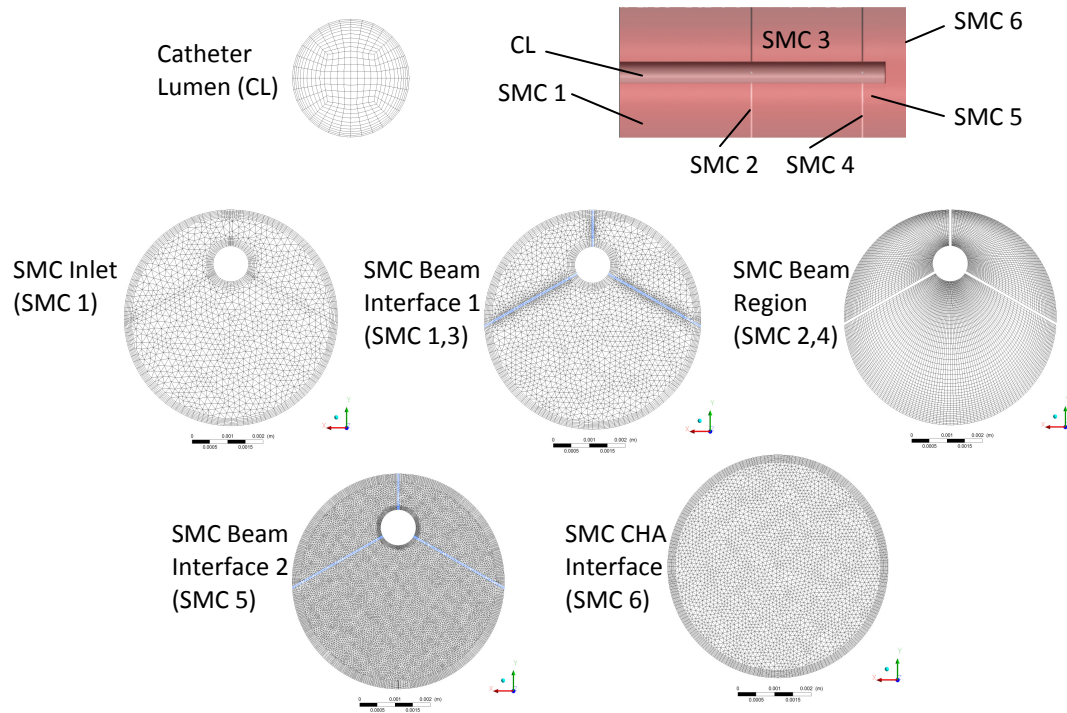


Figure 3.11: Computational mesh of the SMC domain

Table 3.5: Mesh characteristics of the SMC domain

| <u>Parameter</u> | <u>SMC 1</u> | <u>SMC 2</u> | <u>SMC 3</u> | <u>SMC 4</u> | <u>SMC 5</u> | <u>SMC 6</u> | <u>CL</u> |
|---------------------------|--------------|--------------|--------------|--------------|--------------|--------------|-----------|
| Total Number of Elements: | 625,984 | 18,800 | 507,774 | 18,800 | 2,914,109 | 410,616 | 15,744 |
| Tetrahedrals: | 504,298 | 0 | 432,894 | 0 | 2,632,733 | 362,412 | 0 |
| Prisms: | 121,686 | 0 | 74,880 | 0 | 281,376 | 48,204 | 0 |
| Hexahedrals: | 0 | 18,800 | 0 | 18,800 | 0 | 0 | 15,774 |
| Total Number of Nodes | 152,763 | 29,223 | 116,089 | 29,223 | 602,747 | 90,608 | 16,842 |

The total number of elements in the SMC domain was 4,511,827 and when paired with the full CHA domain the total element count was 6,458,247. Thus, the finalized SMC domain mesh has a much larger element count than the computational mesh of the $\frac{1}{2}$ domain CHA.

3.4 Patient-Inspired Replaced Common Hepatic Arterial Geometry

3.4.1 Patient-Inspired Computational Domain

In addition to the representative system of Sect. 3.3.1a, a patient-inspired geometry was created from anonymized abdominal computed-tomography DICOM files of a patient with metastatic liver cancer. The files were obtained via personal communication with Dr. A. Kennedy, a practicing radiation oncologist from Wake Oncology Radiology (Cary, NC). Using the commercial segmentation software, Simpleware (Simpleware Ltd., Exeter, UK), Prof. S. Hyun (Research team collaborator from The Department of Biomedical Engineering at Mercer University, Macon, GA) extracted the centerline and approximate diameter of the hepatic arterial vasculature.

SolidWorks was used to create a 3D volume from the centerpoint and diameter data. Multiple spline curves that traced the centerline specified by the provided data points was first created. Planes normal to the spline curves were then created at the data points along the curves, where circular sketches of the vessel diameter were created. The loft feature was then used to create a 3D object from the multiple 2D cross-sectional profiles on the normal planes. Figure 3.12 depicts the created hepatic geometry and labels the major vessels, where the grey spline curves represent the vessel centerline.

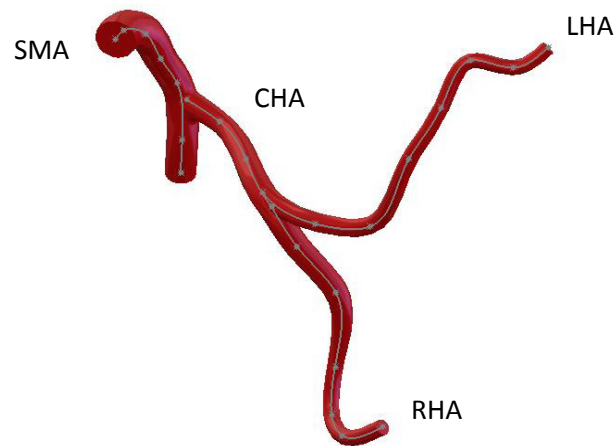


Figure 3.12: Patient-inspired hepatic arterial system geometry

The vessel anatomy illustrated in Fig. 3.12 is classified as a replaced common hepatic artery (CHA) stemming from the superior mesenteric artery (SMA) (cf. Table 3.2). Morphologic data of the anatomy revealed that the SMA inlet had a diameter of 7.3mm and terminated with a diameter of 5.8mm. The CHA had an initial diameter of 4.8mm eventually branching into the LHA and RHA arteries which terminated with diameters of 2.75mm and 3.00mm, respectively. Unfortunately, the downstream vessels included only the RHA and LHA due to the limited pixel resolution and slice thickness of the provided DICOM files.

3.4.2 Mesh Generation

ICEM CFD v.12.0 (ANSYS Inc., Canonsburg, PA) was used to generate the computational mesh. Again, an unstructured tetrahedral mesh with prism elements along the walls anisotropic distributions of element density was created. The first layer of elements in the computational mesh has a maximum distance from the wall of 0.04375mm and a minimum distance of 0.01875mm. Local element size was adjusted such that the local vessel diameter divided by the locally maximum element length was always greater than ten, where most regions had a vessel diameter to element length ratio greater than twenty.

A mesh independence test was performed using steady flow simulations with an inlet Reynolds number of 360 (representative of mean flow conditions, see Ch. 4), outlet boundary conditions of 100mmHg, and a specified solver RMS residual of 1×10^{-5} . The simulations were performed on 10 distributed processors from a remote IBM Blade Center Linux Cluster running a 64bit Linux operating system with 2GB of shared memory per node (cf. henry2 cluster, hpc.ncsu.edu). Table 3.6 illustrates the multiple mesh densities tested and their corresponding characteristics.

Table 3.6: Computational meshes of the patient-inspired hepatic artery system

| Parameter | Mesh1 | Mesh2 | Mesh3 | Mesh4 | Mesh5 | Mesh6 |
|---------------------------|---------|-----------|-----------|-----------|-----------|-----------|
| Total Number of Elements: | 843,336 | 1,403,260 | 2,553,597 | 6,079,797 | 6,757,999 | 9,507,272 |
| Tetrahedrals: | 352,500 | 883,876 | 1,533,269 | 4,231,405 | 4,766,527 | 6,753,000 |
| Prisms: | 490,836 | 519,384 | 1,020,328 | 1,848,392 | 1,991,472 | 2,754,272 |
| Total Number of Nodes | 326,939 | 430,015 | 799,509 | 1,689,809 | 1,855,564 | 2,591,741 |
| Simulation Time [min.] | 4.50 | 5.38 | 9.72 | 21.75 | 16.68 | 24.57 |

The decrease in simulation time of mesh 5 is surprising with the extended simulation times of mesh 4 and 6. However, the blades used to run the mesh 5 simulation were different than the blades used for the mesh 4 and 6 simulations, and had the potential to be more computationally powerful than those used in previous simulations, explaining the decreased simulation time. Velocity profile data at four lines in the computational domain was measured and Figures (3.13) and (3.14) plot the velocity profile data vs. a dimensionless length (L^*), directly comparing the performance of the different meshes.

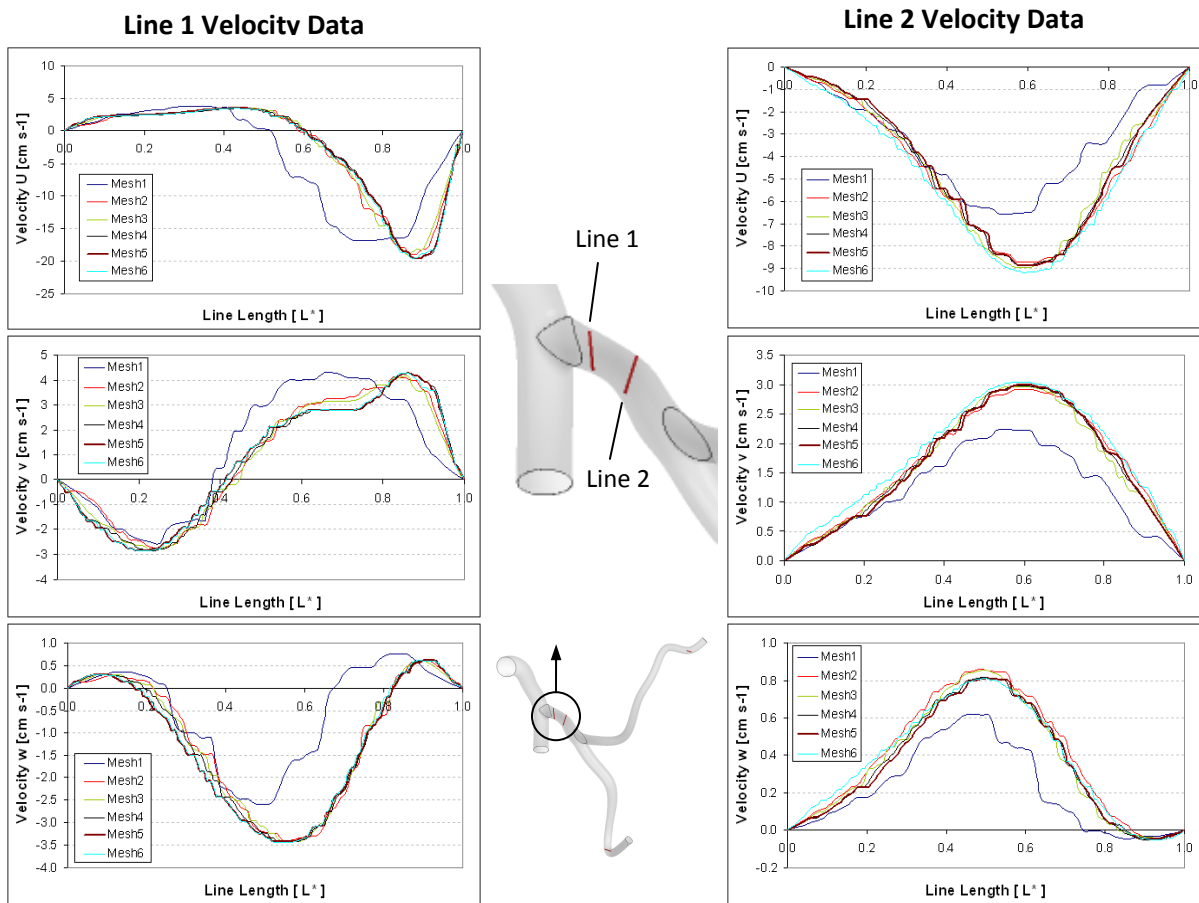


Figure 3.13: Velocity profile data at lines one and two in the patient-inspired hepatic artery geometry from the different meshes

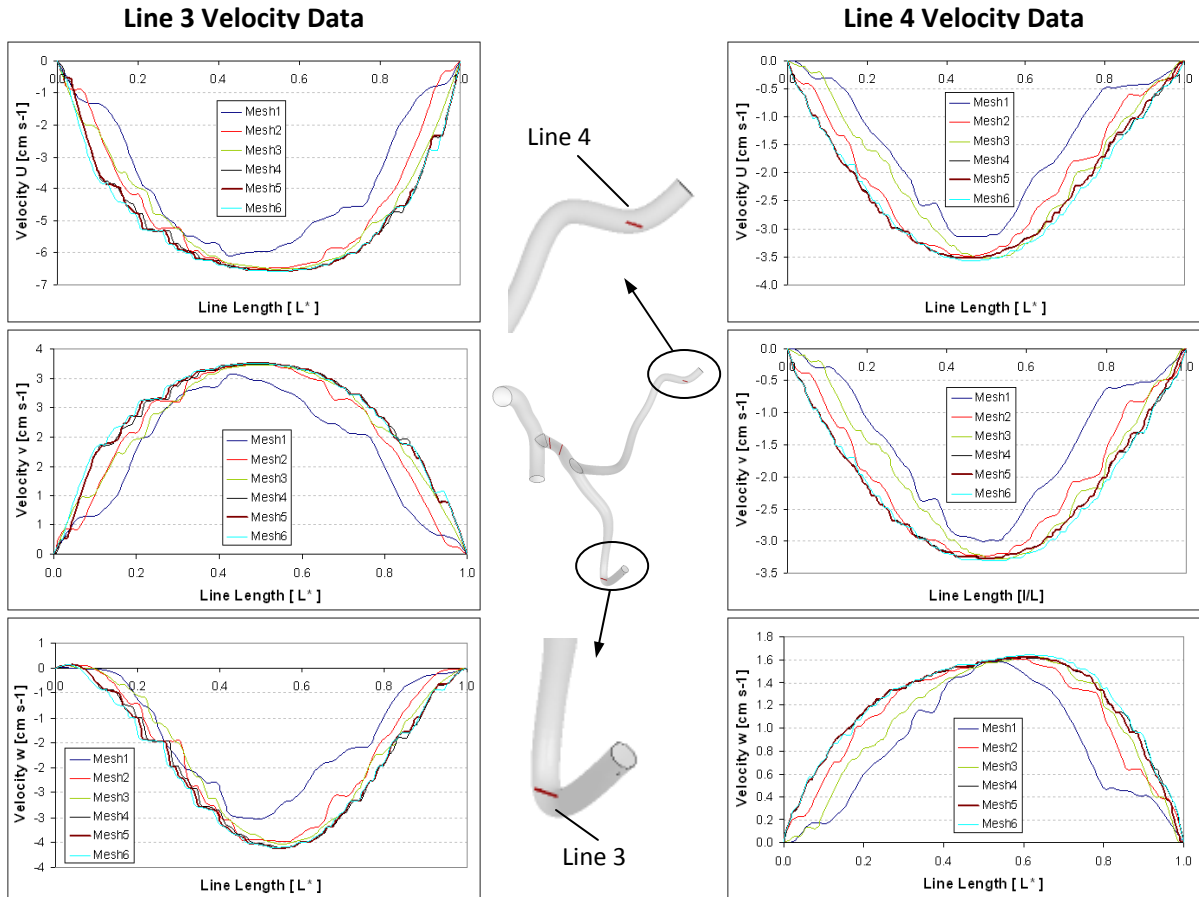


Figure 3.14: Velocity profile data at lines three and four in the patient-inspired hepatic artery geometry from the different meshes

Noticeable differences in the velocity profiles from each mesh are clearly visible (particularly mesh1). The pressure fields of the different meshes showed differences less than 0.1% after mesh 3 and thus were deemed unnecessary to analyze in the same detail as the velocity fields. The profiles in Figs. 3.13 and 3.14 reveal that mesh 5 is capable of sufficiently reproducing the velocity profiles of mesh 6 (where mesh 6 has over two million than mesh 4). Therefore, mesh 5 was deemed capable of providing solutions independent of further mesh refinement and was utilized for the computational analysis.

3.5 Conclusions

The multiple computational domains and their corresponding meshes have been described in Sections 3.2 to 3.4 along with the necessary background information regarding the anatomy of the different arterial vessels. Furthermore, a mesh independence analysis for each computational domain has been documented and the methods used to ascertain the independence of the computational mesh have been clearly described and illustrated. An important component of the analysis is the use of both qualitative and quantitative criteria to determine the performance of each mesh. In conclusion, the work and effort in developing physiologically relevant arterial domains and in determining a suitable computational mesh lays a strong foundation for the particle-hemodynamics analyses.

Chapter 4:

Derivation and Implementation of Numerical Inlet/Outlet Conditions

4.1 Introduction

Prior to solving the numerical equations over the computational domain, the no-slip wall condition as well as the inlet/outlet flow field must be specified. These all-around boundary conditions enforce appropriate physical phenomena and, hence, guide the finite-volume solver to calculate an accurate solution. The current analysis requires notable effort in determining appropriate boundary conditions, since they must be reflective of *in-vivo* hemodynamic conditions to be physiologically and clinically relevant.

Dirichlet boundary conditions specifying velocity, mass flow rate, and/or static pressure are utilized for the current analysis. The AAA inlet/outlet conditions have been well

publicized and multiple sources of quantitative data exist while the transient inlet/outlet conditions and hemodynamics of the hepatic arteries have not been well investigated. The current chapter includes a brief review of the popular AAA boundary conditions used in research literature that precedes a description of the inlet/outlet conditions implemented in the AAA domain. Conversely, an extensive review of the hepatic arterial system's hemodynamics published in research literature precedes a detailed account of determining physiologically relevant boundary conditions for the hepatic arterial system. The determination of physiologically relevant boundary conditions for the hepatic arterial system is an important portion of the study's novel contributions to the scientific field. Hence, the current chapter will have a greater focus on determining the hepatic arterial boundary conditions than the AAA boundary conditions.

4.2 Derivation of Transient, Physiologically Relevant Inlet/Outlet Conditions for Abdominal Aortic Aneurysms

4.2.1 Abdominal Aortic Aneurysm Hemodynamics

AAA-hemodynamics are believed to mostly be in the laminar regime with short temporal spans of turbulence (Les et al., 2010b; Shadden et al., 2008; Li and Kleinstreuer, 2005; Finol and Amon, 2002). Interestingly, representative Reynolds numbers calculated near systolic regions of the volumetric inflow waveform have been shown to be above 2000 and recent studies by Peattie et al. (2004) and Khanafer et al. (2009) have recorded AAA turbulent hemodynamics with computational and experimental models. To date there has not been a comparison between laminar and turbulent computational models of AAA

hemodynamics and the laminar models have been shown to reproduce experimental flow fields in multiple studies (Boutsianis et al., 2009; O'Rourke and McCullough, 2008; Frauenfelder et al., 2006; Li and Kleinstreuer, 2005).

In-vivo AAA-hemodynamics are highly complex and pulsatile with Womersley numbers normally greater than ten. Three-dimensional flow features are present for most flow conditions in the local pulse of blood, where Jamison et al. (2007) calculated the onset of three-dimensional features in a full geometry of an axisymmetric rigid aneurysm under pulsatile flow to be an inlet Reynolds number of 610. Moreover, most patient-specific geometries are asymmetric and naturally cause three-dimensional flow characteristics due to the aneurysm lumen morphology. Specific characteristics of AAA-hemodynamics include large amounts of flow separation and recirculation correlated to aneurysm lumen morphology. Many of the adverse flow characteristics, especially excessive pressure and WSS, are sufficiently mitigated with the successful implantation of a stent graft (Biasseti et al., 2010; Li and Kleinstreuer, 2007; Frauenfelder et al., 2006; Li and Kleinstreuer, 2005).

4.2.2 Selected Inlet/Outlet Conditions

The widely utilized flow and pressure waveforms from Olufsen et al. (2000) were selected for the current study. Another set of popular waveforms are the ones used by Scotti and Finol (2007). Figure 4.1 illustrates the flow rate waveform specified at the AAA domain inlet and the pressure waveform specified at the domain outlets (common iliac arteries).

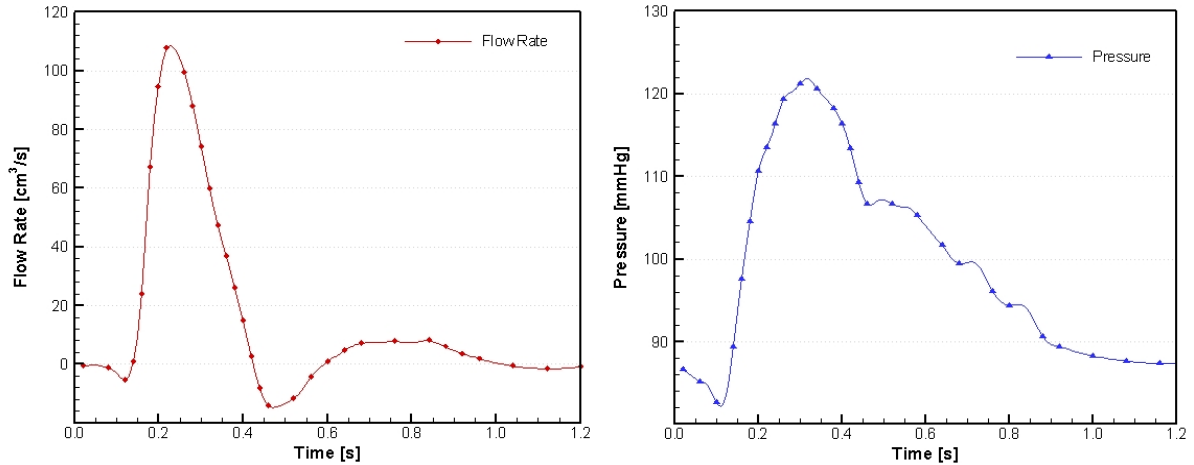


Figure 4.1: Inflow and outlet pressure waveforms used in the AAA study

Fraser et al., (2008) published a mean infrarenal flow waveform from AAA patients and Les et al. (2010a, 2010b) recently published *in-vivo* flow waveforms at the supraceliac and infrarenal locations of 36 AAA patients compiling an average waveform. While their data sets was not implemented in the current study, the utilized infrarenal waveform share many similarities with the one reported by Les et al. (2010b). The systolic flow rates, general shapes, and slopes of the implemented and Les et al. (2010b) waveforms are very similar. However, the Les et al. (2010b) infrarenal waveform has a greater amount of zero inflow present in the diastolic region of the pulse.

The inlet waveform was implemented using a uniform velocity profile specified at the extension inlet, which develops into a time-dependent, spatially-varying profile over the length of the extension upstream the AAA sac. Arterial and ILT walls were modeled as no slip, impermeable, and stationary with restitution coefficients set to zero, forcing all particles whose center of mass crosses the domain boundary to locally deposit on the wall. Since the

patient-specific waveforms were not available to implement in the current study, the selected waveforms allow for sufficient physiological relevance as a first attempt of modeling particle-hemodynamics in the AAA.

4.3 Derivation of Transient, Clinically-Inspired Inlet/Outlet Conditions for the Hepatic Arterial System

4.3.1 Hepatic Arterial System General Physiology and Hemodynamics

The liver is a crucial organ, which regulates multiple biological levels (blood pH, renal blood flow, blood nutrient levels, blood toxicity etc.) in the body to maintain homeostatic balance. A common anatomic configuration of the liver has two main lobes visible from an anterior viewpoint, but a posterior and inferior view of the liver reveals two additional lobes. The two anterior lobes are the right and left lobes, where the right lobe is the largest lobe of the liver. On the microscale, the liver has functional units called lobules that contain unique structures titled portal triads which contain a hepatic arteriole, a portal venule, and a bile duct. The hepatic arteriole and portal venule mix into enlarged capillary-like structures called liver sinusoids, which empty into the central vein (Marieb, 1998; Fox, 1996). An interesting note is that the boundaries of the liver sinusoids are more similar to liver cells (hepatocytes) than a traditional capillary wall located other in regions of the body. Figure 4.2 illustrates the macro- and micro-scale anatomy of the human liver.

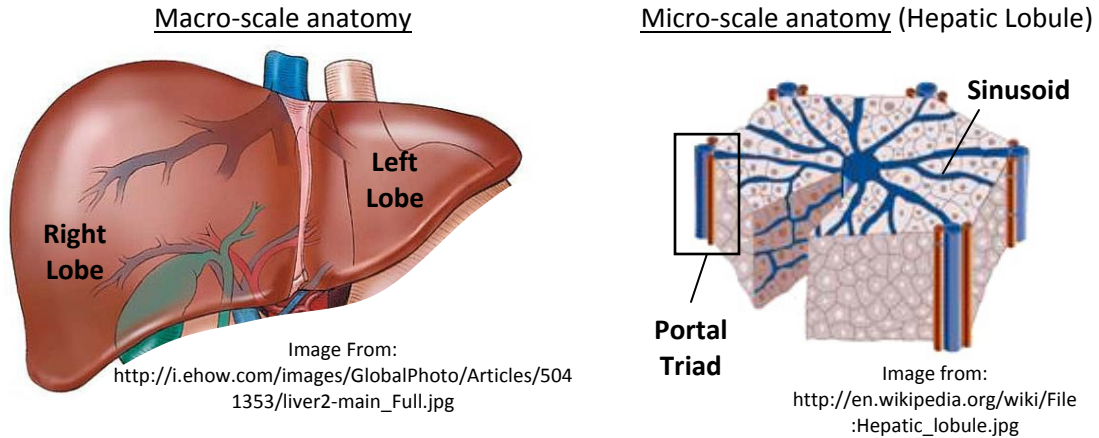


Figure 4.2: Macro and micro anatomy of the human liver

The blood supply to the liver comes from two sources, the hepatic arteries and the portal veins. In general, the hepatic arteries supply approximately 20-25% of the total blood delivered to the liver, where the portal veins supply the remaining 75-80% (Radeleff et al., 2009). Scott (1986) stated the blood delivered to the liver via the hepatic arteries is approximately 10% of total cardiac output.

In order to accurately model the transient fluid dynamics of the hepatic arterial system, the *in-vivo* bulk flow rates through the system's primary arteries need to be quantified. Unfortunately, many of the published studies are only taken with liver-transplant patients (which do not reflect the general population) or do not provide the specific details to identify the flow/velocity measurement location (e.g. in which hepatic artery are the measurements taken). The anatomic description of the hepatic arterial system identified ten individual arteries, but (to the author's knowledge) the left and right gastric arteries have no published bulk flow rates in human studies. Quantified flow rates in the surrounding arteries imply that the gastric arteries receive a small percentage of the blood flow distribution, and are thus not

considered a primary artery of the hepatic arterial system. The eight remaining arteries describe the primary arteries of the hepatic arterial system and are listed below:

- Celiac Axis/Artery (CA)
- Splenic Artery (SA)
- Common Hepatic Artery (CHA)
- Gastroduodenal Artery (GDA)
- Proper Hepatic Artery (PHA)
- Left Hepatic Artery (LHA)
- Right Hepatic Artery (RHA)
- Superior Mesenteric Artery (SMA)

Blood flow in the CA is critical to the hepatic arterial system since in almost 75% of patients, all blood flow delivered to the hepatic arteries stems from the CA. Moore and Ku (1994) calculated a bulk flow rate of 9.833 [cm³/s] in the CA by utilizing data of previous physiologic studies. Other studies also recorded blood flow in the CA during fasting and baseline conditions. Table 4.1 presents the data from multiple sources and a weighted average of the mean flow rate and lumen diameter.

Table 4.1: Blood flow measurements in the celiac artery

| <u>No. of Patients</u> | <u>Measurement Method</u> | <u>Lumen Diameter [mm]</u> | <u>Mean Flow [cm³/min.]</u> | <u>Source</u> |
|--------------------------|---|---|--|--------------------------|
| 18 | Doppler Color Flow Imaging | 5.82 ± 3.58 | 516 ± 292 | Uzawa et al. (1993) |
| 7 | Simultaneous Pulsed and Echo Doppler Ultrasound | 5.20 ± 0.3 | 463 ± 59 | Someya et al. (2008) |
| 7 | Simultaneous Pulsed and Echo Doppler Ultrasound | 5.00 ± 0.2 | 456 ± 50 | Someya et al. (2008) |
| 9 | Phase Contrast MRI | NA | 503 ± 170* | Barthelmes et al. (2009) |
| <u>Total Sample Size</u> | | <u>Weighted Average Lumen Diameter [mm]</u> | <u>Weighted Average Mean Flow [cm³/s]</u> | |
| N = 41 | | 5.505** | 8.231 | |

*A body surface area of 1.84[m²] (Vauthey et al. 2002) was used to calculate flow in [cm³/min]

**A Sample size of n=32 was used to calculate the average diameter

Uzawa et al. (1993) also quantified that the max. blood velocity in the CA is 60 ± 19 [cm/s], which corresponds to a max. flow rate of 13 ± 4.34 [cm³/s]. All measurements were taken in studies that did not include any organ transplantation and each patient was without chronic disease. Combining the data in Table I with the value reported by Moore and Ku (1994), an acceptable range of mean flow rates in the CA is 8.231-9.8 [cm³/s]. An average of the two values yields 9.01 [cm³/s] as a representative flow rate value from multiple sources.

SA blood flow directly influences the percentage of CA blood flow that enters into the CHA and eventually entering the different lobes of the liver. Furthermore, a more realistic portrayal of the fluid dynamics in the arteries that supply blood to the liver can be captured if the SA is included in the computational simulations. Table 4.2 presents the flow rate data from multiple sources in healthy patients.

Table 4.2: Blood flow measurements in the splenic artery

| <u>No. of Patients</u> | <u>Measurement Method</u> | <u>Lumen Diameter [mm]</u> | <u>Mean Flow [cm³/min.]</u> | <u>Source</u> |
|--------------------------|----------------------------|---|--|------------------------|
| 24 | Duplex Doppler Ultrasound | 4.50 ± 3.29 | 179 ± 37 | Sato et al. (1987) |
| 21 | Duplex Doppler Ultrasound | 4.76 ± 2.60 | 370 ± 181 | Nakamura et al. (1989) |
| 18 | Doppler Color Flow Imaging | 4.02 ± 3.29 | 247 ± 179 | Uzawa et al. (1993) |
| 17 | Doppler Color Flow Imaging | NA | 413 ± 110 | Zwiebel et al. (1995) |
| <u>Total Sample Size</u> | | <u>Weighted Average Lumen Diameter [mm]</u> | <u>Weighted Average Mean Flow [cm³/s]</u> | |
| N = 80 | | 4.676* | 4.903 | |

*A Sample size of n=63 was used to calculate the average diameter

The combined results of Table 4.2 and 4.1 suggest that the SA receives approximately 50-60% of the mean flow entering the CA. Such a result is an important boundary condition that can be utilized to include the influence of the SA on the local fluid dynamics in the hepatic arteries.

The first hepatic artery is the CHA and is usually downstream of the RGA and SA bifurcations off the CA, numerous studies have measured flow in the CHA as a measure of liver transplant patency. However, many of the transplant patients have several other medical conditions that will influence their flow distributions and create distributions that are not reflective of normal conditions. Table 4.3 compiles the data from multiple anatomic and hemodynamic studies of the CHA that do not include any liver transplantation.

[Table 4.3 on next page]

Table 4.3: Blood flow measurements in the common hepatic artery

| <u>No. of Patients</u> | <u>Measurement Method</u> | <u>Lumen Diameter [mm]</u> | <u>Mean Flow [cm³/min.]</u> | <u>Source</u> |
|--------------------------|----------------------------------|---|--|--------------------------|
| 18 | Duplex Doppler Ultrasound | 4.19 ± 2.39 | 254 ± 131 | Nakamura et al. (1989) |
| 12 | Duplex Doppler Ultrasound | 5.81 ± 2.08 | 415 ± 150 | Horn et al. (1990) |
| 12 | Duplex Doppler Ultrasound | 5.48 ± 2.74 | 363 ± 125 | Horn et al. (1990) |
| 16 | Duplex Doppler Ultrasound | 4.83 ± 2.52 | 228 ± 161 | Leen et al. (1991) |
| 10 | Duplex Doppler Ultrasound | 6.00 | 359 ± 126 | Carlisle et al. (1992) |
| 22 | Duplex Doppler Ultrasound | 4.84 | 216 ± 136 | Robertson et al. (1992) |
| 18 | Doppler Color Flow Imaging | 3.93 ± 2.45 | 195 ± 128 | Uzawa et al. (1993) |
| 18 | Doppler Color Doppler Ultrasound | NA | 245 ± 87 | Guadagni et al. (2000) |
| 20 | Doppler Ultrasound | NA | 143 ± 54 | Oktar et al. (2006) |
| 9 | Phase Contrast MRI | NA | 117 ± 73* | Barthelmes et al. (2009) |
| 8 | Breath-Hold PC-MRI | 5.79 ± 2.45 | 272 ± 44 | Jin et al. (2009) |
| 8 | Self-Gated PC-MRI | 5.73 ± 2.11 | 262 ± 51 | Jin et al. (2009) |
| <u>Total Sample Size</u> | | <u>Weighted Average Lumen Diameter [mm]</u> | <u>Weighted Average Mean Flow [cm³/s]</u> | |
| N = 171 | | 4.980** | 4.094 | |

* A body surface area of 1.84[m²] (Vauthey et al. 2002) was used to calculate flow in [cm³/min]

**A Sample size of n=124 was used to calculate the average diameter

An interesting note regarding the data from Barthelmes et al. (2009) is that the reported mean flow in the CHA is lower than the reported mean flow in the PHA. Due to the conservation of mass for confined incompressible flows without downstream entrances to flow, such a

result is physically impossible. However, the data was included due its small sample size and to include more than one MRI recorded flow study in the compiled data set. The weighted average data in Tables 4.1, 4.2, and 4.3 along with the calculated data of Moore and Ku (1994) suggest that the CHA receives approximately 40-50% of the blood flow entering the CA. The presented flow data assumes in the CHA assumes the hepatic arterial system is a Type 1 classification. Differences in flow distribution between replaced hepatic artery anatomies and the Type I anatomy has not been quantified, but the data calculated for the CHA in Table 4.3 can be extrapolated to Type 5 anatomies until more flow data is calculated from replaced hepatic artery anatomies.

While the CHA is often the largest hepatic artery in the total hepatic arterial system, the blood actually delivered to the liver is lower than the flow presented in the CHA due to the GDA and branches that offshoot the CHA prior to the lobes of the liver. Due to the size of the GDA, very few studies have quantified the flow in the artery. To the author's knowledge, Uzawa et al. (1993) is the only published study that recorded flow in the GDA, with a mean diameter of 2.62 ± 1.38 [mm] and a mean flow of 1.12 ± 0.33 [cm³/s]. Another method of quantifying flow entering the GDA is to calculate the flow entering the PHA and subtract the PHA flow from the CHA flow. In order to complete this method, the flow in the PHA must also be quantified, which is a more common task than quantifying flow in the GDA. Table 4.4 lists multiple studies that measure flow in the PHA.

Table 4.4: Blood flow measurements in the proper hepatic artery

| <u>No. of Patients</u> | <u>Measurement Method</u> | <u>Lumen Diameter [mm]</u> | <u>Mean Flow [cm³/min.]</u> | <u>Source</u> |
|--------------------------|----------------------------|---|--|--------------------------|
| 10 | Duplex Doppler Ultrasound | 4.00 | 212 ± 75 | Carlisle et al. (1992) |
| 18 | Doppler Color Flow Imaging | 2.74 ± 1.99 | 80 ± 65 | Uzawa et al. (1993) |
| 10 | Echo Doppler Ultrasound | NA | 235 ± 76 | Zoli et al. (1999) |
| 10 | Echo Doppler Ultrasound | NA | 313 ± 117 | Zoli et al. (1999) |
| 10 | Echo Doppler Ultrasound | NA | 318 ± 144 | Zoli et al. (1999) |
| 10 | Echo Doppler Ultrasound | NA | 271 ± 94 | Zoli et al. (1999) |
| 30 | Duplex Doppler Ultrasound | NA | 224 ± 56 | Săftoiu et al. (2002) |
| 30 | Color Ultrasound | 2.8 ± 0.3 | 99 ± 19 | Sudhamshu et al. (2006) |
| 9 | Phase Contrast MRI | NA | 155 ± 61* | Barthelmes et al. (2009) |
| <u>Total Sample Size</u> | | <u>Weighted Average Lumen Diameter [mm]</u> | <u>Weighted Average Mean Flow [cm³/s]</u> | |
| N = 137 | | 2.988** | 3.165 | |

* A body surface area of 1.84[m²] (Vauthey et al. 2002) was used to calculate flow in [cm³/min]

**A Sample size of n=58 was used to calculate the average diameter

An important note regarding the PHA is that normally at this point in the vessel anatomy, all blood entering the PHA is delivered to the liver. Thus, the best measure of total arterial blood delivered to the liver would need to come from a measurement of PHA hemodynamics. Sudhamshu et. al. (2006) also recorded the systolic velocity in the PHA being 55.2±12.0 [cm/s], which is about 100% greater than their recorded PHA mean velocity. Zoli et al. (1999) measured the flow in the PHA for different age groups. The 235±76[cm³/min.] was

from the age group < 45yrs., 313 ± 117 [cm³/min.] was from the age group 45-60 yrs., 318 ± 144 [cm³/min.] was from the age group 60-75 yrs., and 271 ± 94 [cm³/min.] was from the age group > 75 yrs. Statistical analyses of the data showed no statistically significant differences between the age groups. The weighted average flow data shown in Table 4.4 shows a much larger percentage of CHA flow entering the PHA than presented by Carlisle et al. (1992) and Uzawa et al (1993). However, the total sample size of compiled data set is much larger than each study individually and thus provides a better representation of a much larger population. Utilizing both the percentages of the individual studies and the compiled data in Table 4.4 suggests that the PHA receives approximately 70-88% of the blood entering the CHA.

Stemming from the PHA is the RHA and LHA. Due to their location, not many studies have investigated flow in these arteries. To the author's knowledge, Hirata et al. (2001) recorded a mean velocity in the LHA of 26.8 ± 7.2 [cm/s] in twenty patients and is the only published study that reports quantitative hemodynamics in the LHA of normal patients. Other studies have published mean values of RHA hemodynamics, and Table 4.5 compiles a list of the multiple studies.

[Table 4.5 on next page]

Table 4.5: Blood flow measurements in the right hepatic artery

| <u>No. of Patients</u> | <u>Measurement Method</u> | <u>Lumen Diameter [mm]</u> | <u>Mean Flow [cm³/min.]</u> | <u>Source</u> |
|--------------------------|-----------------------------------|---|--|---------------------------|
| 10 | Intravascular Doppler Ultrasound | NA | 108 ± 31* | Hübner et al. (2000) |
| 10 | Transcutaneous Doppler Ultrasound | 7.6 ± 1.9 | 133 ± 59* | Hübner et al. (2000) |
| 20 | Doppler Ultrasound | NA | 152 ± 34* | Hirata et al. (2001) |
| 17 | Duplex Doppler Ultrasound | 2.68 ± 0.69 | 127 ± 98* | Han et al. (2002) |
| 96 | Ex-Vivo Arterial Graft | 2.4 | NA | Ahn et al. (2005) |
| 15 | Cadaver Measurement | 3.6 ± 0.4 | NA | da Silveira et al. (2009) |
| <u>Total Sample Size</u> | | <u>Weighted Average Lumen Diameter [mm]</u> | <u>Weighted Average Mean Flow [cm³/s]</u> | |
| N = 168 | | 2.942** | 2.225*** | |

* The published mean velocity was converted to flow using the cross-sectional area from the weighted average diameter

**A Sample size of n=138 was used to calculate the average diameter

*** A sample size of n=57 was used to calculate the average flow

The compiled data in Table 4.5 suggest that the RHA receives approximately 58-62% of blood flowing through the PHA. Such a result is also matched by ratios of the mean velocity in the LHA and RHA of Hirata et al. (2001) and Kito et al. (2001). The flow data from Kito et al. (2001) was not included in Table 4.5 due to the presence of carcinomas in the liver and gallbladder, making the raw flow data influenced by a pathological condition.

SMA blood flow is also important to the hepatic arteries in Type 3-5 anatomies. Moore and Ku (1994) calculated a bulk flow rate of 6.667 [cm³/s] in the SMA from previous physiologic studies, but other studies have also recorded flow data in both fasting and

baseline conditions. Table 4.6 presents the flow data from several studies that measure flow and/or velocity in the SMA.

Table 4.6: Blood flow measurements in the superior mesenteric artery

| <u>No. of Patients</u> | <u>Measurement Method</u> | <u>Lumen Diameter [mm]</u> | <u>Mean Flow [cm³/min.]</u> | <u>Source</u> |
|--------------------------|---|---|--|--------------------------|
| 9 | Simultaneous Pulsed and Echo Doppler Ultrasound | 5.40 ± 0.4 | 374 ± 40 | Someya et al. (2008) |
| 9 | Simultaneous Pulsed and Echo Doppler Ultrasound | 5.40 ± 0.3 | 381 ± 31 | Someya et al. (2008) |
| 9 | Phase Contrast MRI | NA | 400 ± 146* | Barthelmes et al. (2009) |
| 18 | Doppler Color Flow Imaging | 6.13 ± 4.79 | 374 ± 210 | Uzawa et al. (1993) |
| 6 | Duplex Doppler Ultrasound | NA | 430 ± 15** | Sieber et al. (1992) |
| 20 | Duplex Doppler Ultrasound | NA | 445 ± 63 | Zwiebel et al. (1995) |
| 21 | Duplex Doppler Ultrasound | 6.40 ± 0.7 | 383 ± 90 | Sato et al. (1987) |
| 47 | Duplex Doppler Ultrasound | 6.20 ± 3.57 | 478 ± 168 | Nakamura et al. (1989) |
| 8 | Doppler Ultrasound | NA | 346 ± 27.1 | Sidery et al. (1994) |
| 70 | Duplex Doppler Ultrasound | NA | 517 ± 19 | Qamar et al. (1986) |
| <u>Total Sample Size</u> | | <u>Weighted Average Lumen Diameter [mm]</u> | <u>Weighted Average Mean Flow [cm³/s]</u> | |
| N = 217 | | 6.090 *** | 7.302 | |

*A body surface area of 1.84[m²] (Vauthey et al. 2002) was used to calculate flow in [cm³/min]

**The average velocity from 6 patients was converted to flow rate using the weighted average SMA diameter

***A Sample size of n=104 was used to calculate the average diameter

Uzawa et al. (1993) also quantified that the max. blood velocity in the SMA is 81±13 [cm/s], which corresponds to a max. flow rate of 23.59±3.79 [cm³/s]. All measurements were taken in studies that did not include any organ transplantation and all patients were considered in

the adult stage of life and deemed in good health without chronic disease. Combining the data in Table 4.1 with the value reported by Moore and Ku (1994), an acceptable range of mean flow rates in the CA is 6.667-7.302 [cm³/s]. An average of the two values yields 6.9845 [cm³/s] as a representative flow rate value from multiple sources.

Compiling the results from Tables 4.1 through 4.6 into a single collection of data enables percentages of parent vessel flow to be calculated in each daughter vessel (e.g. – the CHA receives 40-50% of the CA flow). Furthermore, the flows in the hepatic vessels can also be extrapolated to the SMA parent vessel to estimate flow percentages for replaced and accessory anatomies of the hepatic arterial system. Table 4.7 lists the compiled flow data for different parent vessels.

Table 4.7: Weighted average blood flow measurements of each artery and flow percentages of various parent vessels

| Daughter Arterial Vessels | Weighted Average Mean Flow Rate [cm ³ /s] | Parent Vessel Flow Percentages | | |
|-----------------------------|--|--------------------------------|--------------|--------------|
| | | CA Flow [%] | CHA Flow [%] | PHA Flow [%] |
| Splenic Artery (SA) | 4.903 | 50 – 60 | NA | NA |
| Common Hepatic Artery (CHA) | 4.094 | 40 – 50 | 100 | NA |
| Gastroduodenal Artery (GDA) | 1.120 | 11 – 14 | 20 – 28 | NA |
| Proper Hepatic Artery (PHA) | 3.165 | 36 – 44 | 75 – 88 | 100 |
| Left Hepatic Artery (LHA) | 1.822* | 18 – 22 | 35 – 45 | 40 – 50 |
| Right Hepatic Artery (RHA) | 2.225 | 23 – 27 | 40 – 50 | 50 – 60 |

*The RHA weighted averaged diameter in Table VI was multiplied by the LHA velocity from Hirata et al. (2001) to yield an approximate mean flow in [cm³/min]

The percentage ranges of the parent vessel flow in the hepatic arterial system listed in Table 4.7 are a novel calculation that has not been published nor adequately investigated. Such data is essential for constructing clinically relevant, computational models of the hepatic arterial system. Additionally, the data greatly enhances the understanding of typical flow distribution in hepatic arterial system's primary arteries, which is critical to design and optimize intra-arterial therapies that utilize the hepatic arterial flow as a delivery mechanism.

4.3.2 Blood Supply to Liver Tumors

In contrast to normal livers, several studies have shown that liver tumors are primarily supplied by arterial blood flowing through the hepatic arteries. However, other studies have identified a certain contribution of the portal vein blood flow to the overall tumor blood supply (Dezsó et al., 2009). Regardless of the source of the blood delivered to the tumor, the presence of liver tumors has the ability to alter the flow of blood delivered to the liver through the hepatic arteries. Although not specifying which hepatic artery, Jakab et al. (1996) measured a statistically significant increase in hepatic arterial flow of approximately 46% with $p < 0.01$. Additionally, the ratio between hepatic arterial flow and portal vein flow was 1.24 ± 0.246 in patients with primary liver tumors and 0.66 ± 0.259 in healthy control patients, which suggests that the portal blood flow delivered to the liver, is diminished in patients with primary hepatic tumors. Jakab et al. (1996) also reported that there was no statistically significant difference in the total blood delivered to the liver (summation of portal vein and hepatic arterial flows) for patients with primary liver tumors and healthy control patients. Multiple other studies have quantitatively measured the arterial blood flow in a specific

hepatic artery and have all shown a statistically significant increase in the blood flow in arterial vessels. Table 4.8 lists the results of the different studies.

Table 4.8: Blood flow measurements in patients with liver tumors

| <u>No. of Patients</u> | <u>Specific Artery</u> | <u>Mean Flow [cm³/min.]</u> | <u>Ratio to Healthy Mean Flow</u> | <u>Source</u> |
|------------------------|------------------------|--|-----------------------------------|---|
| 26 | Common Hepatic (CHA) | 813 ± 385 | 3.566 | Leen et al. (1991) |
| 42 | Common Hepatic (CHA) | 635 ± 364 | 2.873 | Robertson et al. (1992) |
| 19 | Common Hepatic (CHA) | 362 ± 107 | 1.477 | Guadagni et al. (2000) |
| 28 | Common Hepatic (CHA) | 343 ± 107 | 2.399 | Oktar et al. (2006) |
| 34 | Proper Hepatic (PHA) | 730 ± 119 | 3.259 | Săftoiu et al. (2002) |
| <u>CHA Sample Size</u> | | <u>Weighted Average Mean Flow [cm³/s]</u> | | <u>Weighted Average Ratio to Healthy Flow</u> |
| N = 115 | | 9.317 | | 2.684 |

The data in Table 4.8 included pathological conditions of primary and secondary liver tumors and reveals a clear trend of increased arterial blood flow in the presence of liver metastases. P-values between the flows in the healthy and pathological condition of the different studies range from $p < 0.0001$ (Leen et al., 1991) to $p < 0.001$ (Oktar et al., 2006; Săftoiu et al., 2002) which implies convincing statistical trends that the mean flows of the healthy and tumor afflicted states are statistically different. The weighted average ratio to healthy flow shown in Table 4.8 (2.684) is relatively close to the ratio calculated from the weighted average mean flows in the CHA from Tables 4.8 and 4.7 (2.276). Repeating the same calculation for the PHA, the flow ratio in Table 4.8 (3.259) is close to the value calculated by dividing the PHA flow rate in Table 4.8 by the PHA flow rate in Table 4.7 (3.389). Thus, the

presence of liver metastases should be expected to increase arterial flow in the CHA over twice the normal flow value and arterial flow in the PHA to around three times the normal value. Săftoiu et al. (2002) is the only published study of flow in the PHA with liver metastases. Since the PHA is a direct conduit to the liver, an elevated flow in the PHA results in increased amounts of arterial blood actually delivered to the liver. Thus, the results of Săftoiu et al. (2002) suggest that the increased flow in the CHA caused by liver metastases (both primary and secondary) should increase flow entering the liver through the PHA and not primarily distributing to the SA or GDA.

The data from Tables 4.2 – 4.8 quantify the flow in the hepatic arteries. To bring additional insight to the mined data, the mean Reynolds number in the different arteries is calculated in both normal conditions and under the influence of liver metastases and are located in Table 4.9. A range of tumor-influenced Reynolds numbers was calculated by multiplying the ratios of diseased to healthy flow in Table 4.8 to the mean flow rates listed in Table 4.8. The equation below defines the Reynolds number in terms of flow rates and a circular cross-sectional area:

$$\text{Re} = \frac{\bar{U} D \rho}{\mu} = \frac{4 Q \rho}{\pi D \mu} \quad (4.1)$$

where \bar{U} , Q , D , ρ , and μ are the characteristic velocity, volumetric flow rate, characteristic length (often the vessel diameter), the fluid density, and the fluid's apparent viscosity respectively. A blood density of 1.06 [g/cm³] and a blood viscosity of 0.0345 [g/(cm·s)] was used for all Reynolds number calculations listed in Table 4.9.

Table 4.9: Representative mean Reynolds numbers in the hepatic arterial system

| Specific Artery | Mean Reynolds Number | |
|----------------------------------|----------------------|--------------------------|
| | Healthy Conditions | Presence of Liver Tumors |
| Celiac Artery (CA) | 638 | NA |
| Splenic Artery (SA) | 410 | NA |
| Common Hepatic Artery (CHA) | 322 | 700 – 869 |
| Gastroduodenal Artery (GDA) | 167 | NA |
| Proper Hepatic Artery (PHA) | 414 | 1200 – 1410 |
| Left Hepatic Artery (LHA) | 242 | NA |
| Right Hepatic Artery (RHA) | 296 | NA |
| Superior Mesenteric Artery (SMA) | 469 | NA |

An interesting note about the Reynolds numbers shown in Table 4.9 is that the values for the PHA are larger than the CHA, and Reynolds Number values in the RHA are similar to those listed in the CHA. The data in Table 4.9 is very important to develop representative conditions of the hepatic arterial system that are independent of specific dimension or physical properties.

4.3.3 Processing Transient in-vivo Clinical Data

Attempts to describe the velocity waveform in the hepatic arteries date back to Taylor et al. (1985). Since then many studies have provided qualitative ultrasound spectra in order to understand the hemodynamics in the hepatic arteries (Perišić et al., 2009; Oktar et al., 2006; Hübner et al., 2000). Jin et al. (2009) published the first MRI flow waveform data and

showed antegrade flow in the diastolic region of the pulse with a shape resembling an asymmetric 2nd – 3rd degree polynomial with only one local and global maximum. Unfortunately, quantitative data is not easily extracted from those publications and *in vivo* pressure waveforms have not been published, both being essential for a realistic computational fluid-particle hemodynamics analysis. By collaborating with a practicing radiation oncologist and a ⁹⁰Y-microsphere therapeutic team (Wake Radiology Oncology Services, Cary, NC), ultrasound spectra and Radi PressureWire® (St. Jude Medical, St. Parul, MN) were used to record *in vivo* arterial velocity and pressure data. The hemodynamic data were recorded for the same patient whose geometric data was used to construct the patient-inspired hepatic arterial system geometry (see. Sect. 3.4).

Data recorded with the Radi PressureWire® (St. Jude Medical, St. Parul, MN) was an upstream measurement location, a downstream measurement location, calculated local mean values that vary with time, and a calculated ratio between the two recordings. The recording time of the data was over four minutes, where the patient was not asked to hold their breath and the signal was recorded continuously throughout the microsphere therapy. Additionally, the ultrasound sound spectra were recorded in the common, left, and right hepatic arteries. Figure 4.3 plots the upstream and downstream raw Radi PressureWire® (St. Jude Medical, St. Parul, MN) data over the entire temporal recording span, while, Fig. 4.4 illustrates the waveform spectra and color Doppler images from each of the hepatic arteries.

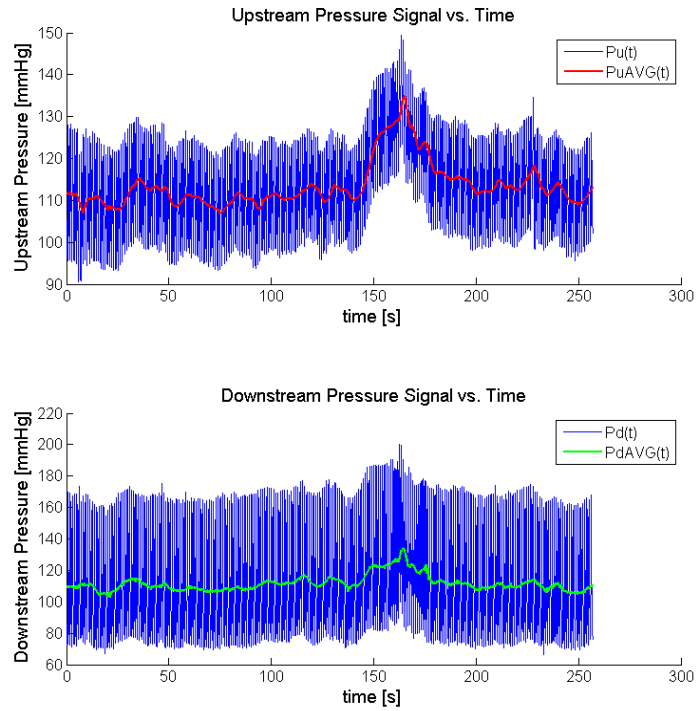
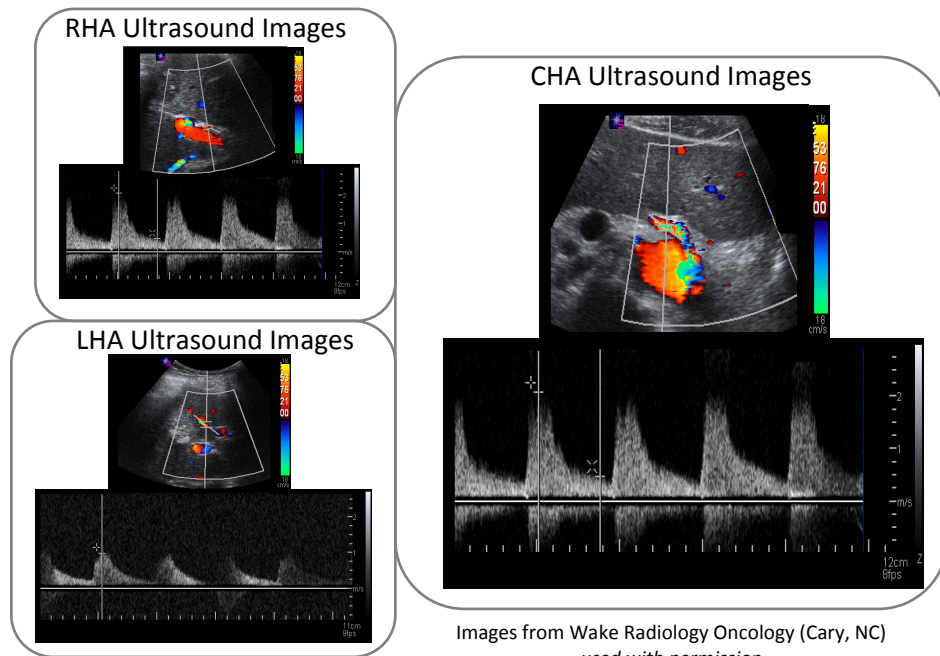


Figure 4.3: Raw pressure data from the Radi PressureWire®



Images from Wake Radiology Oncology (Cary, NC)
used with permission

Figure 4.4: Waveform spectra and color Doppler images in the patient's hepatic arteries

Custom MATLAB programs were written to process the flow and pressure data into representative waveforms. Regardless of the waveform, each data set contains discrete data points of a nearly periodic signal. Such behavior is easily seen in the ultrasound spectra in Fig. 4.4, but the pressure data needs to be viewed over a much smaller time span to visualize its periodic behavior. Figure 4.5 depicts the pressure data over a time interval of five seconds, clearly revealing a pulsatile, repetitive waveform.

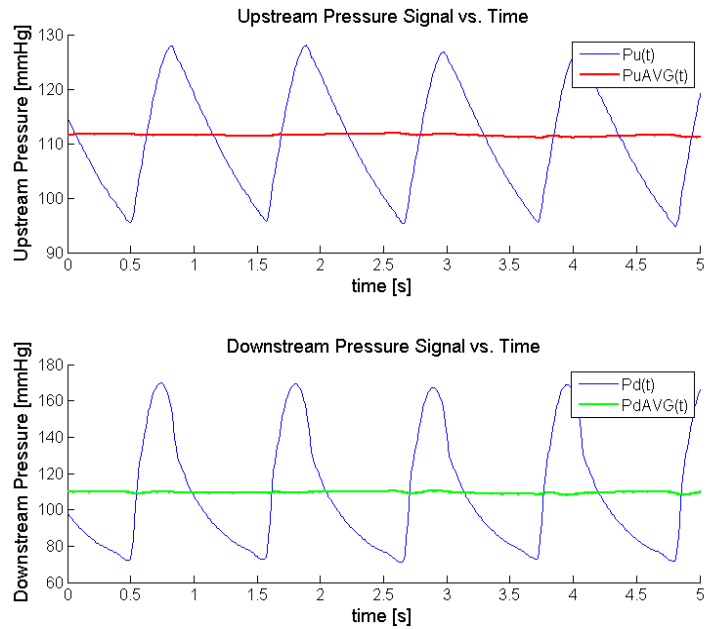


Figure 4.5: Raw pressure data from zero to five seconds

A true periodic signal has an infinitely reproducible signal such that the function value of any time point (t) is equal to the function value at the time point (t) plus the signal period (T). Equation (4.2) prescribes this definition as:

$$f(t) = f(t + T) \quad (4.2)$$

where $f(*)$ is an arbitrary continuous function, t is a discrete point in time, and T is the signal period. Medical signals rarely satisfy the exact definition of a periodic signal listed in Eq. (4.2), but a good approximation of the baseline signal can be achieved by treating the data as a true periodic waveform.

In vivo biomedical waveforms often require processing to remove noise that can drown out the signal and must be filtered without damaging the desired biomedical signal. Thus, filtering in the amplitude/time domain is often not an acceptable strategy since the amplitude of the desired signal can be masked by electronic noise or machine induced artifacts. Hence, filtering the data in the frequency domain is preferred to isolate the frequency range of the desired biomedical signals and the signal noise. Hemodynamic waveforms tend to be in the lower frequency range since accentuated, elevated heart rates are approximately 240 beats per minute which corresponds to about 4 beats per second, i.e., a frequency of 4Hz. Therefore, the waveform data can be filtered to cancel out high frequency noise using a low-pass filter, which maintains the signal strength of signal components below the cut-off frequency but diminishes the signal strength of signal components above the cut-off frequency. The unaffected frequency range is called the “passband” and the attenuated frequency range is the “stopband”. A popular filter used in biomedical signal processing is the Butterworth filter due to its smooth monotonic behavior and its ability to maintain the most constant frequency response in the passband as mathematically possible. The primary trade-off of using the Butterworth filter is a lower rate of signal attenuation in the stopband. Thus, higher orders of the Butterworth filter need to be used to obtain the same attenuation rate of popular filters of a lower order (i.e., Chebyshev or elliptic filters).

The custom MATLAB programs were written to require minimal input from the user and automatically i) filter the data with established filter design parameters, ii) segment the continuous collection of waveform data into individual waveforms, and iii) calculate a representative waveform. Primary input from the user is the data file(s) name and location. In order to accomplish the subsequent tasks, the signal processing toolbox (for filter design and implementation) and native commands within MATLAB R2008a were utilized.

The first section of the program imports the discrete data of the *in vivo* hemodynamic signals, assigns appropriate variables, and separates the data into appropriate arrays of the hemodynamic variables. A time scale array with constant sampling rate is then constructed from the raw data using piecewise cubic Hermite interpolation, which enables cubic spline interpolation with discontinuous 2nd derivatives. The ultrasound spectra data was digitized by hand and introduced a number of artificial discontinuities caused by the hand-driven process. To remove these artifacts, an eleven-point moving average filter was used to smooth the ultrasound data, whereas no smoothing was performed on the pressure data. Figure 4.6 illustrates the moving average filter's response of the ultrasound data.

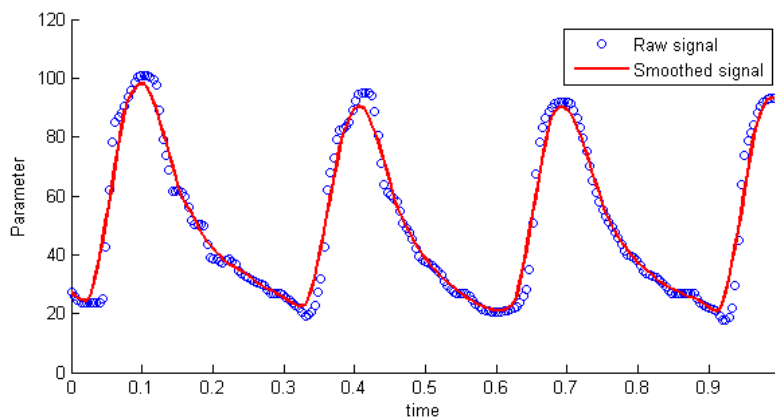


Figure 4.6: Smoothing response using an eleven-point moving average filter

The fast Fourier transform (FFT) was then used to determine the signal's frequency behavior. The number of Fourier points was set to be twice that of the signal's data points and the power of the frequency spectrum was calculated by dividing the magnitude of MATLAB's FFT output coefficients by half the number of Fourier points. Subsequently, the signal's first and second derivatives with respect to time were calculated using a first-order central difference scheme. The derivative calculations introduced high frequency noise in the pressure data and thus were filtered with a zero-phase shift, low pass, fourth-order Butterworth filter with a cut-off frequency of 10 Hz. Nearly equivalent digital filter parameters have been implemented in processing of cardiovascular signals with similar frequency ranges (Stålhand, 2009; Fetics et al., 1999). The MATLAB function *filtfilt* was used to implement the filter. Interestingly, the raw pressure data from the Radi PressureWire® were already filtered to remove 60Hz noise and did not require implementing the filter prior to the derivative calculations. Due to the digitization process of the ultrasound spectra, the sampling rate was not large enough to generate artificial high frequency noise when calculating the derivatives. Thus, the Butterworth filter was not used on the ultrasound spectra. Figures 4.7a,b illustrate the Butterworth filter's response and the FFT spectrum of the raw and filtered 2nd derivative pressure signal. Subsequently, Fig. 4.8 plots the raw and unfiltered time-domain signals of the original, 1st derivative, and 2nd derivative downstream pressure data from zero to three seconds.

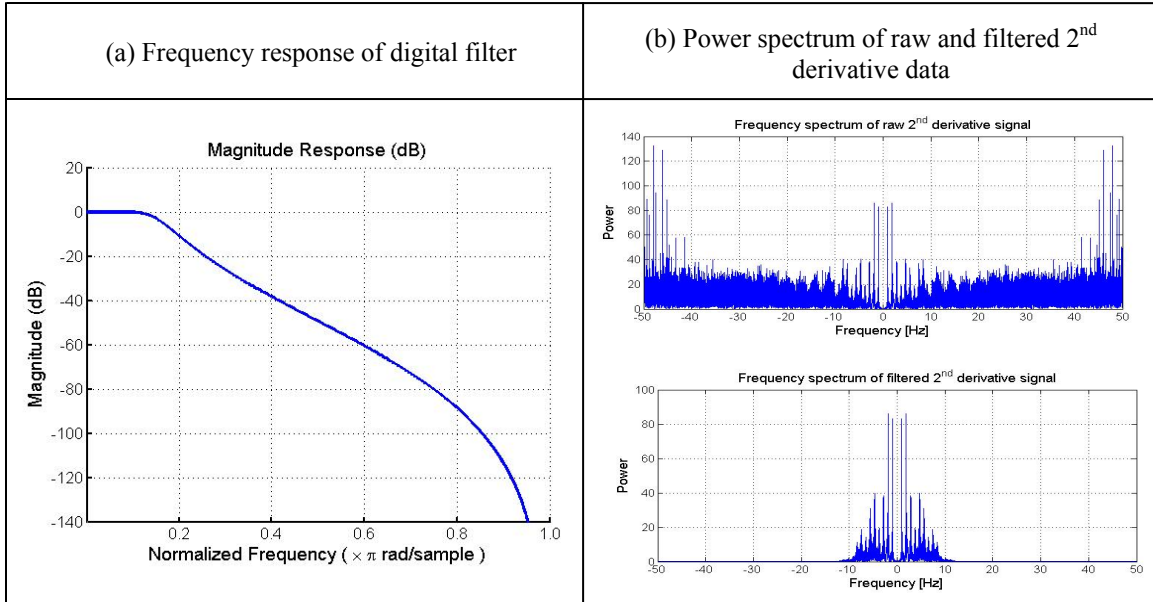


Figure 4.7: (a) Filter response and (b) effect on frequency power spectrum of 2nd Derivative Data

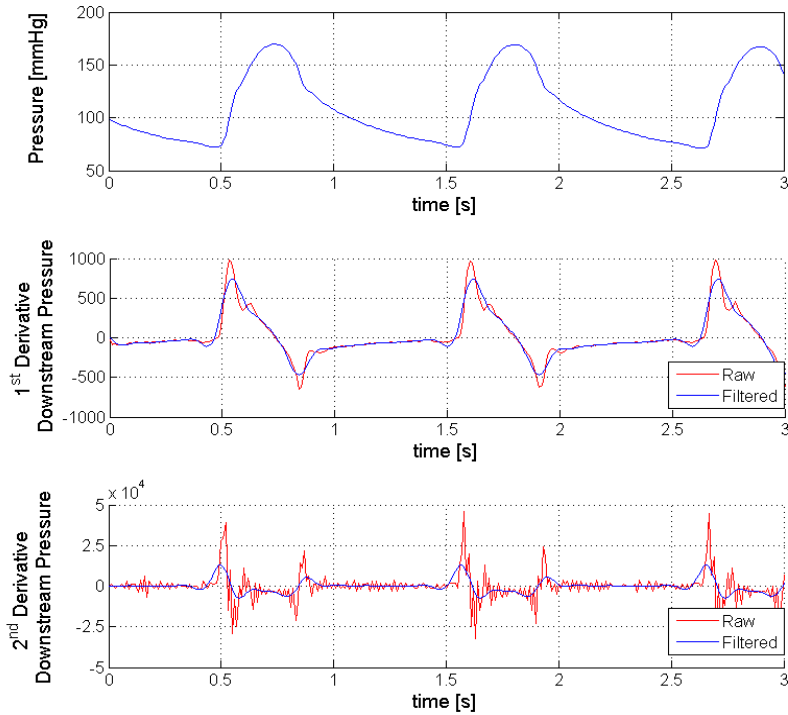


Figure 4.8: Raw and filtered data of downstream pressure waveforms from zero to three seconds

The first and second derivative signals were used by an algorithm for determining the beginning and ending data of each pulse. A “for” loop cycled through the all points in the derivative waveforms with a starting index of 2 and an ending index of one less than the total number of samples. For each point in the derivative waveform an “if” conditional statement is utilized to check whether the 1st derivative changes sign from negative to positive and if the 2nd derivative is greater than 100 times the rms value of the original signal. If the conditional statement satisfied, a tracking array is used to record the period number, the array index, and the point in time. The current pulse’s local period is calculated by from the difference between the time at the origin of the next pulse and the time at the origin of the current pulse. Figure 4.9 on pg. 113 illustrates the algorithm in flowchart form.

A second algorithm of nested “for” loops and conditional “if” statements were then used to i) isolate the local waveform, ii) calculate a local non-dimensional timescale that varies from zero to one, iii) resample the individual waveforms using a piecewise cubic Hermite interpolation so that each waveform had the same number of points, and iv) place the resampled waveform data into columns of a new array. The local waveforms were isolated by cycling through the data points and seeing if the local time value fell between the previously stored time values in the tracking array. Once the code began processing the data in the local waveform, the timescale of each local waveform was set to move from zero to the local period time value by subtracting all time values by the initial time value of the local waveform. The third processing step nondimensionalized the time scale by dividing every zero-based time point by the local period such that the local scale varied from zero to one. The corresponding signal value to the nondimensional time values was then recorded in a

temporary array. After the program has cycled through the data and recorded the time and values of the local waveform, a cubic spline interpolation of the signal values was completed such that the known X-values were the non-dimensional time points, the known Y-values were the corresponding signal points, and the desired X-values was a uniform-spaced nondimensional timescale from zero to one with one hundred data points. Additional calculations were then performed on the interpolated waveforms such as calculating the difference between the value at the first point in the wave and the value at the last point in the pulse (a measure of periodicity). Figure 4.10 on pg. 114 illustrates the loops and calculations in the second algorithm. Prior to viewing Figs. 4.9 and 4.10, Table 4.10 provides a condensed listing of variable names and the physical value they represent.

[see next page for Table 4.10]

Table 4.10: Variables used in the flowchart diagrams

| Variable Name | Physical Meaning |
|----------------|--|
| k , kk | Iterative index variable |
| N_s | Number of samples |
| p_x | Array of signal values |
| counter , ctr2 | Iterative counter variable |
| Track | Array that stores indexes and time points of individual waveforms |
| T_p | Array of local period values |
| np | Iterative index variable of period |
| N_p | Maximum number of periods in data |
| ϵ | Threshold of second derivative |
| t | Array of time values |
| Pt | Time points of each waveform |
| Pp | Pressure points of each waveform |
| Pi | Interpolated / resampled pressure data |
| Pp_diff | Difference between pressure at first and last points of individual pressure waveform |

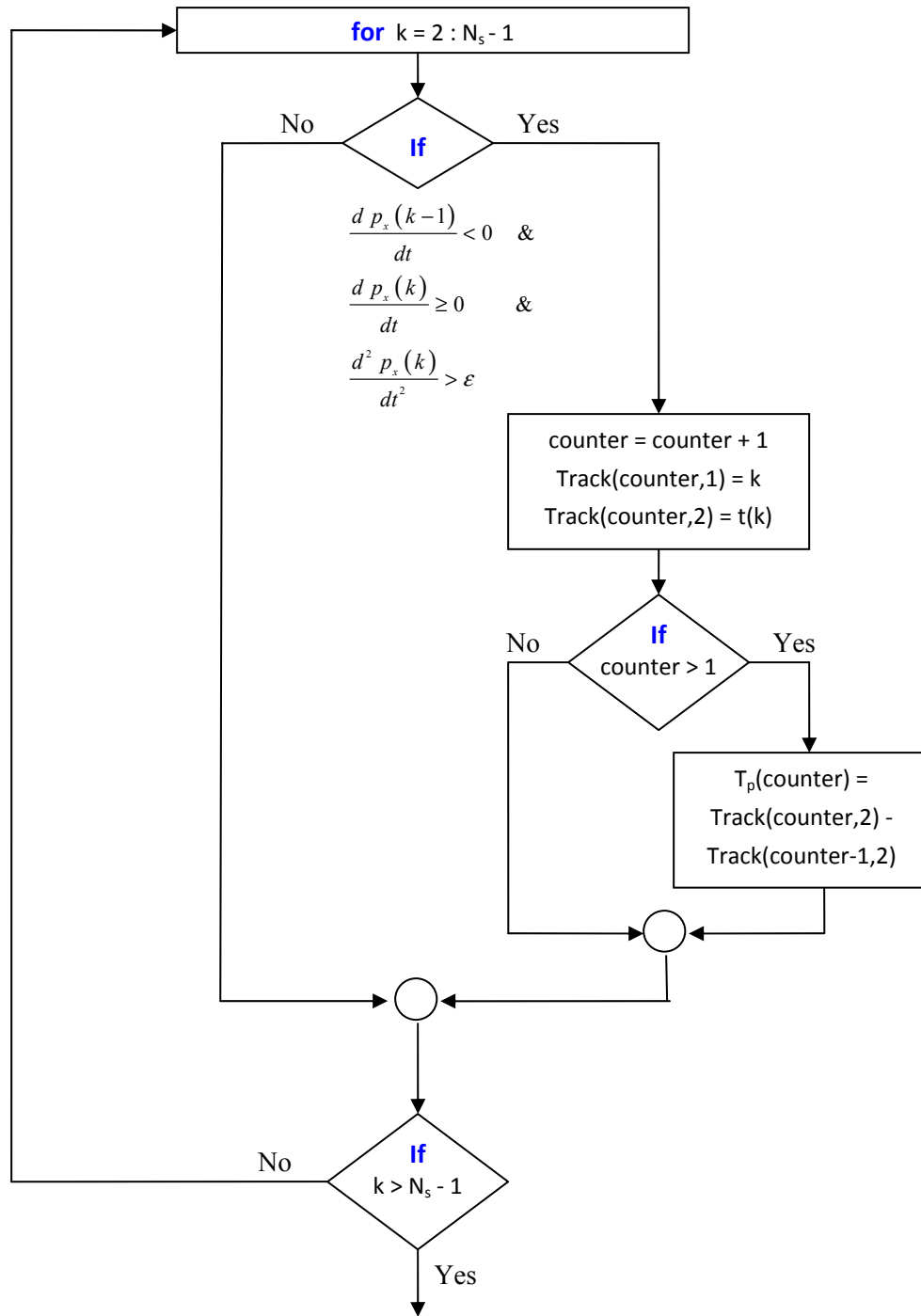


Figure 4.9: Flowchart of algorithm used to track individual waveforms and periods

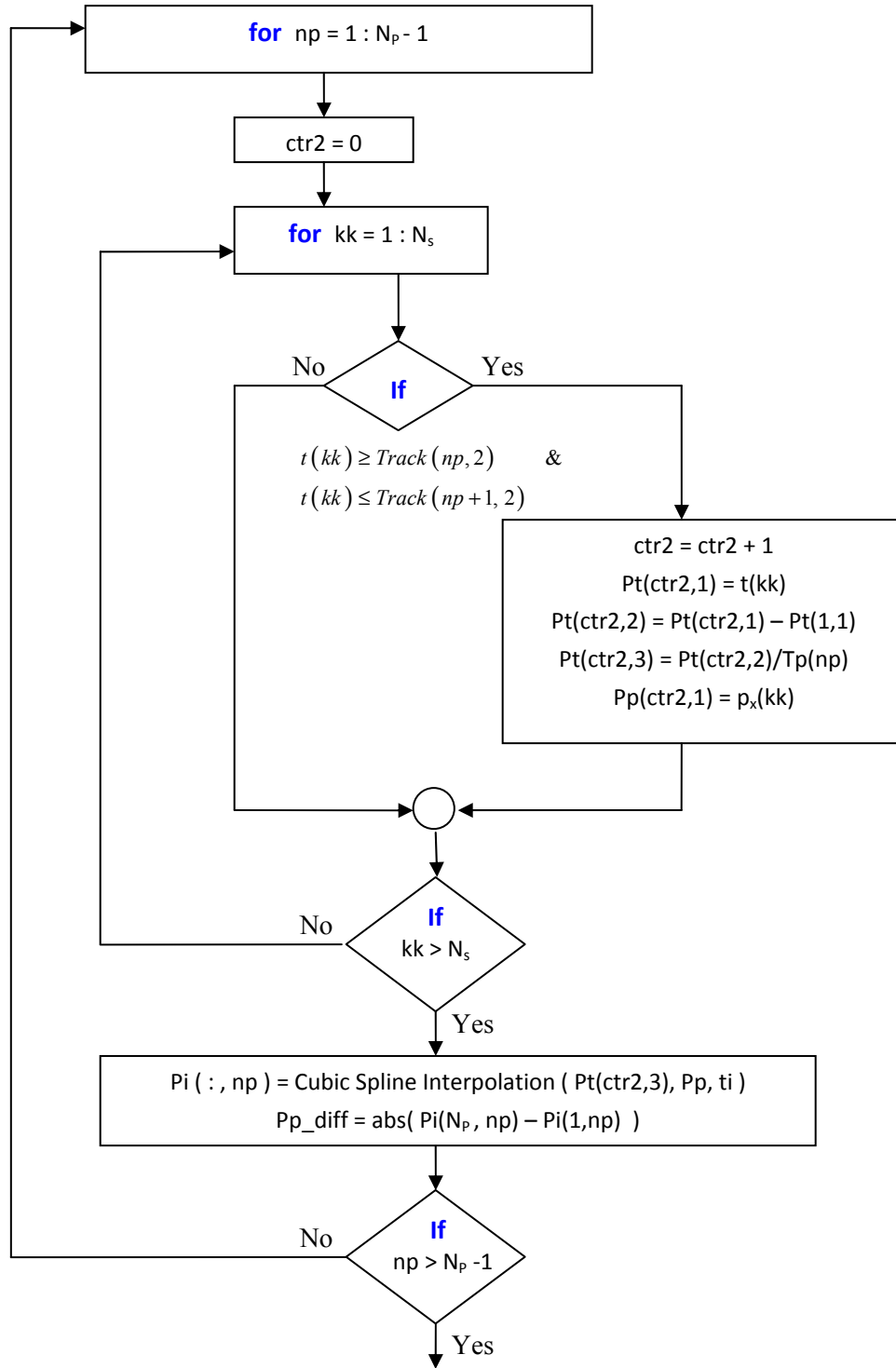


Figure 4.10: Flowchart of algorithm used to isolate individual waveforms

A mean waveform was then calculated on a non-dimensional point-by-point basis, such that for each nondimensional time point, every individual pulse's corresponding signal (velocity or pressure) were averaged together. Thus, for a single nondimensional time value, the corresponding pressure values of all the desired waveforms were averaged together to yield a single representative value for that non-dimensional point in time. The variance, maximum, and minimum values of each non-dimensional point were also calculated. Appendix II contains the MATLAB code used to segment the continuous signal and average the individual waveforms over a nondimensional timescale.

Figures 4.11 and 4.12 plot the mean pressure waveforms and right and left hepatic artery velocity waveforms respectively. The pressure pulses after the first 120 are believed to be post microsphere injection and were not used to determine a baseline mean waveform. Error bars in both figures correspond to \pm one standard deviation, the red points represent the maximum signal value, and the blue points represent the minimum signal values of each point. It is important to note that the max. and min. values may not be from the same waveform and are shown here as ranges for each data point in the representative mean waveform. Additionally, upon examining the waveforms in Figs. 4.11 and 4.12, the full range of data is within three standard deviations from the calculated mean waveform. Thus, the mean waveforms are a sufficient representation of the selected data set.

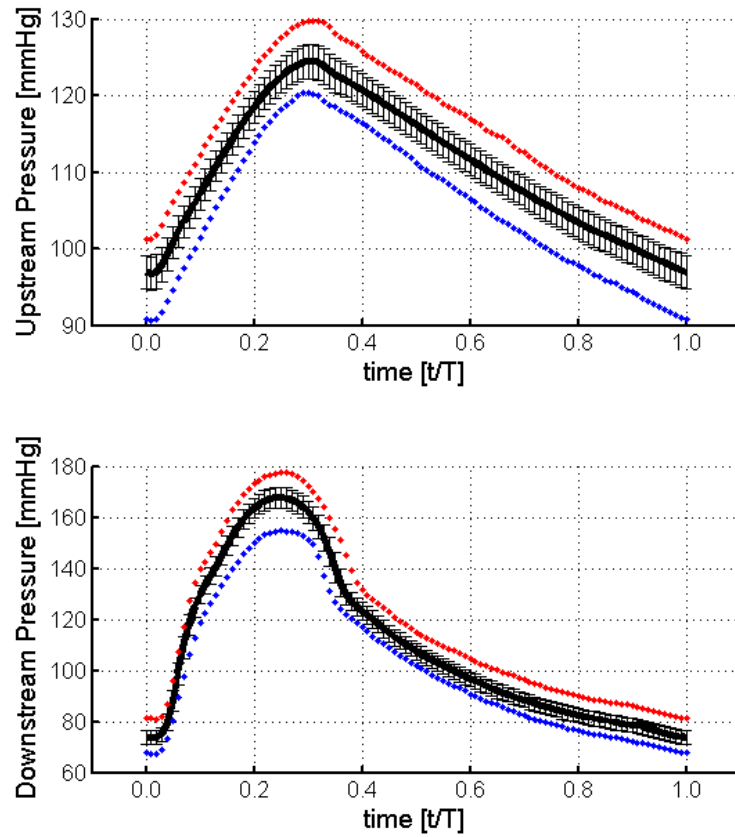


Figure 4.11: Representative mean pressure waveforms with one standard deviation and range of values

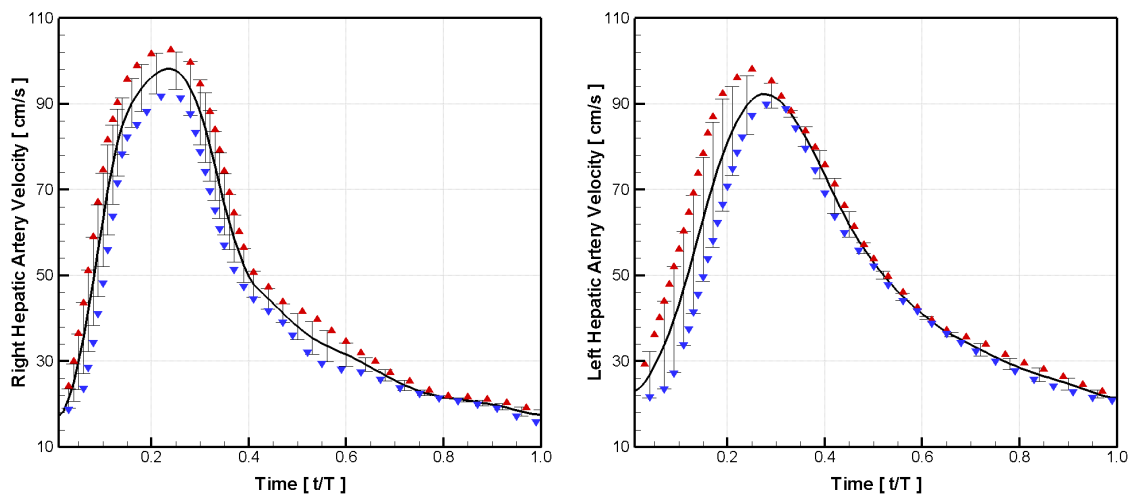


Figure 4.12: Mean velocity waveforms from ultrasound spectra

The absolute difference between the initial and final points of the mean pressure waveforms was calculated as a measure of periodicity. An ideal case would be an absolute difference of zero since the waveform should have exactly the same values at time points one period apart (see Eq. (4.2)). The maximum difference of mean pressure waveforms was 0.039mmHg and the maximum difference of the mean velocity waveforms was 1.22cm/s, corresponding to percent differences of 0.557% and 5.3%, respectively. Thus, the mean waveforms from the single patient also exhibit a sufficient amount of periodicity.

The local periods of each segmented pressure waveform were calculated (see T_p in Fig. 4.9) and compared to analyze their distribution and to check if a common period length exists. Eighty percent of the period data falls between 1.05s and 1.10s for the upstream waveforms and 1.04s and 1.10s for the downstream waveforms. Figure 4.13 presents period histograms of each pressure waveform.

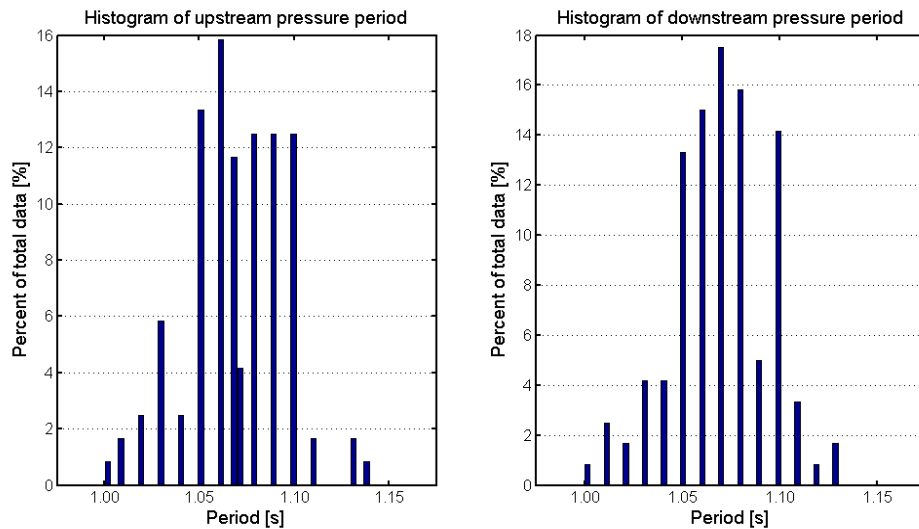


Figure 4.13: Histograms of the pressure waveforms' periods

The arithmetic mean of both the upstream and downstream data sets is 1.0696s whereas the weighted average using the different bins of the histogram in Fig. 4.13 is 1.0694s for the upstream waveforms and 1.0695s for the downstream waveforms. A Kolmogorov-Smirnov test of normality was performed on each histogram distribution, and the calculated p-values were below 0.05 for both distributions, which rejects the null hypothesis that the data follows a normal distribution. Despite the rejection of normality, the arithmetic mean and weighted average values are near the center of the eighty percent window that contains most of the data. Figure 14 plots the mean values amidst scatterplots of the period values and reveals the total span of the data is within $\pm 6.51\%$ of the arithmetic mean period.

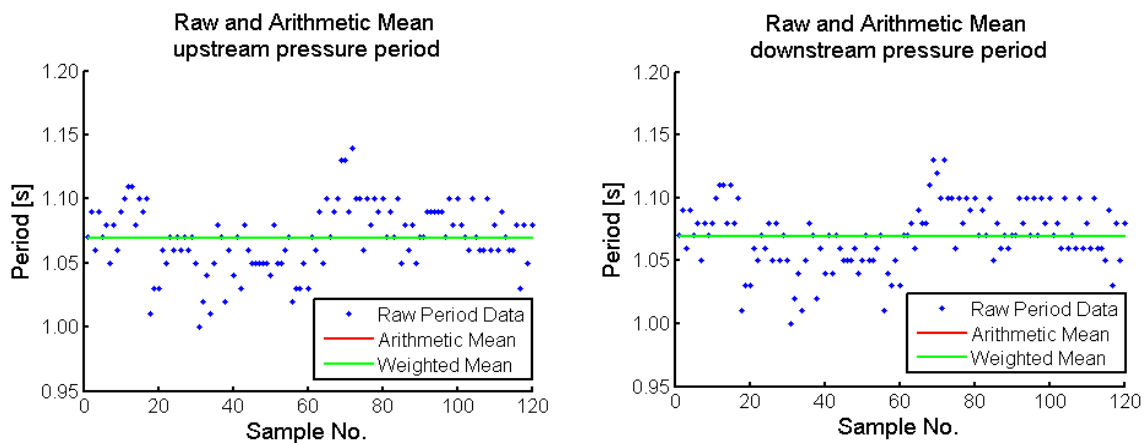


Figure 4.14: Scatter plots of the periods from each pressure waveform

Thus, despite the statistics suggesting the data does not follow a normal distribution, the data's arithmetic mean can be used as a representative value for all pressure waveform periods.

Patient-inspired inflow and outflow waveforms for the RHA, LHA, CHA, SMAin, and SMAout were derived from the velocity waveforms in Fig. 4.12 using the conservation of

mass, the diameter information of the patient-inspired geometry listed in Section 3.4, and the population averaged mean SMA flow listed in Table 4.6. The RHA and LHA flow rate waveforms were calculated by taking the velocity waveforms in Fig. 4.12 as the average velocity and multiplying it by the cross sectional area of the corresponding vessels assuming a circular cross section. CHA flow was calculated as the sum of RHA and LHA flows and the mean SMA outflow was assumed to be the population averaged mean flow ($7.302\text{cm}^3/\text{s}$) in Table 4.6. SMA inflow and outflow waveforms were calculated by deriving a factor relating the population average mean SMA flow and the patient's calculated mean CHA flow. Figure 4.15 plots the patient-inspired flow waveforms in each artery of the corresponding geometry and lists the equations dictating the mathematical procedure used to calculate a patient-inspired SMA inflow waveform, specifically formulated for the computational geometry described in Section 3.4.

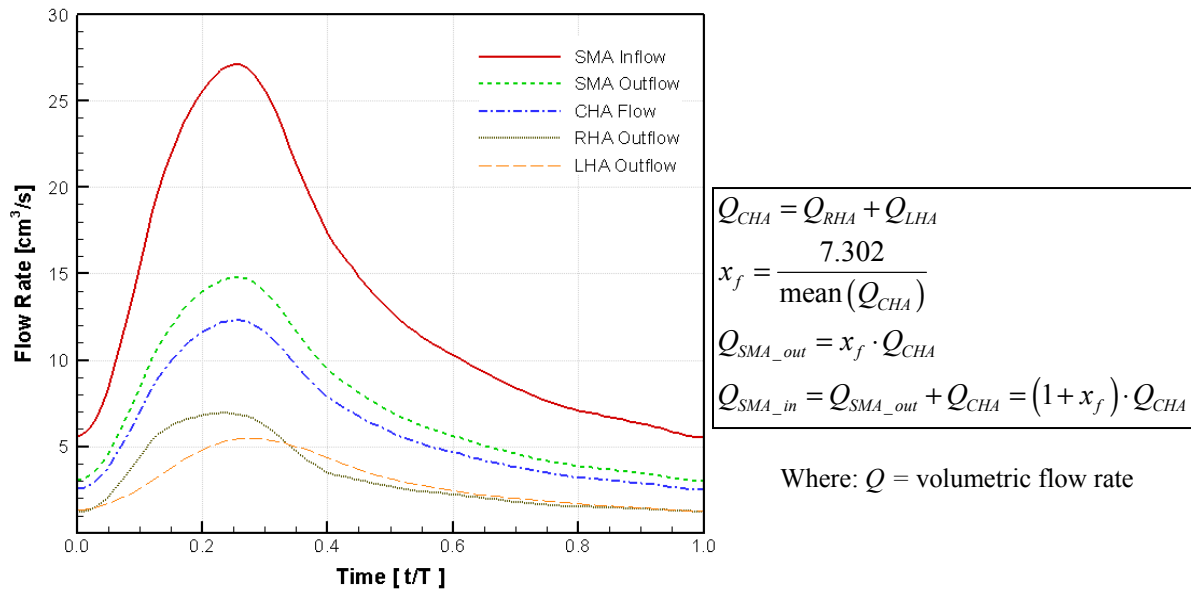
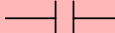
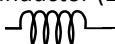


Figure 4.15: Patient-inspired flow rate waveforms and corresponding equations

4.3.4 Windkessel Models Utilized to Construct Additional Inflow and Outflow Waveforms

The Windkessel models are lumped parameter models of the cardiovascular system that have a physical interpretation of flow through a compliant reservoir (Kleinstreuer, 2006 – pp.210-212). Often times, the models are represented through electrical circuit analogues to various components of the circulatory system. Hence, a differential equation can be constructed that relates: i) the flow rate vs. time waveform, ii) the pressure vs. time waveform, and iii) specific parameters of the circuit. A two-element Windkessel (WK) model is the simplest model following the original WK reservoir proposed by Otto Frank in 1899. Since then, multiple extensions have been formulated, extending the original two element circuit to three and four element models that include additional circuit parameters in various configurations (Westerhoff et al., 2009; Segers et al., 2008; Burattini and Di Salvia, 2007; Stergiopoulos et al., 1999). Two-, three- and four-element WK models were utilized to construct additional inflow/outflow waveforms based on patient-specific and population averaged hemodynamics. Table 4.11 lists the physical interpretation of the circuit elements composing each WK model and Figure 4.16a provides a sketch of the physical reservoir, and Fig. 4.16b illustrates the circuit analogue of each utilized WK model.

Table 4.11: Physical interpretations of each electrical circuit component

| <u>Electrical Circuit Components</u> | <u>Physical Interpretation</u> |
|--|--------------------------------|
| Resistor (R)  | Resistance to blood flow |
| Capacitor (C)  | Compliance of arterial wall |
| Inductor (L)  | Inertia of flowing blood |

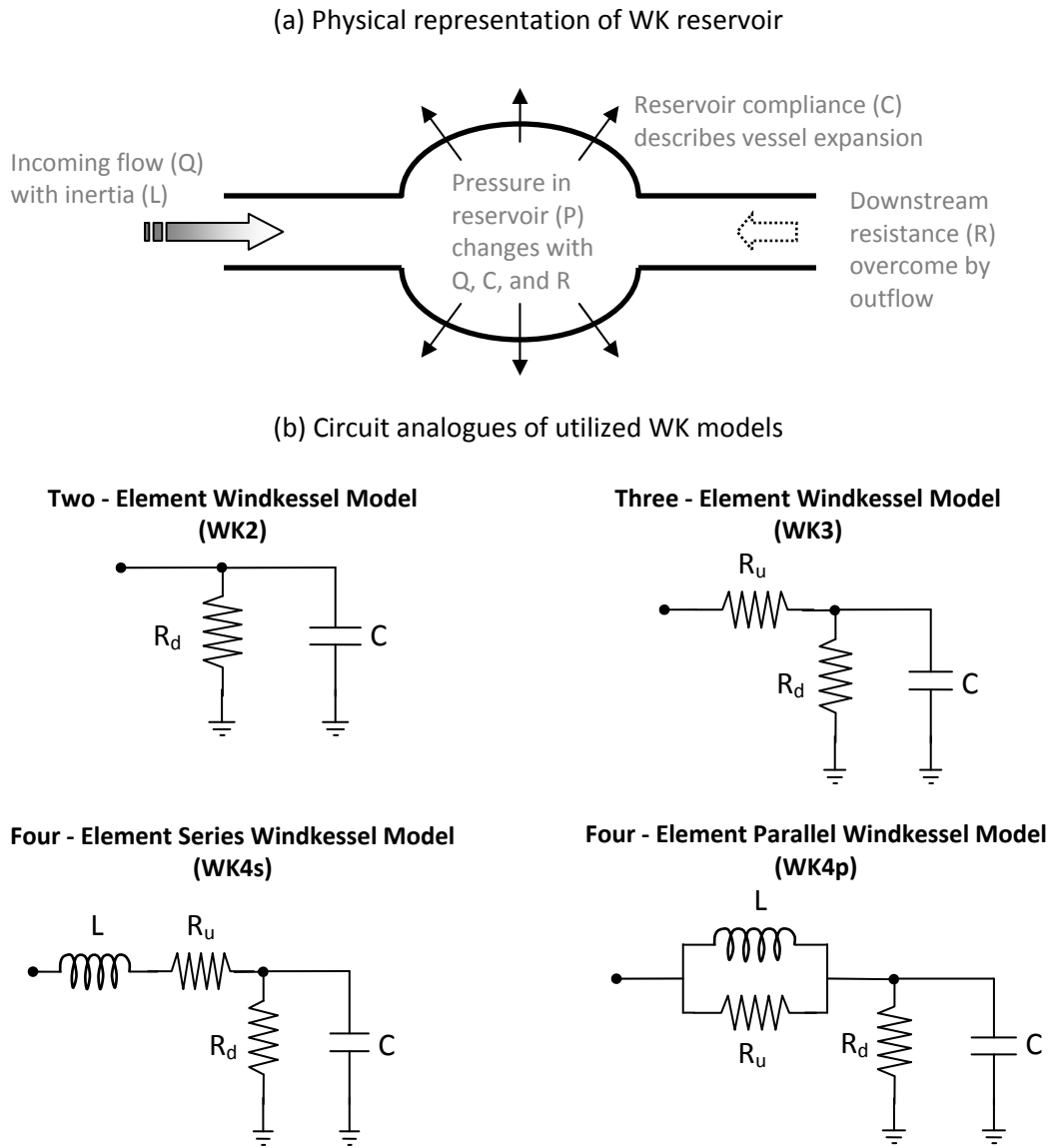


Figure 4.16: ^(a) Physical sketch of Windkessel reservoir and
^(b) Electrical circuits of the utilized Windkessel models

Electric current and voltage in the different circuits pictured in Fig. 4.15 are analogous to the flow of blood (Q) and the blood pressure (p) in the body, respectively. Circuit analysis fundamentals (Ohms Law, Kirchhoff's Current and Voltage Laws) were used to derive a differential equation (transfer function) that relates Q and p in each WK model. Using the

Fourier transform equations shown below, the time-domain differential equations were converted to the frequency domain, and the impedance between Q and p was derived for each WK circuit. Equations (4.3a-d) define the Fourier representation of the time-domain flow (Q) and pressure (p) signals found in the Windkessel models and Eqs. (4.4a-e) define the impedance of each Windkessel circuit model in the frequency domain:

$$\begin{aligned}
 p(t) &= \sum_{n=-\infty}^{\infty} F_p[n] \exp(jn\omega_0 t) \\
 \frac{dp}{dt} &= \sum_{n=-\infty}^{\infty} F_p[n] \exp(jn\omega_0 t) \cdot (jn\omega_0)
 \end{aligned}
 \tag{4.3a-d}$$

$$\begin{aligned}
 Q(t) &= \sum_{n=-\infty}^{\infty} F_Q[n] \exp(jn\omega_0 t) \\
 \frac{dQ}{dt} &= \sum_{n=-\infty}^{\infty} F_Q[n] \exp(jn\omega_0 t) \cdot (jn\omega_0)
 \end{aligned}$$

$$\begin{aligned}
 Z_{WK}[n] &= \frac{F_p[n]}{F_Q[n]} \Rightarrow F_p[n] = Z_{WK}[n] \cdot F_Q[n] \\
 &\Rightarrow F_Q[n] = \frac{1}{Z_{WK}[n]} \cdot F_p[n]
 \end{aligned}
 \tag{4.4a-e}$$

$$Mod_Z = \text{abs}(Z_{WK})$$

$$Phase_Z = \arctan\left(\frac{\text{imag}(Z_{WK})}{\text{real}(Z_{WK})}\right)$$

where j is the imaginary unity (square root of negative one). Equations (4.5a-d) – (4.8a-d) fully describe each Windkessel model's governing equations in both the time and frequency domain, where WK model's impedance function is also listed. Furthermore, each model's zero-frequency impedance is derived in relation to the individual model's circuit parameter(s).

WK2

$$\text{Time: } Q = \frac{1}{R_d} p + C \frac{dp}{dt}$$

$$\text{Frequency: } F_Q(n)[R_d] = F_p(n)[jn\omega_0 CR_d + 1] \quad (4.5a-d)$$

$$\text{Impedance: } Z_{WK2}(n) = \frac{R_d}{jn\omega_0 CR_d + 1}$$

$$\text{Zero-Frequency: } Z_{WK2}^0 = Z_{WK2}(n=0) = \frac{R_d}{1}$$

WK3

$$\text{Time: } \frac{dQ}{dt} + \frac{1}{C} \left(1 + \frac{R_u}{R_d}\right) Q = \frac{dp}{dt} + \frac{1}{C R_d} p R_u$$

$$\text{Frequency: } F_Q(n)[jn\omega_0 CR_d R_u + R_d + R_u] = F_p(n)[jn\omega_0 CR_d + 1] \quad (4.6a-d)$$

$$\text{Impedance: } Z_{WK3}(n) = \frac{jn\omega_0 CR_d R_u + R_d + R_u}{jn\omega_0 CR_d + 1}$$

$$\text{Zero-Frequency: } Z_{WK3}^0 = Z_{WK3}(n=0) = \frac{R_d + R_u}{1}$$

WK4s

$$\text{Time: } \frac{dp}{dt} + \frac{1}{C R_d} p = L \frac{d^2 Q}{dt^2} + \left(R_u + \frac{L}{C R_d}\right) \frac{dQ}{dt} + \frac{1}{C} \left(1 + \frac{R_u}{R_d}\right) Q$$

$$\text{Frequency: } F_Q(n) \left[LCR_d (jn\omega_0)^2 + (CR_d R_u + L) jn\omega_0 + R_d + R_u \right] = F_p(n) [jn\omega_0 CR_d + 1] \quad (4.7a-d)$$

$$\text{Impedance: } Z_{WK4s}(n) = \frac{LCR_d (jn\omega_0)^2 + (CR_d R_u + L) jn\omega_0 + R_d + R_u}{jn\omega_0 CR_d + 1}$$

$$\text{Zero-Frequency: } Z_{WK4s}^0 = Z_{WK4s}(n=0) = \frac{R_d + R_u}{1}$$

WK4p

$$\text{Time: } \left(1 + \frac{R_u}{R_d}\right) \frac{dQ}{dt} + \frac{R_d}{L} Q = C \frac{R_d}{R_u} \frac{d^2 p}{dt^2} + \left(\frac{CR_d R_u + L}{LR_u}\right) \frac{dp}{dt} + \frac{1}{L} p$$

$$\text{Frequency: } F_Q(n) \left[(LR_u + LR_d) jn\omega_0 + R_d R_u \right] = F_p(n) \left[LCR_d (jn\omega_0)^2 + (CR_d R_u + L) jn\omega_0 + R_u \right] \quad (4.8a-d)$$

$$\text{Impedance: } Z_{WK4p}(n) = \frac{(LR_u + LR_d) jn\omega_0 + R_d R_u}{LCR_d (jn\omega_0)^2 + (CR_d R_u + L) jn\omega_0 + R_u}$$

$$\text{Zero-Frequency: } Z_{WK4p}^0 = Z_{WK4p}(n=0) = \frac{R_d R_u}{R_u} = \frac{R_d}{1}$$

A custom MATLAB code was written to calculate the time-domain flow waveform of each WK model using the *in vivo* RHA pressure waveform and population averaged max and mean flow rates of 11.286 cm³/s and 5.808 cm³/s, respectively. The flow rates were selected based on multiplying the tumor-to-healthy-flow ratio listed in Table 4.8 by the mean and max flow in the RHA surveyed in the cited literature and listed in Table 4.5. Nonlinear constrained minimization was utilized to determine the WK parameters that minimized a defined error magnitude based on the calculated WK waveform and population averaged flow rate data via the “fmincon” function in MATLAB’s Optimization Toolbox. The termination tolerance for error magnitude was set using at 1×10^{-20} via the “TolFun” option and the termination tolerance for the variable input was set at 1×10^{-10} via the “TolX” option. Each WK model’s zero-frequency impedance was forced to be equivalent to the WK2 model’s resistance, which is the WK2 model’s zero-frequency impedance (see Eq. 4.5d). Additional, individual constraints unique to each WK model were implemented to ensure the optimization routine utilized a possible solution space that only consisted of physically plausible values. Table 4.12 lists the individual constraints of each WK model.

Table 4.12: Optimization constraints of each Windkessel model

| <u>Windkessel Model</u> | <u>Optimization Constraints and Specifications</u> |
|-------------------------|---|
| WK2 | <ul style="list-style-type: none"> • Initial guess of $R_d=10$; $C=2$ • Upper bounds of $R_d=$ infinite ; $C=100$ • Lower bounds of 1×10^{-6} for both |
| WK3 | <ul style="list-style-type: none"> • Initial guess of $R_u=5$; $R_d=14$; $C=0.01$ • Upper bounds of $R_u=5.3$; $R_d=$ infinite ; $C=0.1$ • Lower bounds of $R_u=1 \times 10^{-6}$; $R_d=1$; $C=0$ • $WK3 (R_u + R_d) = WK2 (R_d)$ |
| WK4s | <ul style="list-style-type: none"> • Initial guess of $R_u=12$; $R_d=15$; $C=0.1$; $L=0.01$ • Upper bounds of $R_u=$infinite ; $R_d=$ infinite ; $C=WK3(C)$; $L=0.01$ • Lower bounds of $R_u=1 \times 10^{-6}$; $R_d=1 \times 10^{-6}$; $C=0.5 * WK2(C)$; $L=1 \times 10^{-3}$ • $WK4s (R_u + R_d) = WK2 (R_d)$ |
| WK4p | <ul style="list-style-type: none"> • Initial guess of $R_u=53.5$; $R_d=18$; $C=WK3(C)$; $L=0.1$ • Upper bounds of $R_u=100 * WK2 (R_d)$; $R_d=$ infinite ; $C=WK3(C)$; $L=100 * WK3(C)$ • Lower bounds of $R_u=1 \times 10^{-2}$; $R_d=1 \times 10^{-2}$; $C=0.01 * WK2(C)$; $L=1 \times 10^{-4}$ • $WK4s (R_d) = WK2 (R_d)$ |

The conditions listed in Table 4.12 were determined by manually altering the conditions and noting the ability of the optimization routine to converge upon a physically plausible solution. Specific care was taken to merely isolate regions of appropriate physical plausibility and not direct the optimization to converge upon a specific set of WK parameters.

The optimization algorithm followed the same methodology for each WK model: i) specify the initial guess of the optimization, ii) use the frequency-domain impedance expression of each WK model to calculate MATLAB's fft coefficients of the flow waveform, iii) use the "ifft" function to convert the frequency domain flow coefficients to a time-domain flow waveform, and iv) calculate error magnitude as the percent difference between the mean and max values of the WK time-domain flow waveform and the population averaged mean max flow rates, respectively. A base frequency $\omega_0 = 2\pi$ rad/s was assumed for the frequency

domain of all WK models while a single error magnitude was achieved by summing the percent differences of the mean and max flow magnitudes. After each WK model's parameters that minimize their individual error signal were determined, the flow waveforms that minimized the error signals were divided by a factor of 0.55 to calculate population averaged CHA flow rates. The factor 0.55 stems from Table 4.7, where the RHA receives a median of 0.55 of the PHA flow. After a population-averaged CHA flow rate is determined, the formulas associated with Fig. 4.15 were used to calculate corresponding SMA inflow and outflow waveforms. Figure 4.17 depicts the computational flow-chart algorithm and Appendix III contains the developed custom MATLAB code used to construct the population-averaged flow waveforms.

[See next page for Fig. 4.17]

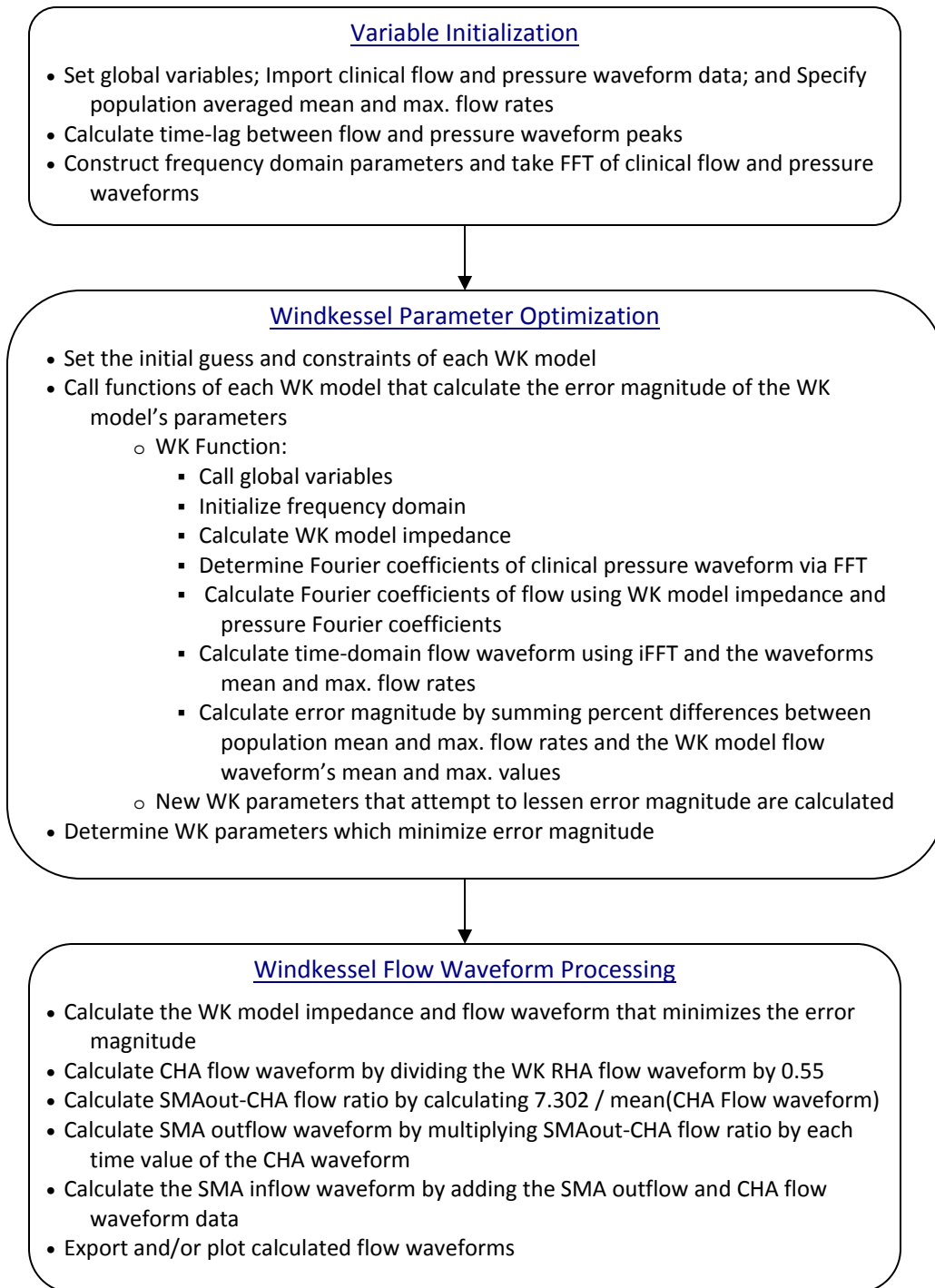


Figure 4.17: Flowchart of custom MATLAB Windkessel algorithm and population averaged SMA inflow waveform calculation

Prior to implementing the algorithm given in Fig. 4.17 for all Windkessel models, a validation of the frequency-based Fourier solution procedure was completed. The analytical time and Fourier frequency flow waveforms of the two-element Windkessel model were calculated and compared. Figure 4.18 illustrates the close match between both solution procedures and gives confidence that the Fourier solutions of the other Windkessel models with no analytical solution can be utilized to accurately determine a time-domain flow waveform.

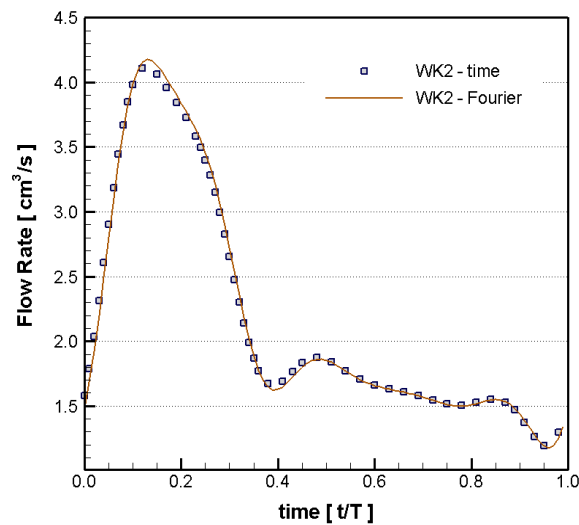


Figure 4.18: Validation of Fourier transforms and frequency-based computational algorithm of Windkessel flow waveform calculation

Table 4.13 lists the Windkessel parameters calculated by the custom MATLAB code, while Figure 4.19 plots the impedance modulus and phase angle vs. the nondimensional frequency of the patient and Windkessel population averaged data sets.

Table 4.13: Parameters of the different Windkessel models

| | <u>WK2</u> | <u>WK3</u> | <u>WK4s</u> | <u>WK4p</u> |
|--|------------|------------|-------------|-------------|
| L $\left[\frac{\text{mmHg}}{\text{cm}^3/\text{s}} \right]$ | NA | NA | 0.0072 | 0.4751 |
| R _u $\left[\frac{\text{mmHg}}{\text{cm}^3/\text{s}} \right]$ | NA | 5.3000 | 4.0922 | 53.5161 |
| R _d $\left[\frac{\text{mmHg}}{\text{cm}^3/\text{s}} \right]$ | 18.9345 | 13.6345 | 14.8425 | 18.9347 |
| C $\left[\frac{\text{cm}^3/\text{s}}{\text{mmHg}} \right]$ | 0.0074 | 0.0127 | 0.0106 | 0.0083 |

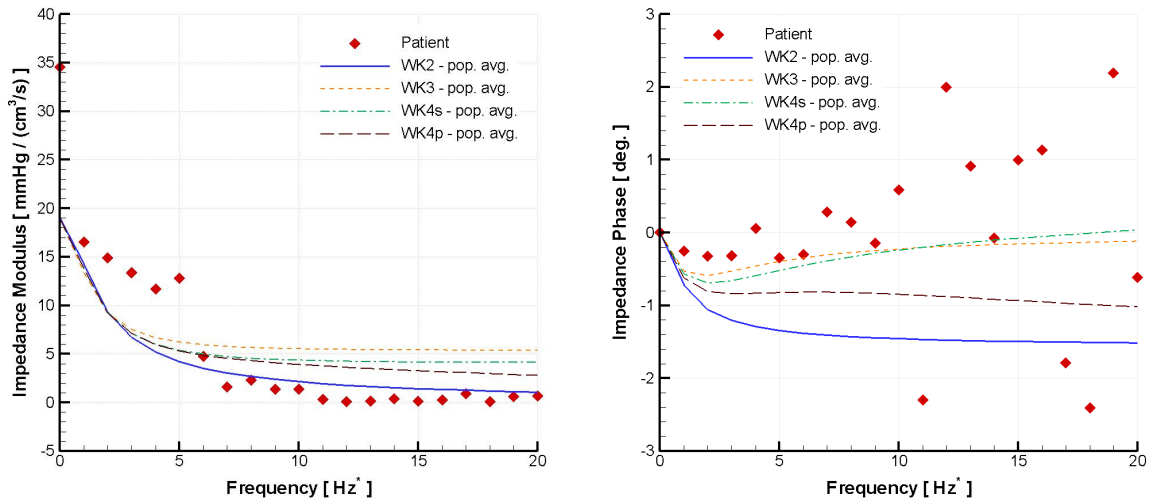


Figure 4.19: Impedance modulus and phase angle vs. nondimensional frequency (Hz.* = 1 / nondimensional time unit)

It is important to note that the WK model parameters were never fit to match the impedance of the patient data. Thus, the apparent disagreement between the WK models and the patient impedance data is expected since the WK models are representative of population averaged conditions rather than a single patient's. The differences between population averaged and single patient's arterial impedance are further seen in the waveforms for the SMA inflow,

SMA outflow, LHA flow rates, and RHA flow rates. Figure 4.20 plots the RHA flow waveforms of the patient and population-averaged Windkessel data sets along with the patient's pressure waveform, which was used in the Windkessel flow calculation.

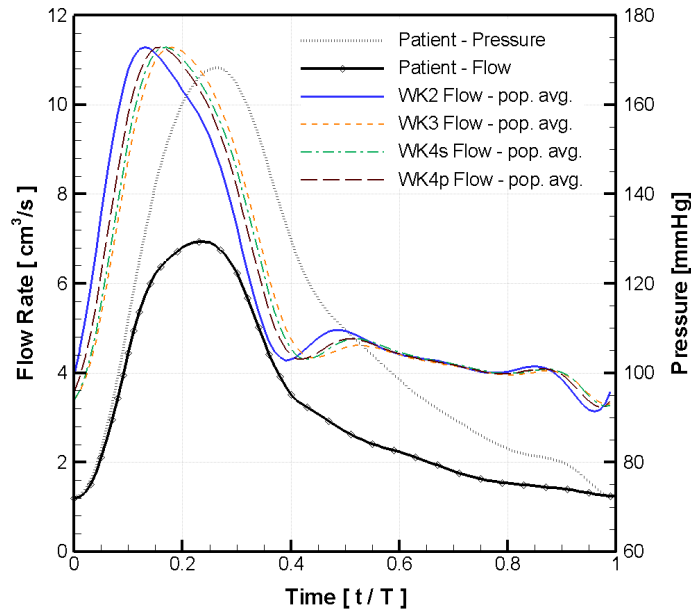


Figure 4.20: RHA flow waveforms of population average Windkessel models and patient-specific data sets

Interestingly, the WK-flow waveforms all exhibit similar features and the lower zero-frequency impedance compared to the patient impedance correlates with the WK models having increased flow rates. Since the WK models were not fitted to the patient data, each waveform (WK and patient) is a unique data set that is equally plausible for representing flows in the hepatic arterial system under tumor flow conditions. A primary reason for constructing multiple waveforms is to analyze the waveform influence on the corresponding particle-hemodynamics. The time delay between the peaks of the flow and pressure waveforms also varies between each data set. Table 4.14 displays the calculated time-delay between the systolic pressure and max flow rate for each waveform.

Table 4.14: Time delay between systolic pressure and max. flow in the RHA waveforms

| Date Set | Time Delay [s] |
|----------|----------------|
| Patient | 0.02 |
| WK2 | 0.13 |
| WK3 | 0.08 |
| WK4s | 0.09 |
| WK4p | 0.10 |

The small time delay seen in the patient’s data set implies a lower degree of pulsatile flow influence and wave reflection than the population-averaged Windkessel model flow waveforms. General shapes of the RHA waveforms in Fig. 4.20 influence the corresponding SMA inflow and outflow waveform. Figure 4.21 illustrates the similar waveform shape for the SMA inflow and outflow waveforms.

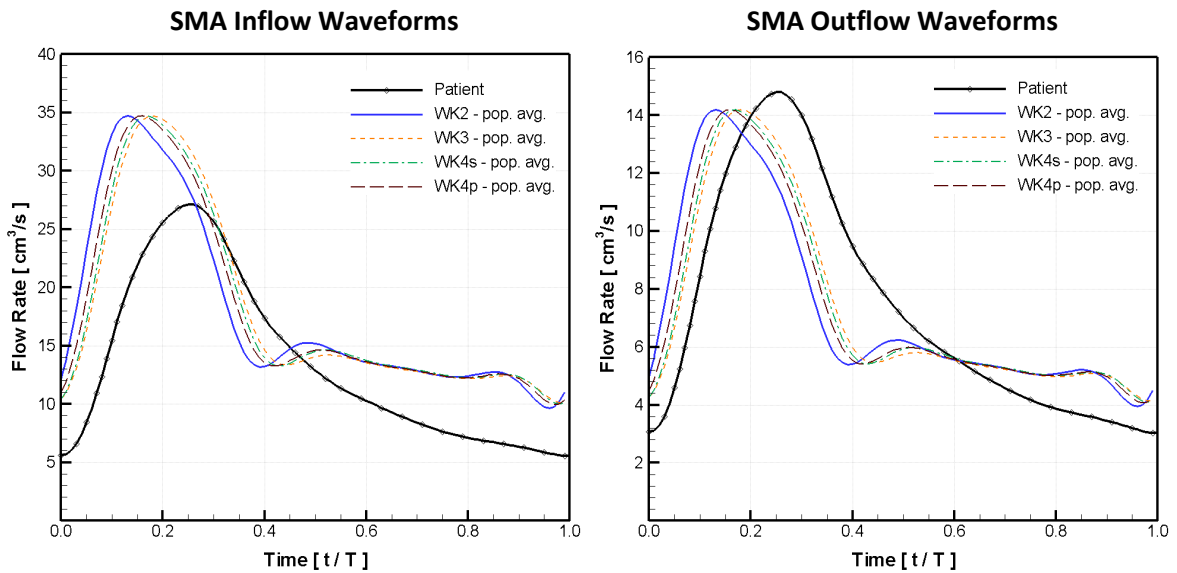


Figure 4.21: SMA inflow and outflow waveforms from the patient and population-averaged Windkessel data sets

Only subtle differences exist between the WK-flow waveforms. However, an interesting observation was made in the SMA outflow waveforms that the patient and WK waveforms had small differences in max values as efforts were made to keep their mean flow rates identical.

Following the calculation of RHA and SMA flow waveforms, the conservation of mass was used to calculate the LHA flow waveform. Specifically, the CHA flow ($Q_{RHA} / 0.55$) is multiplied by 0.45, which is derived by subtracting 0.55 from unity. Figure 4.22 plots the patient and WK LHA flow waveforms revealing similar appearances to those seen in Figs. 4.20 and 4.21.

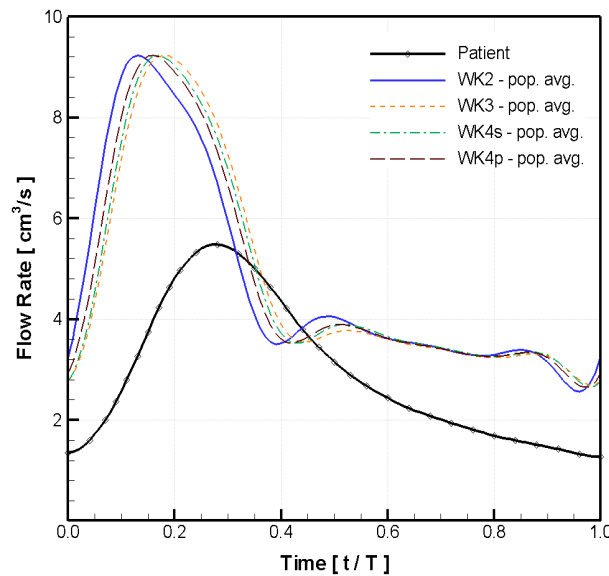


Figure 4.22: LHA flow waveforms of patient and population-averaged Windkessel data sets

Interestingly, the population-average Windkessel flow waveforms all had similar overall appearances with subtle differences in local regions of curvature. Another interesting note is that all of the WK waveforms exhibit similar local minima as the waveform spectra shown in

Hübner et al. (2000) and Taylor et al. (1985), while the patient's in-vivo waveforms exhibit a smoother decline without local minima. The primary reason for this discontinuity is believed to be the difference in arterial morphology of the subjects in Hübner et al. (2000) and Taylor et al. (1985) and the present patient. Such a hypothesis is supported by the patient having a replaced CHA from SMA, which created very different arterial morphology and hence wave reflections, which are fundamental reasons for the existence of local minima in the flow waveform. The WK waveforms selected for use in the computational particle hemodynamic studies were the WK2 and WK4s flow waveforms, since they represent a set of WK waveforms with noticeable differences, and the WK4s waveform is the median between the WK3 and WK4p flow waveforms.

4.4 Implementation of Derived Inlet/Outlet Conditions

Following the successful derivation of the transient inlet/outlet condition waveforms, each waveform must be implemented in the computational mesh at the appropriate two-dimensional surface. In general, the inflow rate waveforms are converted to averaged velocity normal to the boundary surface, which is then utilized in a boundary specific, spatial velocity profile (e.g., uniform, parabolic, Womersley, etc.). The outflow waveforms are implemented as mass flow rates by multiplying the volumetric flow rate magnitude by the blood's constant density. Pressure boundary conditions were implemented as "Opening" entrainment average pressure, which enable small variations in the pressure across the two-dimensional surface while ensuring the average pressure across the surface matches the specified value. The "Opening" boundary condition also enables flow to enter and exit the

system through the two-dimensional surface, which is an important characteristic of systems with retrograde flow at the inlet (i.e., the infrarenal AAA). Implementing the pressure waveforms with the aforementioned configuration increases numerical stability and increasing the solver efficiency when solving nonlinear problems. The selection of which waveform to implement at each boundary is a unique characteristic of each computational simulation. Hence, the implemented waveforms of each simulation will be discussed in Chapters 5 and 6. Quantitative, discrete numerical data of each implemented waveform can be found listed alongside a visual representation of the waveform in Appendix IV.

4.5 Conclusions

The previous chapter constructed inflow/outflow waveforms needed for transient, computational particle-hemodynamics simulations and the methods used to construct each waveform. An infrarenal AAA inflow waveform and common iliac pressure waveform from Olufsen et al. (2000) was presented while some general characteristics of AAA hemodynamics were defined. Additionally, in vivo hemodynamics data from a single patient was processed into flow and pressure waveforms to be utilized of future particle-hemodynamics simulations ⁹⁰Y-microsphere transport. Mean flow rates and flow distribution in the hepatic arteries was also reviewed under healthy and tumor-afflicted conditions. The population averaged data and patient's pressure waveform was then used to construct additional flow waveforms from Windkessel model optimization. In conclusion, the chapter provides a record of arterial flow and pressure data that is essential for particle-hemodynamics simulations and will be utilized in the current computational analysis.

Chapter 5:

Transient Particle-Hemodynamics of an Abdominal Aortic Aneurysm

5.1 Computational Simulation Parameters

ANSYS CFX v.12.1 (Canonsburg, PA) was used to solve the equations listed in Ch. 2 for the computational AAA mesh described in Ch.3. An executable custom solver was obtained from ANSYS code developers and technical support (Dr. Kurt Svihla, Senior Technical Services Manager, ANSYS Inc.) that exports the particle Reynolds number and particle slip velocity to the results file after converged time-steps of the transient simulation.

Inflow/Outflow Waveforms. The flow-rate and pressure waveforms in the previous Fig. 4.1 were specified as the average velocity at the domain inlet extension and average pressure at the domain outlet extensions, respectively. Specifically, Fig. 5.1 depicts the AAA domain

with the inlet/outlet extensions, the corresponding waveforms, and the direction of the gravity vector acting on the particle trajectories.

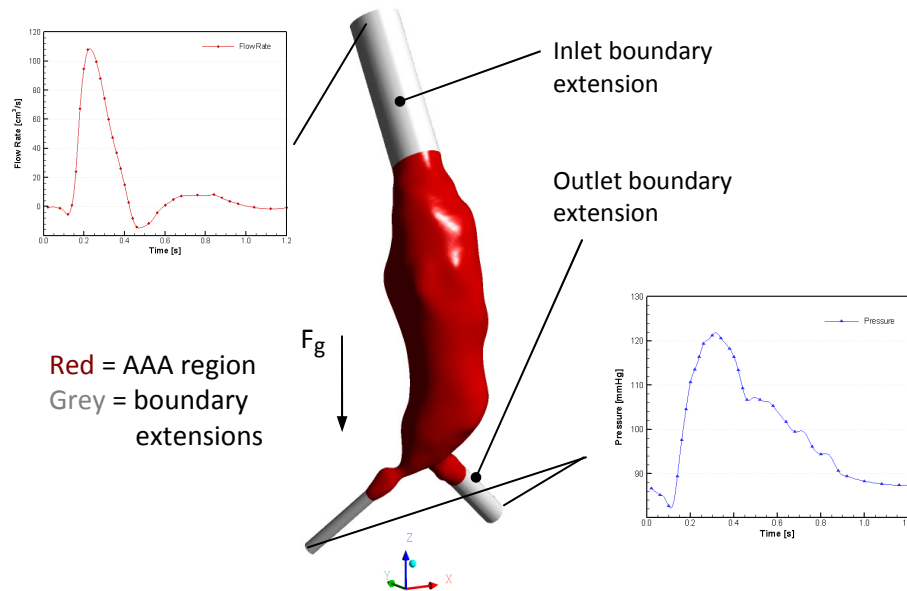


Figure 5.1: AAA domain with inlet/outlet extensions and waveforms

The velocity was implemented as a uniform profile and upon reaching the AAA sac, the spatial profile exhibited asymmetric characteristics that were dependent on time. No-slip boundary conditions were specified along each of the arterial and extension walls, where the walls remained stationary throughout the simulation. The transient, iterative solution procedure used a constant time-step of 1.25×10^{-3} s and continued until RMS mass and momentum maximum residuals were less than 1.0×10^{-5} . Transient results were recorded every 0.025s and a maximum number of twenty iterations per time-step was enforced, which was sufficient to achieve solution convergence.

Blood Particles. Spherical particles representing RBCs, WBCs, and PLTs were injected into the computational domain at the extension's inlet with zero slip velocity and a bulk mass

flow rate equaling the spatially-averaged carrier fluid mass flow rate at the injection boundary. All particles were injected with a uniform, equally spaced distribution across the inlet surface, and each particle type had the same number of injected particles over time. The particle injection rate was specified by multiplying a local concentration (525 particles/cm³) by the fluid's transient bulk mass flow rate. Thus, the number of injected particles varied throughout the transient inflow waveform and a total amount of approximately 10,090 particles were injected during one period. Particle characteristics were selected to be the mean values listed in Table 1.1:

- RBC diameter = 8μm ; RBC density = 1096.5 kg/m³
- WBC diameter = 12.5μm ; WBC density = 1077.5 kg/m³
- PLT diameter = 2μm ; PLT density = 1040 kg/m³

Wall restitution coefficients for the arterial walls (not the boundary extensions) were set to zero, forcing particle deposition when the particle's center of mass crossed the wall boundary. Prior to injection of the particles, five periods of pulsatile flow were simulated in the AAA domain. Subsequently, particles were injected during the sixth period, and four additional periods were simulated to calculate the transport particle transport throughout the domain. Thus, a total of ten periods of pulsatile flow were simulated. The five-periods prior to particle injection were solved in a single simulation conducted on two processors of a 64-bit Dell Precision 670 workstation with four Intel Xeon processors at 3.59GHz and 8GB of RAM. Total simulation time was approximately 336 hours. The five-periods including particle injection and transport were solved in five separate periods and were conducted on

four cores of a 64-bit Dell T3500 Precision Workstation with a quad core Intel Xeon E5520 processor at 2.27GHz and 12GB of RAM. Mean total simulation of each period was 36.7 hrs., resulting in a total time of approximately 180 hours.

Fluid-Element Residence Time. A user-defined transport variable was created to measure the residence time distribution of the Eulerian fluid phase. Equation (5.1a) lists the transport equation of a scalar variable (φ) that were used to construct a spatially varying resident time of the Eulerian carrier fluid

$$\frac{\partial (\rho_f \varphi)}{\partial t} + \nabla_i (v_i^f \rho_f \varphi) = \nabla_i (\rho_f D_\phi \nabla_i \varphi) + S_\varphi \quad (5.1a)$$

where D_ϕ and S_φ are the scalar's kinematic diffusivity and a volumetric source term, respectively. The kinematic diffusivity was set to a numerical value that would remove the term's influence the equation's calculation since diffusive transport is negligible for the current system. Additionally, the source term was set to unity over the AAA domain and the variable's units were set to seconds. Equation (5.1b) lists the simplified transport equation.

$$\frac{\partial (\rho_f \varphi)}{\partial t} + \nabla_i (v_i^f \rho_f \varphi) = 1 \quad (5.1b)$$

By integrating the left hand side of Eq. (5.1b) along the fluid streamlines, the time fluid “particles” require to traverse each streamline is calculated (ANSYS CFX v.12.0 Documentation for more information).

Particle Wall Shear Stress. The average shear stress magnitude on the particles' surface was calculated from the viscous (frictional) drag of the total drag force acting on a spherical

particle. Equation (5.2) describes the total drag force acting on an object in a flow field, where the total drag force is split into its shear and normal components. Specifically,

$$F_i^D = \iint_S (n_j \tau_{ij} + \nabla_i p \cdot \ell) dA \quad (5.2)$$

where $n_j \tau_{ij}$, and $\nabla_i p$ is the shear stress acting on the particle surface and the pressure gradient across the object's characteristic length. After completing the surface integrals for a spherical particle, the magnitude of the total drag can be correlated with the magnitudes of the shear and pressure forces. Equations (5.3a-c) defines the drag force magnitude in terms of the shear and normal force magnitudes

$$\begin{aligned} |F_D| &= |n_j \bar{\tau}_{ij}| \cdot A_s + |\nabla_i p| \cdot \ell \cdot A_r \\ |n_j \bar{\tau}_{ij}| &\equiv \tau_{eff}^p \\ A_s &= 4\pi R_p^2 ; A_r = \pi R_p^2 ; \ell = d_p \end{aligned} \quad (5.2a-c)$$

where $n_j \bar{\tau}_{ij}$, τ_{eff}^p , A_s , A_r , ℓ , R_p , and d_p are the spatial average shear stress, the effective shear stress acting on the particle, particle surface area, particle reference area, characteristic length, particle radius, and particle diameter, respectively. The drag force magnitude can also be calculated utilizing the drag coefficient of a solid, impermeable object suspended in flow according to Eq. (5.3)

$$|F_D| = C_D \frac{\rho_f}{2} |u^r|^2 A_r \quad (5.3)$$

where C_D , $|u^r|$, ρ_f is the drag coefficient, the speed of the sphere relative to the fluid speed and the fluid density, respectively. A single equation relating the effective shear stress on the

particle's surface can thus be derived by substituting Eqs. (5.2b,c) and (5.3) into Eq. (5.2a), where the result is:

$$\tau_{eff}^p = 0.25 \left[C_D \frac{\rho_f}{2} |u|^2 - |\nabla_i p| \cdot d_p \right] \quad (5.4)$$

The relation can be further defined according to specific particle-track variables calculated in the fluid-particle hemodynamics simulations by substituting the Schiller-Naumann drag coefficient (listed as Eq. (2.8e) on pg. 41) and the particle slip velocity (v_p^r) for C_D and u , respectively. As a result:

$$\tau_{eff}^p = 0.25 \left[12 \frac{\rho_f}{\text{Re}_p} \cdot |v_p^r|^2 \cdot \left(1 + 0.15 (\text{Re}_p)^{0.687} \right) - |\nabla_i p| \cdot d_p \right] \quad (5.5)$$

Hence, the effective shear stress acting on the cellular components of blood can thus be calculated to assess the potential role of PLT and WBC shear stress activation in the elevated physiological conditions of blood coagulation and clotting in AAAs and hence ILT formation/growth.

5.2 Transient Particle-Hemodynamics of a Patient's Abdominal Aortic Aneurysm

5.2.1 Transient Flow Fields

Velocity Vector Fields. The velocity profile at the terminal end of the inlet extension region (just prior to the AAA sac region), exhibited different contour orientations and off-center locations of maximum velocity throughout the inflow waveform. Moreover, the profiles were often asymmetric at multiple locations in the inflow waveform and could not be represented by a Womersely profile implemented without the inlet extension. Figure 5.2 plots

the contour and vector plots of the inflow velocity at the terminal end of the extension region throughout the inflow waveform.

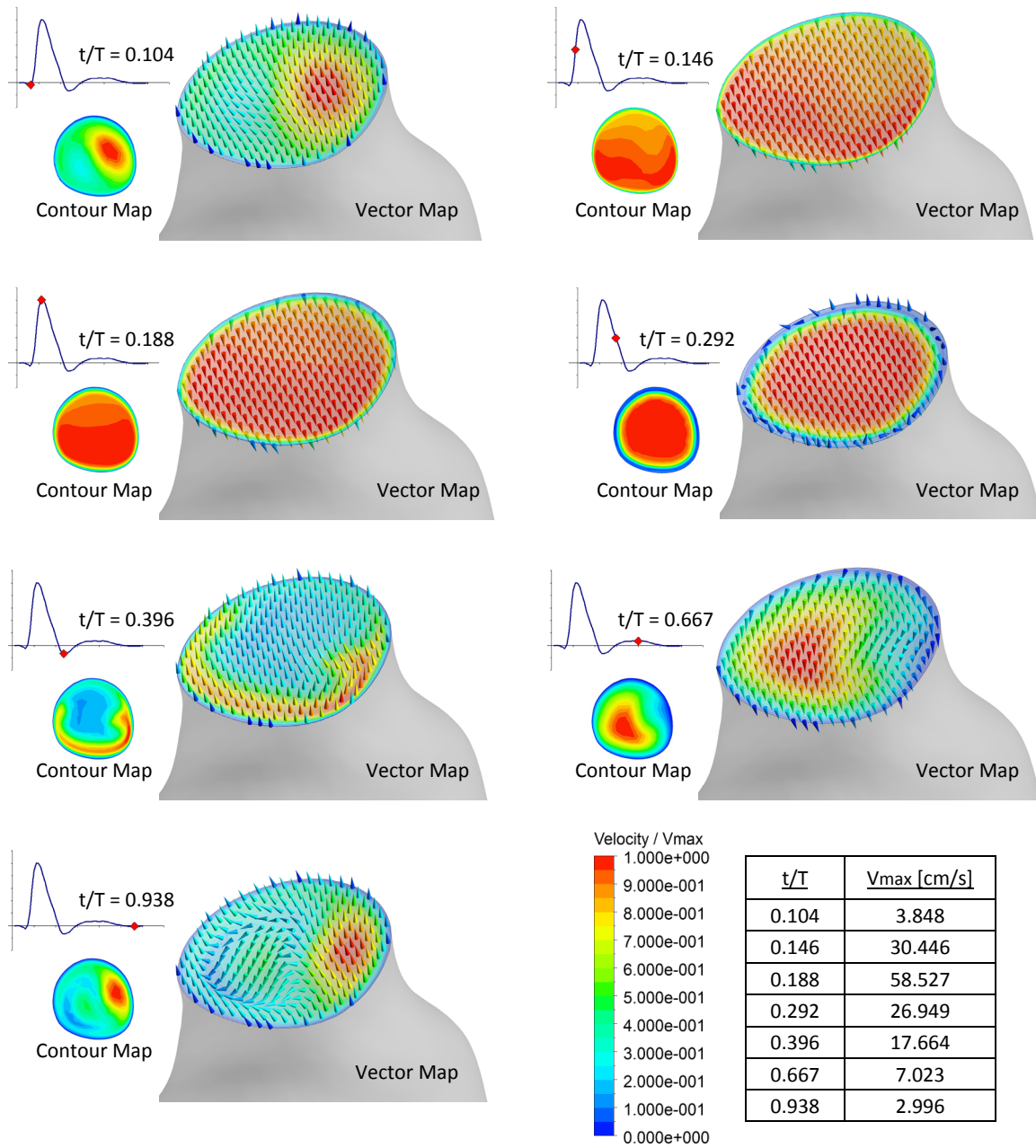


Figure 5.2: Velocity profile at the terminal end of the AAA inlet extension

In the regions of retrograde flow with relatively low magnitude, the max. velocity occurs in the right portion of the plane; where at the low inflow magnitudes the max. velocity is in the left portion of the plane. Interestingly, the right iliac outlet has a higher downstream resistance than the left iliac (due to the difference in vessel diameter), and is believed to be a major cause for the regions of elevated velocity during low magnitudes of inflow and outflow. The velocity field of AAAs is a continued area of study and is dependent on the upstream bifurcations off the abdominal aorta and even the curvature of the aortic arch. Such bifurcations and vessel curvature create asymmetric profiles with noticeable amounts of secondary velocity about the vessel centerline. An assumption was made in the current study to neglect the influence of upstream branching arteries and the aortic arch, but the uniform velocity profile (derived from a physiologically relevant flow rate waveform) developed into a transient profile that could produce asymmetric contour orientations and include the presence of secondary flows. Thus, while the assumptions simplify the system, they still enable physiological relevant boundary conditions for the region of interest, which is the AAA sac.

The transient streamlines exhibit a great deal of recirculation throughout the period of a single pulse, where net antegrade flow through the iliac arteries is maintained for approximately 0.5s of the physiologic pulse. Only 25% of that half second contains flow fields without major recirculation regions. Figure 5.3 depicts the velocity streamlines with vector arrows illustrating the flow magnitude and direction at multiple time-points throughout the period of a single blood pulse.

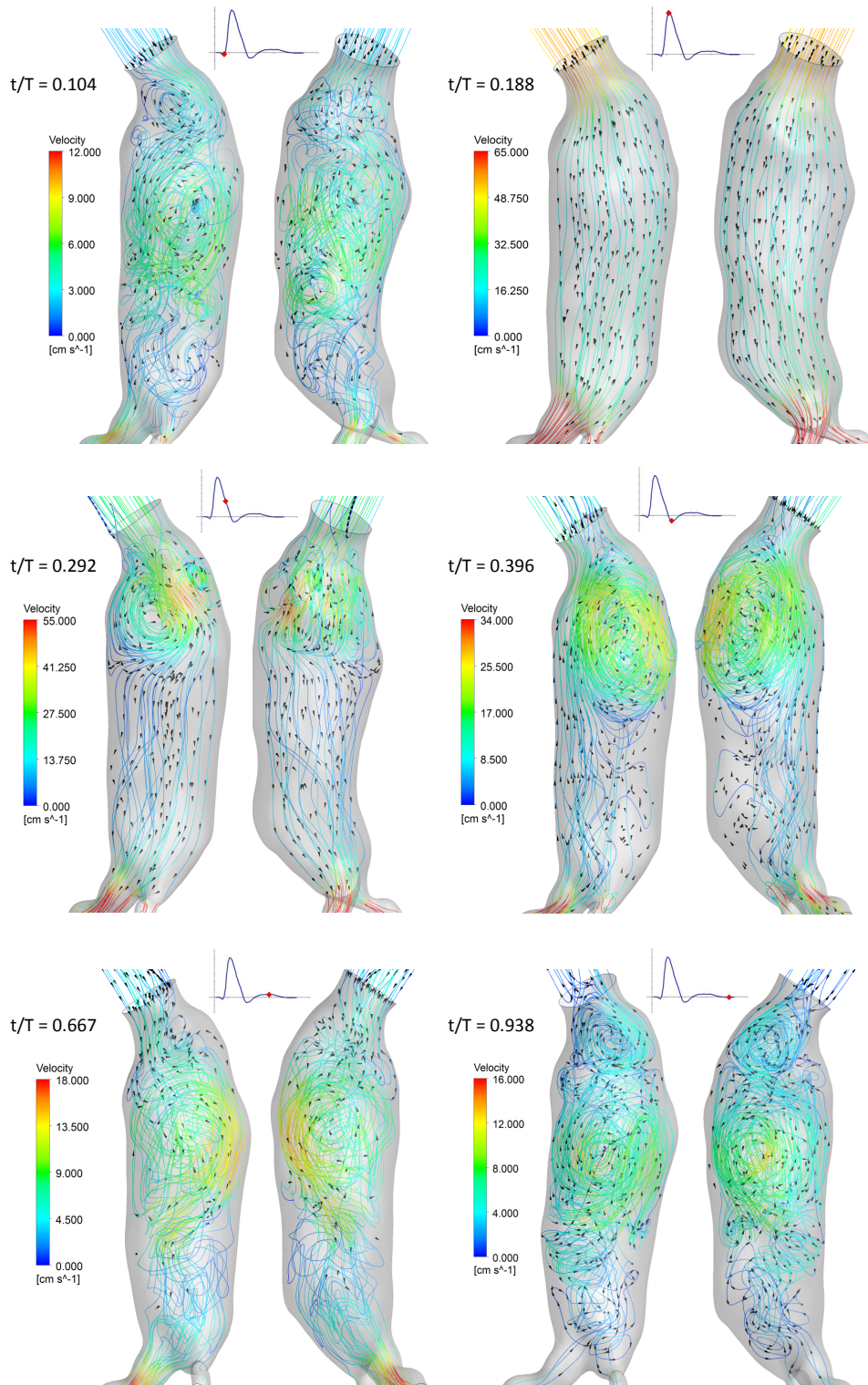


Figure 5.3: Velocity streamlines in the AAA throughout the arterial pulse

An important characteristic of the transient flow is seen at the onset of the decelerating region ($t/T=0.292$), where the inflow magnitude is not strong enough to overcome the circulating flow. The same flow characteristic is seen at the smaller inflow magnitude at $t/T=0.667$. Moreover, at the flow reversal immediately following the decelerating inflow ($t/T=0.396$), the local velocity magnitude in the circulation region is approximately one half of max velocity in the AAA region. Thus, the circulating flow not only is present for most of the pulse, but also maintains sufficient strength that will not be overcome by inflows of small magnitudes. Figure 5.4 plots the transient velocity along the axial plane that passes through the iliac common iliac bifurcation point.

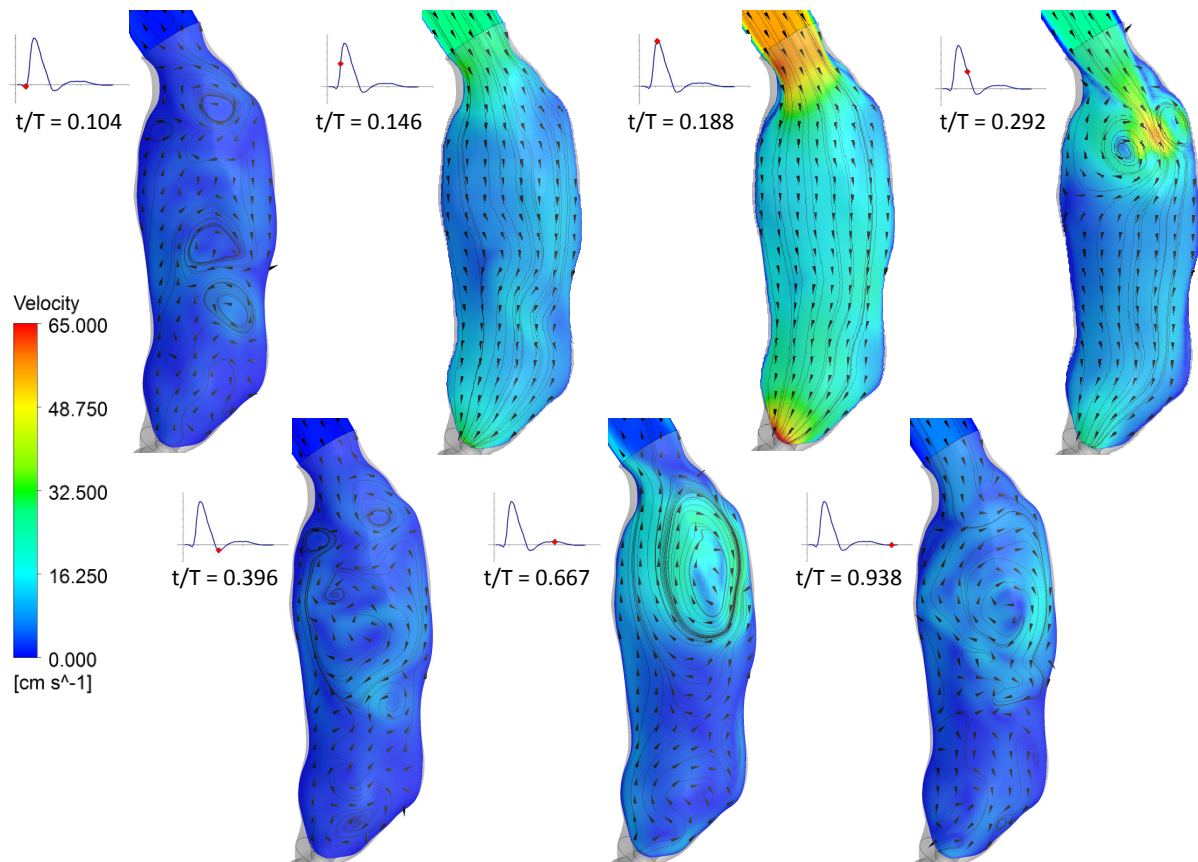


Figure 5.4: Transient velocity vectors on axial plane of AAA sac

The recirculation regions in Figs. 5.3 and 5.4 reveal noticeable redirection of flow in the primary flow direction with multiple vortices present at different portions of the pulse. No information is easily gleaned from the figures regarding secondary (cross-sectional) flow fields in the AAA sac. Figure 5.5 addresses the need for a detailed view of the transient secondary flow fields in the AAA sac.

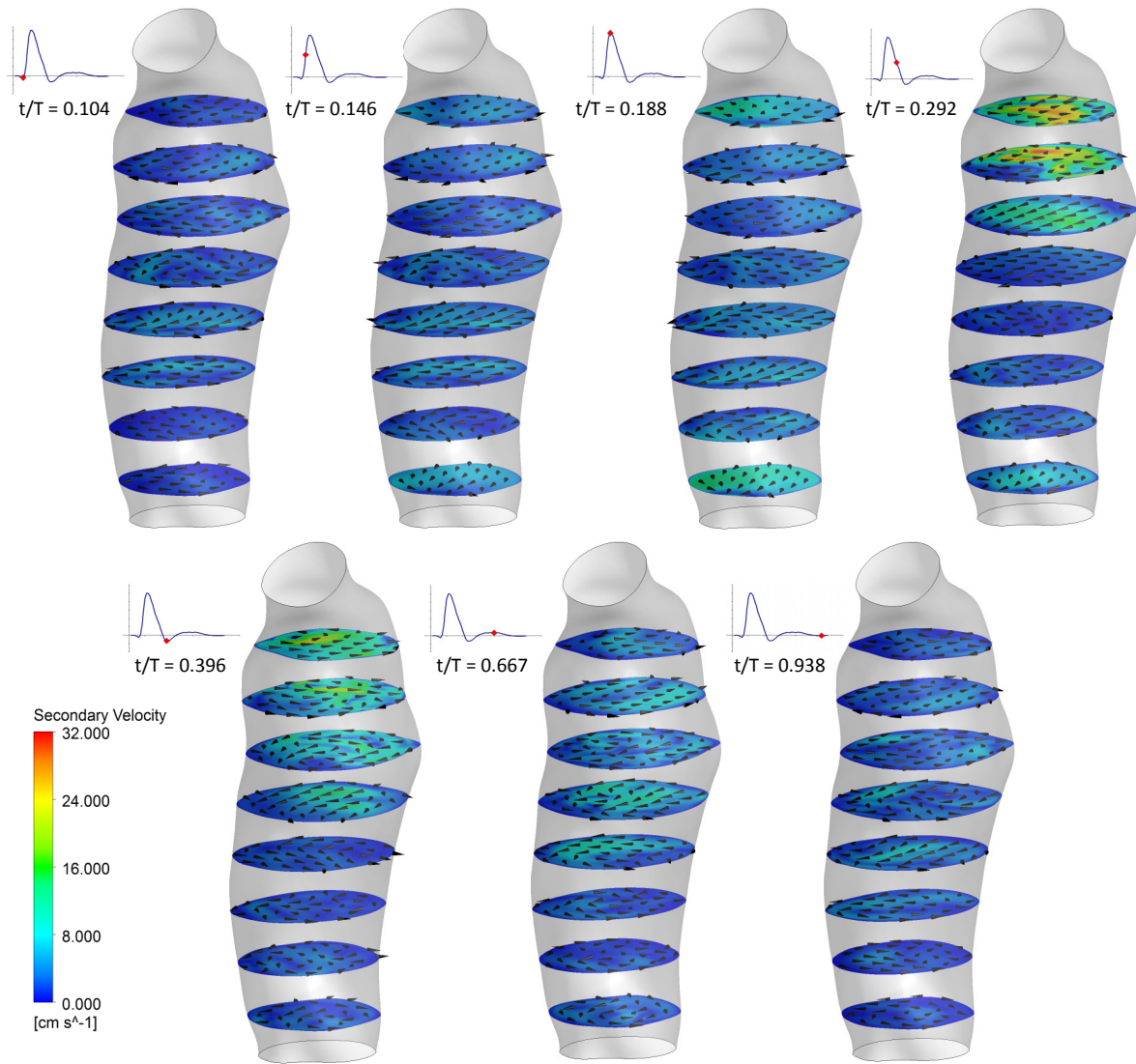


Figure 5.5: Transient secondary flow fields in the AAA sac

The secondary velocity contours in Fig 5.5 reveal that the temporal regions of maximum secondary velocity occurs in the decelerating and flow reversal regions after the systolic inflow. Additionally, the location of the max secondary velocity magnitude occurs where most of the flow reversal is present, in the upper region of the AAA. The elevated secondary velocity at the lowest plane is attributed to the blood shifting the common iliac vessels prior to the bifurcation. A very important deduction from the prevalent recirculation in the proximal region of the AAA sac is the enhanced potential to for shear activation of platelets clotting mechanism. Biasetti et al. (2010) postulated that the platelets are initially activated in the proximal regions of the AAA, and then deposit or initiate a thrombogenic response in the distal region of the AAA sac. The flow patterns in Figs. 5.3-5.5 support this hypothesis in that particles suspended in the proximal AAA flow would potentially traverse through several loops of the recirculation region prior to entering the distal region, which provides a region of potential stagnations due to low levels of flow for most of the pulse.

Non-Newtonian Blood Viscosity Contours. As mentioned in the steady AAA particle-hemodynamics simulations in Appendix V, the local non-Newtonian, shear-rate dependent blood viscosity can reveal elevated regions of particle density by the increase of viscosity in regions of low shear rate. The pulsatile flow results in viscosity contours are noticeably different than those associated with steady flow (see Fig. A4.3). While the steady flow had indefinite time of flow recirculation and attachment, the recirculation regions of the pulsatile simulations last less than one second for the current study. Thus, the transient viscosity plots do not reveal as high viscosities in the AAA sac as the steady flow simulation, and most near-wall regions exhibit a lower viscosity than in the center of the lumen. It indicates that

elevated shear rates still exist at the wall and would not normally induce aggregation or condensing of blood cells in that region. Figure 5.6 plots the cross sectional planes with the transient non-Newtonian viscosity contours and corresponding fluid streamlines while Fig. 5.7 depicts the non-Newtonian viscosity at the AAA sac wall throughout the arterial pulse.

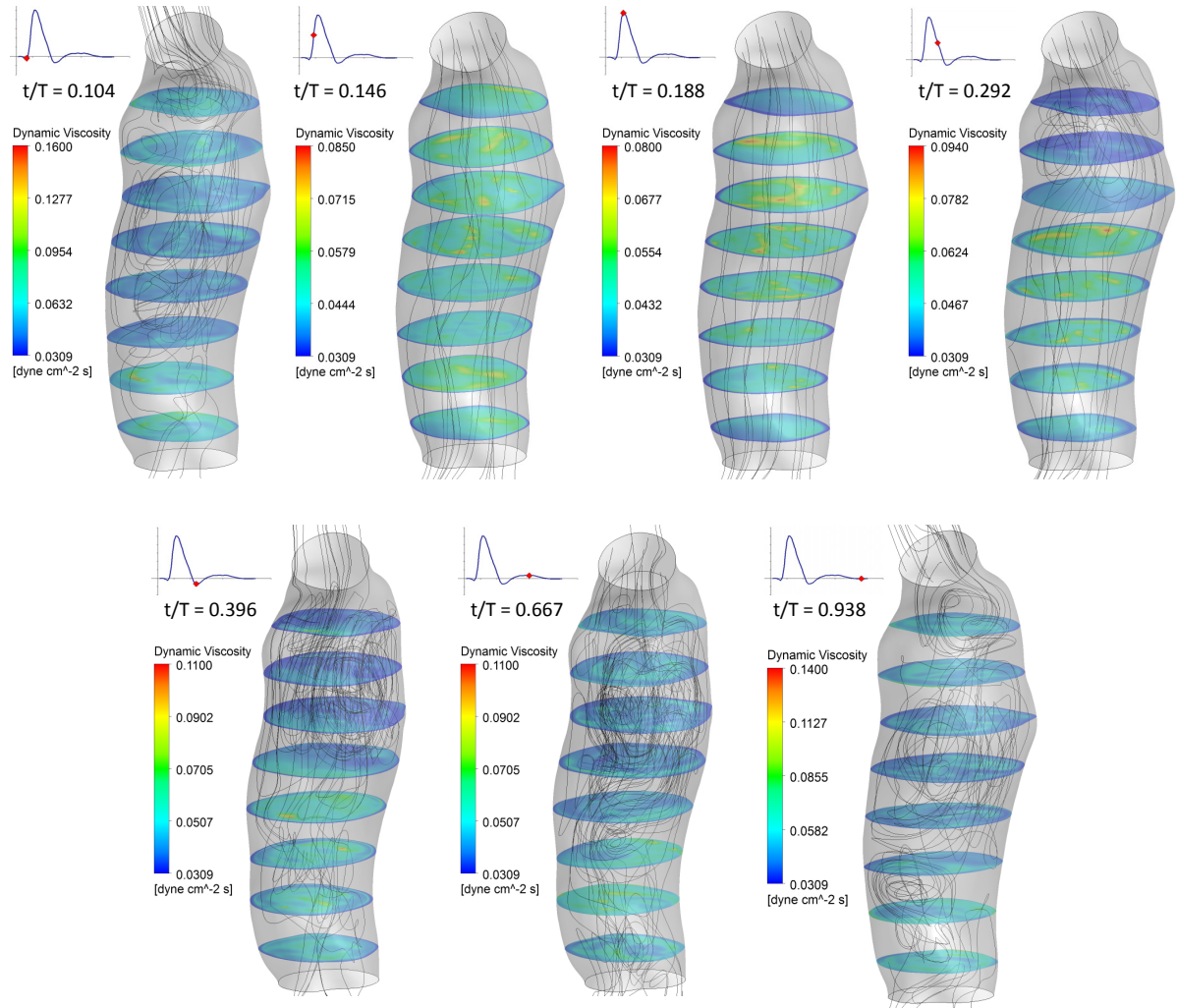


Figure 5.6: Transient cross-sectional plots of dynamic viscosity in the AAA sac

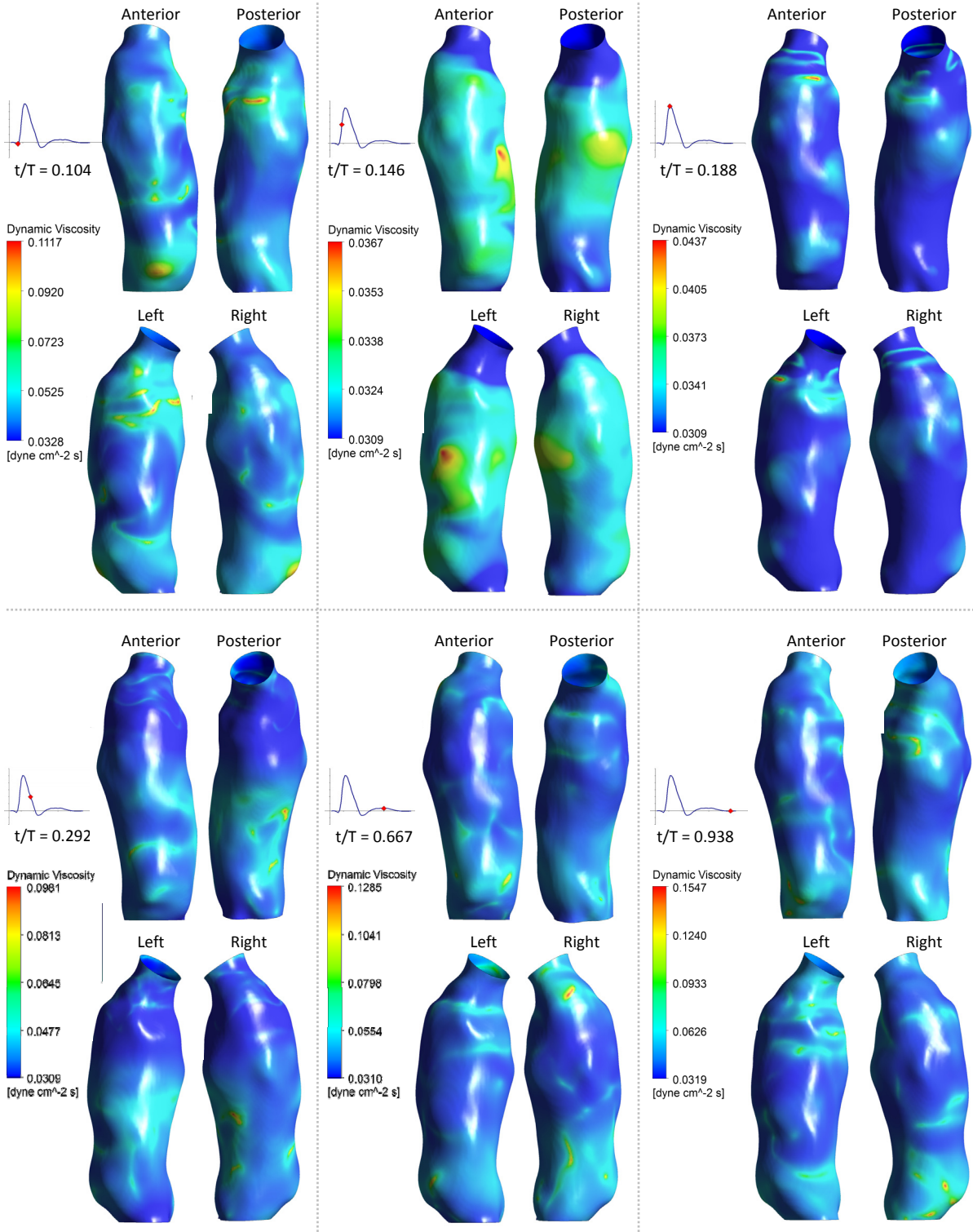


Figure 5.7: Transient contours of dynamic viscosity along the AAA sac wall

The dynamic viscosity plots in Figs. 5.6 and 5.7 illustrate that the magnitude and location of the maximum viscosity is dependent on the temporal position in the pulsatile waveform. Higher maximum viscosities were seen at lower inflow magnitudes in the latter portion of the pulsatile waveform, where the distal region of the AAA sac tended to have more regions of elevated viscosity than the proximal regions. Figure 5.6 provides additional viscosity contours inside the AAA sac revealing asymmetric distributions and localized regions of elevated viscosity that exist near the wall. An important note from the viscosity contours throughout the pulse is that not every bulge or circulating flow is correlated with elevated viscosity. Thus, one may imply that not every bulge or region of flow recirculation is correlated with enhanced presence of blood particles revealing the need for additional analysis of actual particle trajectories and behavior.

Time-Averaged Flow Quantities. The magnitudes of each solved quantity's time-averaged vector components may provide additional physical insight and can be used as a representation of pseudo-consistent conditions of pulsatile flow. However, an important note is that the time-averaged conditions only exist for a brief period of time and are not perpetually continued at each point of the pulsatile waveforms. Still, they can provide a measure of reoccurring flow features of the arterial pulse. Figure 5.8 plots the magnitudes of time-averaged velocity streamlines and secondary flow vector fields in the AAA, where one primary region of flow recirculation exists in the proximal region of the AAA sac and notable elevated regions of secondary flow are caused due to the neck angle directing flow towards the anterior wall.

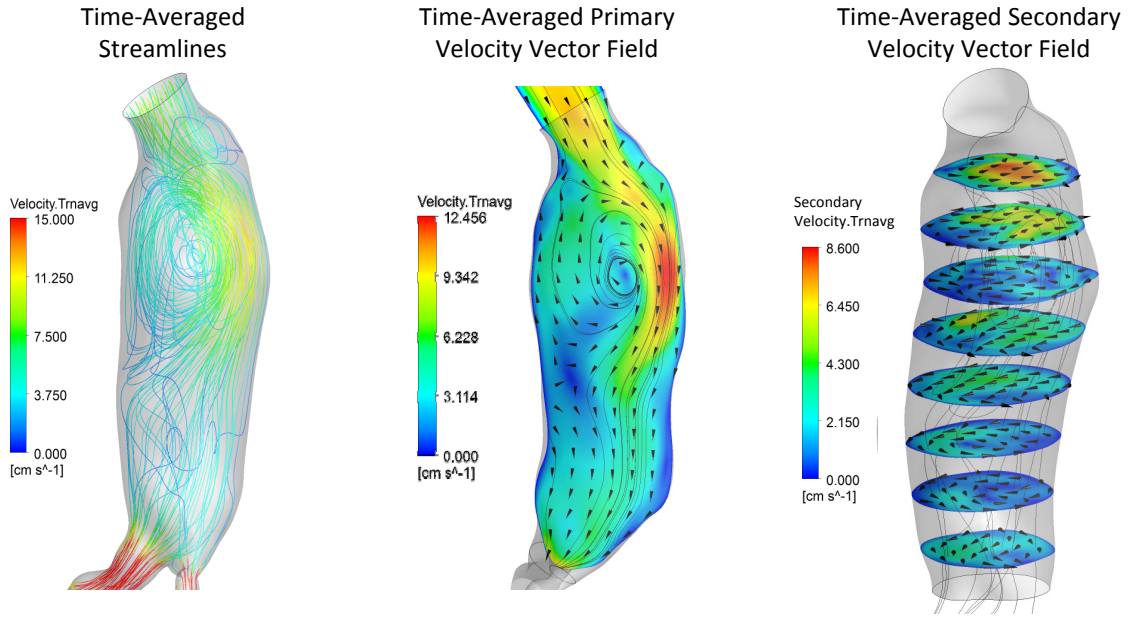


Figure 5.8: Magnitudes of time-averaged velocity vector components

The time-averaged viscosity contours in Fig. 5.9 supplement the time-averaged velocity data and also reveal similar observations correlating to the velocity fields shown in Fig. 5.8.

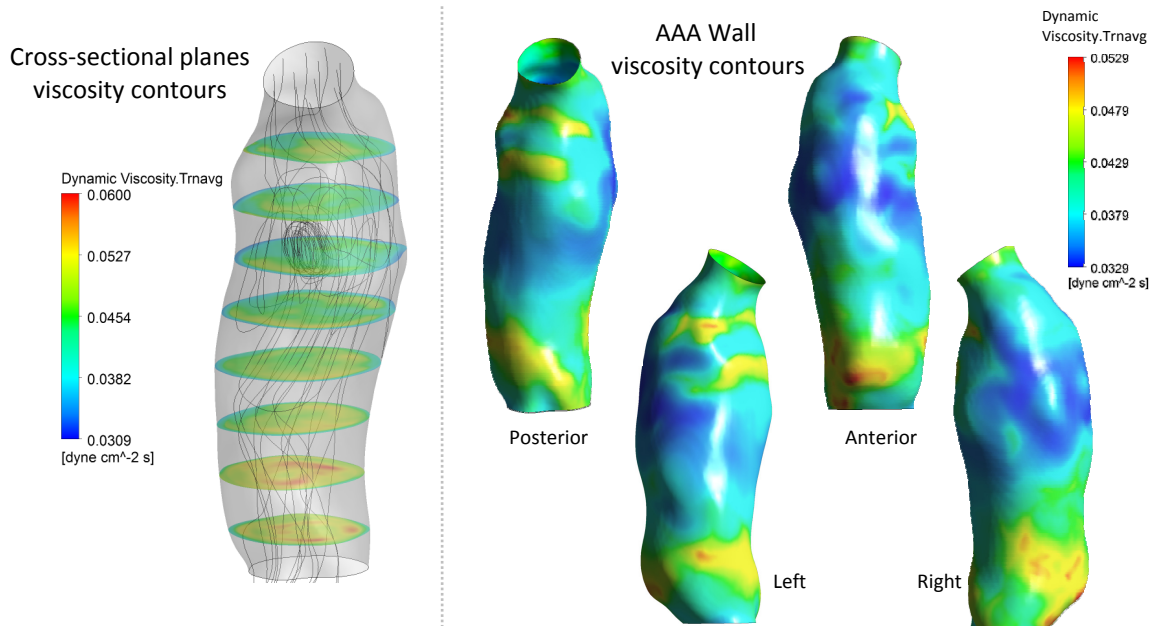


Figure 5.9: Time-averaged viscosity inside the AAA sac and along the AAA wall

The magnitude of the time-averaged wall shear stress (WSS) components provides a representative view of the shear load that the AAA wall (or ILT) experiences during one cardiac cycle. Figure 5.10 plots the magnitude of the time-averaged WSS vectors revealing localized regions of elevated and low values correlating with regions of elevated viscosity and morphologic features of the AAA sac.

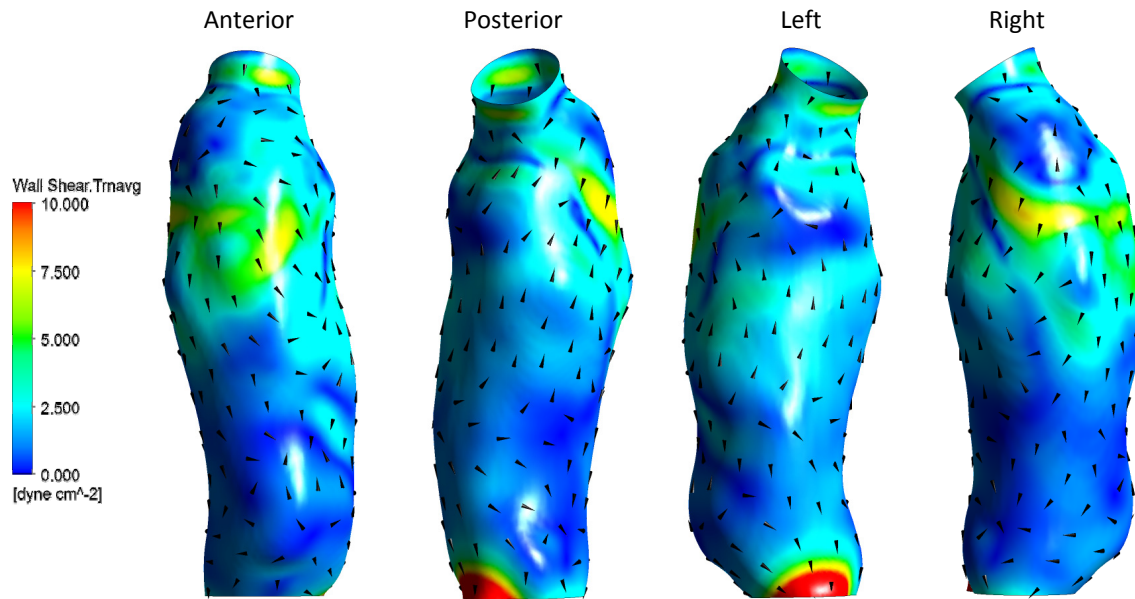


Figure 5.10: Magnitude of the time-averaged WSS vector components

The region of highest time-averaged WSS at the distal region is caused by the nozzle-like flow structure of fluid entering the left iliac artery. Another observation is that high time-averaged WSS magnitudes tend to correlate with low viscosity contours. Thus, the shear rate of the fluid caused by the AAA morphology and hemodynamics has a larger influence than local viscosity on the time-averaged WSS magnitude. Directions of the time-averaged WSS vector components clearly illustrate the flow recirculation and reattachment points along the

AAA wall, where regions of opposite or antagonistic vector directions frequently have a low WSS magnitude.

Oscillatory Shear Index. A measure of pulsatility and oscillatory flow is the oscillatory shear index (OSI) often used to determine regions of frequent changes in the WSS vector direction and magnitude. The OSI is defined in Eq. (5.6) after the formulation by He and Ku (1996)

$$OSI = 0.5 \left[1 - \frac{\left| \frac{1}{T} \int_0^T \bar{\tau}_w dt \right|}{\frac{1}{T} \int_0^T |\bar{\tau}_w| dt} \right] \quad (5.6)$$

where the magnitude of the time-averaged WSS vector components is divided by the time-averaged WSS magnitude. An expansion of the WSS time integrals in Eq. (5.6) reveal the different mathematical formulation of integrals as listed in Eqs. (5.7a,b):

$$\left| \frac{1}{T} \int_0^T \bar{\tau}_w dt \right| = \frac{1}{T} \left[\left(\int_0^T (\tau_w)_x dt \right)^2 + \left(\int_0^T (\tau_w)_y dt \right)^2 + \left(\int_0^T (\tau_w)_z dt \right)^2 \right]^{1/2} \quad (5.7a-b)$$

$$\frac{1}{T} \int_0^T |\bar{\tau}_w| dt = \frac{1}{T} \int_0^T \left[\{(\tau_w)_x\}^2 + \{(\tau_w)_y\}^2 + \{(\tau_w)_z\}^2 \right]^{1/2} dt$$

where $(\tau_w)_x$, $(\tau_w)_y$, $(\tau_w)_z$ are the x, y, and z components of the WSS vector respectively.

Figure 5.11 plots the OSI along the AAA wall and reveals localized regions of high oscillation at proximal and distal regions of the AAA sac.

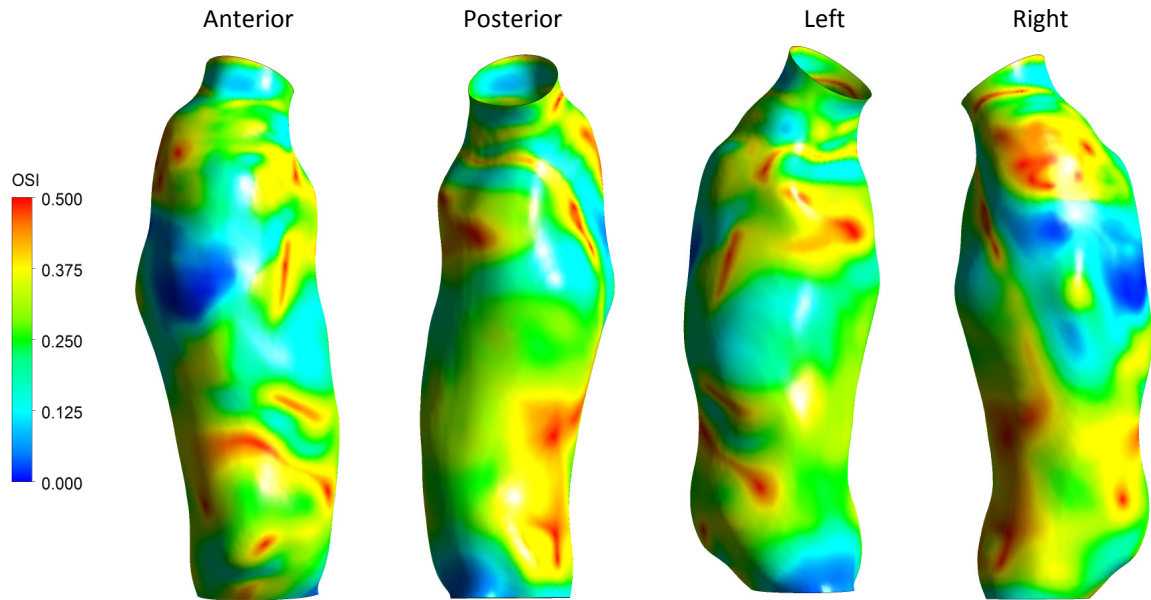


Figure 5.11: OSI contours along the AAA wall

An important deduction from the OSI contours is the primary outward bulge in the proximal region of the anterior AAA wall has a low OSI, which implies a more unidirectional flow throughout the cardiac cycle at this region. Such a result is echoed by the high time-averaged WSS magnitudes and the transient velocity vectors. The catalyst for such flow through the noticeable outer wall expansion is the neck angle directing flow across this anterior portion of the wall. Thus, if the neck angle should change with time and direct flow away from the anterior portion of the wall, flow separation and recirculation would be expected in this expanded region.

5.2.2 Particle Transport and Mechanical Loading of Particles

ILT Formation Hypothesis. The foundational hypothesis being tested is that a AAA patient's particle-hemodynamics characteristics in the AAA sac play a role in future development of ILT. Specifically, elevated near-wall particle residence time and shear-induced activation of the particles are thought to be correlated with future ILT development.

Particle Terminal Locations and Trajectories. Particle transport through the transient flow field revealed that approximately 70% of all particles entering the AAA sac, exit the region (which is defined as the lumen distal to the AAA neck and proximal to the aorto-iliac bifurcation) in less than six seconds (five continuous arterial pulses). Whereas, the remaining 30% of particles entering the region do not exit in the allotted time and less than 1% of all particle types deposit along the AAA sac wall. Of the particles that exit the AAA sac region and the global AAA domain, approximately 82% exit the left iliac artery and 18% leave the right iliac artery. The mean flow distribution has a similar trend with approximately 79% and 21% of time-averaged exiting flow traversing the left and right iliac arteries, respectively. Figure 5.12 visualizes the aforementioned data by plotting the AAA sac's time-averaged exiting flow distribution along with the particles' injection and exit fraction percentages.

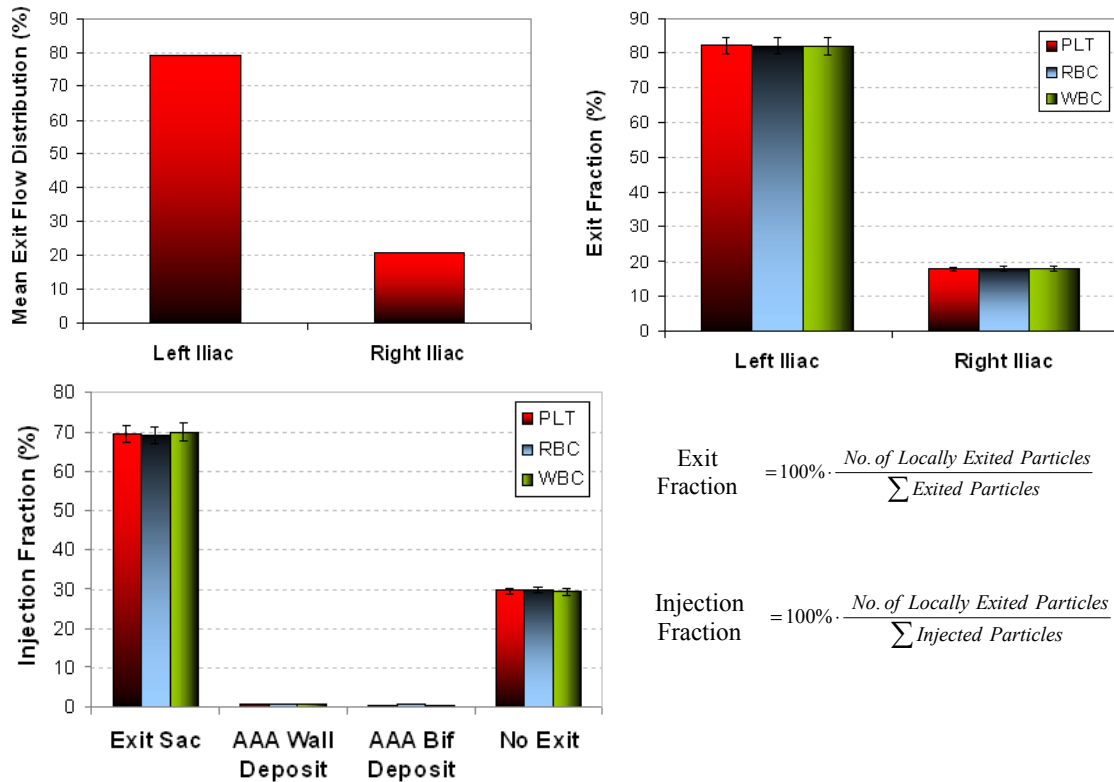


Figure 5.12: Transient mean exiting flow distribution, particle exit fractions, and particle injection fractions

The large percentages shown in Fig. 5.12 have a negligible dependence on particle type as shown by the intersecting 3% error bars on each of the bars. Thus, lumen geometric characteristics and transient hemodynamics are believed to be more influential than the particle characteristics when determining whether a particle remains in the AAA sac longer than 6 seconds or preferentially exits the left or right iliac artery. The relatively small number of particles depositing decreases the ability to draw strong conclusions with each particle type since each particle had less than 1% of particles entering the AAA sac deposit on the AAA wall. However, differences greater than $\pm 3\%$ were seen between the particle types. Moreover, the terminal positions of deposited particles exhibited some differences between

particle types. Figure 5.13 plots the terminal locations and corresponding trajectories of deposited particles on the AAA wall.

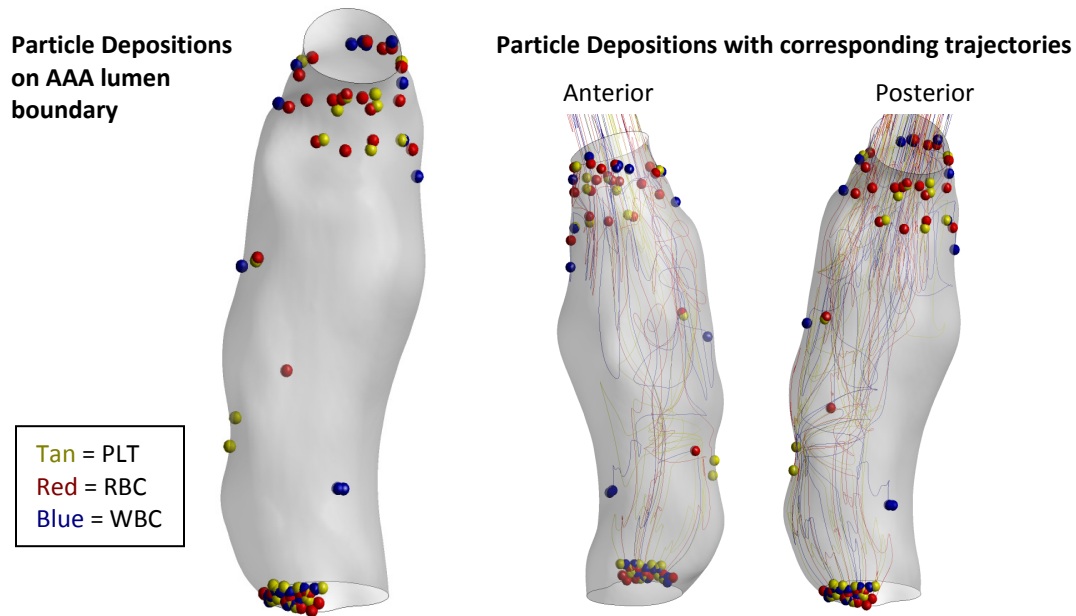


Figure 5.13: Particle depositions along the AAA sac wall

The distal region of localized particle deposition is caused by the enhanced flow delivered to the left iliac artery, where a local increase in velocity is seen due to the funneling of blood into a smaller conduit. The neck region also showed regional deposition increases due to the initial expansion of the lumen causing noticeable flow recirculation. An important note is that all particles that deposit in the AAA sac (excluding the left iliac region) correspond to regions of maximum OSI in Fig. 5.11. Particle trajectories in the transient flow exhibit noticeably different paths depending on their terminal location. Those that deposit along the wall (shown in Fig. 5.13) exhibit erratic trajectories and follow flow streamlines that repeatedly collide with the lumen boundary. Figure 5.14 plots the transient trajectories of

particles that exit the computational domain during the simulation time of four periods while Figure 5.15 illustrates the recirculation of particles that did not exit the AAA sac.

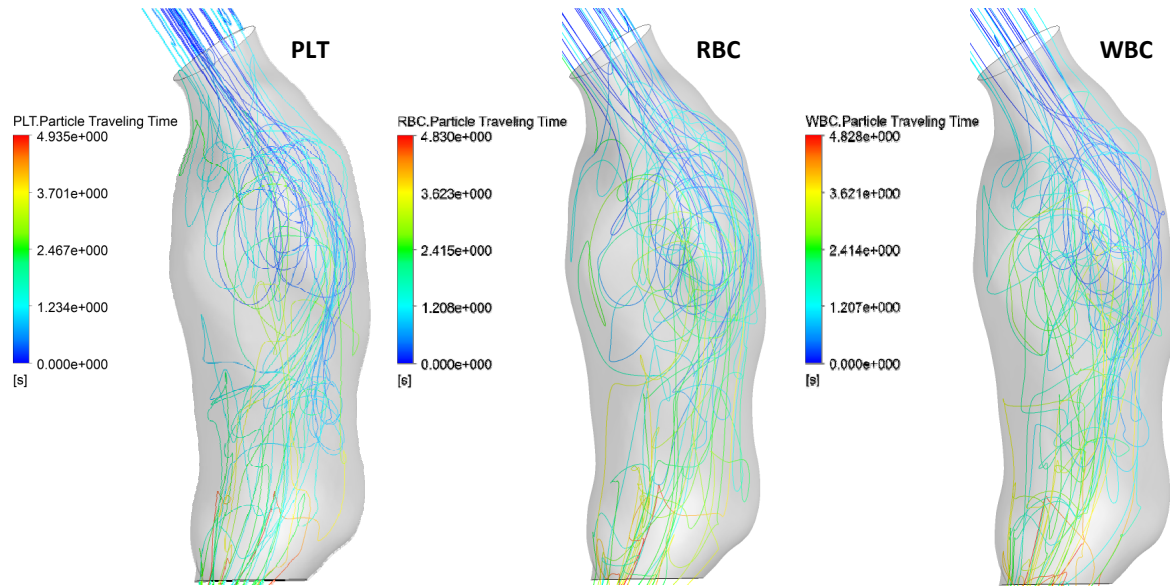


Figure 5.14: Transient particle trajectories that exit the AAA domain

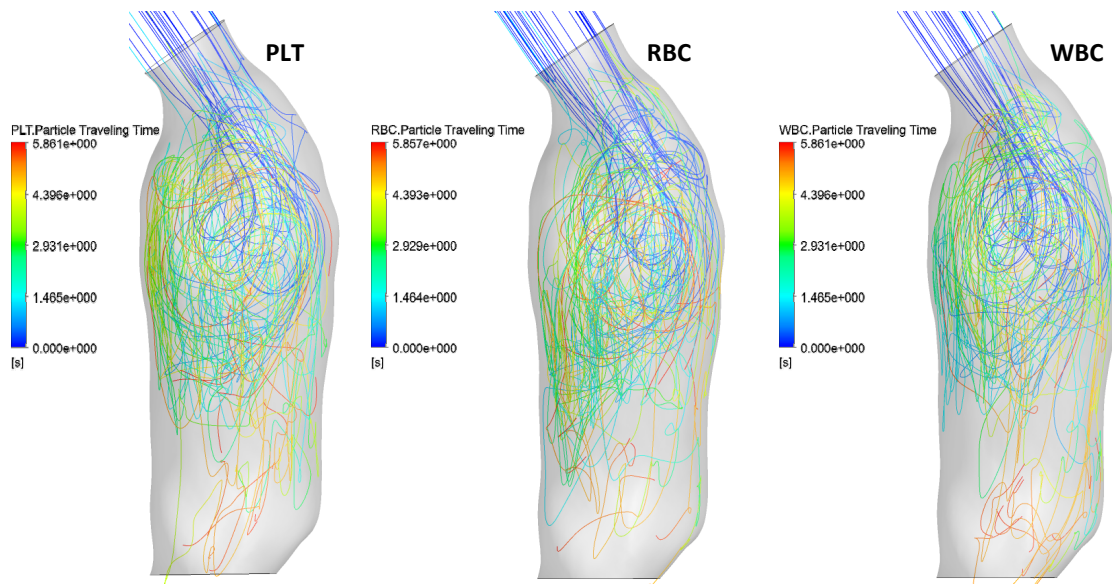
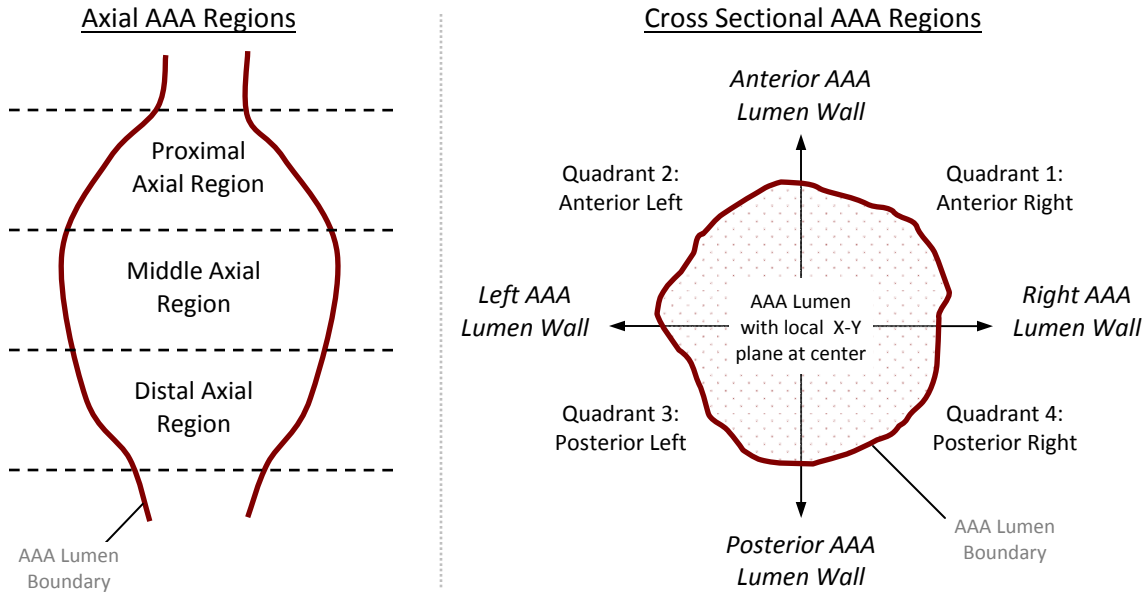


Figure 5.15: Transient particle trajectories that remain in the AAA sac

Comparing the trajectories in Figs 5.13-5.15 reveals apparent differences. The defining characteristic of particle trajectories remaining the AAA sac is the complete entrainment of the particle's in the circulatory flow fields. More specifically, while particles that exit the domain exhibit some circulatory motion, those that remain in the AAA sac have a larger circulation pattern that brings the particles very close to the posterior AAA lumen boundary. As the flow nears the posterior surface, the retrograde inflow and/or flow separation carries the particles towards the proximal region of the AAA sac and not the distal. Interestingly, the steady-state flow models also predicted particle entrapment in the proximal posterior region of the AAA lumen.

Individual trajectories of particles not exiting the AAA domain were processed with a custom Perl script in CFD Post v.12.1 (ANSYS Inc., Canonsburg, PA), and exported for further processing with several custom MATLAB routines (see Appendix VI for the Perl script and MATLAB functions). The MATLAB routines determined particle behavior near the AAA wall and in specific regions inside the AAA sac. Twelve regional zones were constructed based on the axial and cross-sectional positions inside the AAA sac. Figure 5.16 illustrates the different regions and lists their corresponding numerical identifier, where the bold, dark red lines represent the AAA lumen boundaries. The region numbering system used a counterclockwise iteration of the numbers where quadrant one of the proximal region was the unity and quadrant four of the distal region as twelve.



| <u>Region Number</u> | <u>Spatial Description</u> | <u>Region Number</u> | <u>Spatial Description</u> | <u>Region Number</u> | <u>Spatial Description</u> |
|----------------------|----------------------------|----------------------|----------------------------|----------------------|----------------------------|
| 1 | Proximal Anterior Right | 5 | Middle Anterior Right | 9 | Distal Anterior Right |
| 2 | Proximal Anterior Left | 6 | Middle Anterior Left | 10 | Distal Anterior Left |
| 3 | Proximal Posterior Left | 7 | Middle Posterior Left | 11 | Distal Posterior Left |
| 4 | Proximal Posterior Right | 8 | Middle Posterior Right | 12 | Distal Posterior Right |

Figure 5.16: Spatial regions of the AAA sac with their numbering system

A near-wall region was defined as 1mm from the AAA lumen's minimum circular radius extending from the axial position's local centroid. Figure 5.17 illustrates the cross-sectional and three-dimensional views of the near wall region.

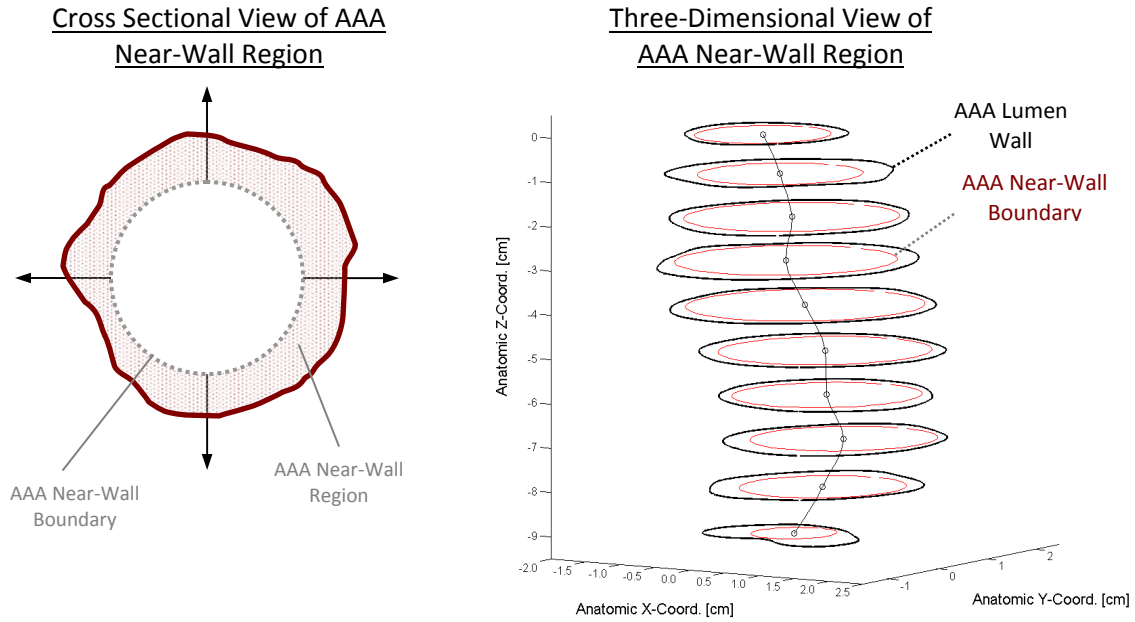


Figure 5.27: Cross-sectional and three dimensional views of the AAA near-wall region

The number of particles, regional particle residence time, and particle shear stress loads were calculated in the near-wall portion of each region for each particle entering the corresponding region and remained in the AAA sac after the four periods of pulsatile flow.

The transient movement of particles in and out of the near-wall regions of the AAA sac is represented by the number of particles in the near-wall regions at the end of the four periods of pulsatile flow following the particle injection. Figure 5.18 plots the number of particles in each region at the time points of 2.4, 3.6, 4.8, and 6.0 seconds.

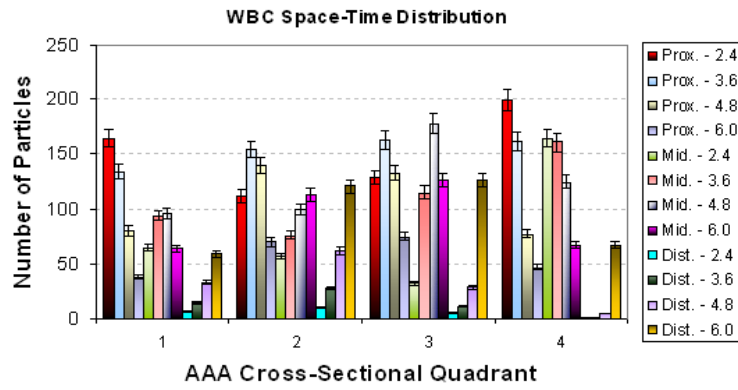
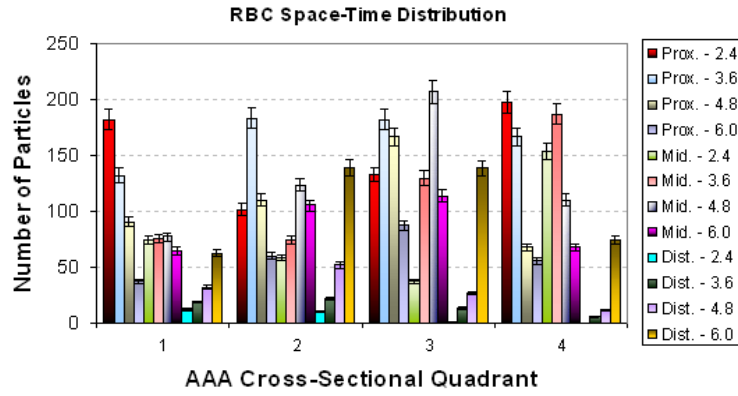
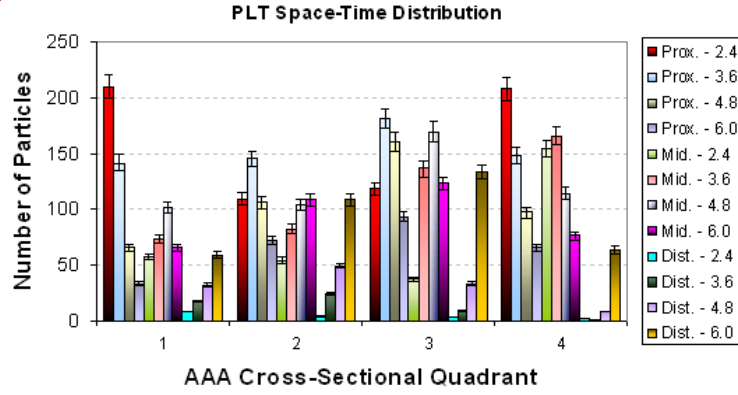
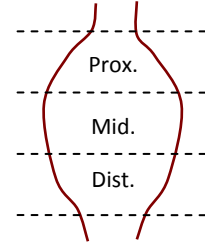
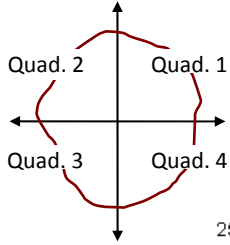


Figure 5.18: Number of particles in each near-wall region at 2.4, 3.6, 4.8, and 6.0 seconds (error bars = ±5%)

A three-dimensional visualization of the near-wall particle transport is depicted in Fig. 5.19, where the PLT particles are shown as points throughout a wireframe of the AAA sac.

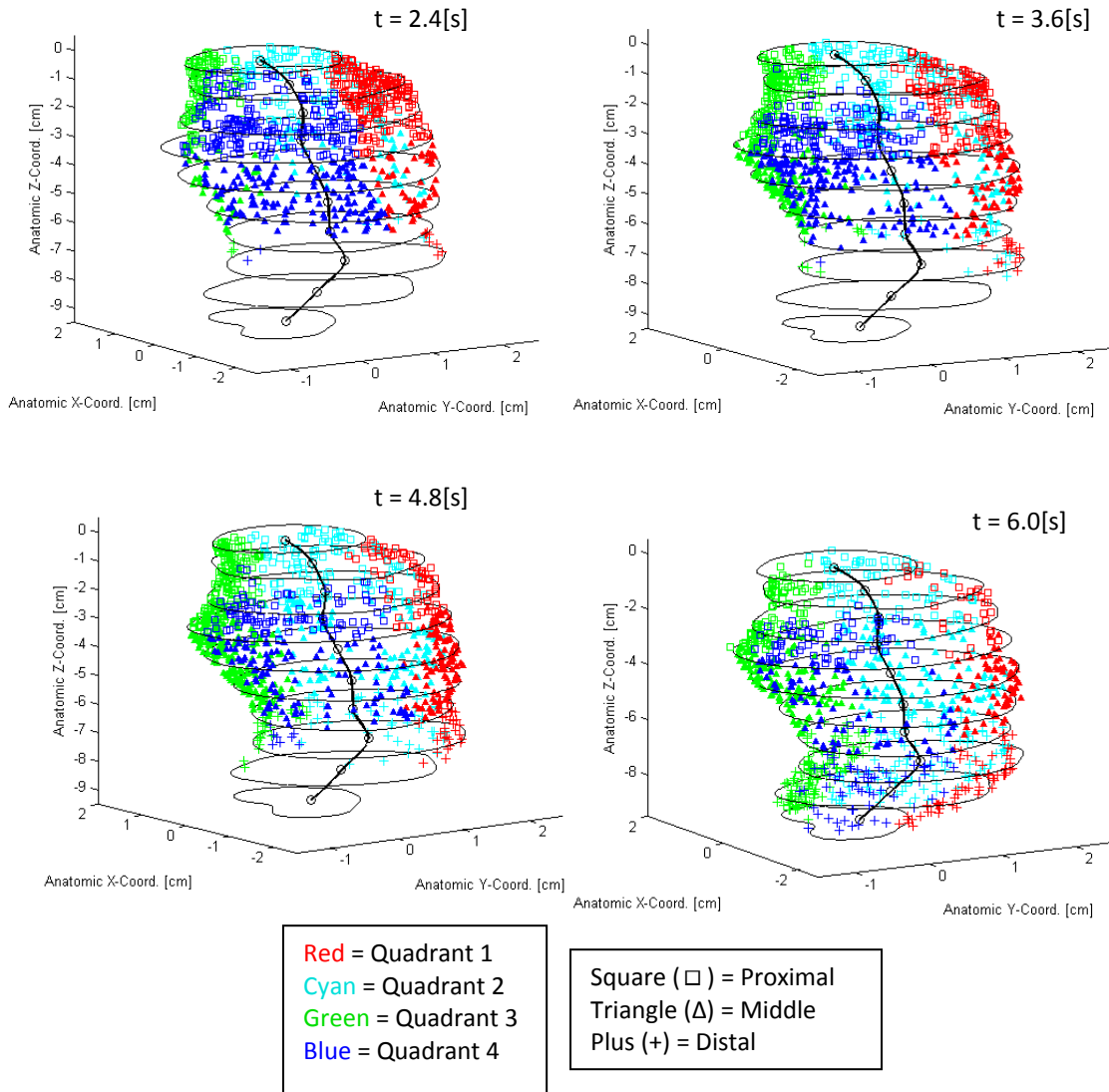


Figure 5.19: Near-wall particle distribution throughout the AAA sac at 2.4, 3.6, 4.8, and 6.0 seconds

Figures 5.18 and 5.19 depict a clear progression of particles leaving the proximal near-wall regions and entering the middle and distal near-wall regions with increasing time. Despite the

continued trend, particles were still present in the proximal AAA region at the end of the four pulses, *revealing the potential of particles to be entrapped in the AAA domain*, where they may contribute to the formation/growth of ILT. Spatial distributions of particles in each of the quadrants and regions exhibited some dependence on time and particle type. However, the general behavior and number of particles in each region were similar and most of the increases or decreases in regional particle presence over time were observed in all three particle types.

Particle Shear-Stress Loads. Biasetti et al. (2010) showed that AAA flow fields are notably different than those in healthy abdominal aortas, and particles that remain in the AAA sac for extended periods of time have increased exposure to the AAA's pathologic flow conditions. To assess the potential of shear-induced clotting and inflammatory activity of the PLTs and WBCs caused by the AAA hemodynamics, the shear stress acting on the surface of near-wall PLTs and WBCs was calculated according to Eq. (5.5). Figure 5.20 contains box-and-whisker plots that depict the shear stress on all PLTs and WBCs remaining in the AAA sac after the four simulated pulse over the final three periods of pulsatile flow. The figure illustrates the periodic loading of all particles and the wide variation of particle loading throughout the AAA sac. Each vertical collection of data represents all particle shear stress magnitudes at a single point in time. The horizontal red line is the median of the sample, the blue box outlines the upper and lower quartiles of the sample, and the vertical bars extending from the boxes represent 1.5x the interquartile range. Red + signs represent data points that lie outside the range of the vertical bars.

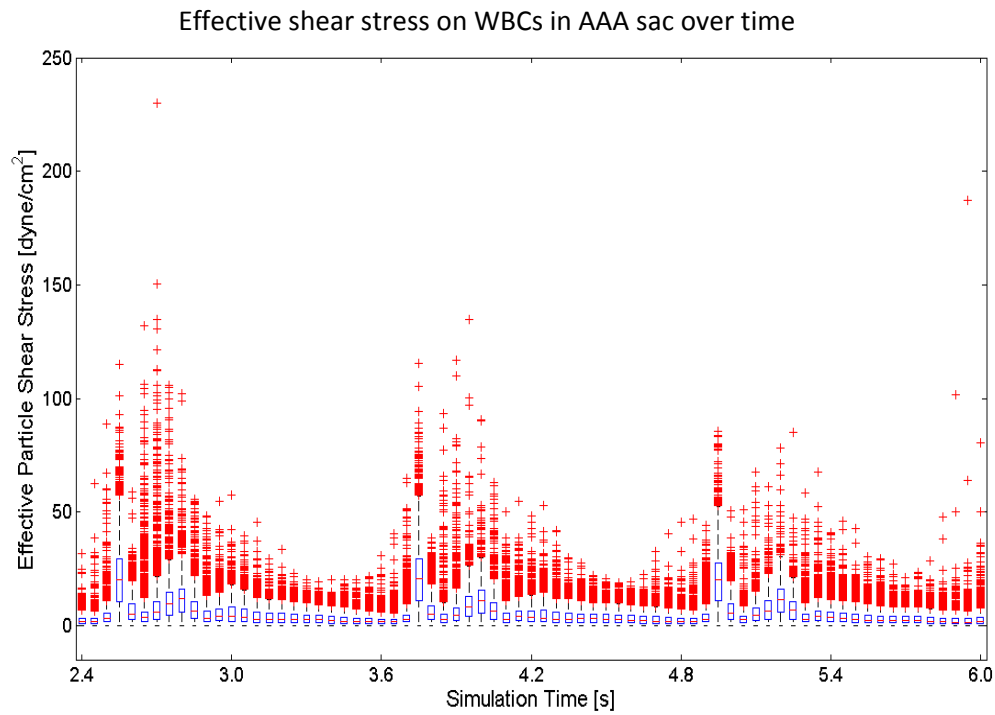
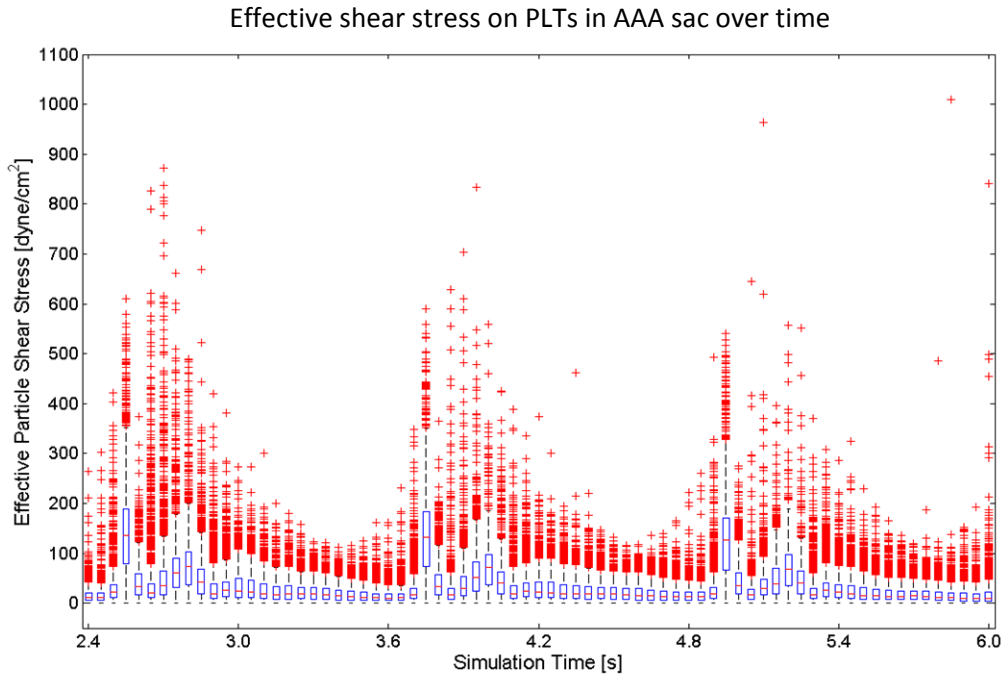


Figure 5.20: Shear stress on the PLTs and WBCs in the AAA sac from 2.4 to 6.0 seconds

The sample trends illustrated in Fig. 5.20 clearly show a dependence on particle type and time, where periodic shear loading is observed. Interestingly, the diastolic region of the inflow waveform corresponded with particle shear stresses less than 200 dynes/cm² for PLTs and less than 40 dynes/cm² for WBCs. Thus, conditions of potentially elevated shear stress may be followed by lower shear, which Sheriff et al. (2010) showed that once PLTs are activated by fluid shear stresses at or above 60 dynes/cm² for 40s, they become highly sensitive to subsequent low shear values. Specifically, they found if PLTs were previously exposed to elevated shear stress magnitudes for brief (less than one minute) periods of time, they activate at least twenty times faster in subsequent low shear conditions. Shankaran et al. (2003) found that platelets exposed to fluid shear stresses at or above 80 dyne/cm² were sufficiently activated and that platelets expressed stages of coagulation within 10s of shear stress exposure. Hence, the shear loads in the total AAA sac may lead to shear-induced activation of PLTs, which would thus begin forming the fibrin mesh necessary for ILT formation and growth. The shear stress loads in the near-wall regions of the lumen are thus crucial for determining potential activation states of PLTs and WBCs near the wall. Figure 5.21 plots the time-averaged shear stress magnitudes of PLTs and WBCs in each of the previously introduced, near-wall regions of the AAA lumen. The box-plot format is again used to illustrate the range of each sample set and similar to Fig. 5.20, the horizontal red line is the median of the sample, the blue box outlines the upper and lower quartiles of the sample, and the vertical bars extending from the boxes represent 1.5x the interquartile range. Red + signs represent data points that lie outside the range of the vertical bars.

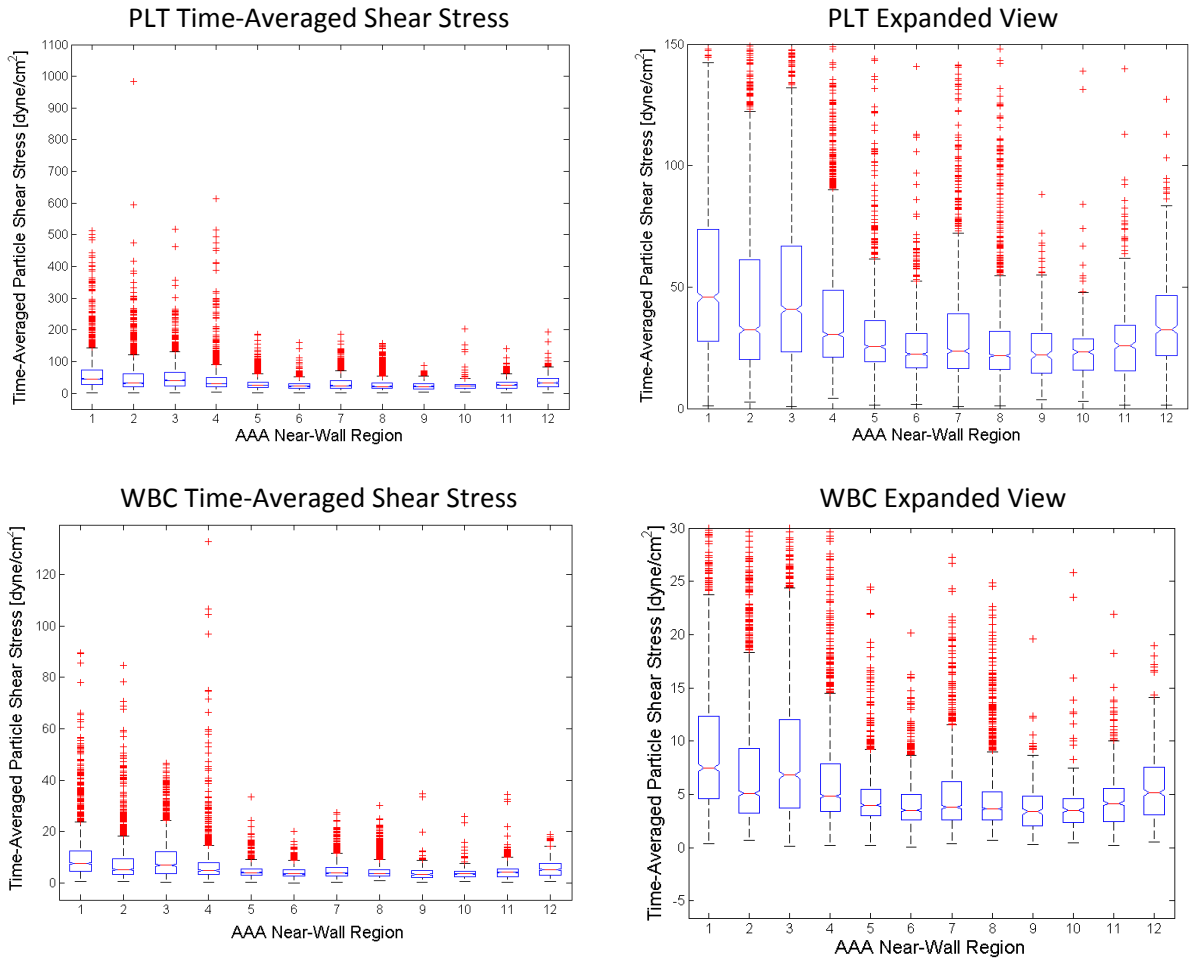


Figure 5.21: Time-averaged particle shear stress magnitudes in the near-wall regions of the AAA lumen

The outlier points of Fig. 5.21 reveal that the proximal and middle AAA regions exhibit larger maximum shear stress loads than the distal region. Such an observation further supports the hypothesis that particles have a greater potential to be activated and/or sensitized in the proximal AAA regions, where upon reaching the distal region, they elicit the thrombogenic cascade.

Due to the novel use of Eq. (5.5) to predict shear stress magnitudes on micron particles, the numerical values were compared against the spatially-averaged wall shear stress equation of Stokes flow around a sphere. Equations (5.8a-d) describe the shear stress on the surface of the sphere in spherical coordinates (see Panton, 2005):

$$\begin{aligned}
 \tau_{r\theta} &= \frac{3}{2} \mu \frac{U}{r_0} \sin(\theta) \left(\frac{r}{r_0} \right)^{-4} \\
 \tau_{rr} &= 3\mu \frac{U}{r_0} \cos(\theta) \left[\left(\frac{r}{r_0} \right)^{-4} - \left(\frac{r}{r_0} \right)^{-2} \right] \\
 \tau_w &= \tau_{r\theta}(\theta, r = r_0) \\
 \tau_w(\theta) &= \frac{3}{2} \mu \frac{U}{r_0} \sin(\theta)
 \end{aligned} \tag{5.8a-d}$$

where: U , μ , r_0 , r , and θ are the sphere velocity relative to the fluid, the fluid Newtonian viscosity, the sphere radius, the sphere's radial coordinate, and the sphere's azimuth coordinate, respectively. By taking the area average of the sphere's wall shear stress ($\tau_w(\theta)$) across the surface of the sphere, an effective value can be obtained to compare with the shear stress levels. Moreover, the sphere's velocity with respect to the fluid becomes the particle's slip velocity (v_p^r), the sphere's radius becomes the particle radius (r_p), and the Newtonian viscosity becomes an effective viscosity (η_{eff}) mimicking blood. Equations (5.9a-e) list the resulting equations, where Eq. (5.9d) lists the area averaged wall shear stress magnitude in terms of the particle and fluid parameters.

$$\tau_w(\theta) = \frac{3}{2} \eta_{eff} \frac{v_p^r}{r_p} \sin(\theta)$$

$$\tau_w|_{max} = \frac{3}{2} \eta_{eff} \frac{v_p^r}{r_p}$$

$$\tau_w|_{avg} = \frac{1}{A} \iint_S \tau_w(\theta) dA = \int_0^{2\pi} \int_0^\pi \tau_w(\theta) r^2 \sin(\theta) d\theta d\phi \quad (5.9a-e)$$

$$\tau_w|_{avg} = \frac{3\pi}{8} \eta_{eff} \frac{v_p^r}{r_p}$$

$$\tau_w|_{avg} = \frac{\pi}{4} \tau_w|_{max}$$

Table 5.3 lists the input parameters for WBCs and PLTs (that were extreme values in the simulation results) and the resulting shear stress values showing the values displayed in Figs. 5.30 and 5.31 are within reasonable limits set by the fluid-particle parameters.

Table 5.1: Particle shear-stress calculations for Stokes flow

| <u>Particle</u> | <u>Slip Velocity Range [cm/s]</u> | <u>Particle Radius [cm]</u> | <u>Effective Viscosity Range [g/cm/s]</u> | <u>Stokes Flow Shear Stress [dyne/cm²]</u> |
|-----------------|-----------------------------------|-----------------------------|---|---|
| PLT | 1x10 ⁻⁶ - 7.00 | 2x10 ⁻⁴ | 0.0309 - 0.1600 | 1x10 ⁻⁴ - 6600 |
| WBC | 1x10 ⁻⁵ - 4.10 | 12.5x10 ⁻⁴ | 0.0309 - 0.1600 | 2x10 ⁻⁴ - 620 |

5.2.3 Fluid-Particle Entrapment and Transit Time

Contours of the fluid's residence time distribution revealed an elevated increase of transit time in the AAA's distal region and unlike the steady residence time contours, localized elevated zones were present on both the anterior and posterior AAA lumen walls. Figure 5.22 plots the fluid's residence time distribution after five periods of pulsatile flow through the AAA domain.

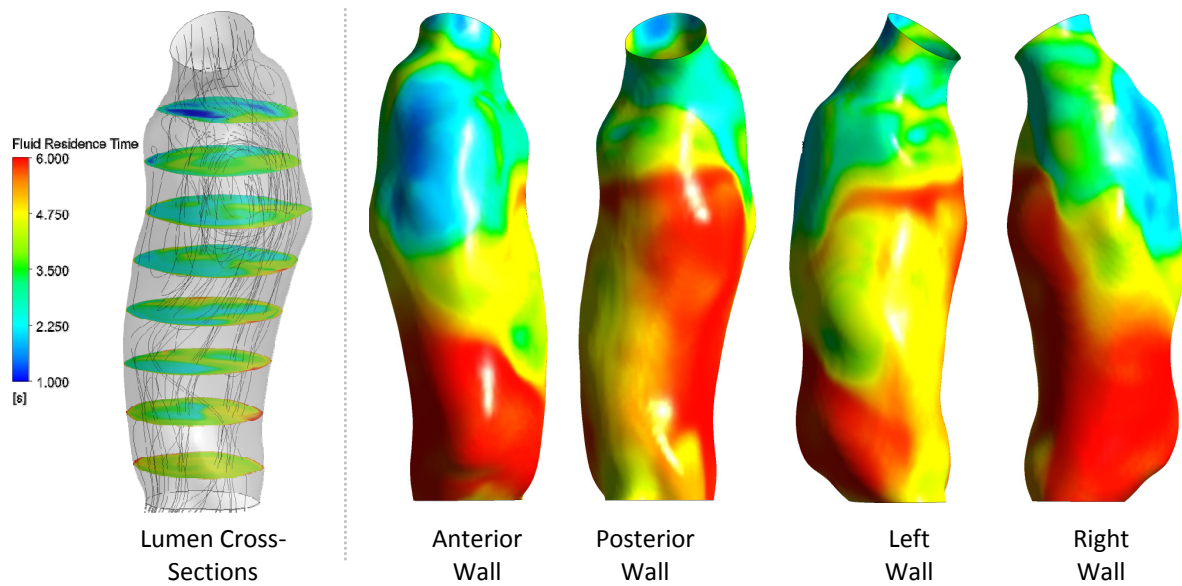


Figure 5.22: Fluid residence time distribution in AAA lumen along AAA wall after five periods of pulsatile flow

The flow recirculation in the proximal regions and shortened presence of antegrade flow in the AAA distal region are the main causes for the increase in fluid residence time. An important note is the fluid residence time predicts the lowest value for the anterior region of the AAA lumen wall where the incoming flow is predominantly directed. Despite the natural bulge which exists in the location, the WSS and OSI plots also confirm that the incoming flow is directed in such a way that negates the bulge's ability to cause flow separation and increased residence time. While the simulation only covers 6 sec., the steady and transient residence time results support the hypothesis that the AAA causes elevated regional transit times inside its domain, which may contribute to ILT formation and/or growth. The increased carrier fluid residence time can be extrapolated to suggest particles suspended in the region's flow also possess the same residence time if the particle Reynolds numbers are low, which is satisfied in the AAA sac. Moreover, the elevated wall deposition potential implied by the

transient fluid residence time distributions of the AAA distal region indirectly supports the hypothesis of ILT formation postulated by Biasseti et al. (2010). Specifically, an increased residence would increase the potential that PLTs and WBCs, after being exposed to the circulatory flows in the proximal AAA region, would collide with the distal AAA lumen wall.

Himburg et al. (2004) deduced that the magnitude of near-wall blood particle residence time is inversely proportional to the OSI and time-averaged WSS magnitude. Equation (5.10) lists their derived expression.

$$t_r^{OSI} \sim \left[(1 - 2 \cdot OSI) \cdot \frac{1}{T} \int_0^T |\bar{\tau}_w| dt \right]^{-1} \quad (5.10)$$

In the current case, the advantage of t_r^{OSI} over the fluid residence time distribution is its ability to calculate times greater than six seconds and has a more direct application to the suspended blood particles. Figure 5.23 illustrates the t_r^{OSI} contours, where the distal AAA region very localized regions of maximum residence times.

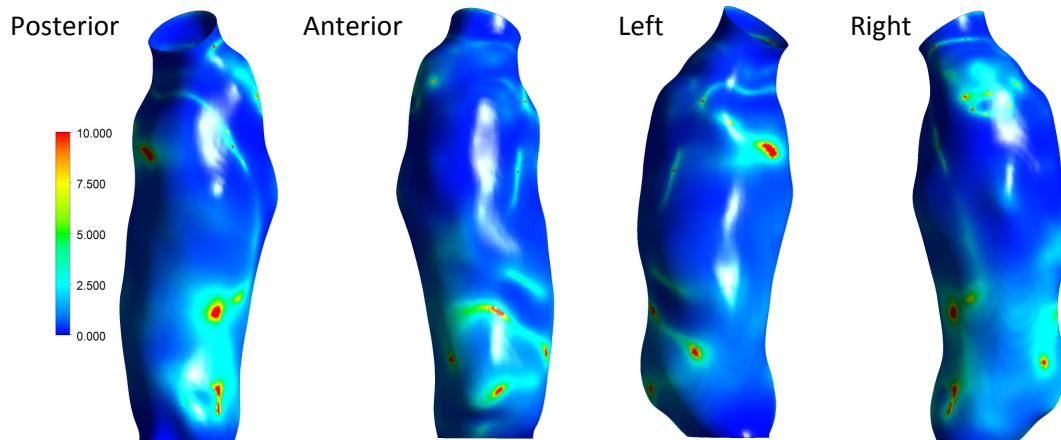


Figure 5.23: Relative near-wall residence time derived from OSI

A very interesting observation is that locations of $\max t_r^{OSI}$ have a similar appearance to the particle deposition locations in Fig. 5.13, which suggests increased particle deposition in regions of elevated near-wall time. Furthermore, the t_r^{OSI} maximum contours occur at specific locations that were not always the pinnacle of local expansions of the AAA lumen.

Regional near-wall particle residence times revealed elevated times in almost every region, where some particles that did not leave their original region for almost the entire simulation. The box-plots in Fig. 5.24 plot the distribution of regional near-wall transit times of all particles entering the appropriate region.

[See next page for Fig. 5.24]

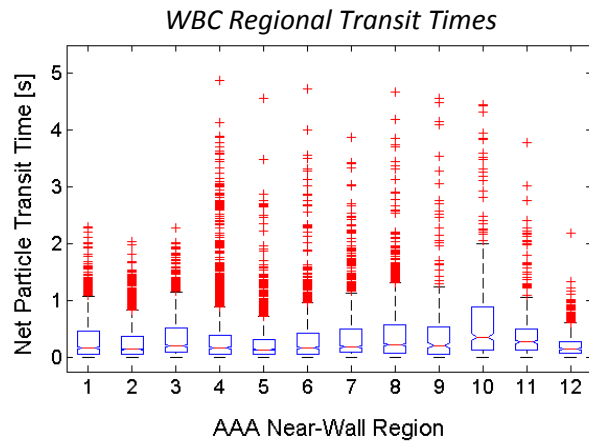
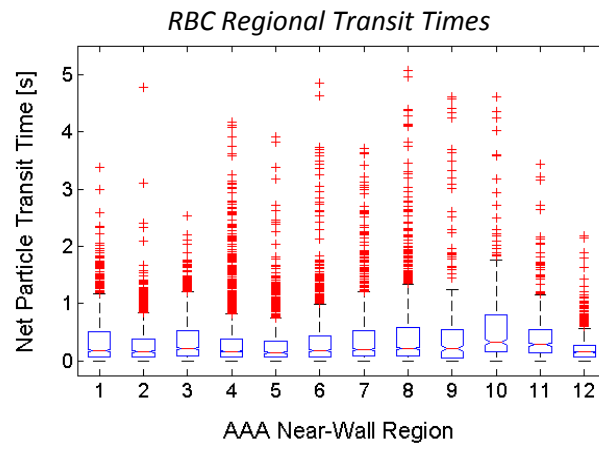
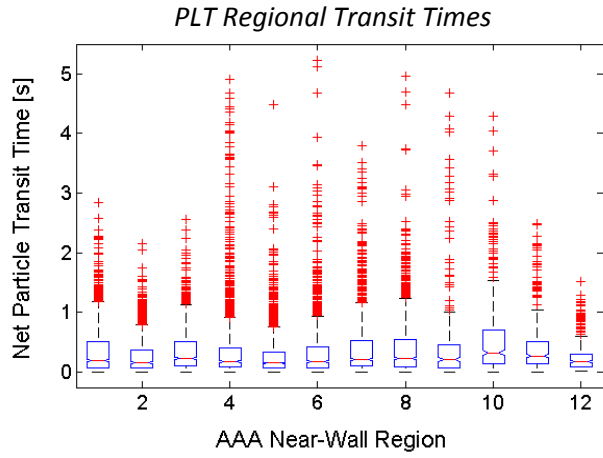


Figure 5.24: Regional distribution of particle near-wall residence times for PLTs, RBCs, and WBCs

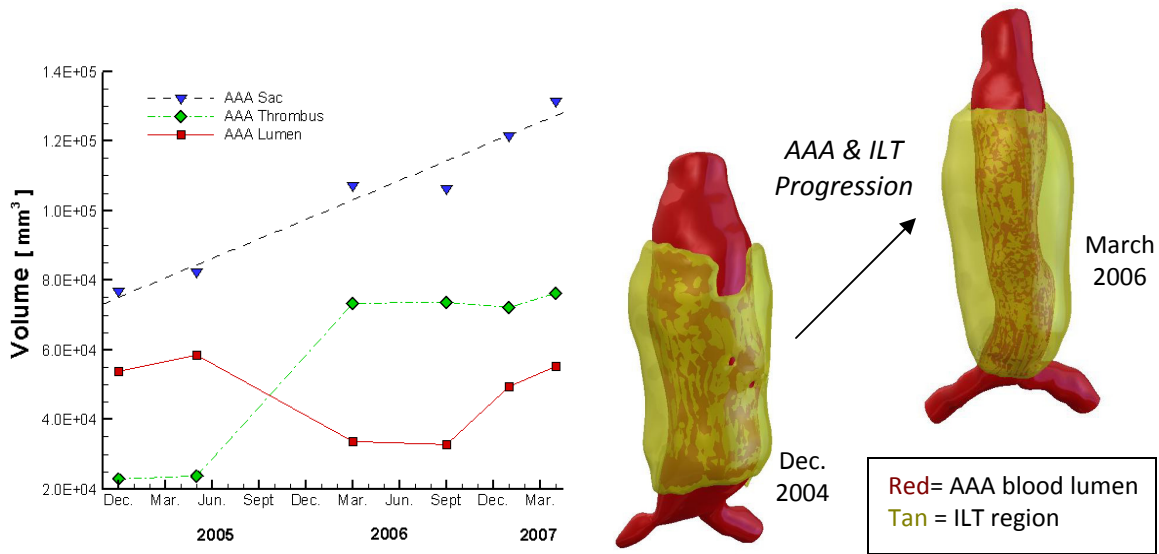
The plots in Fig. 5.24 reveal large distributions in times primarily due to differences in the normal thickness of each near-wall region. Despite the wide ranges, multiple regions have distributions that with a 95% confidence interval have statistically different mean values. Furthermore, while most particles exhibit regional transit times less than one second, a single activated platelet can lead to aggregation of numerous other particles and in-turn cause an “avalanche-like” effect of future platelet activation. The mere fact that a few particles of PLTs, RBCs, and WBCs have elevated transit times lasting nearly the entire simulation time gives credit to the underlying ILT formation hypothesis that AAAs provide appropriate conditions to entrap particles in near wall regions, where if activated, could contribute to ILT formation and/or growth.

5.3 Potential Regions of Intraluminal Thrombus Development in Relation to Particle Transport and Entrapment

The particle-hemodynamics simulations of PLTs, RBCs, and WBCs in the AAA domain revealed localized regions of enhanced fluid and particle residence time. Comparing the regions of the elevated residence time, oscillation, and particle deposition of the current AAA lumen with future regions of ILT development in the current lumen geometry reveal a qualitative correlation between previous particle-hemodynamics and future ILT development. Specifically, the localized regions of elevated t_r^{OSI} had a strong correlation with particle deposition locations, which all occurred along regions of future ILT development. Local particle residence times in twelve different spatial, near-wall regions revealed an anisotropic distribution of maximum particle residence times and support the hypothesis that

particles can become entrapped in the AAA domain. Shear stress calculations were then completed and revealed that PLTs in particular experienced high levels of shear stress at both the near-wall and throughout the AAA lumen. Moreover, the maximum time-averaged shear stress of the particles was observed to generally be greater in the proximal and middle AAA regions when compared to the distal AAA region. Experimental studies by Sheriff et al. (2010) and Raz et al. (2007) revealed sufficient platelet activation under shear stresses of similar magnitude and extended duration. However, Wurzinger et al. (1985) showed that brief exposures to elevated shear stress magnitudes of even a few milliseconds can lead to platelet activation. These experimental and current computational results support the hypothesis presented by Biasetti et al. (2010) that shear-induced activation of blood particles causes thrombogenic and inflammatory response in the proximal portions of the AAA sac, and may begin fibrogenesis upon reaching the posterior AAA region. Furthermore, the study's computational results of elevated residence times support the hypothesis that AAA sac entraps blood particles, which play a role in ILT formation and/or growth. Figure 5.25 attempts to provide a unifying illustration of the patient's AAA geometries over time and relations between ILT formation and particle hemodynamics. Figure 5.25a plots the time history of the patient's AAA domain and Fig. 5.25b depicts a cut-away view of the patient's future AAA geometry with fully-developed thrombus and identifies specific regions that qualitatively correlate with the fluid-particle hemodynamics parameters.

(a) Time history of AAA and development of ILT



(b) Qualitative relation between AAA sac particle-hemodynamics and future ILT development and/or growth

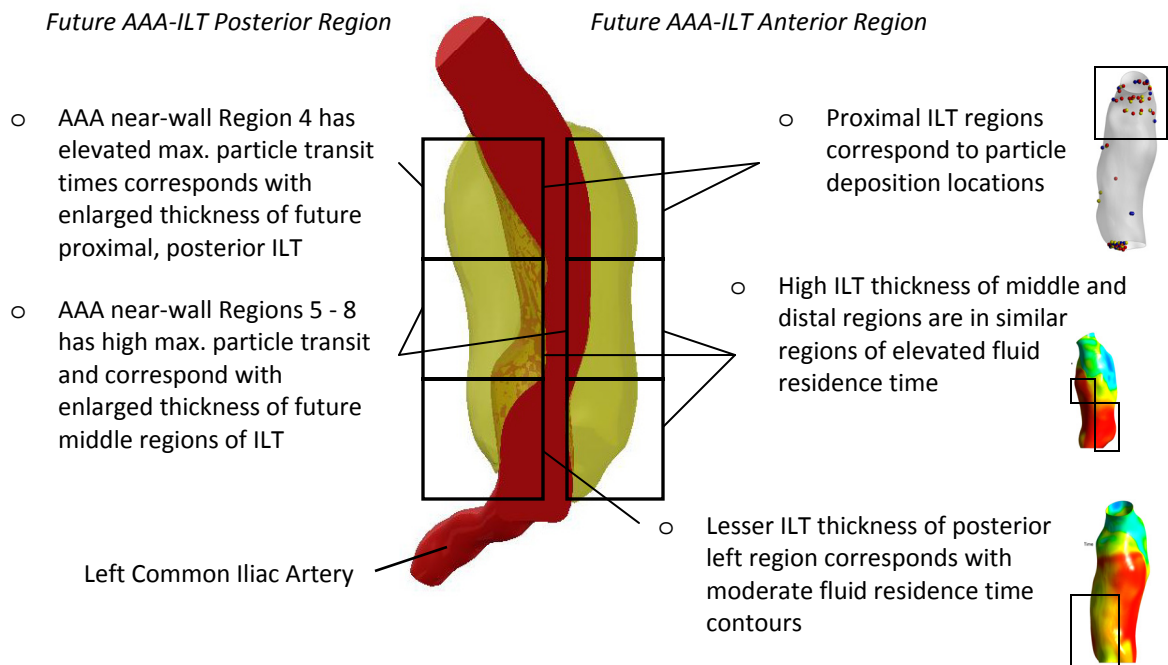


Figure 5.25: (a) History of AAA and ILT development and (b) Qualitative correlation between future ILT presence and previous AAA particle-hemodynamics

5.4 Conclusions

The previous chapter described a novel particle-hemodynamics computational analysis of blood particle transport and shear stress loading in the AAA sac. The results of enhanced particle residence time and elevated shear loads at near-wall regions of the AAA sac support the hypotheses: i) that a patient's AAA particle-hemodynamics have the potential to entrap blood particles, which will play a role in ILT formation and/or growth and ii) platelets and white blood cells may experience shear-induced activation in the proximal regions of the AAA sac, where upon reaching the distal regions induce a thrombogenic and inflammatory response. Thus, the completed simulations are the first computational demonstration providing sufficient evidence that that transient AAA particle-hemodynamics play a role in ILT formation and growth.

Chapter 6:

Steady and Transient Particle- Hemodynamics of Hepatic Arterial Systems

6.1 Computational Simulation Parameters

ANSYS CFX v.12.1 (Canonsburg, PA) was used to numerically solve the equations listed in Ch. 2 using the hepatic artery and SMC computational meshes described in Ch.3. The transient, iterative solution procedure employed constant time-steps of 2.00×10^{-3} s and continued until RMS mass and momentum maximum residuals were less than 5.0×10^{-6} .

Inflow/Outflow Waveforms. A significant number of transient waveforms were constructed in Ch. 4 for the many hepatic artery simulations. Flow rate waveforms were

implemented as spatially averaged, time-dependent velocities at the inlet surface and time-dependent mass flow rates at the outlet locations. Pressure waveforms were implemented as spatially-averaged, time-dependent entrainment pressures at the domain outlet surfaces. Figures 6.1a-c illustrate the multiple hepatic artery domains with their respective gravity vector and the waveforms implemented at each domain inlet/outlet.

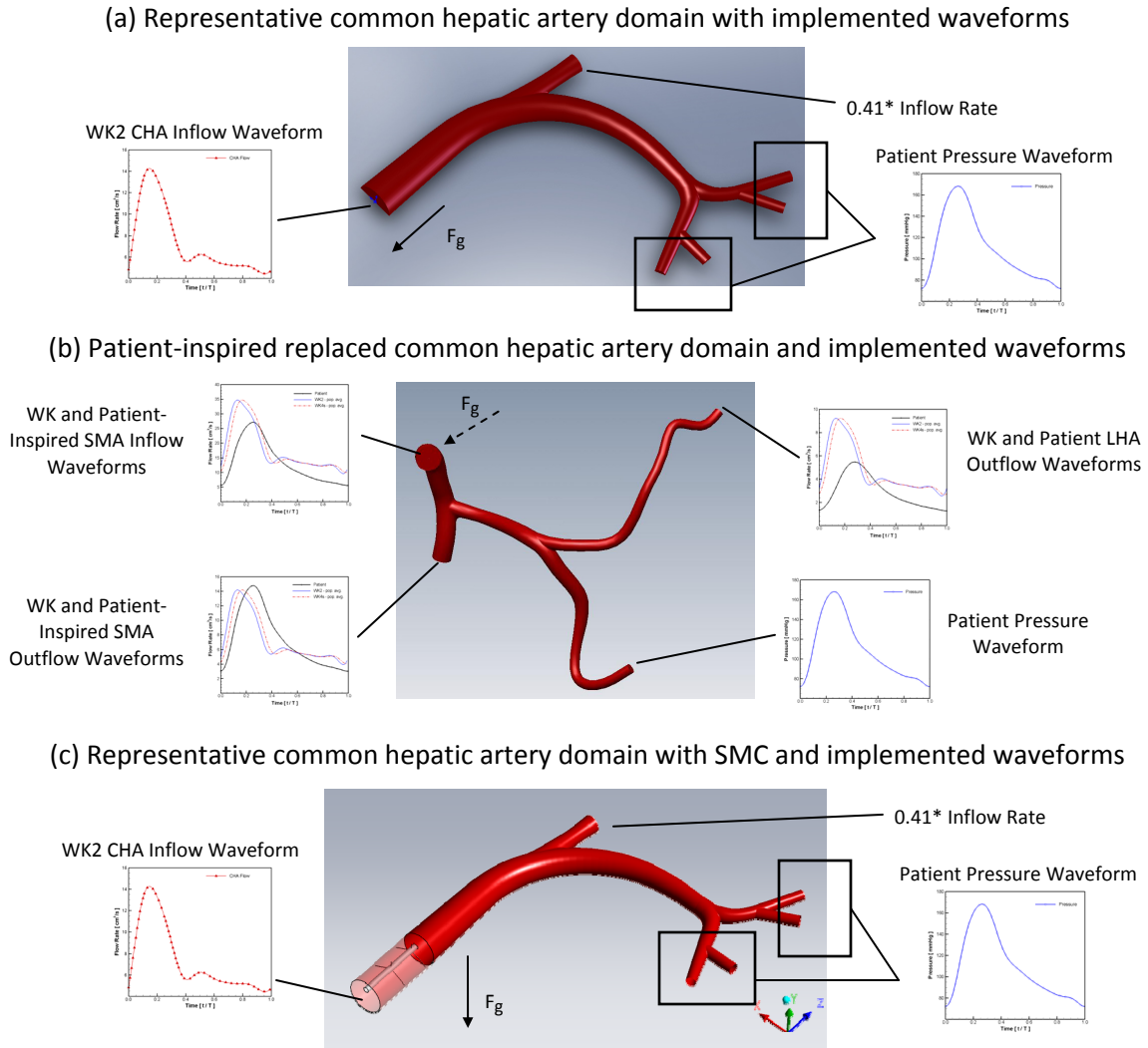


Figure 6.1: (a) Representative common hepatic artery domain with implemented waveforms, (b) Patient-inspired replaced common hepatic artery domain with implemented waveforms, and (c) Representative common hepatic artery domain with SMC attachment and implemented waveforms

The dashed gravity vector of the patient-inspired geometry symbolizes that the vector is protruding from the two-dimensional plane towards the viewer (normal to the inlet boundary plane). Parabolic velocity profiles based on the time-dependent average velocity from the inflow waveforms were specified at the domain inlets and no-slip boundary conditions were enforced along each of the arterial and catheter geometry walls. The walls and SMC surfaces remained stationary throughout all simulations. Transient results were recorded every 0.05s and a maximum number of twenty iterations per time-step was implemented, which was sufficient to achieve solution convergence.

Microsphere Particles. Spherical particle representing SIR-Spheres® and TheraSpheres® were injected into the computational domain at the domains' inlet surface or at the terminal end of the SMC with zero-slip velocity and a bulk mass flow rate equaling the spatially-averaged carrier fluid mass flow rate at the injection boundary. All particles were injected with a uniform, equally spaced distribution across the injection surface, and each particle type had the same number of injected particles over time. The particle injection rate was specified as either a constant number of particles per unit time or by multiplying a local concentration by the fluid's transient bulk mass flow rate. Particle characteristics were selected to match the diameter ranges and density listed in Table 1.3, where the particle diameter range was treated as a normal distribution across the max. and min. diameter with the specified mean diameter and the standard deviation. Thus, the Eulerian-Lagrangian model included influences of different particle diameters on the Lagrangian particles' trajectory. Wall restitution coefficients of the arterial walls were set to one, not allowing any particle deposition on the walls (following clinical outcomes of Y⁹⁰-microsphere therapy).

Simulation Times. Prior to injection of the particles, three periods of pulsatile flow were simulated in the hepatic domains. The three-period fluid-only solutions of each domain were solved on multiple workstations. The three initial periods of the symmetric, representative hepatic artery geometry (Fig. 6.1a) were run on a single core of a 64-bit Dell T7400 Precision workstation with eight cores and 16GB of RAM and required approximately 72.9 hrs of total run-time. The patient-inspired geometry's (Fig. 6.1b) three initial periods were run on 10 processors of a 64-bit remote Linux cluster (henry2 cluster at hpc.ncsu.edu) and took an average of 26.3 hrs per pulse, resulting in an average net running time of 78.9 hours per waveform data set. The SMC representative hepatic artery geometries (Fig. 6.1c) were run on three different workstations: 10 processors on a 64-bit remote Linux cluster (henry2 cluster at hpc.ncsu.edu), a 64-bit Dell T3500 Precision workstation with a quad core Intel Xeon E5520 processor at 2.27GHz and 12GB of RAM, and a Dell T7400 Precision workstation with eight cores and 16GB of RAM. The average simulation time per pulse was 28.2, 40.9, and 45.4 hrs for the Linux cluster, Dell T3500, and DellT7400, respectively.

Transient Initial Conditions. Subsequent to the fluid-only solution, particles were injected over regions of a single pulse. The majority of injected particles exited the domains during this one pulse, so only one pulse with particle transport was simulated. All of the fluid-particle simulations were conducted on three workstations: a 64-bit Dell Precision 670 Workstation with four Intel Xeon processors at 3.59GHz and 8GB of RAM, a 64-bit Dell T3500 Precision workstation with a quad core Intel Xeon E5520 processor at 2.27GHz and 12GB of RAM, and a Dell T7400 Precision workstation with eight cores and 16GB of RAM. The fluid-particle simulations for the symmetric hepatic artery domain were primarily run on

four processors of the Dell 670 Workstation and required an average of 38.2 hours for each fluid-particle simulation. The patient-inspired geometry's fluid-particle simulations were primarily run on six processors of the Dell T7400 and required an averaged of 57.6 hours for each fluid-particle simulation (one simulation was run on four processors of the Dell T3500 and required 45.2 hours). The SMC hepatic artery geometries were run on six processors of the Dell T7400 and four processors of the T3500 machines with an average run-time of 52.5 and 50 hours, respectively.

6.2 Steady Particle-Hemodynamics of a Representative Hepatic Artery System based on Mean Clinical Flow Conditions

6.2.1 Flow Distribution and Local Flow Fields

Basic steady-state simulations on the mid-plane symmetric, representative geometry were first run to gain physical insight on the physics governing particle transport in the hepatic arteries. A large Reynolds number of 1150 was first used to simulate maximum flow conditions in the laminar regime and constant downstream pressures of 100mmHg and 120mmHg were applied to the outlet boundaries. As expected, downstream resistance proved to have a pivotal role on the local velocity field and overall flow distribution. Specifically, a 20% increase in the outlet pressure of the branching vessel (whose centerline is less than 5 degrees from the parent vessel centerline) resulted in a flow reduction greater than 70% through the branch vessel. Figures 6.2a,b plots the flow distributions through the domain outlets and the symmetry plane velocity fields, where the global flow percent is the

percentage of the domain inflow and the local flow percent is the percent of the flow actually delivered to the daughter vessels.

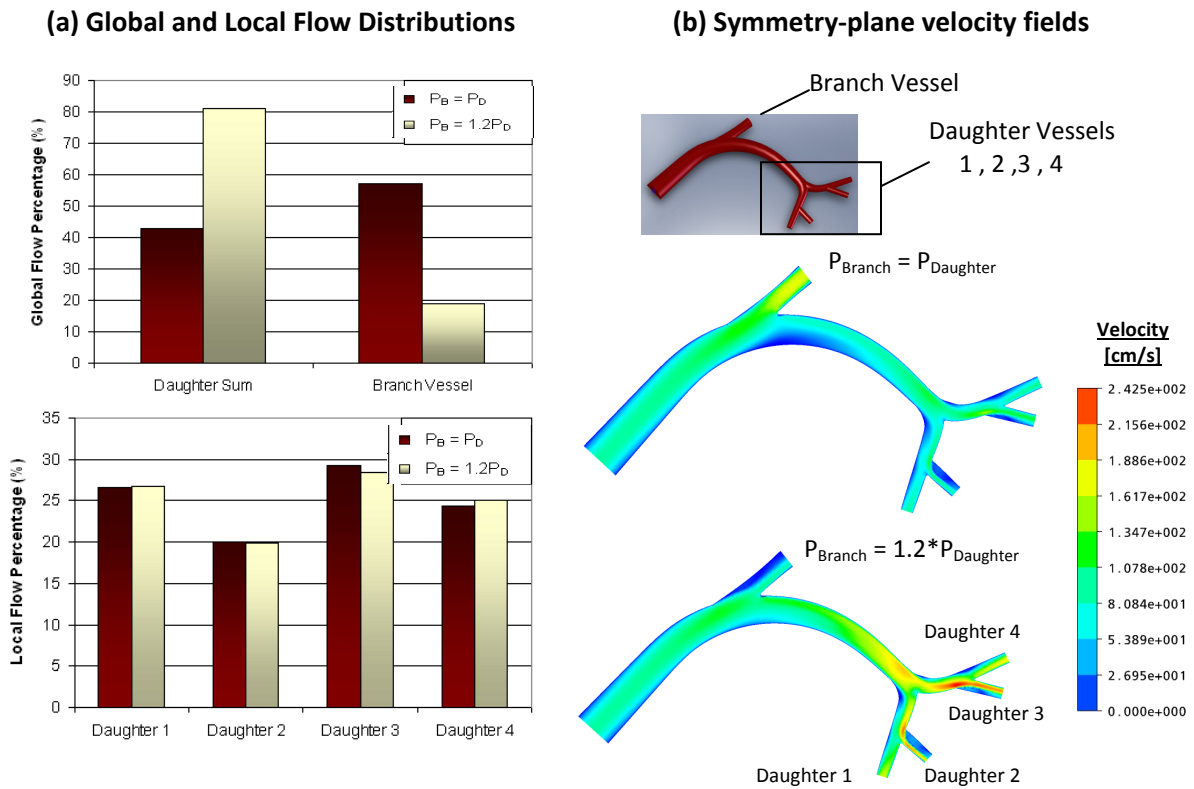


Figure 6.2: (a) Flow distributions and (b) Symmetry-plane velocity fields at steady Reynolds number of 1150

The influence of physiologic inflow magnitudes on the domain's flow conditions was assessed by computing the flow distributions under inflow Reynolds numbers of 328, 470, and 563 with constant pressures or mass flow rates. To represent physiological hepatic nomenclature, the branch vessel is referenced as the GDA and the outflow condition was varied as constant pressure of 100mmHg or 0.41 times the inflow magnitude after the flow distribution values reviewed in Chapter 4. Figure 6.3 plots the flow distributions of the various inlet and outlet conditions revealing noticeable differences in global distributions of

the net daughter vessels and GDA vessel, but only subtle differences between local flow distributions of the different daughter vessels.

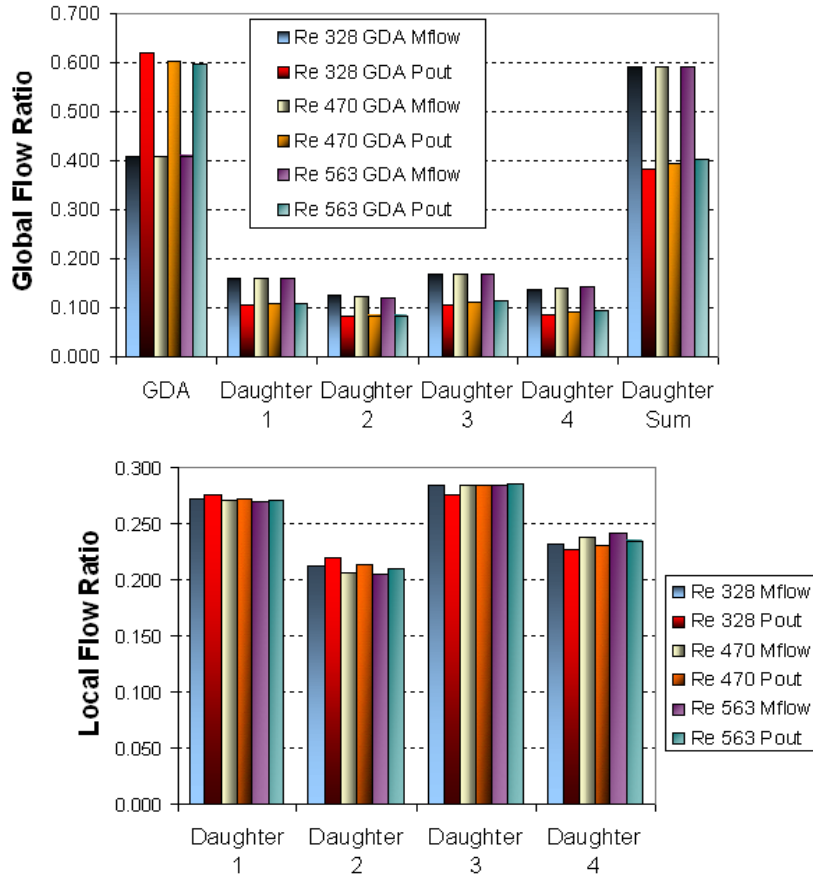


Figure 6.3: Global and local flow distributions under steady physiologic inflow magnitudes

The previous simulation results suggest that while global flow distribution is strongly influenced by downstream resistance, the influence of inflow magnitude on global distribution is diminished. Furthermore, redirecting more flow to the daughter vessels (either due to increased inflow or increased downstream resistance to the GDA / branch vessel) did not result in drastic changes in local flow distribution amongst the different daughter vessels.

The important deduction is that local flow distributions will be primarily determined by local vessel morphologies and the downstream resistance of the local vessels.

6.2.2 Particle Transport and Specific Daughter Vessel Targeting

Ten-thousand particles of 32 μ m in diameter and twice the density of the carrier fluid were released at the inlet plane and a plane past the primary branch bifurcation to analyze their behavior and terminal locations. Particles were injected with a zero-slip velocity in a carrier fluid with an inlet Reynolds number of 1150. Parabolic and uniform spatial dispersions at the injection plane were tested to see if particle exit fractions showed any dependence on spatial dispersion. Figure 6.4 depicts the release positions and distributions of the particles with the corresponding global exit fraction.

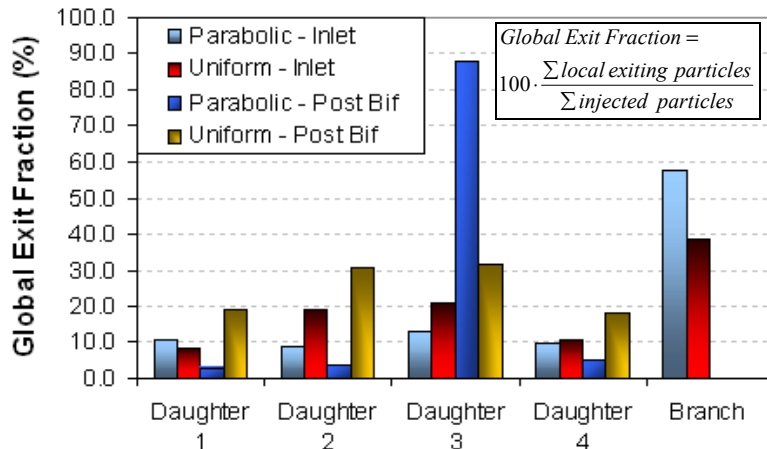
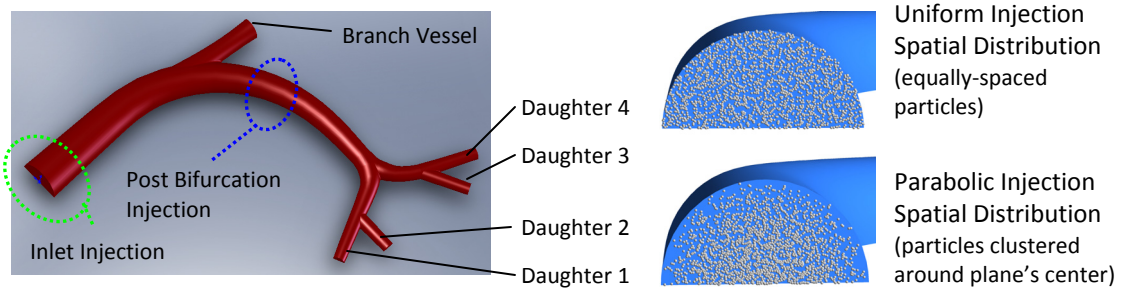


Figure 6.4: Particle global exit fractions of those injected at the domain inlet and past the bifurcation

Due to the absence of retrograde flow, all particles release downstream the bifurcation were delivered to the daughter vessels as seen in the bar graph in Figure 6.4. Hence, the axial position of particle injection is shown to be an important parameter influencing the efficacy of intra-arterial microsphere delivery. The spatial dispersions at both the inlet and post bifurcation injection positions also exhibited noticeable influences on the global exit fractions of particles exiting the daughter vessel, *suggesting that the cross-sectional release position of the particle has a paramount influence on its terminal location*. To verify a potential correlation between cross-sectional position and exit location, particle release maps were constructed at the particle injection planes. The release maps plot the cross-sectional position of each particle that exits the domain, where different exit locations are differentiated by different symbols or colors. Figure 6.5 plots the particle release maps for the inlet and post bifurcation injection planes (see Fig. 6.4).

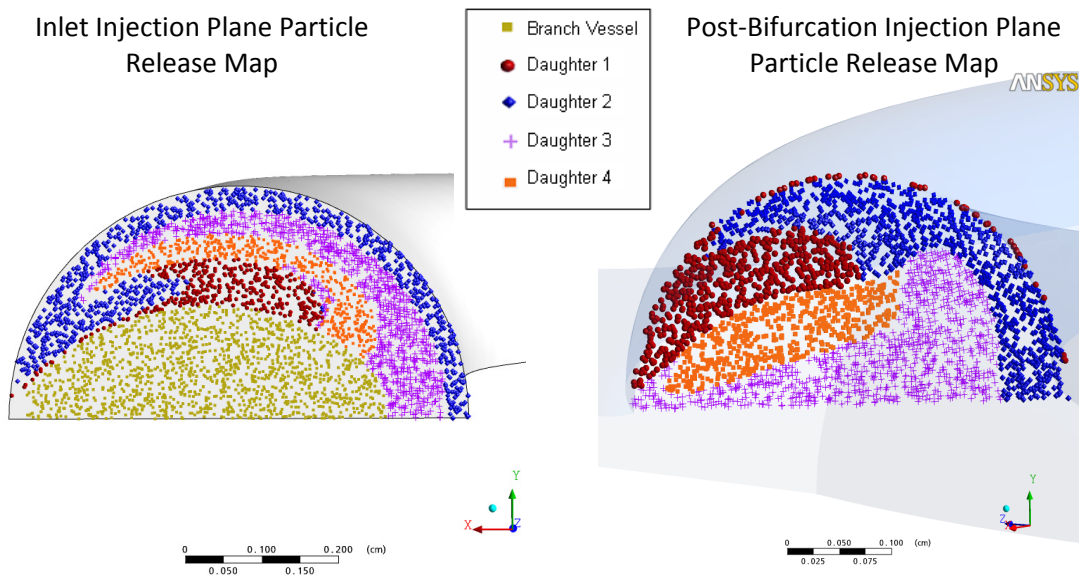


Figure 6.5: Particle release maps of different injection planes under steady flow

Coinciding with the varying exit fractions depicted in Fig. 6.4, organized cross-sectional regions of particles exiting a specific boundary are apparent in the particle release maps. The maps also explain why the branch vessel and daughter 3 vessel receive larger exit fractions for parabolic injection dispersions at the inlet and post-bifurcation planes, respectively. Since the center of each plane is associated with the branch vessel or daughter vessel three, the parabolic dispersion's increase of particles towards the center of the plane injects a greater percentage of particles in zones that correspond to the aforementioned downstream vessels. To assess the potential influence of vessel downstream resistance on the particle release map, the pressure of the branch vessel was increased by 20% (which reduces the outflow through the vessel by more than 70%) and particles were injected at the inlet injection plane. Figure 6.5 illustrates the smaller release zone for the branch vessel when its downstream resistance is increased.

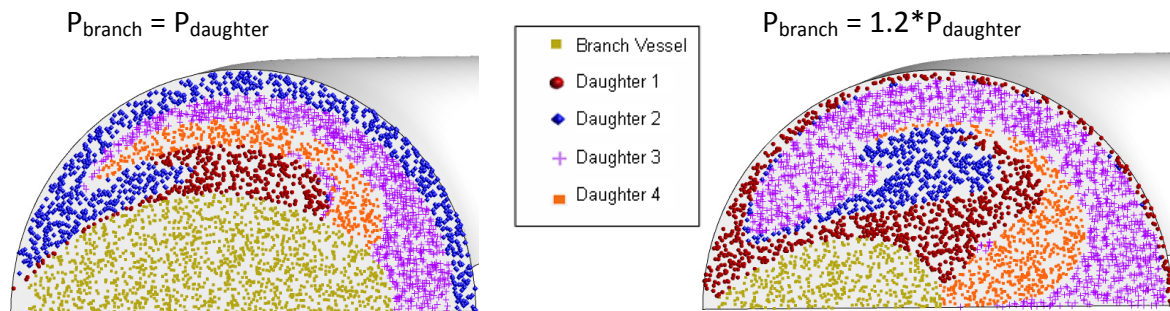


Figure 6.6: Particle release maps at the inlet injection plane for different branch vessel pressures

The branch vessel's increased downstream resistance yielded a very different particle release map, with the daughter vessel 2 region completely altering its shape and location. Thus, the large change in flow distribution caused by the increased downstream resistance carries the particles to different exit locations. A relation between flow distribution and global particle

exit fraction is also confirmed by comparing the exit fractions of the parabolic dispersion inlet injection in Fig. 6.4 with the local flow distributions in Fig. 6.2, yielding similar percentage values for each corresponding ratio. Particle characteristics may also influence the particle release map and the density of injected particles was varied along with the gravitational vector. In this simulation alone, the particles that collided with the wall were not tracked any further, since wall collisions are an adverse influence on predictable terminal locations of the particles. Figure 6.7 illustrates the influence of particle density and the gravity direction on the particle release map.

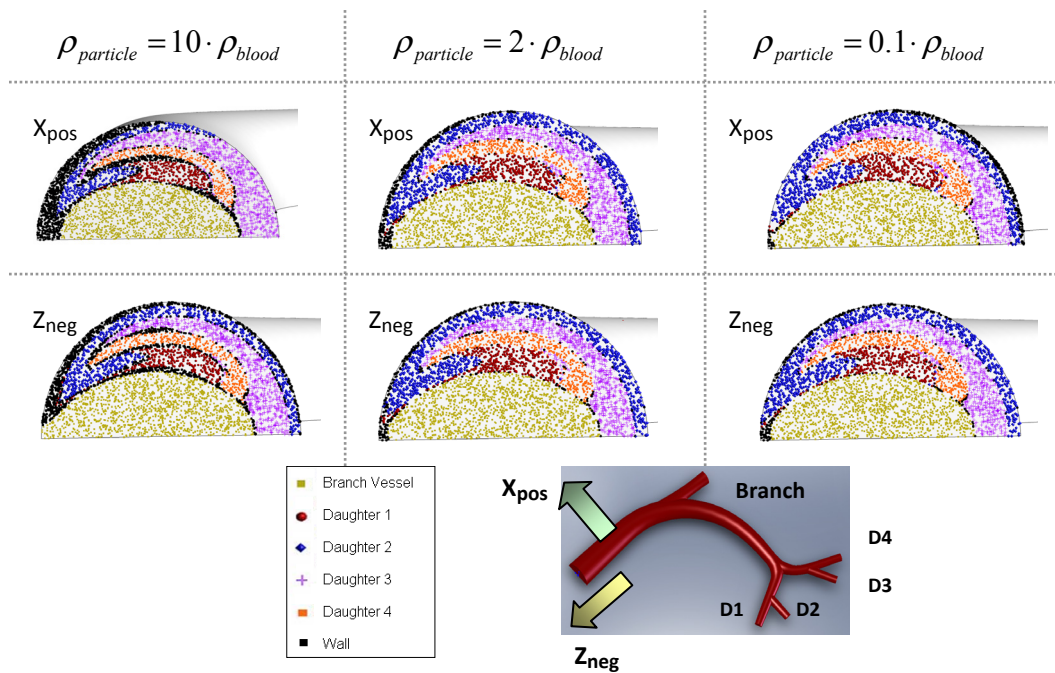


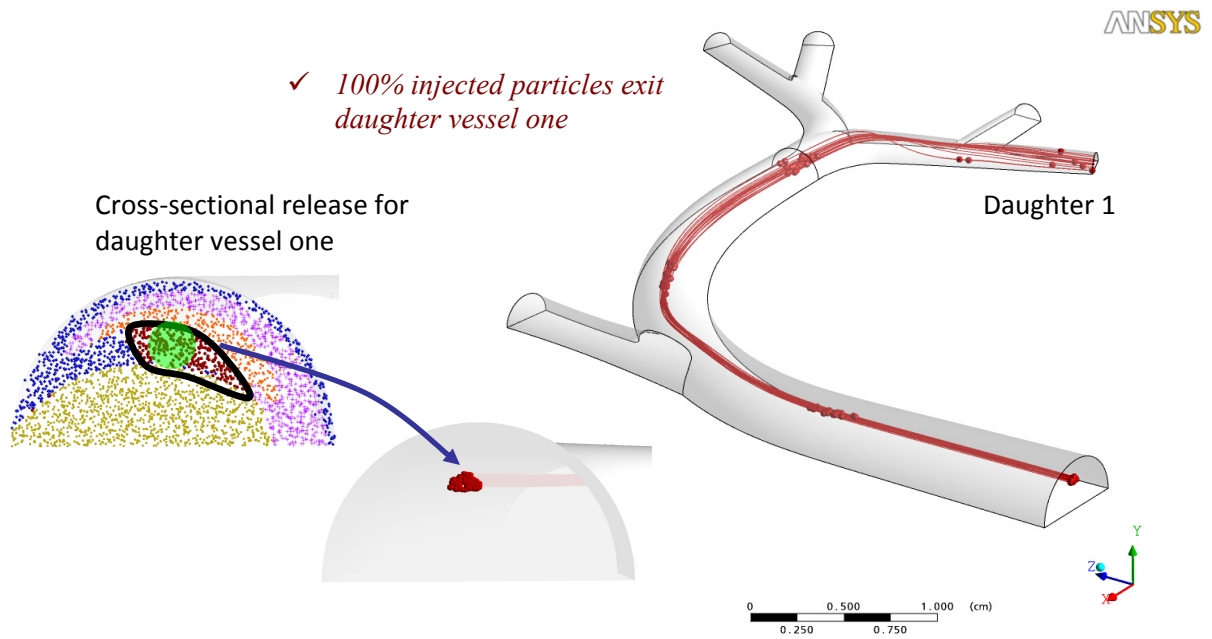
Figure 6.7: Particle release maps of varying density particles and gravity directions

Near-wall particle injection regions exhibited the most dependence on particle density having more particle-wall collisions, but organized particle release zones still existed and were

clearly visible. The number of particles with elevated transit times was found to be directly related to the particle to fluid density ratio. Thus, in addition to causing more particle-wall collisions, the greater density particles have a greater potential to become entrapped in the domain.

The organized regions of the particle release maps confirm the influence of cross-sectional position on a particle's exit location and raise additional questions regarding the ability to target specific downstream locations based on the particle injection's cross-sectional position. Such ability could greatly enhance intra-arterial therapeutic deliveries such as ^{90}Y -microsphere treatment of liver tumors by enabling clinicians to target specific downstream vessels by changing the injection locations cross-sectional position. Hence, new simulations were run with equal downstream pressures only releasing particles at the specific cross-sectional positions according to the particle release map of equal downstream pressure in Fig. 6.6. The simulation results were very promising and revealed excellent targeting potential by adjusting the diameter and cross-sectional position of the release point. Figure 6.8a reveals the most precise targeting scenario of directing 100% of injecting particles towards a single daughter vessel outlet, where Fig. 6.8b illustrates the targeting of different vessels by different cross-sectional injection positions. Such results support the notation that cross-sectional position plays a crucial role with flow distribution (or downstream resistance) of determining particle transport.

(a) Targeting daughter vessel one with cross-sectional injection position



(b) Targeting other vessels with different cross-sectional injection positions

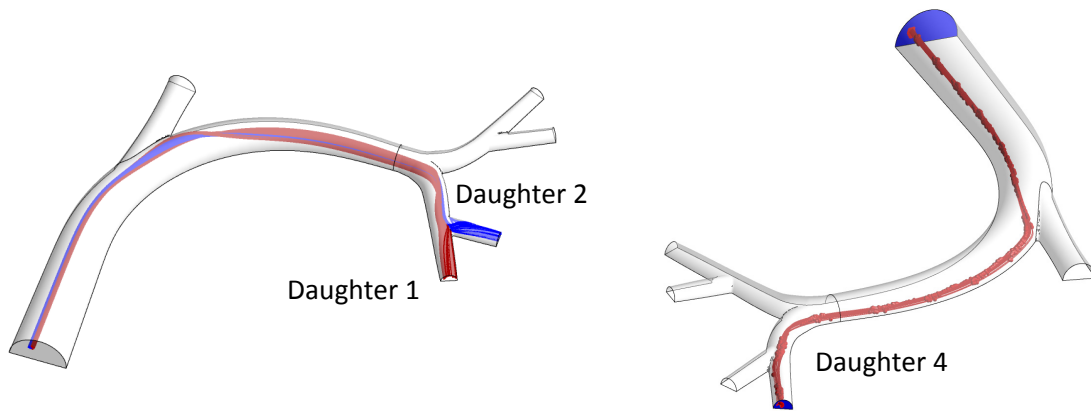


Figure 6.8: ^(a) Daughter vessel one targeting by selecting appropriate particle release position and ^(b) Targeting other daughter vessels with different cross sectional positions

6.3 Transient Particle-Hemodynamics of a Representative Hepatic Artery System using the WK2 Inflow Waveform

While the steady flow results show great promise, arterial flow is characterized by pulsatile, transient physics. Furthermore, the particle characteristics and inflow magnitudes used in the steady-state analysis were not always representative of *in-vivo* hepatic arterial conditions. Thus, transient simulations were constructed according to the descriptions in Section 6.1.

6.3.1 Flow Fields and Patterns

The lack of retrograde flow at the domain inlet plus the symmetric in-plane bifurcations resulted in consistent flow features throughout the physiologic pulse. Figure 6.9 plots the velocity field on the computational domain's symmetric plane.

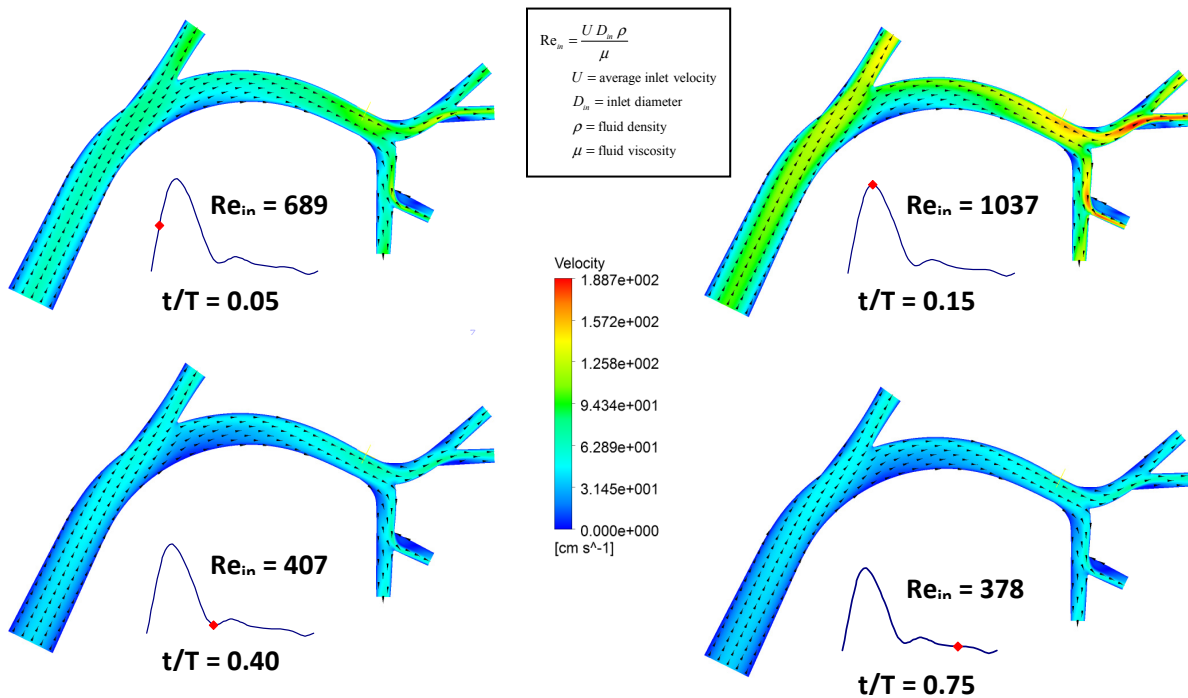


Figure 6.9: Transient flow fields in the symmetric CHA domain

The consistent flow field features exhibit similar regions of high velocity at each time point and similar velocity profiles that retain similar shapes throughout the arterial pulse. An important note is the influence of the primary 90 degree bend has on the local flow features. Specifically, the curvature directs flow away from the wall closest to the curvature and towards the region of the proper hepatic artery (PHA) vessel that supplies the left hepatic artery (LHA) and eventually daughter vessels three and four. Figure 6.10 plots the time-averaged velocity profiles at different regions of the domain illustrating the redirecting flow by the skewing of the local profiles.

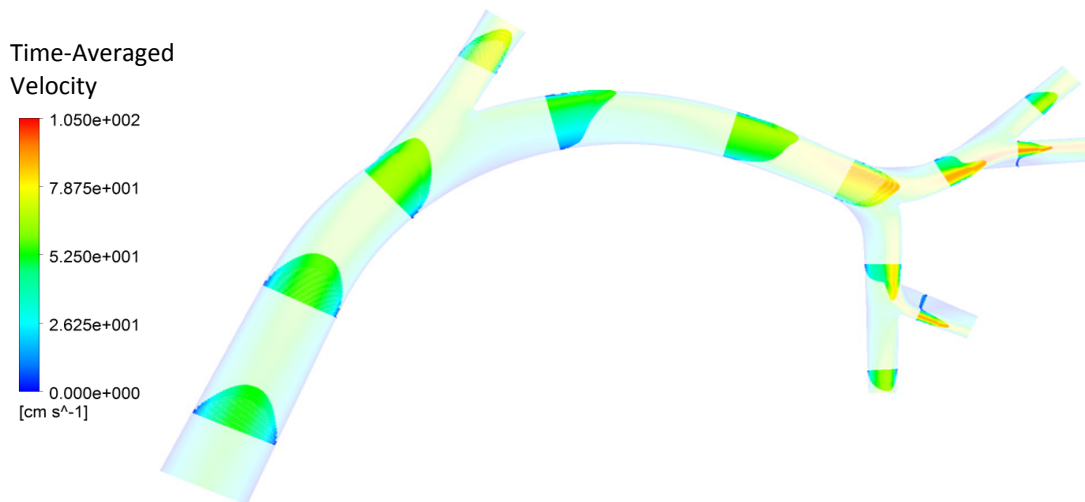


Figure 6.10: Time-averaged velocity profiles in the symmetric CHA domain

While the majority of the flow field exhibits little recirculation, the flow separation at the daughter vessel bifurcations results in two primary regions of flow recirculation that, change in size during the pulse but never detach from their origin and move up or down the vessel. Specifically, the recirculation regions appearing in the daughter vessels showed a primary length that was proportional to the inflow waveform, where both recirculation

regions exhibited percent differences between the max. and min. recirculation lengths greater than 40%. Figure 6.11 provides an enhanced view of the recirculation regions in daughter vessels two and three, where the fluid streamlines clearly show measurable differences at different time points in the physiologic pulse. Figure 6.12 plots each daughter vessel's non-dimensional primary recirculation lengths (primary recirculation length divided by the outlet diameter) time-history behavior throughout the physiologic pulse.

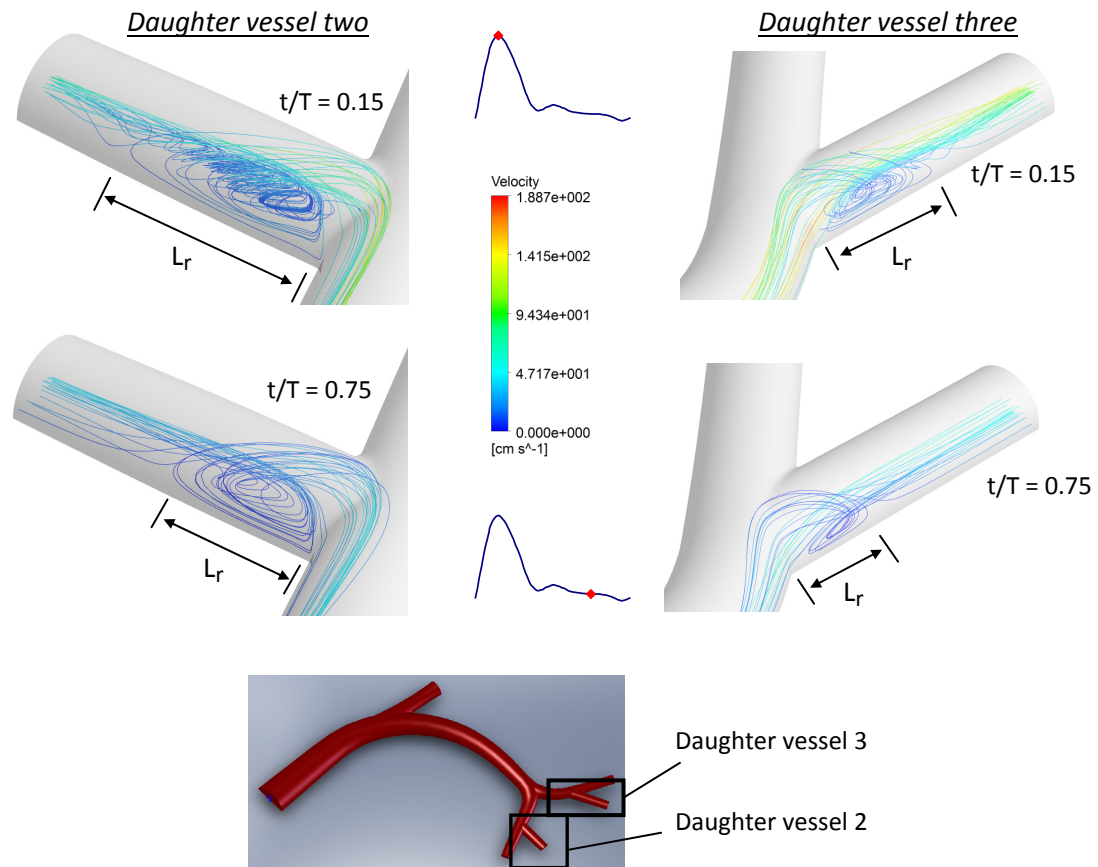


Figure 6.11: Streamlines at recirculation regions in daughter vessels two and three

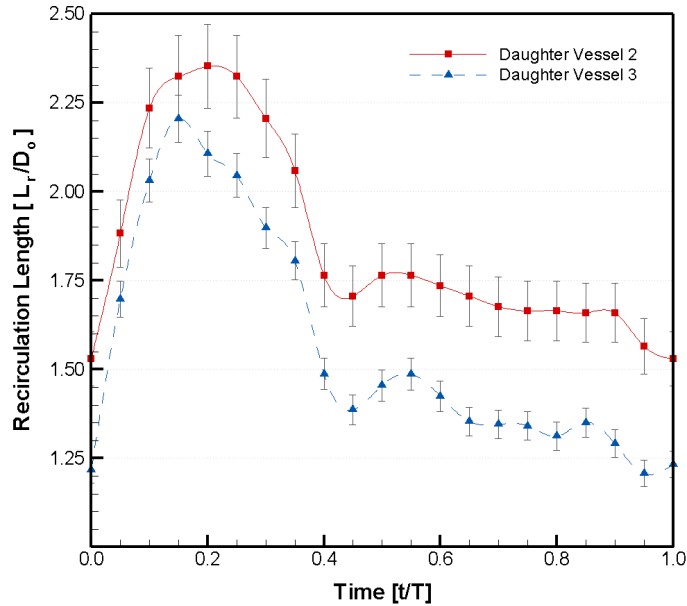
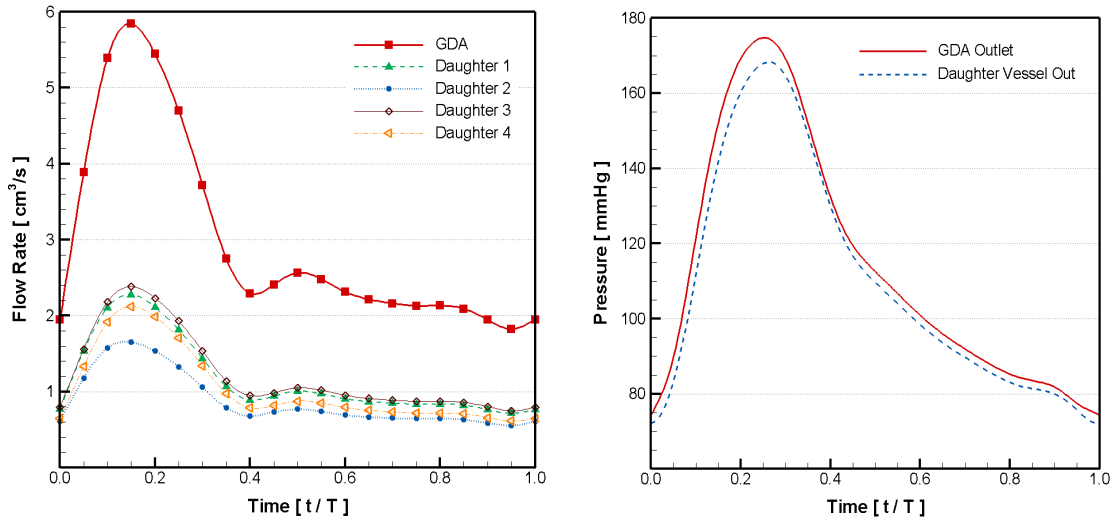


Figure 6.12: Primary non-dimensional recirculation lengths over physiologic pulse (Error bars are arbitrarily set at $\pm 3\%$ and D_0 is the outlet diameter)

The flow distribution throughout the symmetric CHA domain was similar to the steady simulation distributions. A difference in the transient simulations was the implementation of the mass flow outlet at the GDA vessel, which caused the GDA to receive the largest flow rate of all the domain's outlets but a lower flow rate than the flow in the PHA (or sum of all the daughter vessels). The similar diameters, bifurcation angles, and length to radius ratios of the daughter vessel morphology caused similar flow distribution throughout the transient pulse, nearly appearing as steady-state snapshots. Figure 6.13a shows the flow and pressure waveforms at each outlet and Fig. 6.13b indicates the mean, maximum and minimum flow rates through each outlet.

(a) Flow rate and pressure waveforms at through each vessel outlet



(b) Flow rates through each vessel outlet

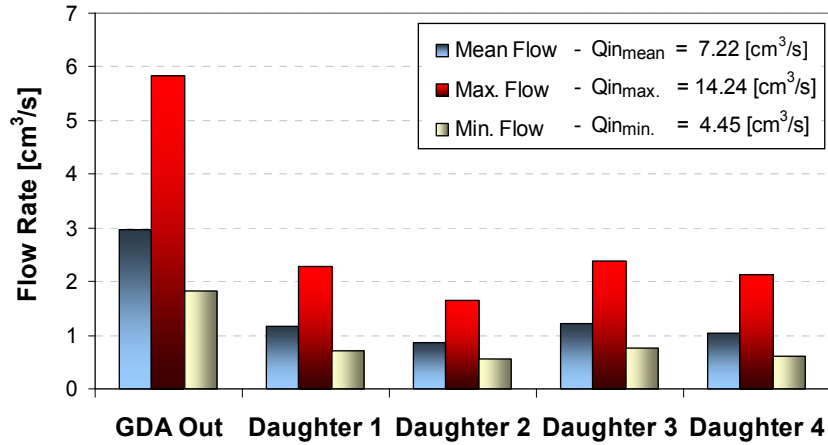


Figure 6.13 (a) Flow rate and pressure waveforms through each outlet and (b) Mean, max., and min. flow rates through each vessel outlet

6.3.2 Particle Transport and Specific Daughter Vessel Targeting

Particles matching the characteristics of clinically available SIR-spheres® and TheraSpheres® were injected during three distinct regions of the inflow waveform to assess temporal influences on particle behavior and vessel targeting capability. The cross-sectional

position was selected based on the inlet injection, equal downstream pressure, steady state simulation's particle release map in Figs. 6.5, 6.6 and published in Kennedy et al. (2010). Figure 6.14a illustrates the temporal particle release regions in the accelerating, systolic, and diastolic portions of the waveform and Fig. 6.14b plots the cross-sectional release position selected in attempts to avoid the GDA artery.

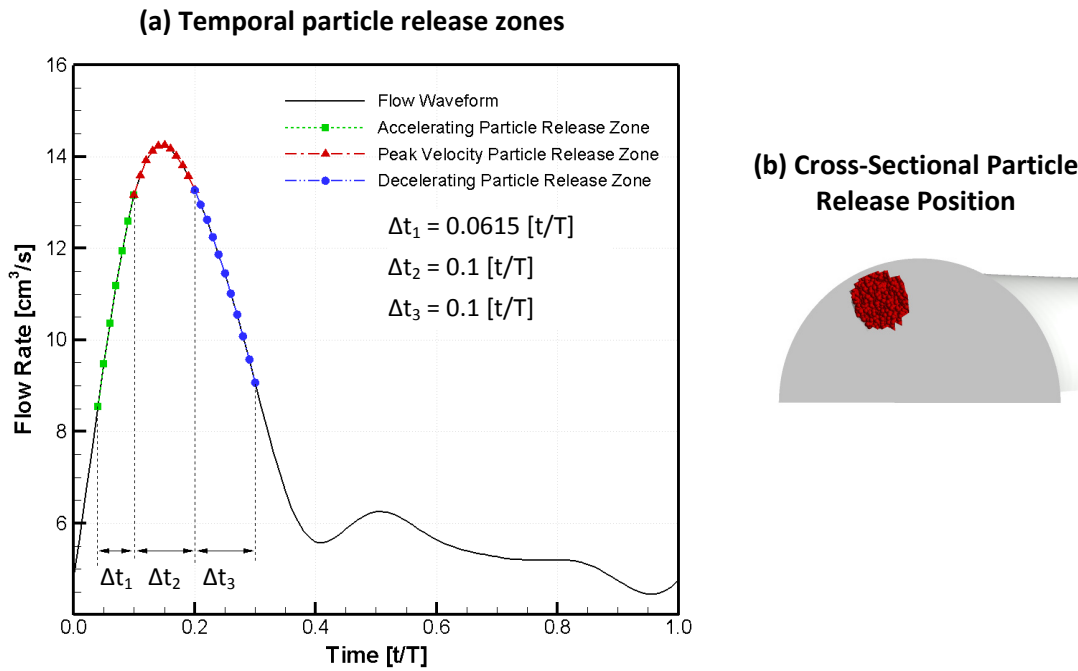


Figure 6.14: ^(a) Temporal particle release zones during the inflow waveform and ^(b) cross-sectional particle release position

The calculated particle trajectories revealed that the temporal time zone of the injected particles had a noticeable influence on the trajectories of both SIR-Spheres® and TheraSpheres®. Figure 6.15 illustrates the different particle trajectories of the three injection time zones (Δt = time duration of particle injection) where the red trajectory lines represent SIR-Spheres® and the blue lines represent TheraSpheres®.

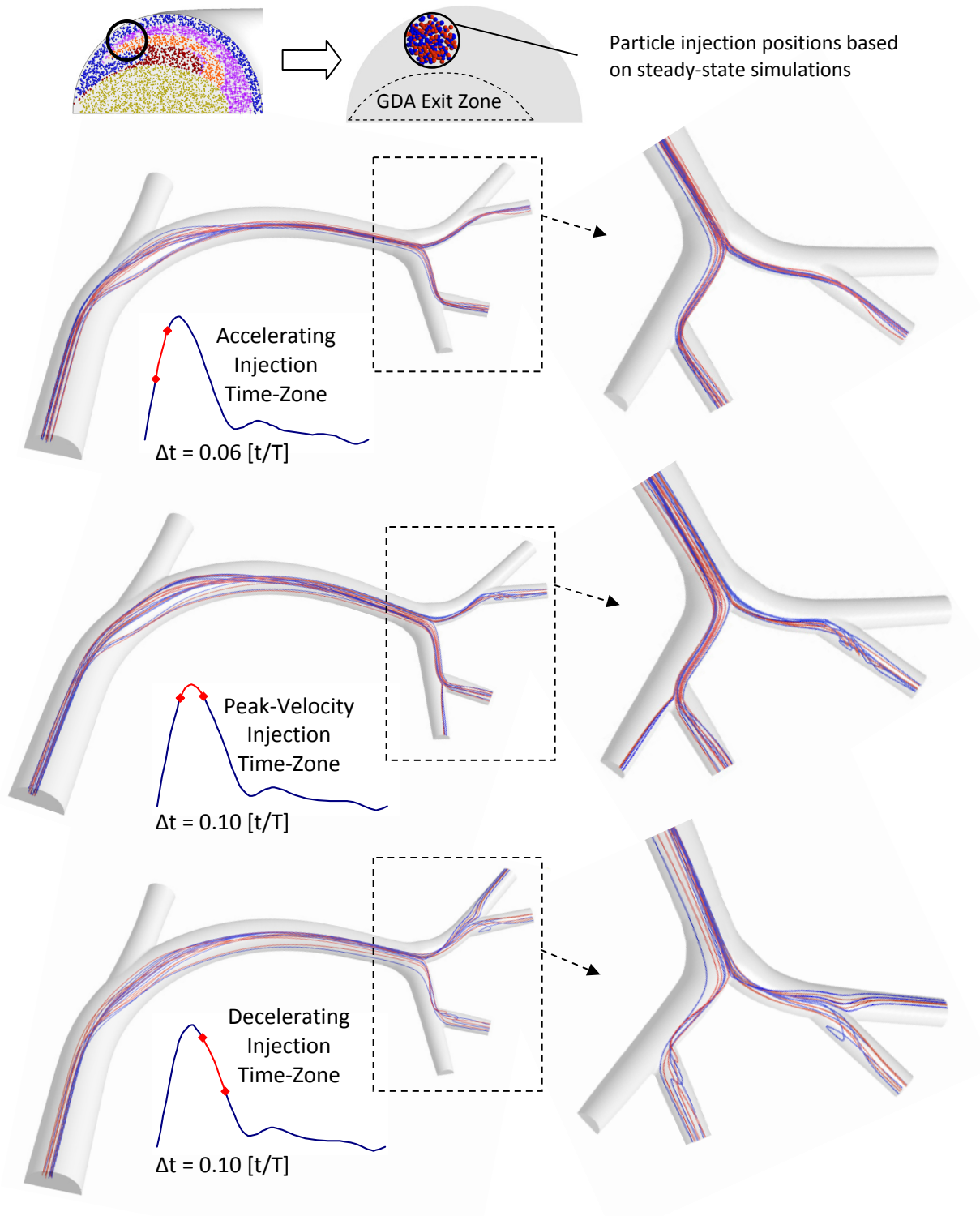


Figure 6.15: Influence of release time on particle trajectories
 (**Red** = SIR-Spheres® , **Blue** – TheraSpheres®)

Figure 6.15 clearly shows no microspheres entered the GDA, implying that a selective cross-section spatial injection region can reduce the likelihood of particles entering the major GDA branch. From the different trajectories illustrated in Fig. 6.15, the different particle characteristics of SIR-Spheres® and TheraSpheres® begin to have an increased influence on particle trajectories when the inertial effects on the particles become lessened, i.e., in the decelerating phase of the physiologic pulse. The injected particles in the decelerating time-zone also exhibit a greater tendency to spread and be influenced by the recirculation regions in daughter vessels two and three. While the majority of the SIR-spheres® and TheraSpheres® exhibit similar behavior, the recirculating flow in daughter vessel two disturbs more SIR-Spheres® than TheraSpheres® as the gravity vector pulls particles away from the recirculation and has greater influence on TheraSpheres® with nearly three times the density of the carrier fluid. The gravitational force has the converse effect in daughter vessel three, where gravity vector points into the recirculation region and hence draws more TheraSpheres® than SIR-Spheres® in the daughter vessel three recirculation regions. An interesting note is larger particles of both TheraSpheres® and SIR-Spheres® are more prone to be captured in both recirculation regions, which is due to a combination of particle momentum and the gravity vector. Figures 6.16 and 6.17 plot particle trajectories injected during the decelerating portion of the inflow waveform and are influenced by the local flow recirculation in daughter vessels two and three, respectively.

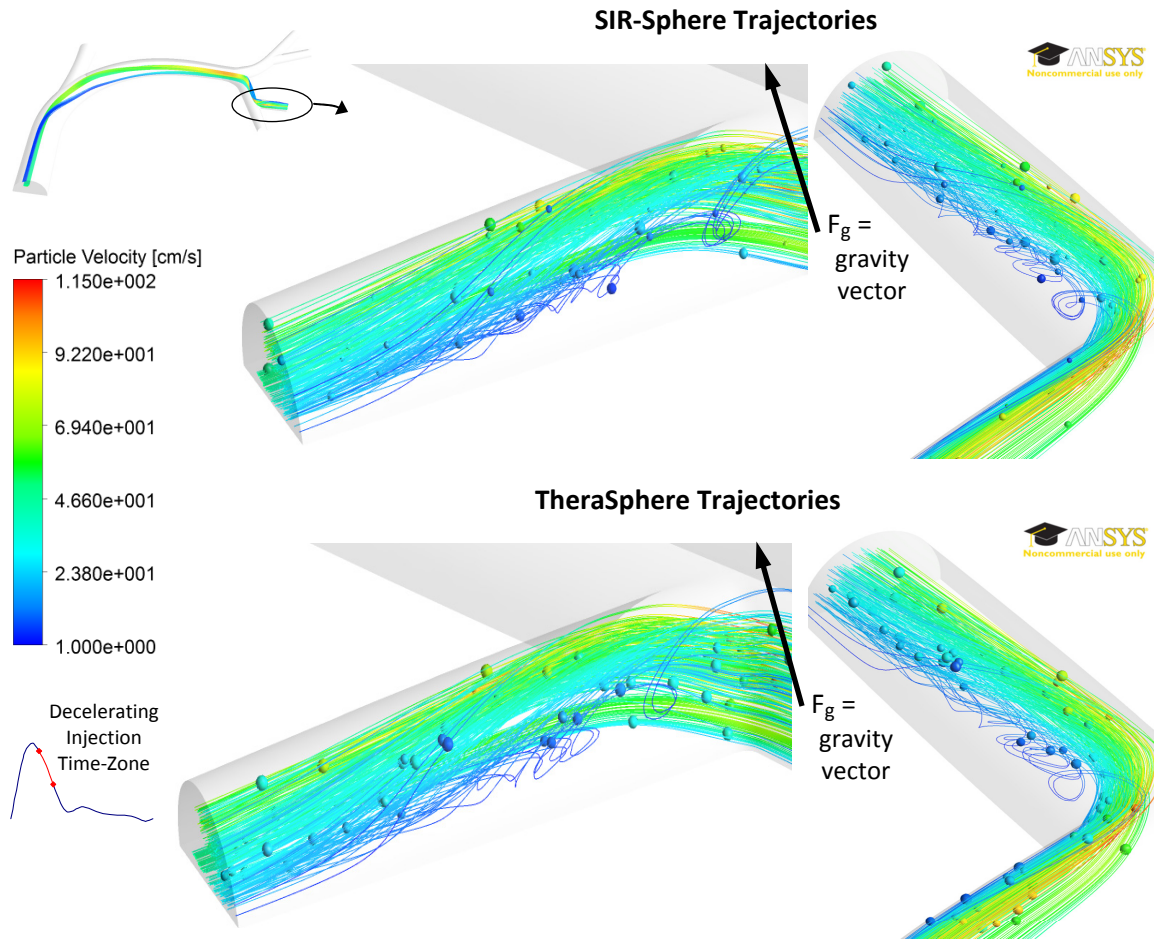


Figure 6.16: Magnified trajectories of ^{90}Y particles injected in the deceleration phase exiting through daughter vessel two

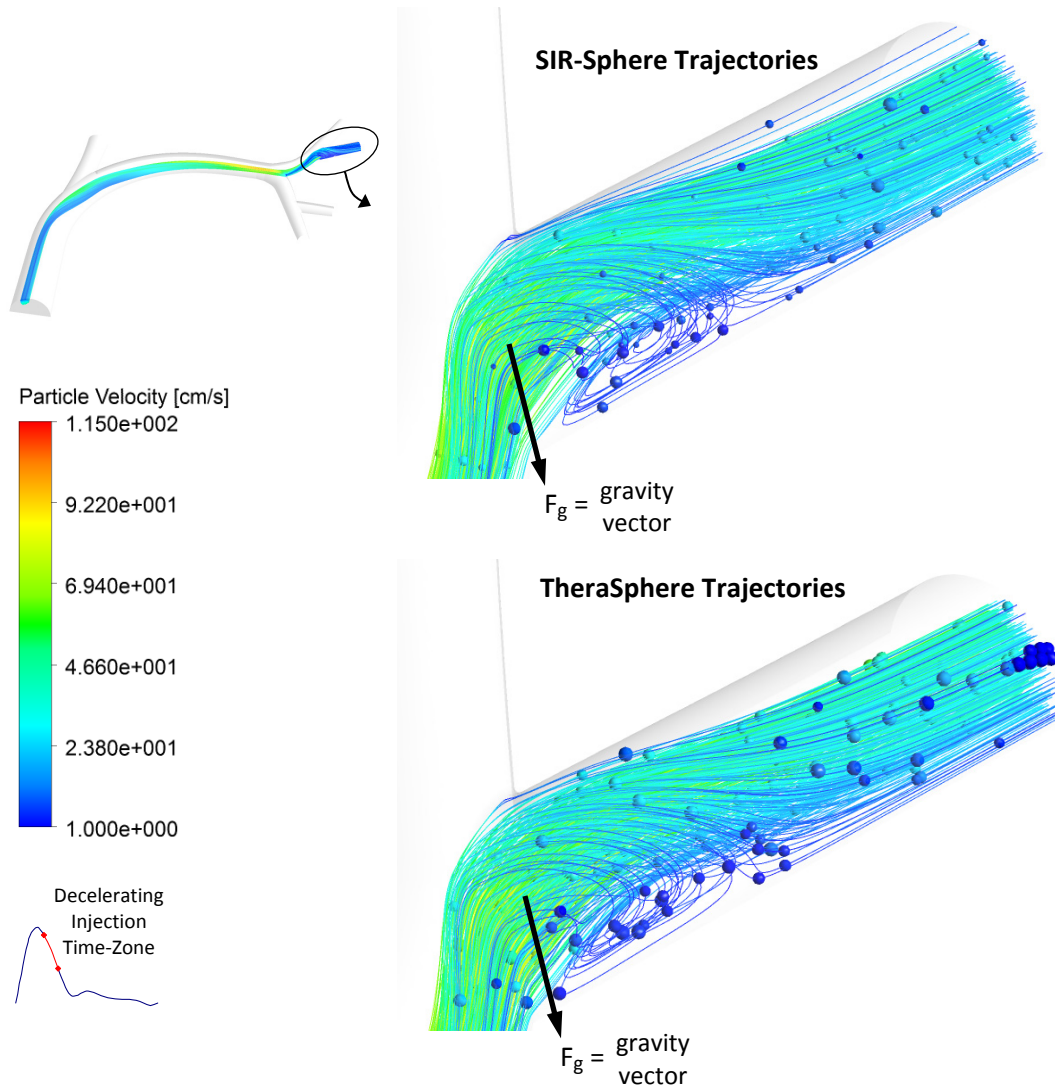


Figure 6.17: Magnified trajectories of ^{90}Y particles injected in the deceleration phase exiting through daughter vessel three

Quantitative information regarding particle exit behavior illustrates the influence of both particle characteristics as well as injection time-zone on the particle's terminal location. Figures 6.18a,b plot the percentage of particles exiting each outlet and the particles' maximum traveling time reaching each outlet with $\pm 3\%$ error bars. The "No Exit"

classification quantifies the percentage of particles that do not exit the computational domain during a single cardiac pulse. Figure 6.18a illustrates the ability to eliminate particles entering the GDA during pulsatile flow by selecting an appropriate cross-sectional particle injection region, as no particles from any time injection zone enter the branch. Additionally, Figure 6.18a illustrates that particle characteristics have significant effects on the preferred outlets of particles when the inertial forces are diminished in the decelerating injection time zone. During that time interval, the gravitational vector pulls more TheraSpheres® than SIR-Spheres® into daughter vessel two and permits a lower percentage of TheraSpheres® than SIR-Spheres® entering daughter vessel four.

The influence of the particle injection time-zone on the preferred exit location of the particles is also demonstrated in Fig.6.18a. The accelerating-phase injection zone has noticeably more particles traversing through daughter vessel two. In contrast, during the decelerating-phase injection zone over 65% of the injected particles travelled through daughter vessel three, whereas the accelerating and peak-velocity phases respectively transported up to 45% and 55% of the injected particles through daughter vessel three. The maximum particle transit times shown in Fig. 6.18b further reveal a dependence on the time of particle injection, where injection during the accelerating time-zone featured the lowest maximum transit time to reach any vessel outlet, which is an interesting result since the particles are injected with a higher velocity during the peak-velocity injection time zone.

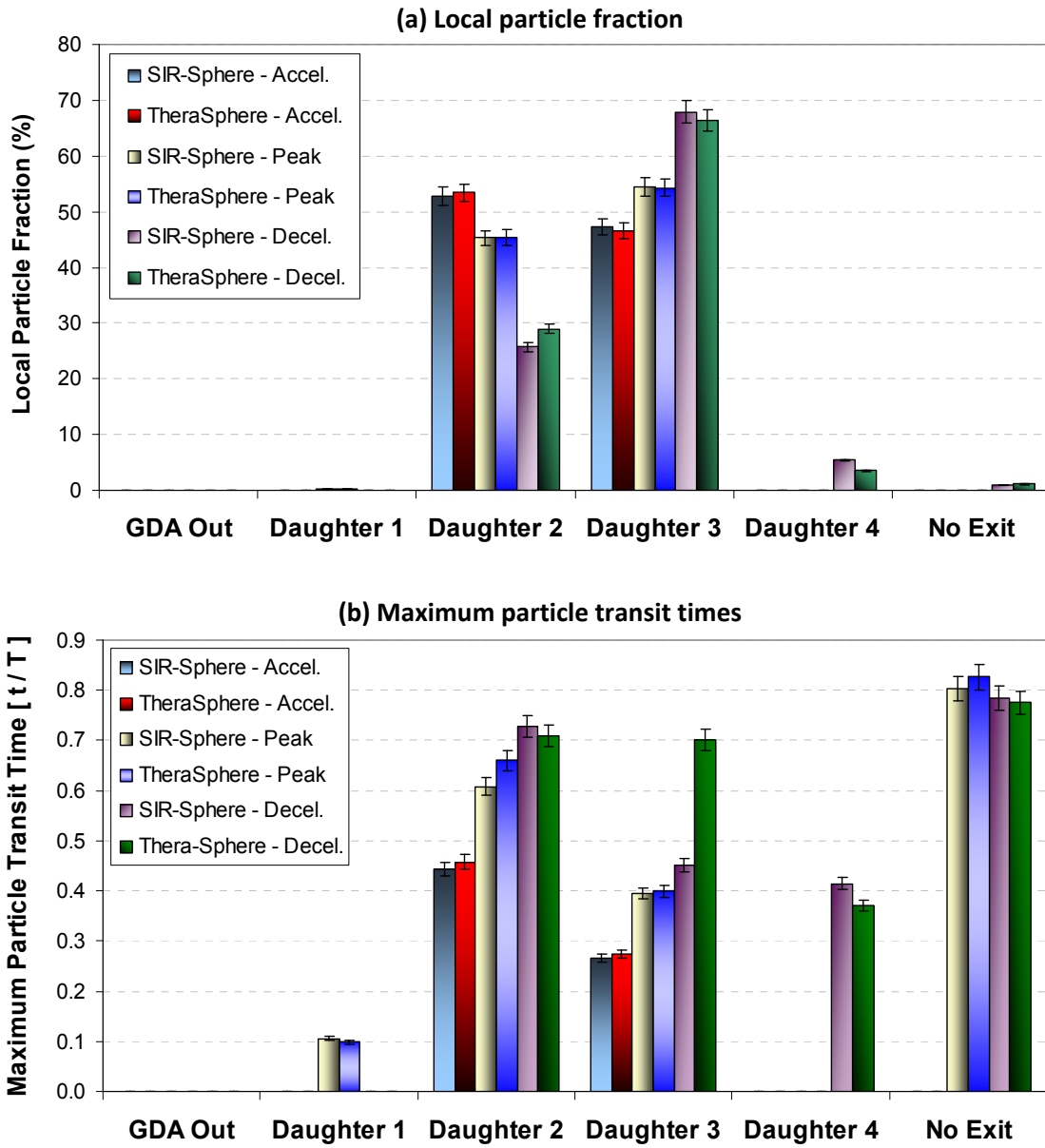


Figure 6.18: ^(a) Particle inlet percentages through each outlet and ^(b) maximum traveling times through each outlet for a single pulse (Error bars are $\pm 3\%$ of graph value)

The influence of the particle injection time-zone on the particle exit percentages is further illustrated by the cross-sectional particle release maps of the particle injection region shown in Fig. 6.19.

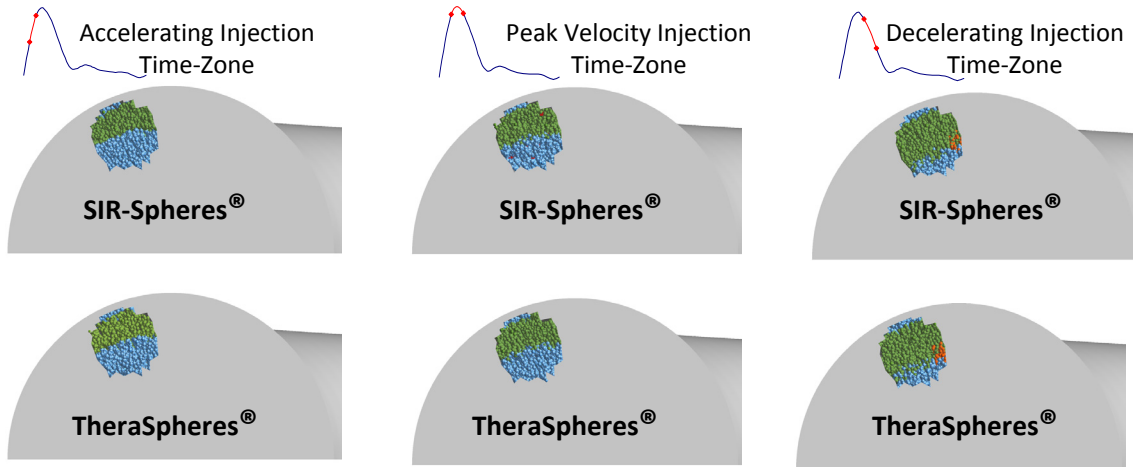


Figure 6.19: Particle release maps of SIR-Spheres® and TheraSpheres® for each time-zone
(**Red** = Daughter 1 , **Blue** = Daughter 2 , **Green** = Daughter 3 , **Orange** = Daughter 4)

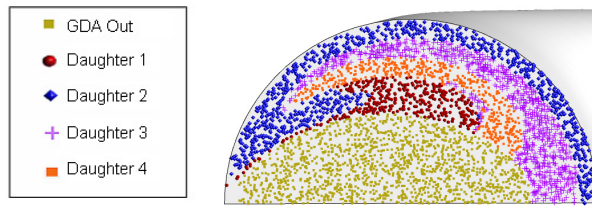
Clear distinctions between the regional areas can be observed between the decelerating and other time injection regions, subtle differences are also noted between the SIR-Spheres® and TheraSpheres® release maps in the decelerating injection time-zone. Furthermore, the size of the cross-sectional spatial zones is directly related to local particle fractions exiting at each outlet shown in Fig. 6.18a.

For the transient particle-hemodynamics simulations thus far, cross-sectional spatial particle injection locations were inspired by the particle release map created from steady-state flow investigations. However, more detail is needed to target specific vessels (moving beyond the ability to avoid specific vessels) in space and time, *time-dependent* particle-release maps for the accelerating time zone were developed via “transient backtracking” (see

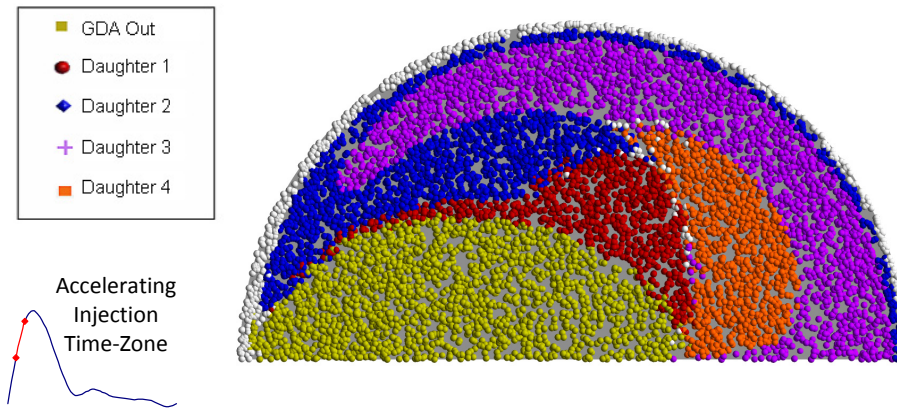
Kleinstreuer et al. 2008). Figures 6.20a,b,c plot the steady-state particle release and the transient SIR-Spheres® and TheraSpheres® respectively. Interestingly, the transient particle-release maps still form organized regions as observed for the steady-flow particle release-map. Additionally, only subtle differences exist between the SIR-Spheres® and the TheraSpheres® release maps, primarily appearing at near-wall regions with low injection velocity and locations near the boundaries of different zones.

Spatial injection locations were calculated using the release maps in Figs 6.20b,c to direct all injected particles through specific exits; for example, targeting daughter vessels two and four. The center-point of the particle injection location for targeting daughter vessel two is 0.7 mm to the left and 1.8 mm above the center-point of the inlet plane, whereas the center-point of the particle injection location for targeting daughter vessel four is 1.55 mm to the right and 0.8 mm above the center-point of the inlet plane. Both injection regions had a circular radius of less than or equal to 0.2 mm. Figures 6.21a,b plot the particle trajectories and spatial injection locations for the simulations targeting daughter vessels two and four, respectively. The particle trajectories in Figs. 6.21a,b show that by combining the accelerating injection time zone and the appropriate spatial inlet location, the particles are directed towards the desired vessels with little dispersion and a focused approach. The different particle characteristics play a negligible role as 100% of all injected particles exit the desired daughter vessels for both daughter vessel two and four.

(b) Steady-state particle release map of Re=1150



(b) SIR-Spheres® particle release map of accelerating time-injection zone from current study's transient simulations



(c) TheraSpheres® particle release map of accelerating time-injection zone from current study's transient simulations

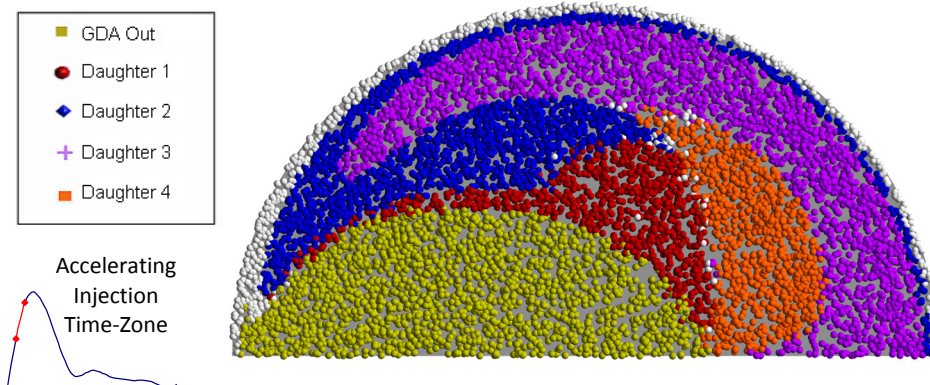
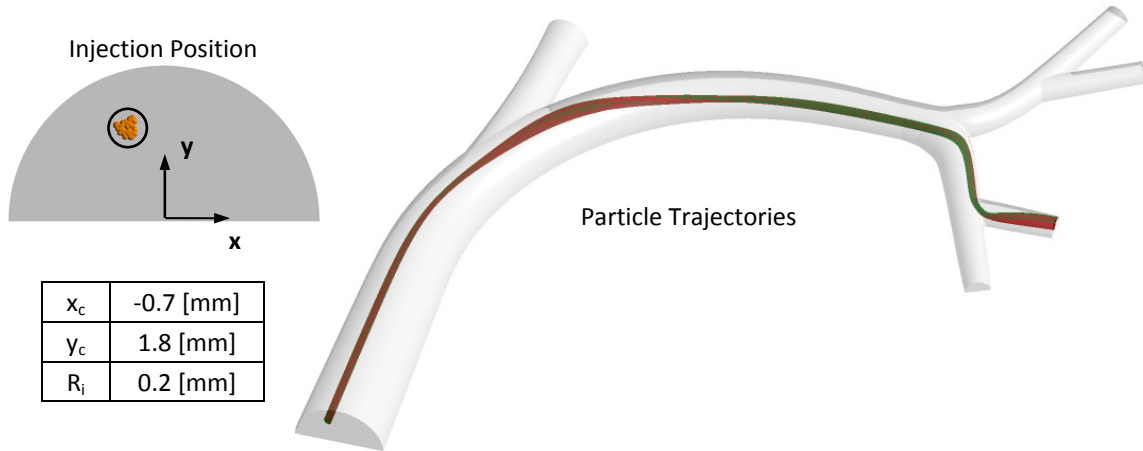


Figure 6.20: (a) SIR-Spheres® particle release map of accelerating injection time-zone (b) TheraSpheres® particle release map of the accelerating time-injection zone (Light grey spheres represent particles that do not exit after one pulse)

(a) Injection position and particle trajectories for daughter vessel two targeting
(Green = SIR-Spheres® ; Red = TheraSpheres®)



(b) Injection position and particle trajectories for daughter vessel four targeting
(Green = SIR-Spheres® ; Red = TheraSpheres®)

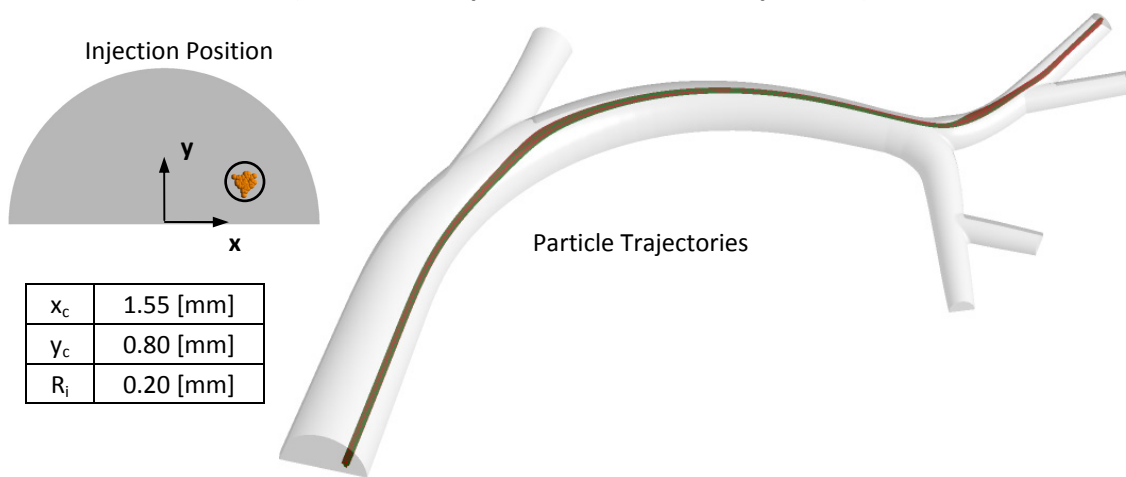


Figure 6.21: Spatial release position and particle trajectories for ^(a)transient simulation targeting daughter vessel two and ^(b)transient simulation targeting daughter vessel four

The particle trajectories of both SIR-Spheres® and TheraSpheres® showed very limited dependence on the particle diameter. Such a result is very interesting, since the range of particle diameters and Reynolds numbers results in changes in Stokes number (ranges

from approximately 3.73×10^{-4} to 1.26×10^{-2}). The most noticeable influence of particle diameter was seen at the daughter vessel three recirculation region, where larger diameter particles of both SIR-Spheres® and TheraSpheres® were captured in the flow recirculation during the decelerating injection time zone. Thus, for both the accelerating and peak-velocity time-zone injections, the carrier fluid provides enough momentum and inertia to overcome the range of microsphere characteristics. The accelerating time-zone injection also transported the particles with lowest transit time and organized patterns without crossing the carrier fluid streamlines (see Figs. 6.15 and 6.18). Such observations are very encouraging as they demonstrate the potential of controlling the trajectories of injected particles in transient flow by selecting appropriate temporal and spatial conditions that result in a stable blending of all particle forces. It implies that when all particles are injected, the carrier fluid velocity transports them well into the daughter vessel region prior to the major deceleration that occurs after the systolic phase of the arterial pulse.

6.3.3 Influence of Micro-Catheter and its Position on Transient Flow Fields and Microsphere Transport

Transient Flow Fields. All of the previous simulations were completed neglecting the local influence of the endovascular catheter used to actually release the ^{90}Y -microspheres in clinical therapies. To extend the analysis including these effects, particle-hemodynamics simulations were run on a postulated smart micro-catheter (SMC) geometry with the representative CHA geometry (see Fig. 6.1c and Fig. 3.10). The current set of simulations primary goal was to assess the influence of the catheter and its anchoring beams' geometric footprint would have on the surrounding flow and particle transport. Thus, in attempts to

model conditions prior to ^{90}Y -microsphere release, no flow was simulated coming out of the catheter. However, as an interesting test run, a uniform dispersion of particles was injected in a particle injection plane at the terminal end of the SMC lumen. Particles were only injected during the accelerating region of the inflow waveform.

Three different angular cross-sectional positions of the catheter were considered. The first being at 0 degrees from the vertical direction, the second at 45 degrees in the clockwise direction from the vertical direction, and the third being 90 degrees in the clockwise direction.

Figure 6.22 illustrates the different cross-sectional angular positions of the SMC.

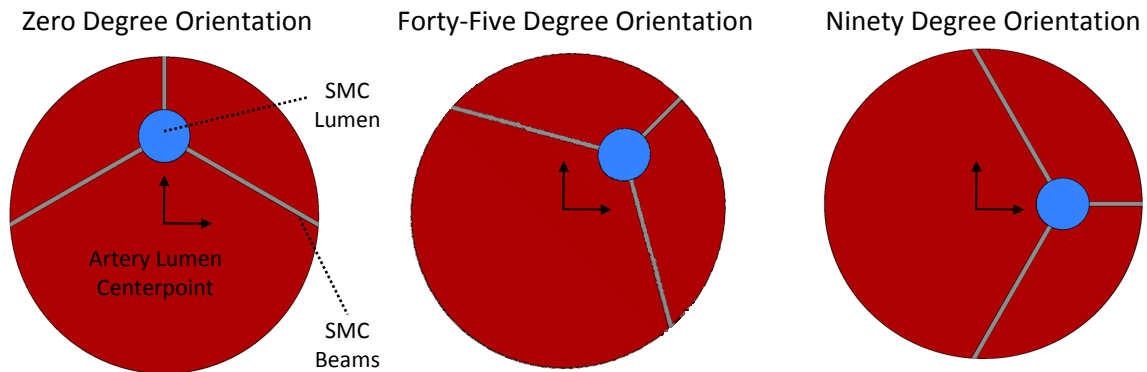


Figure 6.22: Angular cross-sectional positions of SMC

The velocity fields near the SMC exhibited noticeable influences from the presence of the SMC, but similar local flow features existed between each of the SMC angular orientations. The velocity profile at the terminal end of the SMC along the radial direction connecting the artery and SMC lumen centerpoints was the same for all orientations. Figure 6.23 provides a visual representation of the local influence by plotting the axial velocity profiles at multiple time points along the connecting radial direction connecting the artery and SMC centerpoints

and the radial direction from the lumen centerpoint that does not intersect any of the SMC beams.

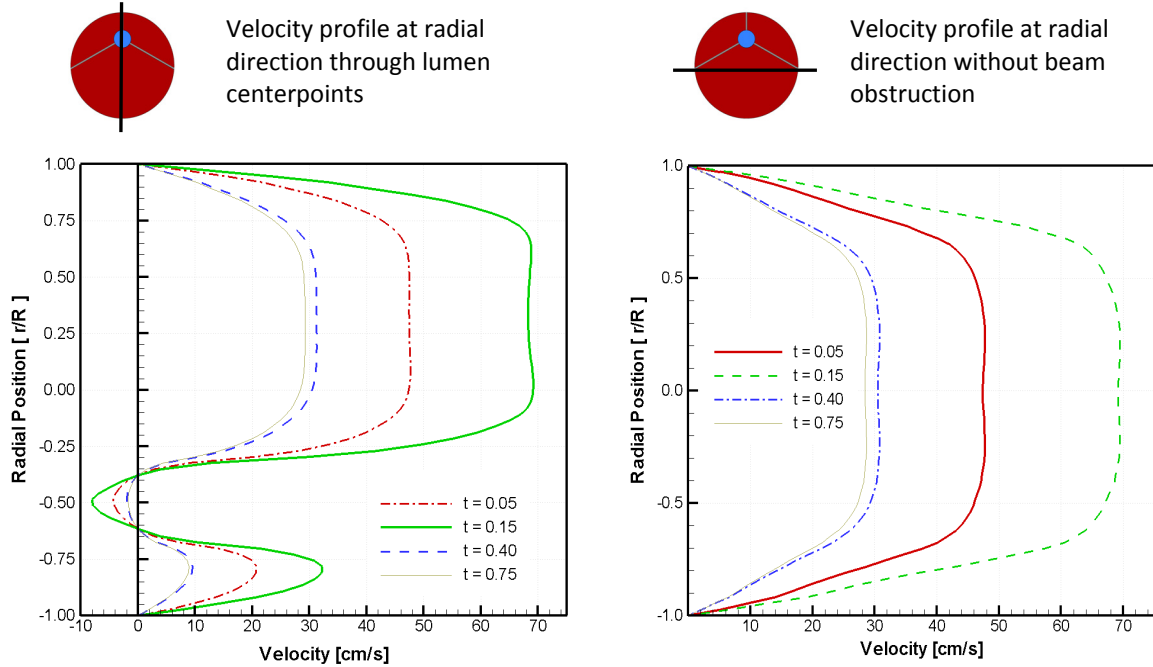


Figure 6.23: Velocity profiles at terminal end of SMC

Of notable interest is that the velocity profile connecting the centerpoints does exhibit some influence from the upstream SMC beams, which are (at upstream locations) along the path that the axial velocity is recorded for the velocity profiles. Such a flow pattern is very important, suggesting that beams of the thickness used in the current simulation have some influence on the overall flow field. Due to no flow coming out of the catheter, some fluid outside the catheter's terminal end does move into the catheter lumen resulting the retrograde flow seen in Fig. 6.23. The existence of the retrograde flow, implies some flow recirculation occurs at the terminal end of the SMC. Figure 6.24 depicts the representative streamlines and

nondimensional length (recirculation length, L_r , divided by the catheter diameter, d_c) of the recirculation zone.

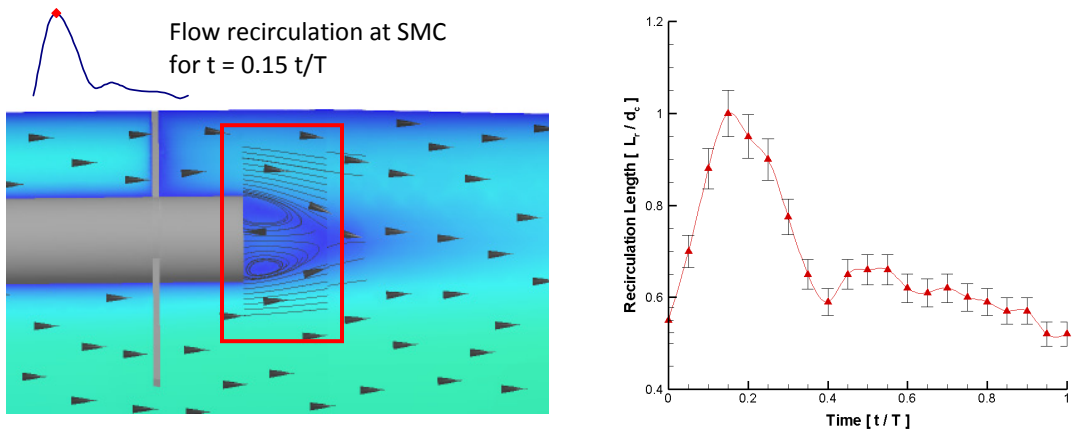


Figure 6.24: Transient flow recirculation at the terminal end of the SMC

While the SMC catheter plus beams influence the local fluid flow, the velocity vector fields along the $y=0$ plane of each SMC orientation had the same appearance in the downstream regions as the representative symmetric CHA geometry without the upstream SMC boundaries. Figure 6.25 plots the vector fields of each orientation at the systolic and nearly diastolic times.

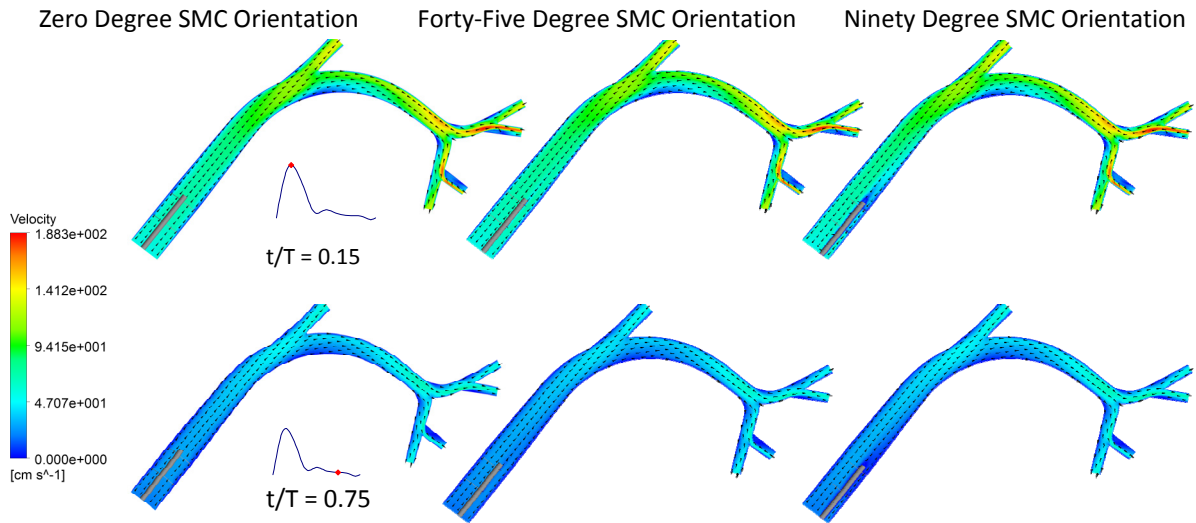


Figure 6.25: Transient flow fields in the SMC domain at plane $y = 0$

Even when the SMC is in the same plane as the recorded velocity vectors, the flow fields in near the GDA and PHA possess no visible alterations the vector fields without the SMC. The flow distribution amongst the different artery outlets also showed no dependence on the presence of the SMC geometry. Thus, while the SMC does create local flow disturbances near the catheter geometry, all disturbances are eliminated in less than five catheter diameters from the terminal end of the SMC and the resulting in downstream flow fields indistinguishable from those in Fig. 6.9.

Particle Transport. Most particle trajectories injected at the terminal plane of the SMC exhibited similar trajectories as those traversing through the domain without the SMC present. However, particles injected at a cross-sectional position that was within the outer diameter of the SMC catheter were caught within the local flow recirculation and had different terminal locations than that was predicted by the particle release maps in Figs. 6.20b

and 6.20c. Figure 6.26 illustrates the altered particle trajectories at the terminal end of the SMC.

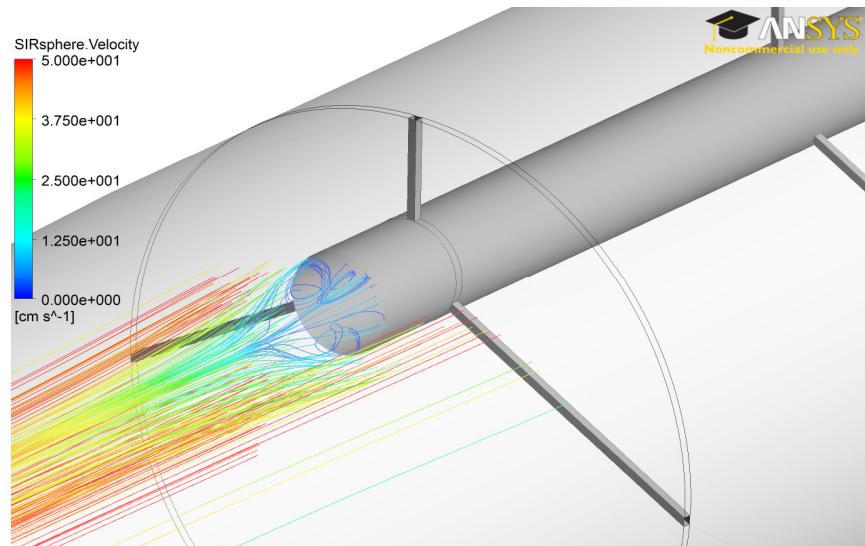


Figure 6.26: Particle trajectories altered by flow recirculation near the SMC

The particle release maps of all the injected particles clearly show a local alteration caused by the SMC flow recirculation. Figure 6.27 plots the particle release maps from a full-sized (no symmetry assumption), representative CHA domain without the SMC and the three SMC implemented geometries, where the black lines depict the SMC position.

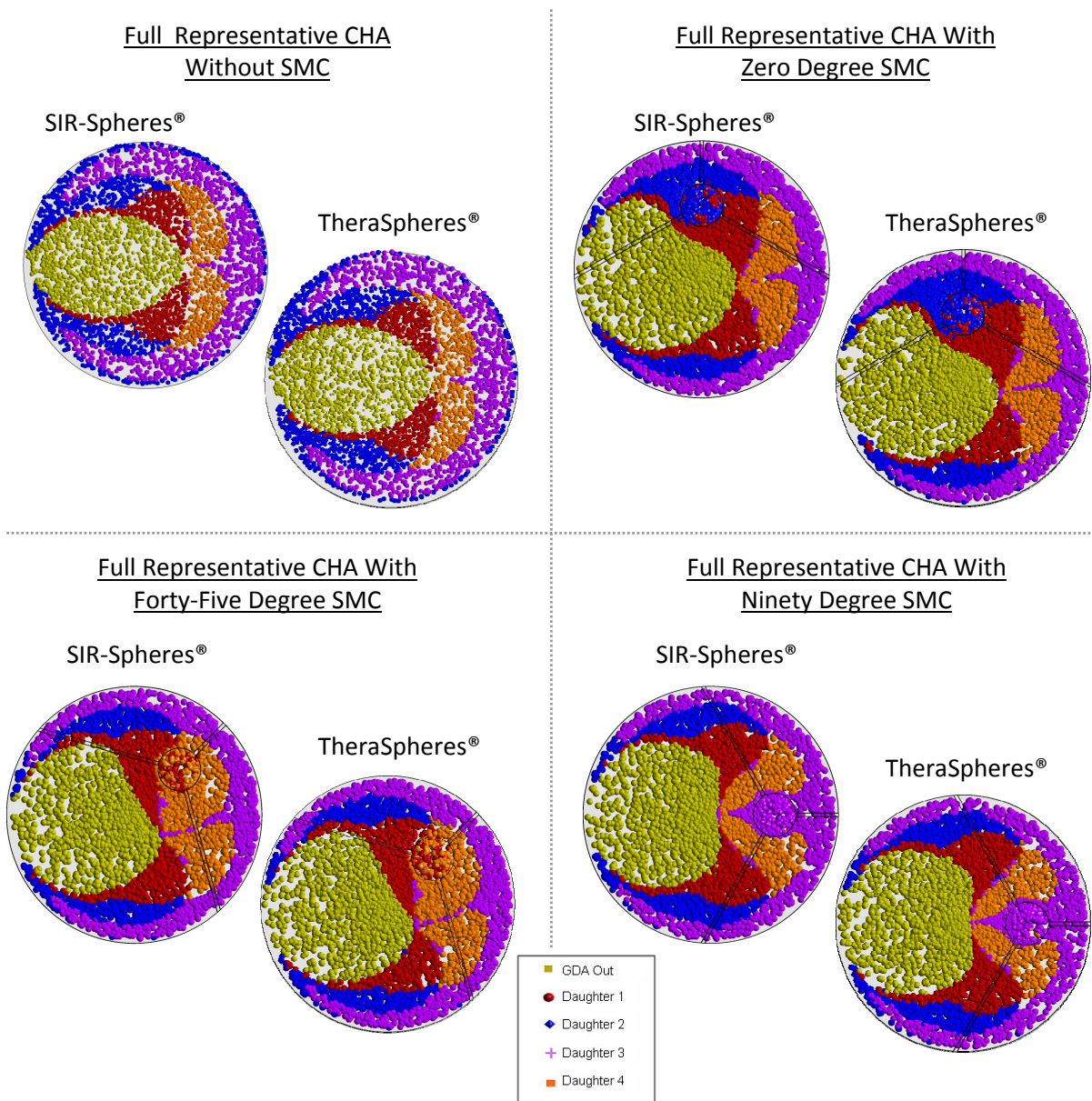


Figure 6.27: Particle release maps with and without the SMC

From the particle release maps several deductions can be made regarding the SMC's influence on particle trajectories. First, representative CHA with the SMC domain's particle release map zones are indistinguishable from the symmetric half domain's zones in Fig. 6.20. Most notable influences of the SMC are the blending of the particle release zones in the

footprint of the SMC. The regions outside the footprint of the SMC noticeably influenced are the near-wall daughter vessel 2 regions and the GDA region, whose shape deforms in response to the SMC position. As previously noted, often the cross-sectional area of the particle release zones is directly related to percentage of injected particles having the same terminal location. The same trend continues with the SMC as seen in Fig. 6.28, which plots the global exit fractions of all transient fluid-particle simulations with and without the SMC.

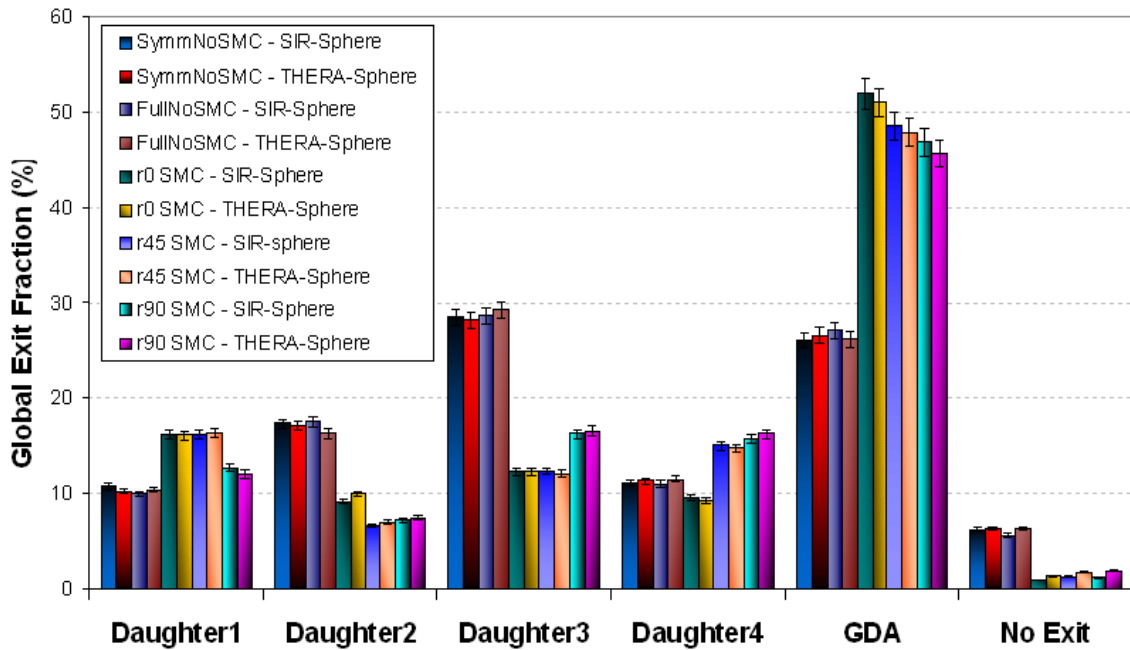


Figure 6.28: Global exit fractions of all transient fluid-particle simulations in representative CHA domains

The presence and angle orientation of the SMC was shown to have a measurable influence on the global particle exit fractions, whereas the full vs. symmetric calculations without the SMC showed no measurable difference. Specifically, the GDA region of all SMC maps grew noticeably and also exhibited a large increase in global exit fraction percentage of both SIR-

Spheres® and TheraSpheres®. The increase in GDA exit fraction resulted in a decrease of daughter vessels two and three's exit fractions for the SMC domain. Daughter vessel one in the zero-degree SMC orientation and daughter vessel four in the Ninety degree SMC orientation exhibited an increase in exit fraction due to the SMC footprint being over the appropriate outlet zone and increasing the level to surpass the no SMC geometries. In general, the SMC exhibited local flow field changes, which resulted in system-wide particle transport influences since the particle injection plane was influenced by the local changes in flow velocity.

6.3.4 Steady Flow Approximation of Transient Particle-Hemodynamics

In some clinical situations, there is not enough time for radiation oncologists to contemplate detailed, transient fluid-particle simulations of ⁹⁰Y-microsphere transport. Thus, establishing approximate operating conditions assuming a steady-state simulation, which requires far less time (hours compared days or weeks), would be extremely beneficial to assisting computational simulations in clinical practice.

The accelerating portion of the inflow waveform has been previously shown in Figs. 6.15 and 6.18 to have favorable conditions for transient particle release; hence, steady-state simulations were run with an inflow magnitude and outflow pressures/flow rates as those in the middle timepoint of the accelerating portion of the inflow waveform (time is 0.065 t/T). Specifically, the inflow magnitude was 10cm³/s and the outflow pressures were 90mmHg for the daughter vessels, while the GDA vessel had a flow magnitude of 0.41*inflow. The forty-five degree SMC geometry was tested under the aforementioned boundary conditions with particles injected with a uniform dispersion across the same injection plane as the previous

SMC simulations. To eliminate the local flow recirculation at the terminal end of the catheter, a uniform inflow velocity was set at the catheter inlet that was equivalent to the cross-sectional spatial average velocity at the artery inlet.

The velocity vector field along the $y = 0$ plane revealed similar flow features as those in the transient, SMC simulations with downstream features representative of the flow recirculation measure in the transient simulations without the SMC. Flow distribution in the artery outlets was also representative of the two previous simulations. Figures 6.29a and 6.29b depict the flow field and flow distribution respectively.

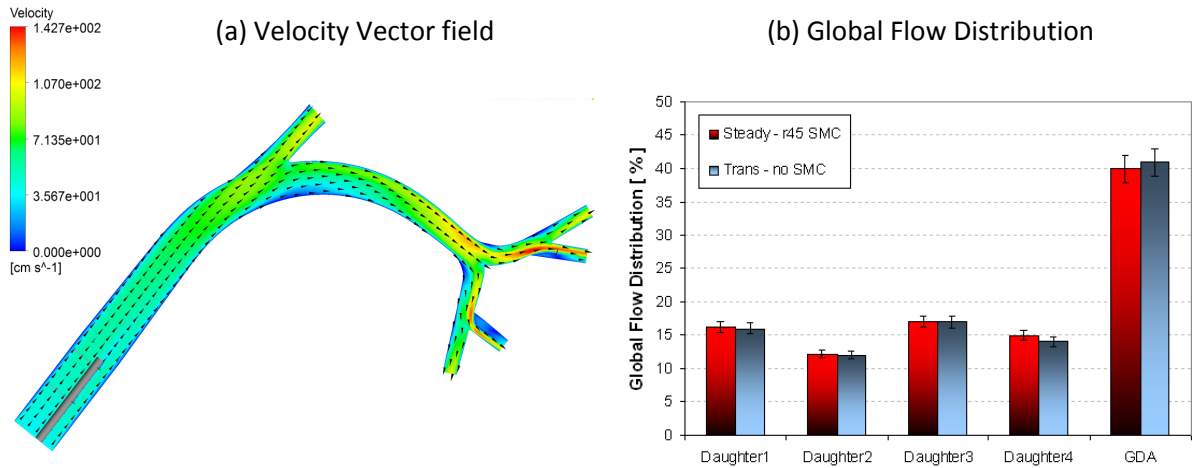


Figure 6.29: (a) Velocity vector field at the $y = 0$ plane and (b) global flow distribution of steady flow representing transient flow

The sum of the inlet Reynolds number for the artery flow (using the hydraulic diameter) and the inlet Reynolds number of the catheter flow is approximately 700, which closely matches the anticipated transient value. Particle release maps and global exit fractions also matched previous values. However, while the steady flow simulation's global exit fractions matched

the transient SMC simulation well the steady flow exit fractions did not match the transient simulation without the SMC.

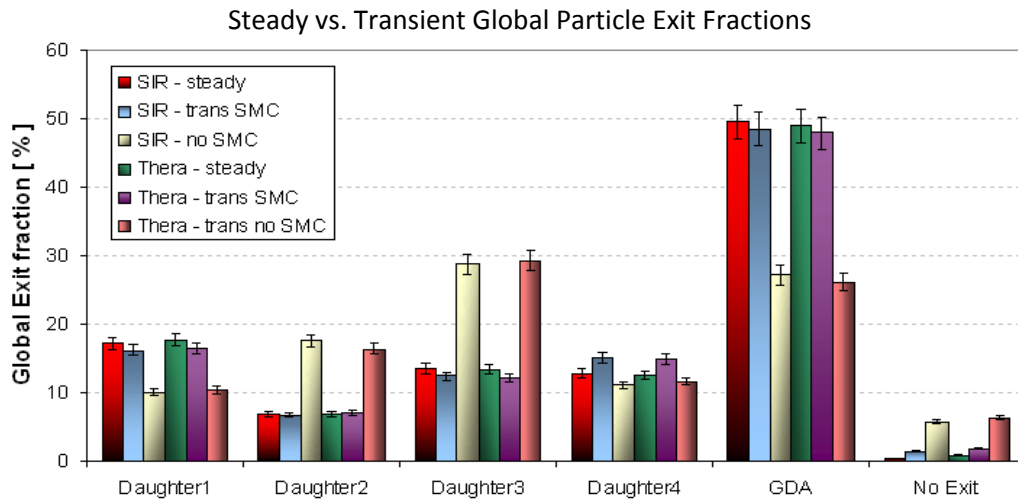
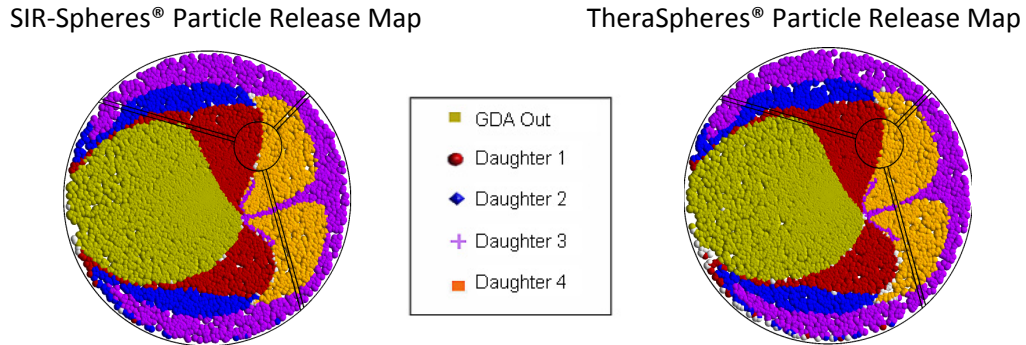


Figure 6.30: Steady particle release maps and global exit fractions

Interestingly, the flow coming out of the SMC created unique particle release zones in the footprint of the SMC, unlike the SMC particle release maps in Fig. 6.27. Additionally, the ability of the steady simulation to reproduce the global exit fractions of the transient SMC simulation is an important result and suggests that by using the flow conditions at the midpoint of the accelerating inflow waveform, a steady state simulation that would represent transient particle transport results could be conducted.

6.3.5 Influence of Particle Injection Velocity on Microsphere Transport and Daughter Vessel Targeting

One of the parameters that the ^{90}Y -microsphere radiation oncologist actively controls is the volumetric flow of the fluid carrying the ^{90}Y -microspheres. Clinical practice varies and the widely accepted guideline is to attempt to keep the catheter flow minimal. Steady and transient simulations with the SMC in the forty-five degree orientation (see Fig. 6.22) were run at different inflow velocities in the SMC with particles only being released from the SMC. Thus, the simulations are the closest to the clinical process of ^{90}Y -microsphere delivery.

The steady-flow conditions representing transient particle transport outlined in the previous sections were implemented in the SMC geometry while modifying the catheter outflow to different magnitudes. The steady-state simulations are used to quickly analyze different SMC inflow magnitudes and construct a transient simulation of ^{90}Y -microsphere injection under a SMC flow magnitude that does not inhibit daughter vessel targeting. All catheter flows were in the laminar regime and varied from 0.0114 to 5.7149 cm^3/s . Noticeable influences on the velocity flow fields near the SMC were observed at 1.143 cm^3/s and on the domain's velocity flow fields at approximately 2.286 cm^3/s . Table 6.1 lists the flows tested and their relation to the arterial fluid velocity, while Fig. 6.31 depicts the flow fields distal to the SMC under the difference SMC outflow magnitudes.

Table 6.1: Catheter flows and their relation to the arterial velocity

| Relation to Arterial Velocity | Catheter Flow [cm ³ /s] |
|-------------------------------|------------------------------------|
| 0.01 times | 0.0114 |
| 1.0 times | 1.1430 |
| 2.0 times | 2.2869 |
| 5.0 times | 5.7149 |
| 10.0 times | 11.430 |

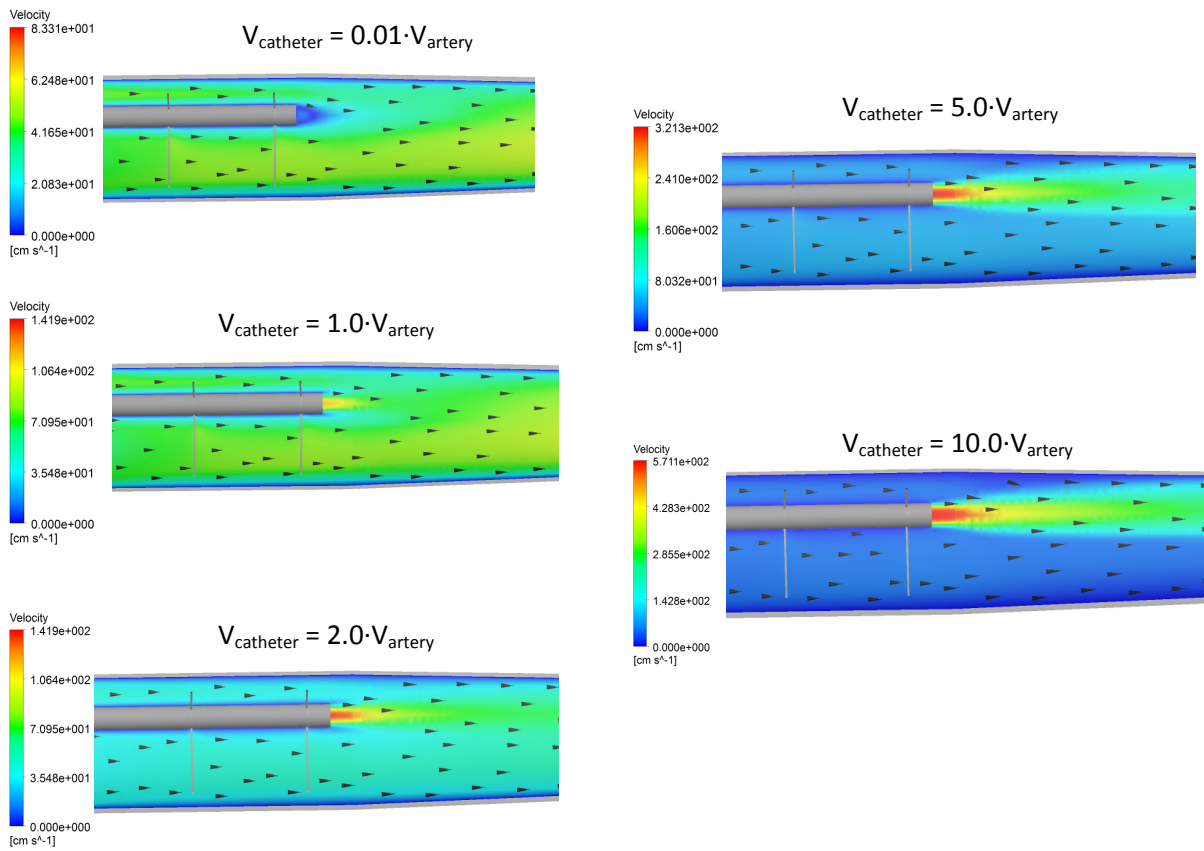


Figure 6.31: Flow fields near SMC under the different SMC outflow magnitudes

Influences on the global flow field are represented by changes in the velocity vector field along the $y = 0$ plane and are plotted in Fig. 6.32.

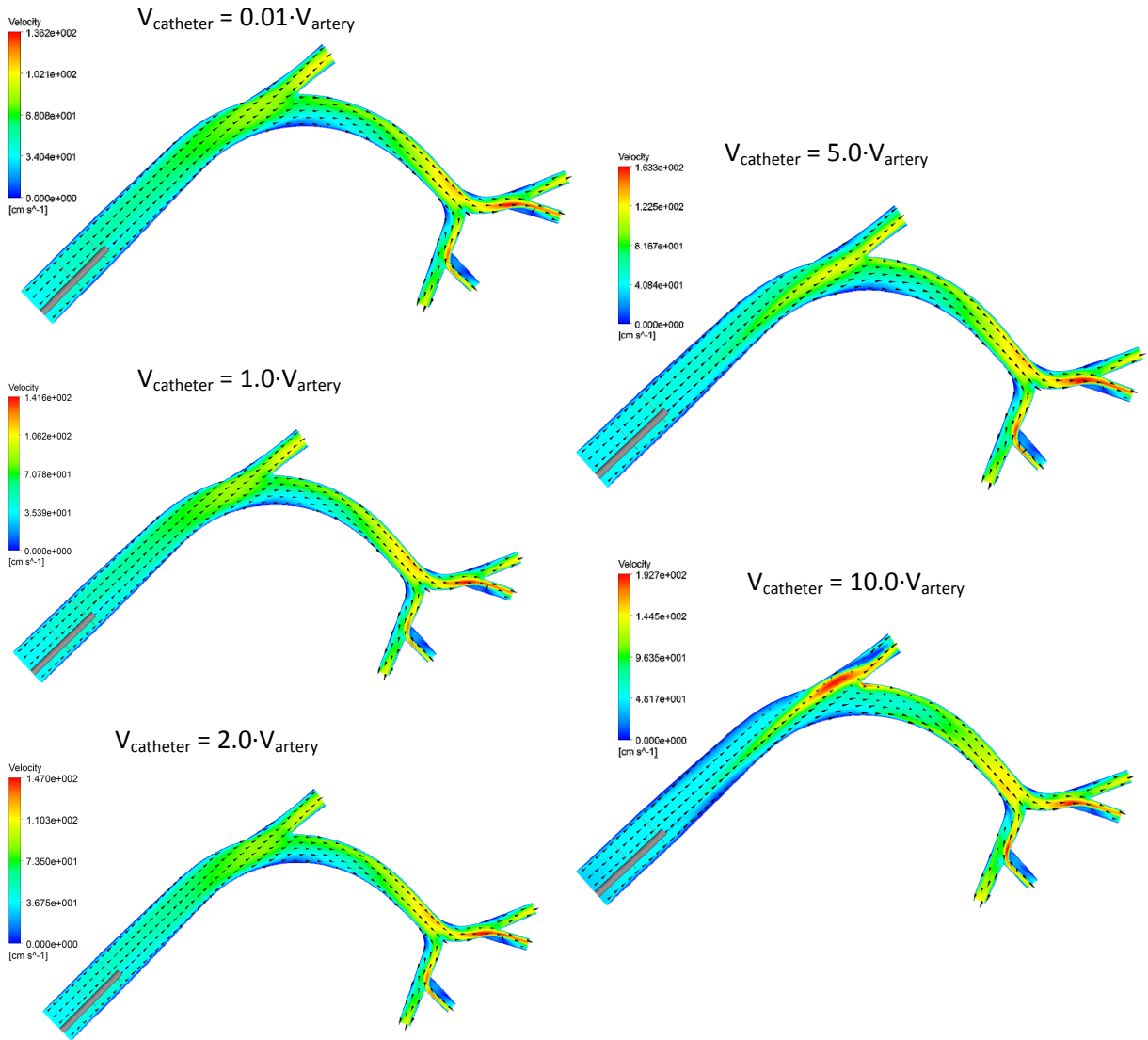


Figure 6.32: General CHA flow fields under the different SMC outflow magnitudes for the 45° SMC-orientation

The region exhibiting apparent changes is near the GDA outlet where high SMC outflows direct a majority of the incoming flow towards the GDA vessel's wall opposite from the bifurcation. Interestingly, the increased velocity in the GDA creates flow recirculation that

ultimately reduces the percentage of flow exiting the artery. Figure 6.33 plots the global flow distribution through each of the outlet vessels.

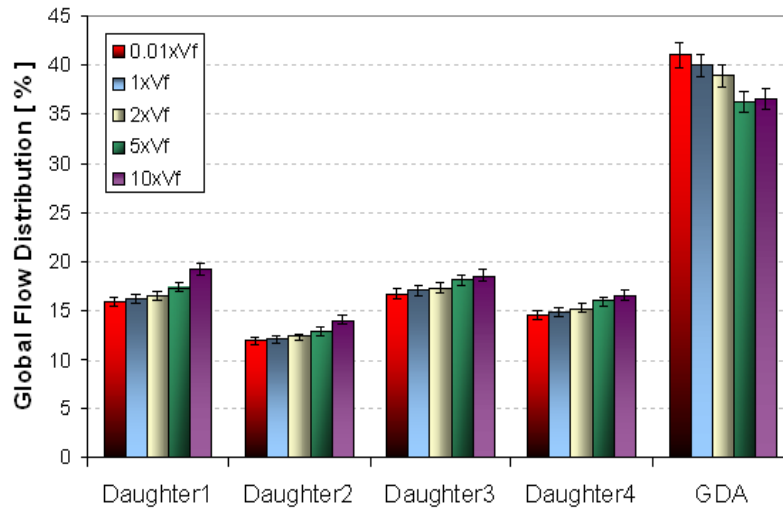
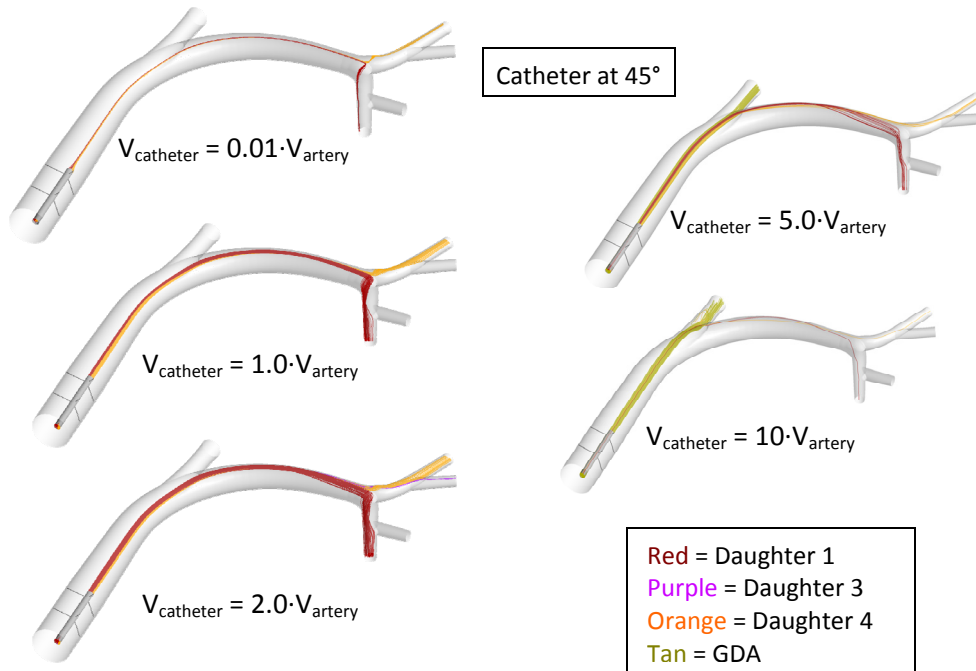


Figure 6.33: Global flow distribution under different SMC outflow magnitudes

Error bars represent a range of $\pm 3\%$ and reveal that when the SMC outflow is five times the surrounding fluid velocity, the influences on the velocity fields begin to significantly influence the flow distribution among the system's outlet vessels.

One hundred particles were injected via the catheter with the same velocity and bulk mass flow as the fluid in the catheter. Trajectories of the particles revealed a clear dependence on the SMC-outflow magnitude, where higher velocities enabled particles to cross fluid streamlines, bounce off walls, and not follow predicted terminal locations based on previous particle release maps given in Fig. 6.30. The unpredictable behavior of the injected particles with elevated velocities is illustrated in Fig. 6.34a and the global exit fractions are presented in Fig. 6.34b.

(a) Particle Trajectories with Different Injection Speeds



(b) Global Exit Fractions of Particles with Different Injection Speeds

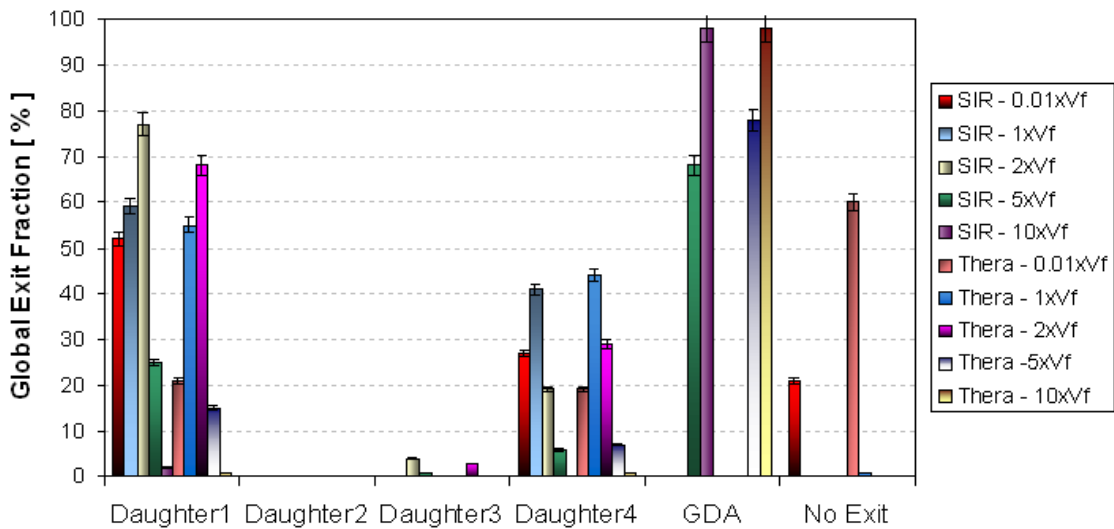


Figure 6.34: (a) Particle trajectories and (b) Global exit fractions under different SMC outflow magnitudes

The combined data in Figs 6.33 and 6.34 clearly show that if microspheres are injected at velocities greater than the velocity of the surrounding fluid, the microspheres will have an increased tendency to cross fluid streamlines. Such a result makes targeting specific vessels difficult to impossible, because particle inertia effects take over. Another observation is that velocities of very low magnitude result in particles not exiting the domain or getting entrapped in the flow recirculation region. Particles that do not exit at low flow are clearly dependent on their physical characteristics. For example, in the case of TheraSpheres® the blood flow may not be able to sufficiently transport the particles through the domain. Current therapy techniques rely on the local blood flow to carry the particles to the tumor sites after microspheres are injected. Thus, creating particle stagnation by injecting the microspheres with too little speed or by disturbing/redirecting the general flow patterns and flow distribution via elevated SMC velocities could result in treatment failure by inadvertently directing all the particles to undesired locations.

The steady-flow results suggest that SMC injection velocities at or around the surrounding blood velocity provides sufficient momentum to overcome flow recirculation at the terminal end of the SMC and minimally disturb the flow distribution and particle exit fractions. Hence, for transient simulations, particles were injected via a well-positioned SMC during the accelerating phase of the inflow waveform. Specifically, the SMC exit velocity was based on a step function that was activated during accelerating time-interval of the arterial waveform (see Fig. 6.15) and return to zero when outside the desired time interval. As expected, the SMC flow did not redistribute the system's global flow distribution nor influence the defining velocity fields. Figure 6.35 illustrates the minimal influence of the

SMC flow on the domain's flow fields by plotting the velocity vector field at the midpoint of the accelerating phase, where the SMC inflow would be fully activated.

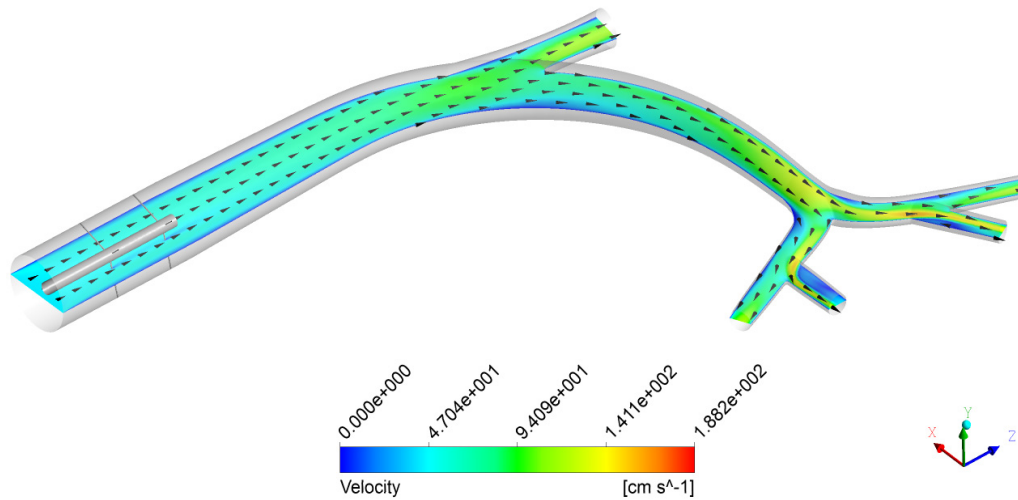


Figure 6.35: Velocity field at midpoint of accelerating region of the inflow waveform for the forty-five degree SMC-CHA domain

Particle trajectories through the domain exhibited three main paths. The first and second were streamlined pathways to daughter vessels one and four, respectively. The third path represented those particles that were left in the domain after one blood pulse. Surprisingly, over one-third of the injected particles did not exit the domain, but primarily remained in the SMC domain. Figure 6.36a depicts the particle trajectories while Fig. 6.36b plots the global exit fractions of the particles.

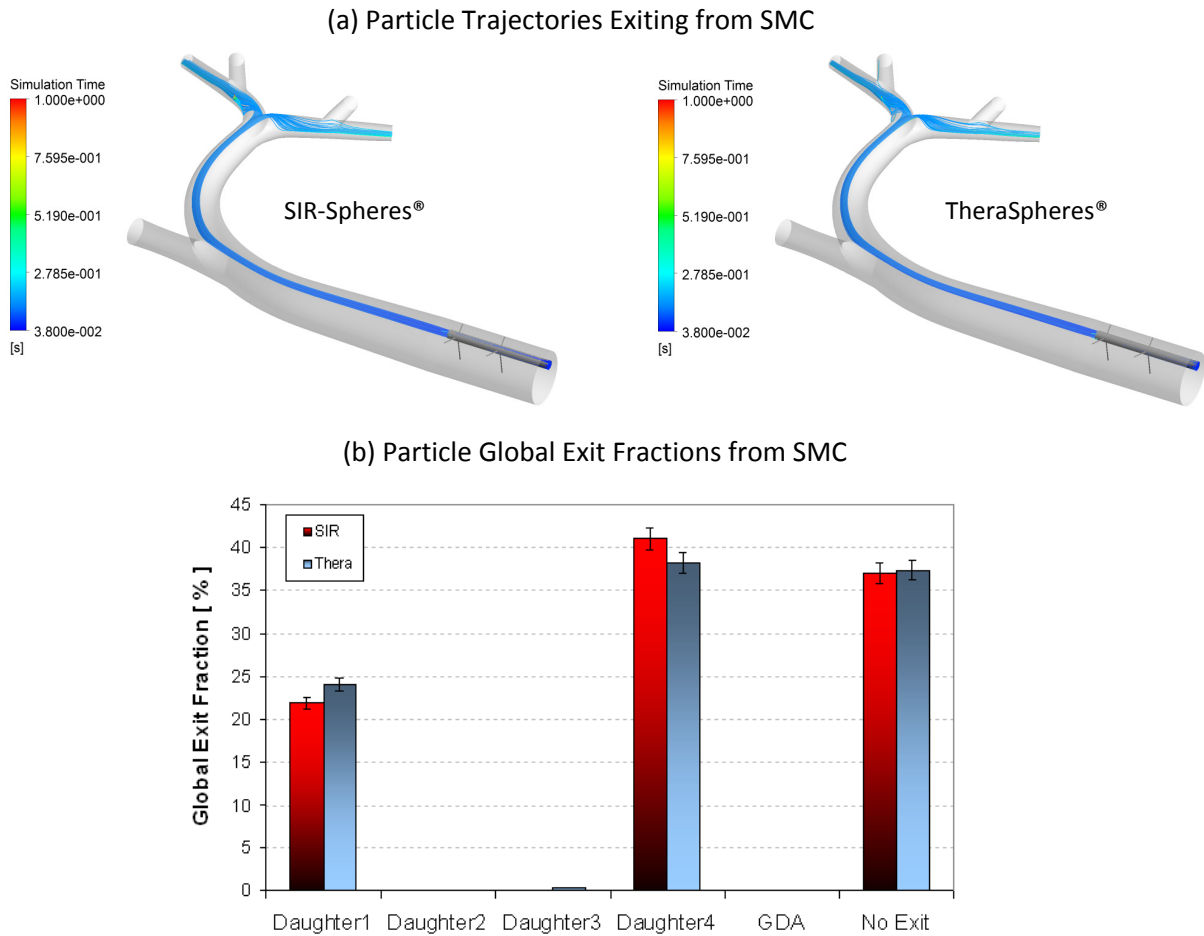


Figure 6.36: (a) Particle trajectories and (b) Global particle exit fractions for transient SMC delivery of particles

The particles that do not exit the domain were injected near the tail end of the accelerating region of the inflow waveform and were caught in suspension suddenly when the SMC inflow quickly turned off. The systolic velocity quickly followed, which was shown to create the most flow recirculation at the terminal end of the SMC, whereby, trapping the particles inside the SMC for the remainder of the pulse. TheraSpheres® had a higher exit fraction at daughter vessel 1 due to subtle differences in the particle release maps and the larger momentum built up by the TheraSpheres® from their elevated density. While less than 1% of

TheraSpheres® did exit daughter vessel three unexpectedly, the overwhelming majority of particles that exit the domain follow the transient and steady particle release maps in Figs. 6.27 and 6.30, respectively. Thus, the ability to target specific daughter vessel via appropriate spatial and temporal locations is demonstrated in the presence of the SMC. Moreover, while more studies are needed to confirm, the presence of the SMC appears to increase the GDA region for the current geometry and when using the SMC to create a particle release map for precise vessel targeting, the SMC geometry should be included in the simulation.

6.4 Transient Particle-Hemodynamics Using a Patient-Inspired, Replaced Common Hepatic Geometry Comparing Clinical, WK2, and WK4s Inflow/Outflow Waveforms

6.4.1 Transient Flow Fields for Different Inflow/Outflow Waveforms

The patient-inspired replaced hepatic geometry depicted in Fig. 6.1c was used to test the influence of different inflow/outflow waveform data sets on the particle-hemodynamics of the geometry. Three different sets of inflow and outflow waveforms were constructed from the multiple waveforms assembled in Chapter 4. The first set was composed almost entirely of the patient's clinical flow and pressure data collected at the right and left hepatic arteries. The second set was the flow and pressure waveforms of the two-element Windkessel model. The third was the flow and pressure waveforms of the four-element series Windkessel model. For all models the in-vivo pressure waveform was implemented at the RHA and flow waveforms corresponding to each data set were specified at the domain inlet, SMA outlet, and LHA outlet.

As a first measure of the influence of the inflow waveform, velocity magnitudes were measured along cross-sectional planes throughout the geometry. Figure 6.37 illustrates the location of each plane and classifies the planes into named groups.

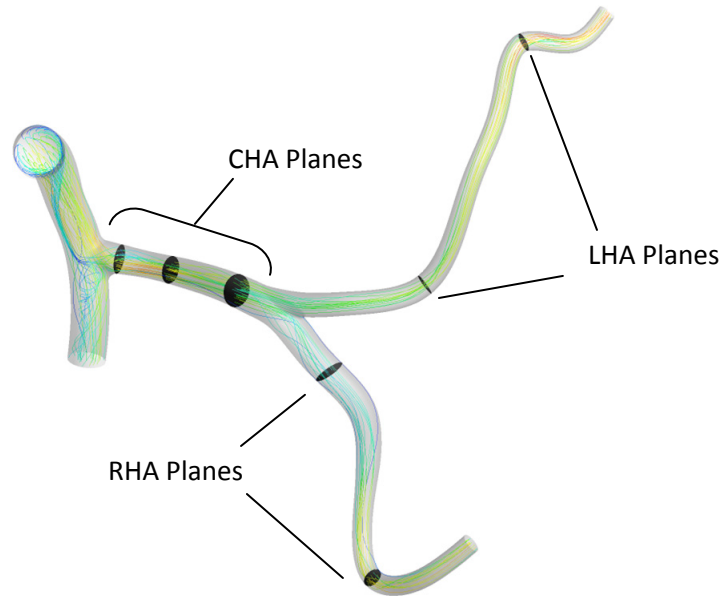
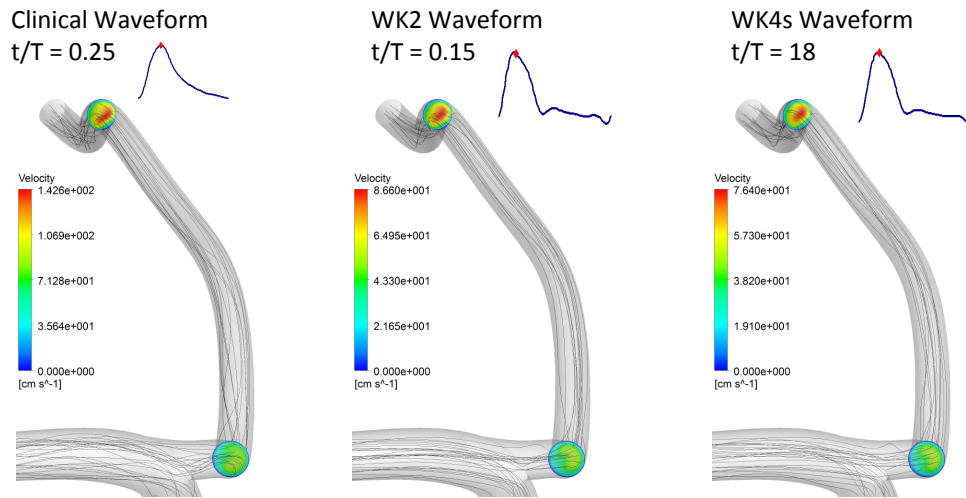


Figure 6.37: Cross-sectional planes in patient-inspired geometry

Transient velocity profiles of the different inflow waveforms in the RHA and LHA planes showed little difference throughout the physiologic pulse. Such a result is not surprising since they have minimal influence from bifurcations and upstream flow separations. Figures 6.38a and 6.38b plot the velocity magnitudes along the RHA and LHA planes for each inflow waveform's systolic velocity, respectively. Of interest is that the velocity magnitudes do vary with each waveform, but the spatial profiles are very similar.

(a) Systolic Velocity Magnitudes at the LHA Planes



(b) Systolic Velocity Magnitudes at the RHA Planes

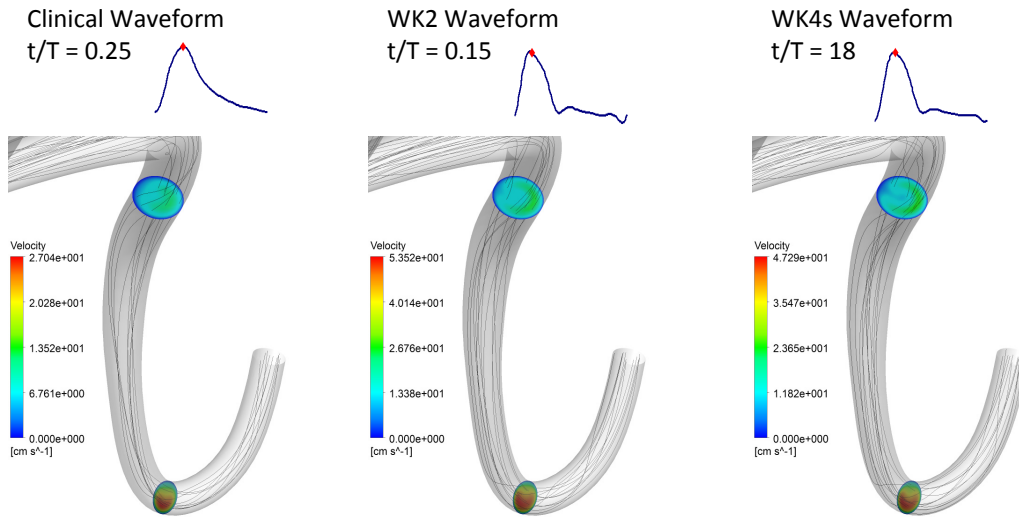


Figure 6.38: Velocity magnitudes at RHA and LHA planes for each inlet waveform's systolic velocity

The CHA planes reveal subtle differences between the waveforms throughout the pulse and the velocity magnitudes are plotted in Fig. 6.39 over the physiologic pulse.

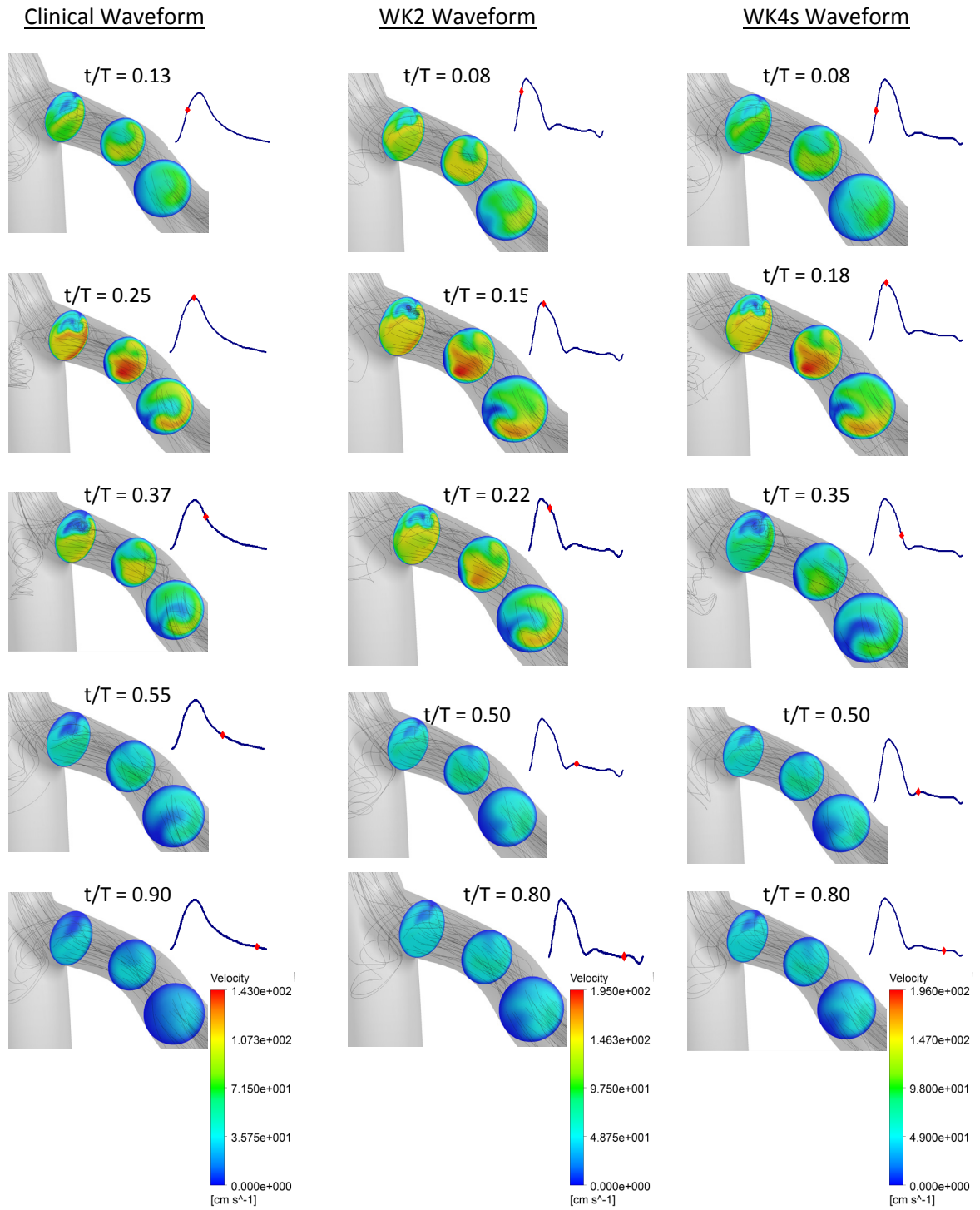


Figure 6.39: Velocity magnitudes at the CHA planes for different time points and each inlet waveform

6.4.2 Microsphere Transport considering Different Inflow/Outflow Waveforms

While the inflow waveforms did not appear to drastically influence the velocity magnitudes, the particle release maps and particle exit fractions of each waveform were also compared. For the current simulations, particles with SIR-Sphere® and TheraSphere® characteristics were injected in the accelerating region of each waveform with zero slip velocity and bulk mass flow rate that is equal to the bulk fluid mass flow rate. Particles were injected at the SMA inlet, which is where the particle release maps are constructed. The particle release maps of SIR-Spheres® and TheraSpheres® were indistinguishable and do not show many unique zones but rather the hepatic artery zones are clouded together. Figure 6.40 displays the particle release maps (representing both SIR-Spheres® and TheraSpheres®), illustrating the non-unique zones and a slight dependence on the inflow waveform.

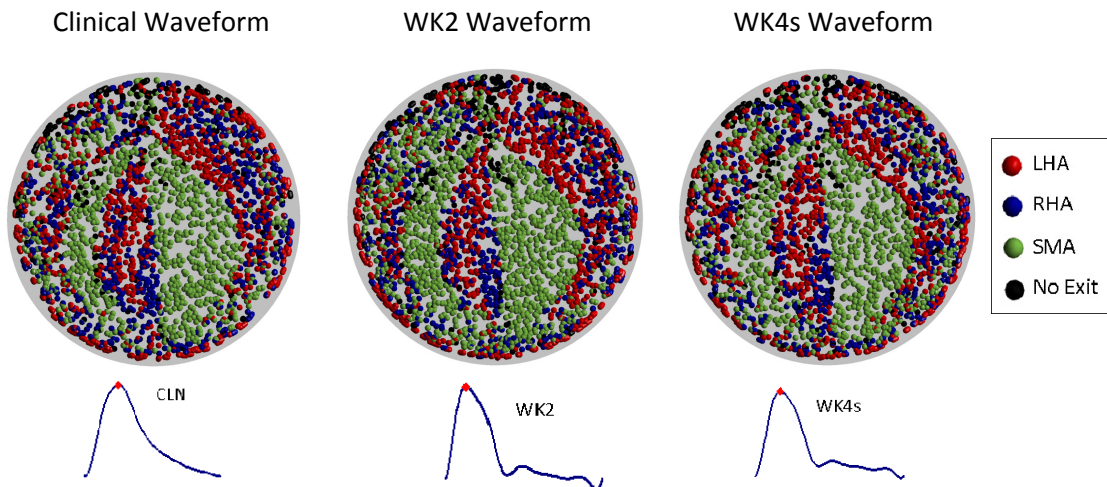


Figure 6.40: Inflow waveform influence on particle release maps

The non-unique release zones are primarily attributed to the axial release position of the microspheres. If a release position further upstream into the common hepatic artery were

completed, unique zones that could be utilized for targeting are expected. Interestingly, the particle exit fractions do exhibit some dependence on the inflow waveform. However, when comparing the particle exit fractions to the time-averaged mean flow at each outlet, the difference in particle exit fraction is attributed more to the difference in mean flow distribution than difference in waveform shape. Figure 6.41a plots the particle exit fractions and Fig. 6.41b plots the flow distribution through the domain.

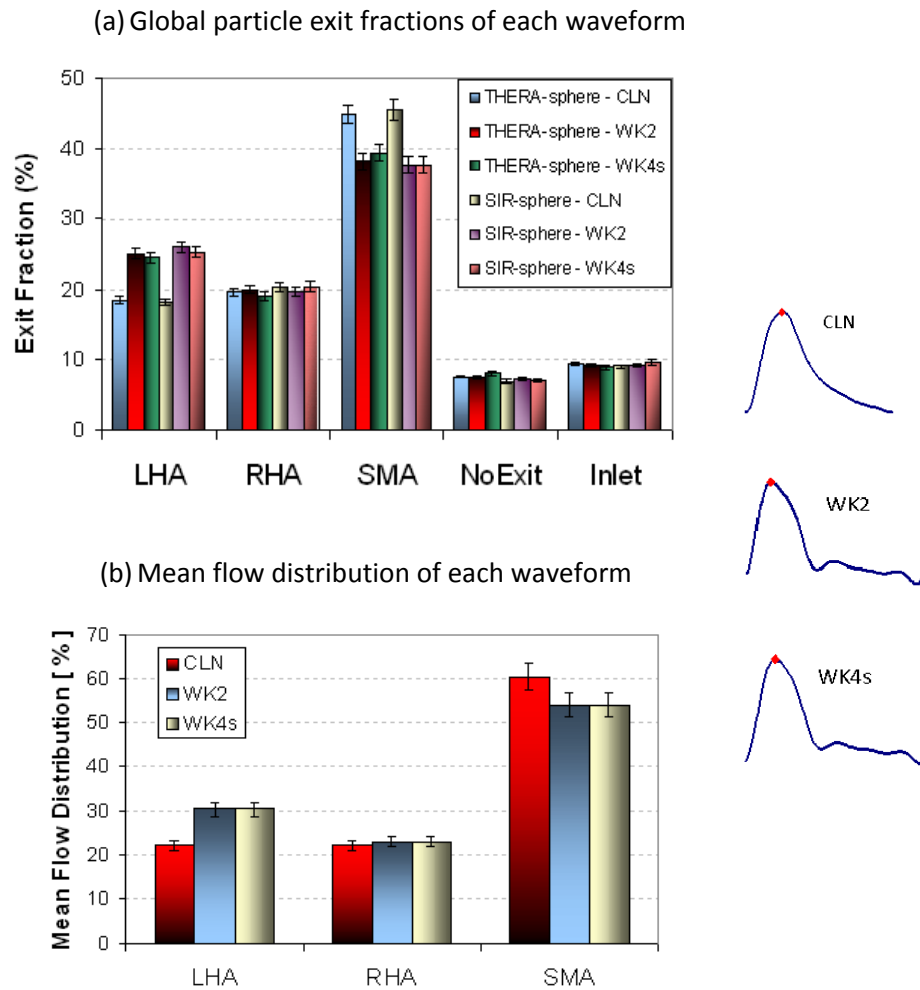


Figure 6.41: (a) Global particle exit fractions and (b) global flow distribution of each inflow waveform

The previous results suggest that the actual waveform shape is not as influential as local geometric features and the arterial system's flow distribution on the particle-hemodynamics of the arterial system. Nevertheless, having antegrade (forward) flow throughout each waveform is a crucial reason for the flow fields' similarity. If retrograde flow had been a portion of one of the waveforms, the resulting flow field would be expected to be noticeably different than those without retrograde flow. The primary limitation of the study is its use of a single geometry. Thus, additional geometries will need to be tested with a similar analysis to draw stronger and more definitive conclusions that would hold for a large number of patients. The results still hold promise despite the limitation because no other study has attempted to analyze the influence of different waveforms on the system's particle-hemodynamics.

6.5 Yttrium-90 Microsphere Injection Conditions Recommended for Liver Targeting

One key motivations of the ^{90}Y -microsphere transport analysis was to identify some important conditions for controlled daughter vessel targeting. The previous results have clearly shown that radial and axial positions of the injection point greatly influence the terminal locations of the injected microspheres and hence enable a new degree of vessel targeting precision. Another factor that was shown to have a role in particle delivery was the time interval when the particles were injected. Clearly, the accelerating time zone of the pulse was demonstrated to be most favorable to reduce particle dispersion and random behavior. The last parameter was the injection velocity of the aqueous microsphere-suspension, which was shown to have a crucial impact on the particles' ability to cross blood-

flow streamlines or remain entrapped within the delivery catheter. Thus, the determined range of microsphere carrier fluid velocities was determined to be greater than 0.01 and less than two times the surrounding blood's average velocity. The combination of all the parameters does not guarantee the ability to achieve precise liver targeting for every patient, but they will greatly enhance the potential for selective targeting and hopefully initiate additional studies refining such a targeting procedure.

6.6 Conclusions

The previous chapter described a novel particle-hemodynamic analysis of ^{90}Y -microsphere transport in steady and transient hepatic artery flows. A new concept of cross-sectional positioning was introduced for daughter-vessel targeting and was shown to be effective for both types of clinically available microspheres. The SMC position and injection velocity may influence fluid flow and particle transport, actually revealing that while the local influence may not be negligible, unique cross-sectional particle release zones were still observed. Finally, the arterial waveform was shown to only have a subtle influence on blood flow and particle transport, while the mean flow distribution was shown to have a direct correlation to the particle exit fractions. The knowledge points from the analysis pave the way for new investigations and enhanced ^{90}Y -microsphere therapy aimed at the improvement of people's lives.

Chapter 7:

Research Summary, Conclusions, and Future Work

7.1 Research Summary

In conclusion, both projects' research objectives have been met. The hypothesis of critical particle-hemodynamics in a patient-specific abdominal aortic aneurysm (AAA) being correlated with intraluminal thrombus (ILT) formation was tested and supported by the selective fluid-particle entrapment and particle surface-stress in the AAA sac. A new degree of microsphere control and targeting has been introduced by selecting appropriate spatial and temporal release positions. Additionally, both AAA and hepatic arterial systems now have novel characterizations of: i) transient shear stress loads in the AAA sac and ii) flow and pressure waveforms in the hepatic arteries. The investigation's collective results lend new

physical insight of ILT formation in AAAs and microsphere transport in the hepatic arteries, which will hopefully improve: i) clinical understanding of both processes and ii) the medical treatment of AAAs and liver tumors.

7.2 Conclusions

Using the same fluid-particle transport theory, a deductive research approach was utilized to investigate the particle-hemodynamics of: i) blood cell entrapment and loading in an abdominal aortic aneurysm (AAA) and ii) microsphere transport and targeting in the hepatic arteries. The completed particle-hemodynamics analysis is the first of its kind, utilizing transient fluid-particle transport theory to investigate AAAs and hepatic arteries and included multiple novel contributions to the scientific community.

A single AAA patient's particle-hemodynamics inside the AAA sac was correlated with future intraluminal thrombus (ILT) development, where elevated blood particle residence times and potentially thrombogenic shear stress exposure existed at near-wall regions that eventually developed ILT. The particle shear stress calculation used a novel extension of drag force theory to spherical, micron particles and is the first attempt of calculating particle shear stress loads inside the AAA sac. Residence times and oscillations of the blood continuum in the AAA sac were shown to correlate with particle depositions along the AAA lumen wall and suggest localized regions of enhanced potential for ILT formation.

The first set of recommended conditions for microsphere targeting of liver tumors was determined by particle-hemodynamics analyses of microsphere transport in the hepatic artery. Primary factors influencing the microsphere terminal locations for a given arterial

geometry were the spatial and temporal microsphere release positions and the microsphere injection velocity. The accelerating portion of the inflow waveform enabled the most streamlined and controlled transport of injected microspheres. Spatial microsphere injection conditions were shown to be geometry-dependent and are slightly altered by the presence of the injection catheter. Inflow waveform shape did not appear to have a notable influence on microsphere transport, whereas mean flow distribution played a more significant role. All transient computational simulations in the hepatic arteries utilized novel sets of flow-rate and pressure waveforms that were constructed from *in vivo* clinical measurements.

The completed work has notable clinical relevance as both investigations generate new knowledge that characterizes serious pathological conditions. Thus, while the current study is a novel application of computational modeling, the fundamental inspiration is to enhance the clinician's ability to better treat both conditions and thus improve lives.

7.3 Future Work

A first step for future work is to extend the current research results to bench-top experiments. For the AAA study, investigating platelet and white blood cell behavior after being exposed to similar shear stress loads reported in the current study would be crucial to assess the cells' physical activation level in AAAs. For microsphere targeting, proof-of-concept experiments testing the ability to target specific daughter vessels by the cross sectional and axial release position are crucial for providing physical evidence of the new targeting method.

Another recommended direction is to extend the current work to multiple geometries. Both the AAA and microsphere transport utilized a small number of arterial geometries, and focused on developing simulation parameters that characterize the corresponding analysis. Thus, an important next step is to repeat the completed analysis on new AAA and hepatic artery geometries. Unfortunately, obtaining such geometries is not trivial since patient data sets chronicling ILT formation or providing the needed resolution for detailed hepatic segmentation are rare. The potential outcomes from analyzing multiple geometries are well worth the needed effort to overcome these obstacles, because more data sets would provide stronger conclusions of the tested hypotheses and begin the process of extrapolating the results from one simulation to an entire patient population.

Other notable directions are to begin working on a quantitative index that would report the potential of ILT formation from local residence times, shear induced clotting activation, previous ILT presence, and AAA morphologic features. Another index could be related to predicted microsphere trajectories based on vessel curvature, mean flow distributions and spatial and/or temporal release positions. The goal of such indexes would be to group a collection of known parameters that influence clinical outcomes into a single parameter that would enable physicians to better administer a patient's recommended treatment.

The novelty of the present work and the current results will hopefully inspire new investigations that seek to improve medical treatment of AAAs and liver tumors. In particular, the author hopes that this analysis will provide fresh ideas to tackling existing problems and a strong foundation that future work can easily extend to new discoveries.

REFERENCES

- Ackerman, N.B., Lien, W.M., Kondi, E.S., Silverman, N.A., 1969, "The blood supply of experimental liver metastases I: The distribution of hepatic artery and portal vein blood to "small" and "large" tumors." *Sugery*, **66(6)**:1067-1072.
- Ahn, C.S., Lee, S.G., Hwang, S., Moon, D.B., Ha, T.Y., Lee, Y.J., Park, K.M., Kim, K.H., Kim, Y.D., Kim, K.K., 2005, "Anatomic variation of the right hepatic artery and its reconstruction for living donor liver transplantation using right lobe graft." *Transplantation Proceedings*, **37**:1067-1069.
- Araujo, R.P., McElwain, D.L., 2004, "A history of the study of solid tumour growth: The contribution of mathematical modeling." *Bulletin of Mathematical Biology*, **66**:1039-1091.
- Armaly, B.F., Durst, F., Pereira, J.C.F., Schönung, B., 1983, "Experimental and theoretical investigation of backward-facing step flow." *Journal of Fluid Mechanics*, **127**:473-496.
- Adolph, R., Vorp, D.A., Steed, D.L., Webster, M.W., Kameneva, M.N., Watkins, S.C., 1997, "Cellular content and permeability of intraluminal thrombus in abdominal aortic aneurysm." *Journal of Vascular Surgery*, **25**:916-926.
- Barthelmes, D., Parviainen, I., Vainio, P., Vanninen, R., Takala, J., Ikonen, A., Tueller, D., Jakob, S.M., 2009, "Assessment of splanchnic blood flow using magnetic resonance imaging." *Journal of Gastroenterology and Hepatology*, **21**:693-700.
- Basciano, C.A., Ng, J.H.Y., Finol, E.A., Kleinstreuer, C., 2009, "A relation between particle hemodynamics and intraluminal thrombus formation in abdominal aortic aneurysms." *Proceedings of the ASME 2009 Summer Bioengineering Conference*, Lake Tahoe, CA.
- Basciano, C.A., Kleinstreuer, C., 2009, "Invariant-based anisotropic constitutive models of healthy and aneurysmal abdominal aortic aneurysm wall." *Journal of Biomechanical Engineering (AMSE)*, **131**:DOI:10.1115/1.3005341.
- Basciano, C.A., 2007, *Computational analysis and simulation of the non-linear arterial wall dynamics with application to abdominal aortic aneurysms*. MS Thesis under Prof. Clement Kleinstreuer. Department of Mechanical and Aerospace Engineering at North Carolina State University, Raleigh, NC.

- Befeler, A.S., Di Bisceglie, A.M., 2002, "Hepatocellular carcinoma: Diagnosis and treatment." *Gastroenterology*, **122**:1609-1619.
- Biasetti, J., Gasser, T.C., Auer, M., Hedin, U., Labruto, F., 2010, "Hemodynamics of the normal aorta compared to fusiform and saccular abdominal aortic aneurysms with emphasis on a potential thrombus formation mechanics." *Annals of Biomedical Engineering*, **38(2)**:380-390:DOI:10.10007/s10439-009-9843-6.
- Biswas, G., Breuer, M., Durst, F., 2004, "Backward facing step flows for various expansion ratios at low and moderate Reynolds numbers." *Journal of Fluids Engineering (ASME)*, **126**:362-374.
- Bluestein, D., Niu, L., Schoepfoerster, R.T., Dewanjee, M.K., 1997, "Fluid dynamics of arterial stenosis: Relationship to the development of mural thrombus." *Annals of Biomedical Engineering*, **25**:344-356.
- Bluestein, D., Niu, L., Schoepfoerster, R.T., Dewanjee, M.K., 1996, "Steady flow in an aneurysm model: Correlation between fluid dynamics and blood platelet deposition." *Journal of Biomechanical Engineering (ASME)*, **118**:280-286.
- Boschetti, F., Di Martino, E., Gioda, G., 2007, "A poroviscoelastic model of intraluminal thrombus from abdominal aortic aneurysms." *Proceedings of the ASME 2007 Summer Bioengineering Conference*, Keystone, CO, USA.
- Bosch, F.X., Ribes, J., Borrás, J., 1999, "Epidemiology of primary liver cancer." *Seminars in Liver Disease*, **19**:271-285.
- Boutsianis, E., Guala, M., Olgac, U., Wildermuth, S., Hoyer, K., Ventikos, Y., Poulidakos, D., 2009, "CFD and PTV steady flow investigation in an anatomically accurate abdominal aortic aneurysm." *Journal of Biomechanical Engineering (ASME)*, **131**: DOI: 10.1115/1.3002886.
- Bruix, J., Sherman, M., 2005, "Management of hepatocellular carcinoma." *Hepatology*, **6**:1208-1236.
- Buchanan, J.R., Kleinstreuer, C., Comer, J.K., 2000, "Rehological effects on pulsatile hemodynamics in a stenosed tube." *Computers and Fluids*, **29**:695-724.
- Buchanan, J.R., 2000, *Computational Particle Hemodynamics in the Rabbit Abdominal Aorta*. PhD Dissertation under Prof. Clement Kleinstreuer. Department of Mechanical and Aerospace Engineering at North Carolina State University, Raleigh, NC.

- Burattini, R., Di Salvia, P.O., 2007, "Development of systemic arterial mechanical properties from infancy to adulthood interpreted by four-element windkessel models." *Journal of Applied Physiology*, **103**:66–79.
- Bushi, D., Grad, Y., Einav, S., Yodfat, O., Nishri, B., Tanne, D., 2005, "Hemodynamic evaluation of embolic trajectory in an arterial bifurcation: an in-vitro experimental model." *Stroke*, **36**:2696-2700.
- Cabibbo, G., Latteri, F., Antonucci, M., Craxi, A., 2009, "Multimodal approaches to the treatment of hepatocellular carcinoma." *Nature Clinical Practice Gastroenterology & Hepatology*, **6**:159-169.
- Campbell, A.M., Bailey, I.H., Burton, M.A., 2000, "Analysis of the distribution of intra-arterial microspheres in human liver following hepatic yttrium-90 microsphere therapy." *Physics in Medicine and Biology*, **45**:1023-133.
- Carlisle, K.M., Halliwell, M., Read, A.E., Wells, P.N., 1992, "Estimation of total hepatic flow by duplex ultrasound." *Gut*, **33**:92-97.
- Choke, E., Cockerill, G., Wilson, W.R.W., Sayed, S., Dawson, J., Loftus, I., Thompson, M.M., 2005, "A review of biological factors implicated in abdominal aortic aneurysm rupture." *European Journal of Vascular Surgery*, **30**:227-244.
- Comer, J.K., Kleinstreuer, C., Zhang, Z., 2001, "Flow structures and particle deposition patterns in double-bifurcation airway models - Part 1: Air flow fields." *Journal of Fluid Mechanics*, **435**:25-54.
- Dai, J., Louedec, L., Philippe, M., Michel, J-B., Houard, X., 2009, "Effect of blocking platelet activation with AZD6140 on development of abdominal aort aneurysm in a rat aneurysmal model." *Journal of Vascular Surgery*, **49**:719-727.
- da Silveira, L.A., Silveira, F.B.C., Fazan, V.P.S., 2009, "Arterial diameter of the celiac trunk and its branches. Anatomical study." *Acta Cirúrgica Brasileira*, **24(1)**:044-047.
- Dawson, L.A., McGinn, C.J., Normolle, D., Ten Haken, R.K., Walker, S., Ensminger, W., Lawrence, T.S., 2000, "Escalated focal liver radiation and concurrent hepatic artery fluorodeoxyuridine for unresectable intrahepatic malignancies." *Journal of Clinical Oncology*, **18(11)**:2210-2218.
- Dezső, K., Bugyik, E., Papp, V., László, V., Döme, B., Tóvári, J., Tímár, J., Nagy, P., Paku, S., 2009, "Development of arterial blood supply in experimental liver metastases." *The American Journal of Pathology*, **175(2)**:835-843.

- Di Martino, E., Matero, S., Inzoli, F., Melissano, G., Astore, D., Chiesa R., Fumero R., 1998, "Biomechanics of abdominal aortic aneurysm in the presence of endoluminal thrombus: Experimental characterization and structural static computational analysis." *European Journal of Vascular and Endovascular Surgery*, **15(4)**:290-299.
- Doyle, B.J., Eng, A.C., Burke, P.E., Grace, P.A., Walsh, M.T., Vorp, D.A., McGloughlin, T.M., 2009, "Vessel asymmetry as an additional diagnostic tool in the assessment of abdominal aortic aneurysms." *Journal of Vascular Surgery*, **49**:443-454.
- El-Serag, H.B., Rudolph, K.L., 2007, "Hepatocellular carcinoma: Epidemiology and molecular carcinogenesis." *Gastroenterology*, **132(7)**:2557-2576.
- Fectics, B., Nevo, E., Chen, C.H., Kass, D.A., 1999, "Parametric Model Derivation of Transfer Function for Noninvasive Estimation of Aortic Pressure by Radial Tonometry." *IEEE Transactions of Biomedical Engineering*, **46**:698-706.
- Finol, E.A., Amon, C.H., 2002, "Flow-induced wall shear stress in abdominal aortic aneurysms: Part II – pulsatile flow hemodynamics." *Computer Methods in Biomechanics and Biomedical Engineering*, **5**:319-328.
- Fontaine, V., Touat, Z., Mtairag, E.M., Vranckx, R., Louedec, L., Houard, X., Andreassian, B., Sebbag, U., Palombi, T., Jacob, M.P., Meilhac, O., Michel, J.B., 2004, "Role of leukocyte elastase in preventing cellular re-colonization of the mural thrombus." *American Journal of Pathology*, **164(6)**:2077-2087.
- Fontaine, V., Jacob, M.P., Houard, X., Rossignol, P., Plissonnier, D., Angles-Cano, E., Michel, J.B., 2002, "Involvement of the mural thrombus as a site of protease release and activation in human aortic aneurysms." *American Journal of Pathology*, **161(5)**:1701-1710.
- Fox, S.I., 1996, *Human Physiology 5th Edition*. Wm. C. Brown Publishers, Dubuque, IA.
- Frauenfelder, T., Lotfey, M., Boehm, T., Wildermuth, S., 2006, "Computational fluid dynamics: Changes in abdominal aortic aneurysm after stent-graft implantation." *CardioVascular and Interventional Radiology*, **29**:613-623:DOI10.1007/s00270-005-0227-5.
- Fraser, K.H., Meagher, S., Blake, J.R., Easson, W.J., Hoskins, P.J., 2008, "Characterization of abdominal aortic velocity waveform in patients with abdominal aortic aneurysm." *Ultrasound in Medicine and Biology*, **34(1)**:73–80.

- Gasser, T.C., Görgülü, G., Folkesson, M., Swedenborg, J., 2008, "Failure properties of intraluminal thrombus in abdominal aortic aneurysm under static and pulsating mechanical loads." *Journal of Vascular Surgery*, **48**:179-188.
- Georgakarakos, E., Ioannou, C.V., Kamarianakis, Y., Papaharilaou, Kostas, T., Manousaki, E., Katsamouris, A.N., 2010, "The role of geometric parameters in the prediction of abdominal aortic aneurysm wall stress." *European Journal of Vascular and Endovascular Surgery*, **39**:42-48.
- Guadagni, S., Pizzutilli, A., Mancini, E., Varrone, A., Palumbo, G., Amicucci, G., Perri, S., Deraco, M., Fiorentini, G., 2000, "Significance of duplex/colour Doppler sonography in hepatic arterial chemotherapy for patients with liver metastases from colorectal carcinoma." *European Journal of Surgical Oncology* **26**:381-386.
- Guimarães, T.A.S., GGarcia, G.N., Dalio, M.B., Bredarioli, M., Bezerra, C.A.P., Moriya, T., 2008, "Morphological aspects of mural thrombi deposition residula lume route in infrarenal abdominal aortic aneurysms." *Acta Cirúgica Brasileira*, **23**(Supplement1):151-156.
- Han, S.H.B., Rice, S., Cohen, S.M., Reynolds, T.B., Fong, T.L., 2002, "Duplex Doppler ultrasound of the hepatic artery in patients with acute alcoholic hepatitis." *Journal of Clinical Gastroenterology*, **34**(5):573-577.
- Hans, S.S.S., Jareunpoon, O., Balasubramaniam, M., Zelenock, G.B., 2005, "Size and location of thrombus in intact and ruptured abdominal aortic aneurysms." *Journal of Vascular Surgery*, **41**(4):584-588.
- Harter, L.P., Gross, B.H., Callen, R.A., Barth, R.A., 1982, "Ultrasonic evaluation of abdominal aortic thrombus." *Journal of Ultrasound in Medicine*, **1**:315-318.
- He, C.M., Roach, M.R., 1994, "The composition and mechanical properties if abdominal aortic aneurysms." *Journal of Vascular Surgery*, **20**:6-13.
- He, X., Ku, D.N., 1996, "Pulsatile flow in the human left coronary artery bifurcation: average conditions." *Journal of Biomechanical Engineering (ASME)*, **118**:74-82.
- Hiatt, J.R., Gabbay, J., Busuttil, R.W., 1994, "Surgical Anatomy of the Hepatic Arteries in 1000 Cases." *Annals of Surgery*, **220**(1):50-52.
- Himburg, H.A., Grzybowski, D.M., Hazel, A.L., LaMack, J.A., Li, X.-M., Friedman, M.H., 2004, "Spatial comparison between wall shear stress measures and porcine arterial endothelial permeability." *American Journal of Physiology – Heart and Circulatory Physiology*, **286**:1916-1922:doi:10.1152/ajpheart.00897.2003.

- Hinnen, J.W., Rixen, D.J., Koning, O.H., van Bockel, J.H., Hamming, J.F., 2007, "Development of fibrinous thrombus analogue for in-vitro abdominal aortic aneurysm studies." *Journal of Biomechanics*, **40(2)**:289-295.
- Hirata, M., Akbar, S.M.F., Horiike, N., Onji, M., 2001, "Noninvasive diagnosis of the degree of fibrosis using ultrasonography in patients with chronic liver disease due to hepatitis C virus." *European Journal of Clinical Investigation*, **31**: 528-535.
- Hochmuth, R.M., 1986, "Properties of red blood cells," In: Skalak, R., Chein, S., eds., *Handbook of Bioengineering*. McGraw-Hill Co., New York, NY.
- Hoffman, R-T., Jakobs, T.F., Reiser, M.F., 2008, "Identification of candidates and selection criteria." Eds. Bilbao, J.I., Reiser, M.F., *Liver Radioembolization with ⁹⁰Y Microspheres*, Springer-Verlag, Berlin, pp:11-14.
- Horn, J.R., Zierler, B., Bauer, L.A., Reiss, W., Strandness, D.E., Jr, 1990, "Estimation of hepatic blood flow in branches of hepatic vessels utilizing a noninvasive, duplex, Doppler method." *The Journal of Clinical Pharmacology*, **30**: 922-929.
- Houard X., Touat, Z., Ollivier, V., Louedec, L., Philippe, M., Sebbag, U., Meilhac, O., Rossignol, P., Michel, J-B., 2009, "Mediators of neutrophil recruitment in human abdominal aortic aneurysms." *Cardiovascular Research*, **82**:532-541.
- Houard, X., Rouzet, F., Touat, Z., Philippe, M., Dominguez, M., Fontaine, V., Sarda-Mantel, L., Meulemans, A., Le Guludec, D., Meilhac O., Michell, J-B., 2007, "Topology of the fibrinolytic system within the mural thrombus of human abdominal aortic aneurysms." *Journal of Pathology*, **212**: 20–28.
- Houard, X., Leclercq, A., Fontaine, V., Coutard, M., Martin-Ventura, J-L., Ho-Tin-Noé, B., Touat, Z., Meilhac, O., Michel, J-B., 2006, "Retention and activation of blood-borne proteases in the arterial wall: Implications for atherothrombosis." *Journal of the American College of Cardiology*, **48(9)**:A3-A9.
- Hübner, G.H., Steudel, N., Kleber, G., Behrmann, C., Lotterer, E., Fleig, W.E., 2000, "Hepatic artery blood flow velocities: assessment by transcutaneous and intravascular Doppler sonography." *Journal of Hepatology*, **32**:893-899.
- Hyun, S., Kleinstreuer, C., Longest, P.W., Chen, C., 2004, "Particle-hemodynamics simulations and design options for surgical reconstruction of diseased carotid artery bifurcations." *Journal of Biomechanical Engineering (ASME)*, **126(2)**:188–195.

- Ishigami, K., Zhang Y., Rayhill S., Katz D., Stolpen, A., 2004, "Does variant hepatic artery anatomy in a liver transplant recipient increase the risk of hepatic artery complications after transplantation?" *American Journal of Roentgenology*, **183**:1577-1584.
- Jakab, F., Rath, Z., Schmal, F., Nagy P., Falller, J., 1996, "Changes in hepatic hemodynamics due to primary liver tumours." *HPB Surgery*, **9**:245-248.
- Jamison, R.A., Sheard, G.J., Ryan, K., 2007 "Non-axisymmetric flow development in pulsatile blood flow through an Aneurysm." *16th Australasian Fluid Mechanics Conference*, Gold Coast, Australia.
- Jakobs, T.F., 2008, "Radiological detection and assessment of tumor response." Eds. Bilbao, J.I., Reiser, M.F., *Liver Radioembolization with ⁹⁰Y Microspheres*, Springer-Verlag, Berlin, pp:93-106.
- Jin, N., Lewandowski, R.J., Omary, R.A., Larson, A.C., 2009, "Respiratory self-gaiting for free-breathing abdominal phase-contrast blood flow measurements." *Journal of Magnetic Resonance Imaging*, **29**:860-868.
- Karino, T., Goldsmith, H.L., 1977, "Flow behavior of blood cells and rigid spheres in an annular vortex." *Philosophical Transactions of the Royal Society of London. Series B, Biological Sciences*, **279(967)**:413-445.
- Kazi, M., Thyberg, J., Religa, P., Roy, J., Eriksson, P., Hedin, U., Swedenborg, J., 2003, "Influence of intraluminal thrombus on structural and cellular composition of abdominal aortic aneurysm wall." *Journal of Vascular Surgery* **38**:1283-1292.
- Kennedy, A., Kleinstreuer, C., Basciano, C.A., Dezarn, A., 2010, "Computer modeling of ⁹⁰Y microsphere transport in the hepatic arterial tree to improve clinical outcomes." *International Journal of Radiation Oncology Biology Physics (Red Journal)*, **76(2)**:631-637.
- Kennedy, A.S., Salem, R., 2010, "Radioembolization (Yttrium-90 microspheres) for primary and metastatic hepatic malignancies." *The Cancer Journal*, **16(2)**:163-175.
- Kennedy, A.S., 2010, "Radiation therapy for hepatocellular carcinoma." Ed. Carr, B.I., *Hepatocellular Carcinoma: Diagnosis and Treatment Second Edition*. Humana Press, New York, NY, pp:615-640.
- Kennedy, A.S., Dezarn, W.A., McNeillie, P., 2008a, "90Y microspheres: Concepts and principles." Eds. Bilbao, J.I., Reiser, M.F., *Liver Radioembolization with ⁹⁰Y Microspheres*, Springer-Verlag, Berlin, pp:1-9.

- Kennedy, A.S., Dezarn, W.A., McNeillie, P., 2008b, "Dosimetry and dose calculation" Eds. Bilbao, J.I., Reiser, M.F., *Liver Radioembolization with ⁹⁰Y Microspheres*, Springer-Verlag, Berlin, pp:51-59.
- Kennedy, A.S., Dezarn, W.A., McNeillie, P., Coldwell, D., Nutting, C., Carter, D., Murthy, R., Rose, S., Warner, R.R., Liu, D., Palmedo, H., Overton, C., Jones, B., Salem, R., 2008c, "Radioembolization for unresectable neuroendocrine hepatic metastases using resin 90Y-microspheres: early results in 148 patients." *American Journal of Clinical Oncology*, **31(3)**:271-279.
- Kennedy, A., Nag, S., Salem, R., Murthy, R., McEwan, A.J., Nutting, C., Benson, A., Eespat, J., Bilbao, J.I., Sharma, R.A., Thomas, J.P., Coldwell, D., 2007, "Recommendations for radioembolizations of hepatic malignancies using yttrium-90 microsphere brachytherapy: a consensus panel report from the radioembolization brachytherapy oncology consortium." *International Journal of Radiology Oncology Biology Physics (Red Journal)*, **68(1)**:13-23.
- Kennedy, A.S., Coldwell, D., Nutting, C., Murthy, R., Wertman Jr., D.E., Loehner, S.P., Overton, C., Meranze, S., Niedzwiecki, J., Sailer, S., 2006, "Resin 90Y-Microsphere brachytherapy for unresectable colorectal liver metastases: modern USA experience." *International Journal of Radiology Oncology Biology Physics (Red Journal)*, **65(2)**:412-425.
- Kennedy, A.S., Nutting, C., Coldwell, D., Gaiser, J., Drachenberg, C., 2004, "Pathological response and microdosimetry of 90Y microspheres in man: review of four explanted whole livers." *International Journal of Radiation Oncology Biology Physics (Red Journal)*, **60(5)**:1552-1563.
- Khanafer, K.M., Bull, J.L., Berguer, R., 2009, "Fluid-structure interaction of turbulent pulsatile flow within a flexible wall axisymmetric aortic aneurysm model." *European Journal of Mechanics B/Fluids*, **28**:88-102.
- Kim, C.S., Fisher, D.M., 1999, "Deposition characteristics of aerosol particles in sequentially bifurcating airway models." *Journal of Aerosol Science and Technology*, **31**:198-220.
- Kito, Y., Nagino, M., Nimura, Y., 2001, "Doppler sonography of hepatic arterial blood flow velocity after percutaneous transhepatic portal vein embolization." *American Journal of Roentgenology*, **176**:919-912.
- Kleinstreuer, C., 2010, *Modern Fluid Dynamics: Basic Theory and Selected Applications in Macro- and Micro-Fluidics*. Springer, Dordrecht, The Netherlands.

- Kleinstreuer, C., 2009, "Methods and devices for targeted injection of radioactive microspheres." *U.S. Patent Application* 61/127,889, July 28; NC State University, Raleigh, NC.
- Kleinstreuer, C., Zhang, Z., Donohue, J.F., 2008, "Targeted drug-aerosol delivery in the human respiratory system." *Annual Reviews in Biomedical Engineering*, **10**:195-220.
- Kleinstreuer, C., Li, Z., Farber, M., 2007, "Fluid-structure interaction analyses of stented abdominal aortic aneurysms." *Annual Review of Biomedical Engineering*, **9**:169-204.
- Kleinstreuer, C., 2006, *Biofluid Dynamics: Principles and Selected Applications*. CRC Press: Taylor and Francis, Boca Raton, FL.
- Kleinstreuer, C., Li, Z., 2006, "Analysis and computer program for rupture-risk prediction of abdominal aortic aneurysms." *Biomedical Engineering Online*, **5**:19-32.
- Kleinstreuer, C., 2003, *Two-Phase Flow: Theory and Applications*. Taylor and Francis, New York, NY.
- Koops, A., Wojciechowski, B., Broering, D.C., Adam, G., Krupski-Berdien, G., 2004, "Anatomic variations of the hepatic arteries in 604 selective celiac and superior mesenteric angiographies." *Surgical and Radiologic Anatomy*, **26**:239-244.
- Laird, A.K., 1964, "Dynamics of tumor growth." *British Journal of Cancer*, **18**:490-502.
- Lasheras, J.C., 2007, "The biomechanics of arterial aneurysms." *Annual Review of Fluid Mechanics*, **39**:293-319.
- Lau, W.Y., Leung, W.T., Ho, S., Leung, N.W., Chan, M., Lin, J., Metreweli, C., Johnson, P., Li, A.K., 1994, "Treatment of inoperable hepatocellular carcinoma with intrahepatic arterial yttrium-90 microspheres: a phase I and II study." *British Journal of Cancer*, **70**:994-999.
- Lee, T., Mateescu, D., 1998, "Experimental and numerical investigation of 2-D backward-facing step flow." *Journal of Fluids and Structures*, **12**:703-716.
- Leen, E., Goldberg, J.A., Robertson, J., Sutherland, G.R., Hemingway, D.M., Cooke, T.G., McArdle, C.S., 1991, "Detection of hepatic metastases using duplex/color Doppler sonography." *Annals of Surgery*, **214**(5):599-604.

- Les, A.S., Shadden, S.C., Figueroa, A., Park, J.M., Tedesco, M.M., Herfkens, R.J., Dalman, R.L., Taylor, C.A., 2010a, "Quantification of hemodynamics in abdominal aortic aneurysms during rest and exercise using magnetic resonance imaging and computational fluid dynamics." *Annals of Biomedical Engineering*, **38(4)**:1288-1313:DOI:10.1007/s10439-010-9949-x.
- Les, A.S., Yeung, J.J., Schultz, G.M., Herfkens, R.J., Dalman, R.L., Taylor, C.A., 2010b, "Supraceliac and infrarenal aortic flow in patients with abdominal aortic aneurysms: Mean flows, waveforms, and allometric scaling relationships." *Cardiovascular Engineering and Technology*, **1(1)**:39–51DOI: 10.1007/s13239-010-0004-8.
- Lewandowski, R.J., Kulik, L.M., Riaz, A., Senthilnathan, S., Mulcahy, M.F., Ryu, R.K., Ibrahim, S.M., Sato, K.T., Baker, T., Miller, F.H., Omary, R., Abecassis, M., Salem, R., 2009, "A comparative analysis of transarterial downstaging for hepatocellular carcinoma: chemoembolization versus radioembolization." *American Journal of Transplantation*, **9(8)**:1920-1928.
- Lien, W.M., Ackerman, N.B., 1970, "The blood supply of experimental liver metastases II: A microcirculatory study of the normal and tumor vessels of the liver with the use of perfused silicone rubber." *Surgery*, **68(2)**:334-340.
- Li, Z., Kleinstreuer, C., 2007, "A comparison between different asymmetric abdominal aortic aneurysm morphologies employing computational fluid–structure interaction analysis." *European Journal of Mechanics B/Fluids*, **26**:615-631.
- Li, Z., Kleinstreuer, C., 2005, "Blood flow and structure interaction in a stented abdominal aortic aneurysm model." *Medical Engineering and Physics*, **27**:369-382.
- Lindholt, J.S., Jørgensen, B., Fasting, H., Henneberg, E.W., 2001, "Plasma levels of plasmin-antiplasmin-complexes are predictive for small abdominal aortic aneurysms expanding to operation-recommendable sizes." *Journal of Vascular Surgery*, **34(4)**:611-615.
- Liu, L.X., Zhang, W.H., Jiang, H.C., 2003, "Current treatment for liver metastases from colorectal cancer." *World Journal of Gastroenterology*, **9(2)**:193-200.
- Longest, P.W., Kleinstreuer, C., Buchanan, J.R., 2004, "Efficient computation of micro-particle dynamics including wall effects." *Computers and Fluids*, **33**:577-601.
- Longest, P.W., 2002, *Computational Analyses of Transient Particle Hemodynamics with Applications to Femoral Bypass Graft Designs*. PhD Dissertation under Clement Kleinstreuer. Department of Mechanical and Aerospace Engineering at North Carolina State University, Raleigh, NC.

- Marieb, E.N., 1998, *Human Anatomy and Physiology 4th Edition*. Benjamin Cummings Science Publishing Menlo Park, CA.
- Martufi, G., Di Martino, E.S., Amon, C.H., Muluk, S.C., Finol, E.A., 2009, "Three-Dimensional geometrical characterization of abdominal aortic aneurysms: Image-based wall thickness distribution." *Journal of Biomechanical Engineering (ASME)*, **131(6)**:DOI:10.1115/1.3127256.
- Meade, V.M., Burton, M.A., Gray, B.N., Self, G.W., 1987, "Distribution of different sized microspheres in experimental hepatic tumors." *European Journal of Clinical Oncology*, **23(1)**:37-41.
- Merrill, E.W., 1969, "The rheology of blood." *Physiological Reviews* **26**:863-888.
- Michels, N.A., 1966, "Newer anatomy of the liver and its variant blood supply and collateral circulation." *American Journal of Surgery*, **112**:337-347.
- Moloni, D.S., Callanan, A., Kavanagh, E.G., Walsh, M.T., McGloughlin, T., 2009, "Fluid structure interaction of a patient-specific abdominal aortic aneurysm treated with an endovascular stent-graft." *Biomedical Engineering Online*, **8**:DOI:10.1186/1475-925X-8-24.
- Moore, J.E., Ku, D., 1994, "Pulsatile velocity measurements in a model of the human abdominal aorta under simulated exercise and postprandial conditions." *Journal of Biomechanical Engineering (ASME)*, **116**:107-111.
- Muraki, N., 1983, "Ultrasonic studies of the abdominal aorta with special reference to hemodynamic considerations on thrombus formation in the abdominal aortic aneurysm." *Journal of Japanese College Angiology*, **23**:401-413.
- Murthy, R., Nunez, R., Szklaruk, J., Erwin, W., Madoff, D.C., Gupta, S., Ahar, K., Wallace, M.J., Cohen, A., Coldwell, D.M., Kennedy, A.S., Hicks, M.E., 2005, "Yttrium-90 microsphere therapy for hepatic malignancy: Devices, indications, technical considerations, and potential complications." *RadioGraphics*, **25**:S41-S55.
- Nakamura, T., Moriyasu, F., Ban, N., Nishida, O., Tamada, T., Kawasaki, T., Sakai, M., Uchino, H., 1989, "Quantitative measurement of abdominal arterial blood flow using image-directed Doppler sonography: Superior mesenteric, splenic, and common hepatic blood flow in adults." *Journal of Clinical Ultrasound*, **17**:261-268.
- Nakeeb, A., Pitt, H.A., Sohn, T.A., Coleman, J., Abrams, R.A., Piantadosi, S., Hruban, R.H., Lillemo, K.D., Yeo, C.J., Cameron, J.L., 1996, "Cholangiocarcinoma. A spectrum of intrahepatic, perihilar, and distal tumors." *Annals of Surgery*, **224(4)**:463-475.

- Nichols, W.W., O'Rourke, M.F., 2005, *McDonalds Blood Flow in Arteries: Theoretical, Experimental, and Clinical Principles 5th Edition*. Hodder Arnold: Oxford University Press, New York, NY.
- Oktar, S.O., Yücel, C., Demirogullari, T., Üner, A., Benekli, M., Erbas, G., Özdemir, H., 2006, "Doppler sonographic evaluation of hemodynamic changes in colorectal liver metastases relative to liver size." *Journal of Ultrasound in Medicine*, **25**:575-582.
- Olufsen, M.S., Peskin, C.S., Yong Kim, W., Pederson, E.M., Nadim, A., Larsen, J., 2000, "Numerical simulation and experimental validation of blood flow in arteries with structured-tree outflow conditions." *Annals of Biomedical Engineering*, **28**:1281-1299.
- O'Rourke, M.J., McCullough, J.P., 2008, "A comparison of the measured and predicted flowfield in a patient-specific model of an abdominal aortic aneurysm." *Journal of Engineering in Medicine*, **222(H)**:737-750: DOI: 10.1243/09544119JEIM357.
- Panek, B., Gacko M., Palka, J., 2004, "Metalloproteinases, insulin-like growth factor-I and its binding proteins in aortic aneurysm." *International Journal of Experimental Pathology*, **85**:159-164.
- Panton, R.L., 2005, *Incompressible Flow 3rd Edition*. John Wiley and Sons Inc., Hoboken, NJ.
- Pappu, S., Dardik, A., Tagare, H., Gusberg, R.J., 2008, "Beyond fusiform and saccular: a novel quantitative tortuosity index may help classify aneurysm shape and predict aneurysm rupture potential." *Annals of Vascular Surgery*, **22**:88-97.
- Peattie, R.A., Riehle, T.J., Bluth, E.I., 2004, "Pulsatile flow in fusiform models of abdominal aortic aneurysms: Flow fields, velocity patterns and flow-induced wall stresses." *Journal of Biomechanical Engineering (ASME)*, **126**:438-446:DOI: 10.1115/1.1784478.
- Perišić, M., Jurišić, V., Kerkez, M., 2009, "Doppler ultrasonography of hepatic artery in malignant liver tumors." *Archive of Oncology*, **16(3-4)**:46-48.
- Pui, D.H., Romay-Novas, F., Liu, B.Y.H., 1987, "Experimental study of particle deposition in bends of circular cross section." *Journal of Aerosol Science and Technology*, **7(3)**:301-315.
- Qamar, M.I., Read, A.E., Skidmore, R., Evans, J.M., Wells, P.N.T., 1986, "Transcutaneous Doppler ultrasound measurement of superior mesenteric artery blood flow in man." *Gut*, **27**:100-105.

- Radeleff, B., Sommer, C-M., Heye, T., Lopez-Benitez, R., Sauer, P., Schmidt, J., Kauczor, H-U., Richter, G.M., 2009, "Acute increase in hepatic arterial flow during TIPS identified by intravascular flow measurements." *Cardiovascular and Interventional Radiology*, **32**:32-37.
- Raz, S., Einav, S., Alemu, Y., Bluestein, D., 2007, "DPIV prediction of flow induced platelet activation – comparison to numerical predictions." *Annals of Biomedical Engineering*, **35**(4):493-504:DOI:10.1007/s10439-007-9257-2.
- Riaz, A., Lewandowski, R.J., Kulik, L.M., Mulcahy, M.F., Sato, K.T., Ryu, R.K., Omary, R.A., Salem, R., 2009, "Complications following radioembolization with Yttrium-90 microspheres: A comprehensive review." *Journal of Vascular and Interventional Radiology*, **20**:1121-1130.
- Robertson, P.L., Ten Haken, R.K., McShan, D.L., McKeever, P.E., Ensminger, W.D., 1992, "Three-dimensional tumor dosimetry for hepatic Yttrium-90-microsphere therapy." *Journal of Nuclear Medicine*, **33**:735-738.
- Rodriguez, J., Chopitea, A., Viudez, A., Garcia-Foncillas, J., 2008, "⁹⁰Y microspheres for other liver metastases." Eds. Bilbao, J.I., Reiser, M.F., *Liver Radioembolization with ⁹⁰Y Microspheres*, Springer-Verlag, Berlin, pp:125-134.
- Sakalihasan, N., Delvenne, P., Nusgens, B.V., Limet, R., Lapière, C.M., 1996, "Activated forms of MMP2 and MMP9 in abdominal aortic aneurysms." *Journal of Vascular Surgery*, **24**:127-33.
- Salem, R., Thurston, K.G., 2006, "Radioembolization with ⁹⁰Yttrium microspheres: A state-of-the-art brachytherapy treatment for primary and secondary liver malignancies. Part 1: Technical and methodological considerations." *Journal of Vascular and Interventional Radiology*, **17**:1251-1278.
- Salem, R., Lewandowski, R.J., Atassi, B., Gordon, S.C., Gates, V.L., Barakat, O., Sergie, Z., Wong, C-Y.O., Thurston, K.G., 2005, "Treatment of Unresectable Hepatocellular Carcinoma with Use of ⁹⁰Y Microspheres (TheraSphere): Safety, Tumor Response, and Survival." *Journal of Vascular and Interventional Radiology*, **16**:1627–1639.
- Salsac, A-V., Sparks, S.R., Chomaz, J-M., Lasheras, J.C., 2006, "Evolution of the wall shear stresses during progressive enlargement of symmetric abdominal aortic aneurysms." *Journal of Fluid Mechanics*, **560**:19-51.
- Salsac, A-V., Sparks, S.R., Lasheras, J.C., 2004, "Hemodynamic changes occurring during the progressive enlargement of abdominal aortic aneurysms." *Annals of Vascular Surgery*, **18**:14-21:DOI:10.1007/s10016-003-0101-3.

- Sangro, B., Carpanese, L., Ezzidin, S., Kolligs, F., Golfieri, R., Gasparini, D., Cianni, R., Bilbao, I., Maini, C., Wilhelm, K., Hoffmann, R., Geatti, O., Salvatori, R., 2009, "Nodularity is a strong predictor of survival following treatment with radioembolisation using 90Y-labelled resin microspheres in unresectable hepatocellular carcinoma: Preliminary results from a European multi-centre evaluation." *Proceedings of the 3rd Annual Liver Cancer Association Conference*, September 4-6, Milan, Italy.
- Sato, S., Ohnishi, K., Sugita, S., Okuda, K., 1987, "Splenic artery and superior mesenteric artery blood flow: nonsurgical Doppler US measurement in healthy subjects and patients with chronic liver disease." *Radiology*, **164**:347-352.
- Săftoiu, A., Ciurea, T., Gorunescu, F., 2002, "Hepatic arterial blood flow in large hepatocellular carcinoma with or without portal vein thrombosis: assessment by transcutaneous duplex Doppler sonography." *Journal of Gastroenterology and Hepatology*, **14**:pp.167-176.
- Schmid-Schoenbein, G.W., 1986, "Rheology of leukocytes," In: Skalak, R., Chien, S., eds., *Handbook of Bioengineering*. McGraw-Hill Co., New York, NY.
- Schurink, G.W.H., van Baalen, J.M., Visser, M.J.T., van Bockel, J.H., 2000, "Thrombus within an aortic aneurysm does not reduce pressure on the aneurysm wall." *Journal of Vascular Surgery*, **31**:501-506.
- Schoepherster, R.T., Oynes, F., Nunez, G., Kapadvanjwala, M., Dewanjee, M.K., 1993, "Effects of local geometry and fluid dynamics on regional platelet deposition on artificial surfaces." *Arteriosclerosis, Thrombosis, and Vascular Biology*, **13**:1806-1813.
- Scott, E.M., 1986, *Cardiovascular Physiology: An Integrative Approach*. Manchester University Press, Wolfeboro, NH.
- Scotti, C.M., Finol, E.A., 2007, "Compliant biomechanics of abdominal aortic aneurysms: A fluid–structure interaction study." *Computers and Structures*, **85**:1097-1113.
- Segers, P., Rietzschel, E.R., De Buyzere, M.L., Stergiopoulos, N., Westerhof, N., Van Bortel, L.M., Gillebert, T., Verdonck, P.R., 2008, "Three- and four-element Windkessel models: assessment of their fitting performance in a large cohort of healthy middle-aged individuals." *Journal of Engineering in Medicine*, **222(H)**:417-428.

- Shadden, S.C., Les. A.S., Taylor, C.A., 2008, "Lagrangian analysis of rest and exercise hemodynamics in patient-specific abdominal aortic aneurysm models." *8th. World Congress on Computational Mechanics and 5th. European Congress on Computational Methods in Applied Sciences and Engineering*, Venice, Italy.
- Shankaran, H., Alexandridis, P., Neelamegham, S., 2003, "Aspects of hydrodynamic shear regulating shear-induced platelet activation and self-association of von willebrand factor in suspension." *Blood*, **101**:2637-2645.
- Sheu, T.W.H., Rani, H.P., 2006, "Exploration of vortex dynamics for transitional flows in three-dimensional backward-facing step channel." *Journal of Fluid Mechanics*, **550**:61-83.
- Sidery, M.B., Macdonald, I.A., Blackshaw, P.E., 1994, "Superior mesenteric artery blood flow and gastric emptying in humans and the differential effects of high fat and high carbohydrate meals." *Gut*, **35**:186-190.
- Sieber, C., Beglinger, C., Jäger, K., Stalder, G.A., 1992, "Intestinal phase of superior mesenteric artery blood flow in man." *Gut*, **33**:497-501.
- Silverberg, E., Boring, C.C., Squires, T.S., 1990, "Cancer Statistics." *A Cancer Journal for Clinicians*, **40**:9-26.
- Someya, N., Yamaoka Endo, M., Fukuba, Y., Hayashi, N., 2008, "Blood flow responses in the celiac and superior mesenteric arteries in the initial phase of digestion." *The American Journal of Physiology – Regulatory, Integrative, and Comparative Physiology*, **294**:R1790-R1796.
- Speelman, L., Schurink, G.W.H., Bosboom, M.H., Buth, J., Breeuwer, M., van de Vosse, F.N., Jacobs, M.H., 2010, "The mechanical role of thrombus on the growth rate of an abdominal aortic aneurysm." *Journal of Vascular Surgery*, **51**:19-26.
- Stålhand, J., 2009, "Determination of human wall parameters from clinical data." *Biomechanics and Modeling in Mechanobiology*, **8**:141-148.
- Steinman, D.A., Vorp, D.A., Ethier, C.R., 2003, "Computational modeling of arterial biomechanics: Insight into pathogenesis and treatment of vascular disease." *Journal of Vascular Surgery*, **37**:1118-1128.
- Stenbaek, J., Kalin, B., Swedenborg, J., 2000, "Growth of thrombus is a better predictor for rupture than diameter in patients with abdominal aortic aneurysms." *European Journal of Vascular and Endovascular Surgery*, **20**:466-469.

- Stergiopoulos, N., Westerhof, B.E., Westerhof, N., 1999, "Total arterial inertance as the fourth element of the windkessel model." *American Journal of Physiology - Heart and Circulation Physiology*, **276**:81-88.
- Sudhamshu, K.C., Matsutani, S., Maruyama, H., Akiike, T., Saisho H., 2006, "Doppler study of hepatic vein in cirrhotic patients: Correlation with liver dysfunction and hepatic hemodynamics." *World Journal of Gastroenterology*, **12(36)**:5853-5858.
- Swedenborg, J., Eriksson, P., 2006, "The intraluminal thrombus as a source of proteolytic activity." *Annals of the New York Academy of Sciences*, **1085**:133-138.
- Tanaka, S., Kitamura, T., Fujita, M., Nakanishi, K., Okuda, S., 1990, "Color Doppler flow imaging of liver tumors." *American Journal of Roentgenology*, **154**:509-514.
- Thubrikar, M.J., Robicsek, F., Labrosse, M., Chervenkov, V., Fowler, B.L., 2003, "Effect of thrombus on abdominal aortic aneurysm wall dilation and stress." *Journal of Cardiovascular Surgery*, **44**:67-77.
- Thubrikar, M.J., Labrosse, M., Robicsek, F., Al-soudi, J., Fowler, B., 2001, "Mechanical properties of abdominal aortic aneurysm wall." *Journal of Medical Engineering and Technology*, **25(4)**:133-142.
- Touat, Z., Ollivier, V., Dai, J., Huisse, M.G., Rossignol, P., Meilhac, O., Guillin, M.C., Michel, J.B., 2006, "Renewal of mural thrombus releases plasma markers and is involved in aortic abdominal aneurysm evolution." *American Journal of Pathology*, **163(3)**:1022-1030:DOI:10.2353/ajpath.2006.050868.
- Truijers, M., Fillinger, M.F., Renema, K.J.W., Marra, S.P., Oostveen, L.J., Kurvers, H.A.J.M., SchultzeKool, L.J., Blankensteijn, J.D., 2009, "In-vivo imaging changes in abdominal aortic aneurysm thrombus volume during the cardiac cycle." *Journal of Endovascular Therapy*, **16**:314-319.
- Urbonavicius, S., Lindholt, J.S., Vorum, H., Urbonaviciene, G., Henneberg, E.W., Honoré, B., 2009, "Proteomic identification of differentially expressed proteins in aortic wall of patients with ruptured and nonruptured abdominal aortic aneurysms." *Journal of Vascular Surgery*, **49**:455-463.
- Uzawa, M., Karasawa, E., Sugiura, N., Saotome, N., Kita, K., Fukuda, H., Miki, M., Togawa, Y., Kondou, F., Matsutani, S., Ohto, M., 1993, "Doppler color flow imaging in the detection and quantitative measurement of the gastroduodenal blood flow." *Journal of Clinical Ultrasound*, **21**:9-17.

- Vallabhaneni, S.R., Gilling-Smith, G., How, T.V., Carter, S.D., Brennan, A., Harris, P.L., 2004, "Heterogeneity of tensile strength and matrix metalloproteinase activity in the wall of abdominal aortic aneurysms." *Journal of Endovascular Therapy*, **11**:494-502.
- Van Hazel, G., Turner, D., Gebiski, V., 2009, "Impact of 90Y resin microspheres on health-related quality of life (HRQoL) in patients with colorectal cancer (CRC) liver metastases receiving first-line chemotherapy." *Proceedings of the American Society of Clinical Oncology (ASCO) Gastrointestinal Cancers Symposium*, Orlando, FL.
- Van Hazel, G., Blackwell, A., Anderson, J., Price, D., Moroz, P., Bower, G., Cardaci, G., Gray, B., 2004, "Randomised phase 2 trial of SIR-Spheres® plus fluorouracil/leucovorin chemotherapy versus fluorouracil/leucovorin chemotherapy alone in advanced colorectal cancer." *Journal of Surgical Oncology*, **88(2)**:78-85.
- Vande Geest, J.P., Wang, D.H.J., Wisniewski, S.R., Makaroun, M.S., Vorp, D.A., 2006a, "Towards a noninvasive method for determination of patient specific wall strength distribution in abdominal aortic aneurysms." *Annals of Biomedical Engineering*, DOI:10.1007/s10439-006-9132-6, **34**:1098-1106.
- Vande Geest, J.P., Sacks, M.S., Vorp, D.A., 2006b, "The effects of aneurysm on the biaxial mechanical behavior of human abdominal aorta." *Journal of Biomechanics*, **39**:1324-1334.
- Vande Geest, J.P., Sacks, M.S., Vorp, D.A., 2006c, "A planar biaxial constitutive relation for the luminal layer of intraluminal thrombus in abdominal aortic aneurysms." *Journal of Biomechanics*, **39**:2347-2354.
- Vauthey, J.N., Abdalla, E.K., Doherty, D.A., Gertsch, P., Fenstermacher, M.J., Loyer, E.M., Lerut, J., Materne, R., Wang, X., Encarnacion, A., Herron, D., Mathey, C., Ferrari, G., Charnsangavej, C., Do, K.A., Denys, A., 2002, "Body surface area and body weight predict total liver volume in western adults." *Liver Transplantation*, **8(3)**:233-240.
- Vega de Céniga, M., Gómez, R., Estallo, L., de la Fuente, N., Viviens, B., Barba, A., 2008, "Analysis of expansion patterns in 4-4.9 cm abdominal aortic aneurysms." *Annals of Vascular Surgery*, **22**:37-44.
- Vorp, D.A., 2007, "Biomechanics of abdominal aortic aneurysm." *Journal of Biomechanics*, **40**:1887-902.
- Vorp, D.A., Vande Geest, J.P., 2005 "Biomechanical determinants of abdominal aortic aneurysm rupture." *Arteriosclerosis Thrombosis Vascular Biology*, **25**:1558-1566.

- Vorp, D.A., Lee, P.C., Wang, D.H.J., Makaroun, M.S., Nemoto, E.M., Ogawa, S., Webster, M.W., 2001, "Association of intraluminal thrombus in abdominal aortic aneurysm with local hypoxia and wall weakening." *Journal of Vascular Surgery*, **34**:291-299.
- Vorp, D.A., Wang, D.H.J., Webster, M.W., Federspiel, W.J., 1998, Effect of intraluminal thrombus thickness and buldge diameter on the oxygen diffusion in abdominal aortic aneurysm." *Journal of Biomechanical Engineering* (ASME), **120**:579-583.
- Vorp, D.A., Raghavan, M.L., Muluk, S.C., Makaroun, M.S., Steed, D.L., Shapiro, R., Webster, M.W., 1996, "Wall strength and stiffness of aneurismal and nonaneurysmal abdominal aorta." *Annals of the New York Academy of Sciences*, **800**:274-276.
- Wang, D.H.J., Makaroun, M.S., Webster, M.W., Vorp, D.A., 2002, "Effect of intraluminal thrombus on wall stress in patient-specific models of abdominal aortic aneurysm." *Journal of Vascular Surgery*, **36**:598-604.
- Wang, D.H.J., Makaroun, M., Webster, M.W., Vorp, D.A., 2001, "Mechanical properties and microstructure of intraluminal thrombus from abdominal aortic aneurysm." *Journal of Biomechanical Engineering* (ASME), **123**:536-539.
- Westerhof, N., Lankhaar, J-W., Westerhof, B.E., 2009, "The arterial windkessel." *Medical and Biological Engineering and Computing*, **47**:131-141:DOI:10.1007/s11517-008-0359-2.
- Wolf, Y.G., Thmoas, W.S., Brennan, F.J., Goff, W.G., Sise, M.J., Bernstein, E.F., 1994, "Computed tomography scanning findings associated with rapid expansion of abdominal aortic aneurysms." *Journal of Vascular Surgery*, **20**:529-535; discussion:535-538.
- Wurzinger, L.J., Opitz, R., Blasberg, P., Schmid-Schonbein, H., 1985, "Platelet and coagulation parameters following milisecond exposure to laminar shear stress." *Journal of Thrombosis and Haemostasis*, **54**:381-386.
- Yamazumi, K., Ojira, M., Okumura, H., Aikou, T., 1998, "An activated stae of blood coagulation and fibrinolysis in patients with abdominal aortic aneurysm." *The American Journal of Surgery*, **175**:297-301.
- Zhang, Z., Kleinstreuer, C., Donohue, J.F., Kim, C.S., 2005, "Comparison of micro-and nano-size particle depositions in a human upper airway model." *Journal of Aerosol Science*, **36(2)**:211-233.
- Zhao, Y., Lieber, B.B., 1994, "Steady inspiratory flow in a model symmetric bifurcation." *Journal of Biomechanical Engineering* (ASME), **166**:488-497.

Zoli, M., Magalotti, D., Bianchi, G., Gueli, C., Orlandini, C., Grimaldi, M., Marchesini, M., 1999, "Total and functional hepatic blood flow decrease in parallel with ageing." *Age and Ageing*, **28**:29-33.

Zwiebel, W.JMountford, R.A., Halliwell, M.J., Wells, P.N.T., 1995, "Splanchnic blood flow in patients with cirrhosis and portal hypertension: Investigation with Duplex Doppler US." *Radiology*, **194**:807-812.

APPENDICES

APPENDIX I: Select Clinical Trials of Yttrium-90

Radioembolization of Primary and Metastatic Liver Malignancies

Introduction

The outcomes of select clinical trials utilizing ^{90}Y -radioembolization to treat primary and secondary liver malignancies will be highlighted in the current section. While the therapy is increasing in popularity and clinical acceptance, phase III trials of ^{90}Y -radioembolization as a first-line of treatment are still ongoing. Nevertheless, at least thirty prospective clinical trials have been reported and the existing retrospective trials have shown encouraging results of relatively low side effects and high response rates (Kennedy and Salem, 2010).

Clinical Trials Results

A phase II randomized trial by Van Hazel et al. (2004) was conducted on first time treatments of chemotherapy with and without ^{90}Y resin microspheres on unresectable colorectal liver metastatic tumors. Eleven patients received the combined therapy where only ten received the chemotherapy alone. The study revealed that a single dose of ^{90}Y -microspheres showed a significant improvement in response rate compared to the chemotherapy alone (91% vs. 0% , $P < 0.001$). Moreover, the time to progression of the combined therapy was noticeably longer than the chemotherapy alone (18.6 vs. 3.6 months , $P < 0.0005$) and the median overall survival after treatment of the ^{90}Y microspheres plus chemotherapy was 29.4 months compared to the chemotherapy alone of 12.8 months ($P <$

0.02). Interestingly, Van Hazel et al. (2009) found that patients who received ^{90}Y -radioembolization plus chemotherapy exhibited a higher quality of life three months subsequent to receiving the therapy compared to those only receiving chemotherapy ($P < 0.03$). Kennedy and Salem (2010) also reported second and third line salvage treatments where ^{90}Y -radioembolization showed sufficient disease response and stabilization in many patients who no longer responded to chemotherapy alone.

Salem et al. (2005) conducted a phase II clinical trial that included forty-three patients receiving first line and second line treatments of hepatocellular carcinoma. Subsequent to therapy, 47% of the patients exhibited objective tumor response when using tumor size as the objective criteria and 79% of patients showed an objective response when tumor size and/or necrosis changes was used as the response criteria. Median overall survival times for Okuda I and II tumor severities was 24.4 and 12.5 months, respectively. A trial by Sangro et al. (2009) showed that for 252 patients with hepatocellular carcinoma treated with ^{90}Y -radioembolization (not as a first-line treatment) the median survival was 14.5 months (range 12.4 – 18.4 months). Lewandowski et al. (2009) conducted a direct comparison between forty-three patients undergoing ^{90}Y -radioembolization and forty-three patients undergoing transarterial chemoembolization (TACE) of hepatocellular carcinoma also reported favorable outcomes for ^{90}Y -radioembolization. The median time of event-free survival was 17.7 vs. 7.1 months ($P < 0.0017$) for the ^{90}Y -radioembolization vs. TACE, respectively. Additionally, the overall survival of ^{90}Y -radioembolization surpassed that of TACE with 35.7 to 18.7 months ($P < 0.18$) for censored patients and 41.6 to 19.2 months ($P < 0.008$) for uncensored patients.

Conclusions

Other metastatic liver tumors have been successfully treated by ⁹⁰Y-radioembolization. A prominent study is by Kennedy et al. (2008c) that showed an overall response rate of 63% and a median overall survival of 70 months for metastatic liver malignancies from neuroendocrine cancer. The results from this study and many others (see Kennedy and Salem, 2010 for others) show the great potential for ⁹⁰Y-radioembolization to increase medical practitioners' ability to treat liver malignancies with greater degree of effectiveness. Of additional importance, is that most clinical trials report minimal side effects with little to no deaths due to the ⁹⁰Y-radioembolization treatment. As the treatment continues to gain more acceptance and more phase III first-line clinical trials are completed, the future of ⁹⁰Y-radioembolization yields exciting possibilities to treat liver malignancies with increased effectiveness and safety.

APPENDIX II: Custom MATLAB Code Used to Process Clinical Hemodynamics Data from Hepatic Arteries

Summary

Appendix II lists the custom MATLAB code that was created to automatically segment a continuous pulsatile hemodynamic signal into multiple periodic waveforms over a nondimensional timescale and average the different waveforms at each nondimensional timepoint to generate a representative, periodic waveform of the continuous signal. The first program is the main driving program (“SignalProcessing.m”) that calls the functions that performs the segmentation and averaging. An additional responsibility of the main drive program is to import the data from the specified file locations with the correct delimiter and spacing. The MATLAB function “dlmread” was utilized to import the numerical data starting at row four, where the first row of the file is considered the row zero. A very important note is that the program assumes that the data files are arranged in a two-column array with the format [time; signal].

The function “AutoSegU.m” performs the segmentation of the continuous signal into multiple periodic signals, the construction of the nondimensional timescales of each period, the resampling of each waveform according to the nondimensional timescale, and the calculation of each waveform’s period. Conversely, the function “AverageU.m” averages the rows of the multidimensional input array into single array of one column with multiple rows. Subsequent to the averaging, the drive program plots the resulting representative waveforms.

SignalProcessing.m

```
% PURPOSE: Process discrete continuous signal data into a single
%           representative period
%
% CODE OVERVIEW: 1) The algorithm will filter out high frequency noise
%                 using a 4th order Butterworth filter
%                 2) Determine the pulsations of the imported data and
%                 separate the different pulsations
%                 3) Average the periodic signals to yield a single
%                 waveform of the averaged results
%
%-----
%                               Written by: Christopher Basciano
%                               March 2010
%                               Mechanical and Aerospace Engineering
%                               North Carolina State University, Raleigh, NC
%-----

clear all
clc

%-----
%                               Import data and implement AutoSegU function
%-----

fpath1 = 'C:\Directory1\File1.txt';
RH1data = dlmread(fpath1, '', 4, 0);

[tnd1, RHv1] = AutoSegU(RH1data);
[n1, m1] = size(RHv1);

%-----
%                               Post-processing of data and implement AverageU function
%-----

[RHVsdv, RHVm, RHVmx, RHVmn] = AverageU(RHv1);
tnd = tnd1;

%plot representative waveform
figure
hold on
plot(tnd, RHVmx, 'ro')
plot(tnd, RHVm, 'k', 'LineWidth', 2)
plot(tnd, RHVmn, 'bo')
errorbar(tnd, RHVm, RHVsdv, 'k')
hold off
xlabel('time [t/T]')
ylabel('Representative Signal')
```

AutoSegU.m

```
% PURPOSE: Function to automatically segment the different pulses into a
%           single pulse with a non-dimensional time scale
%
%-----
%           Written by: Christopher Basciano
%           March 2010
%           Mechanical and Aerospace Engineering
%           North Carolina State University, Raleigh, NC
%-----

function [tnd,Ui] = AutoSegU(data)

%-----
%           Data Processing
%-----

%specify variables from the data file and check for appropriate time scale
[Ns,Nc] = size(data);
tr = data(:,1);
Ur = data(:,2);
for k=2:Ns
    dt = tr(k)-tr(k-1);
    if (dt==0)
        error(['Function has non-unique time points at time '
→(cont. from previous line) num2str(tr(k))])
    end
    if (dt<0)
        error(['Time does not monotonically increase ' num2str(tr(k))])
    end
end

%resample raw signal at constant dt
T = max(tr); %determine max. raw time
dt = T/2/Ns; %set constant dt based on total number of points
t = [0:dt:T]';
Uri = interp1(tr,Ur,t,'cubic'); %cubic spline interpolation
Ns = length(t);

%implement moving average smoothing
U = smooth(Uri,11);

%Calculate frequency power spectrums using FFT
Nfft = 2*Ns; %No. of fft points = 2*no. of raw data points
Fs = 1/dt; %Raw signal sampling frequency
Cr = fft(Uri,Nfft);
Cs = fft(U,Nfft);
Freq = Fs*[0:Nfft/2]'/Nfft;
```

AutoSegU.m [cont.]

```
figure
subplot(2,2,1)
plot(t,Uri)
xlabel('time')
ylabel('Parameter')
subplot(2,2,2), semilogy(Freq,abs(Cr(1:0.5*Nfft+1))/(Nfft/2))
xlabel('Frequency')
ylabel('Power')
subplot(2,2,3)
plot(t,U,'r')
xlabel('time')
ylabel('Smoothed Parameter')
subplot(2,2,4), semilogy(Freq,abs(Cs(1:0.5*Nfft+1))/(Nfft/2),'r')
xlabel('Frequency')
ylabel('Power')

figure
hold on
plot(t,Uri,'bo','MarkerSize',4.5)
plot(t,U,'r','LineWidth',2.0)
hold off
xlabel('time')
ylabel('Parameter')
legend('Raw signal','Smoothed signal')

%-----
%      Compute 1st and 2nd derivative of pulses using central difference
%-----

%Calculated 1st and 2nd derivatives of flow data
UD = zeros(Ns,1);
UD2 = zeros(Ns,1);
for i=2:Ns-2
    k = k+1;
    UD(i) = ( U(i+1)-U(i-1) ) / (2*dt);
    UD2(i) = ( U(i+1) - 2*U(i) + U(i-1) ) / (dt*dt);
end

F2 = 1e2*norm(U)/sqrt(Ns);

%filter derivative signals using 4th order butterworth filter
forder = 4;
wc = 10;
wcn = wc/Fs;
[b,a] = butter(forder,wcn,'low');          %develop butterworth filter
UD2 = filtfilt(b,a,UD2);                  %implement zero phase shift filter
UD = filtfilt(b,a,UD);
```

AutoSegU.m [cont.]

```
%plot parameter signals
figure
subplot(3,1,1)
hold on
plot(t,Uri,'bo','MarkerSize',4.5)
plot(t,U,'r')
hold off
xlabel('time')
ylabel('Parameter')
legend('Raw signal','Filtered signal')
subplot(3,1,2)
hold on
plot(t,UD,'b--')
hold off
xlabel('time')
ylabel('1^s^t Deriv. Parameter')
subplot(3,1,3)
hold on
plot(t,UD2,'b--')
plot([t(1) t(Ns)], [F2 F2], 'k:')
hold off
xlabel('time')
ylabel('2^n^d Deriv. Parameter')

%-----
%           Count, sort, and extract individual pulses data based on the
%           1st and 2nd derivatives of the data pulses
%-----

%cycle through data and construct tracking arrays of index at transition
%points, time at transitions points, and period of each pulse
ctlu = 0;
trU = zeros(1,2);
Tpu = zeros(1,1);
for k=2:Ns-1
    if (UD(k-1)<0) && (UD(k)>=0) && (UD2(k) > F2)
        ctlu = ctlu + 1;
        trU(ctlu,1) = k;
        trU(ctlu,2) = t(k);
        if ctlu > 1
            Tpu(ctlu-1,1) = trU(ctlu,2) - trU(ctlu-1,2);
        end
    end
end
end
```

AutoSegU.m [cont.]

```
%extracts individual pressure waveform pulses from the data, interpolates
%the individual waves so each wave has the same number of data points,
%nondimensionalizes the time scale based on the local/dynamic period,
%calculates integral under each wave, calculates difference between the
%upstream and downstream waves,
dti = 0.01;
tnd = [0:dti:1]';
Npts = length(tnd);
Ui = zeros(Npts,ctlu-1);
Uidiff = zeros(1,1);
UiINT = zeros(ctlu-1,1);
npF = ctlu-1;
for np=1:npF
    ctu2 = 0;
    tU = zeros(1,3);
    Up = zeros(1,1);
    Up = zeros(1,1);
    for kk=1:Ns
        if ( t(kk) >= trU(np,2) ) && ( t(kk) <= trU(np+1,2) )
            ctu2 = ctu2 + 1;
            tU(ctu2,1) = t(kk);
            tU(ctu2,2) = tU(ctu2,1)-tU(1,1);
            tU(ctu2,3) = tU(ctu2,2)/Tpu(np);
            Up(ctu2,1) = U(kk);
        end
    end
    Ui(:,np) = interp1(tU(:,3),Up,tnd,'cubic');
    UiINT(np) = trapz( tnd,Ui(:,np) );
    Uidiff(np) = abs( Ui(Npts,np) - Ui(1,np) );
end

end %end AutoSegU.m function
```

AverageU.m

```
% PURPOSE: Function to average velocity magnitudes at similar
%           non-dimensional time points throughout a physiologic pulse
%
```

```
%
```

```
%-----
```

```
%           Written by: Christopher Basciano
%           March 2010
%           Mechanical and Aerospace Engineering
%           North Carolina State University, Raleigh, NC
%-----
```

```
function [Sdv,Um, umax, umin] = AverageU(data)
```

```
%initialize data variables
```

```
U = data;
[Nr,Nc]=size(U);
Um = zeros(Nr,1);
Sdv = zeros(Nr,1);
umax = zeros(Nr,1);
umin = zeros(Nr,1);
```

```
%Loop through time points and pulse
```

```
for i=1:Nr %time point loop
    Usum = 0;
    for j=1:Nc %pulse loop
        Usum = Usum + U(i,j);
    end
    Um(i) = Usum/Nc;
    Sdv(i) = std( U(i,:) );
    umax(i) = max( U(i,:) );
    umin(i) = min( U(i,:) );
end
```

```
end %end AverageU.m function
```

APPENDIX III: Custom MATLAB Code Used to Construct Population-Averaged Windkessel Flow Waveforms

Summary

Appendix III lists the custom MATLAB code used to calculate population-averaged Windkessel flow waveforms utilizing the representative downstream pressure waveform (see Fig. 4.11) and user-specified mean and max. flow magnitudes of the resulting flow waveform. The first program (“WK_Flow_Calculations.m”) is the main drive program of the process and oversees the needed data import, WK parameter optimization, and flow waveform processing calculations. While the displayed plots in Section 4.3.4 only show the first 21 modes, the calculations are based on a frequency spectrum that is \pm half the nondimensional sampling frequency. The FFT transforms are based on the number of discrete points in the imported periodic flow and pressure waveform. To enforce the imported waveforms periodic behavior, the data point at the nondimensional timescale of unity ($t/T=1.00$) is removed since the FFT processing assumes that first data point is repeated at the end of the period. The exponential form of the Fourier series coefficients are derived by dividing the MATLAB FFT output by the number of FFT points. Individual functions calculating the percent difference of each Windkessel model’s flow waveform with the desired mean and max. flow rates are then minimized and flow distribution calculations specifically formulated for the geometry in Section 3.4 are completed. The resulting waveforms are then plotted and/or exported.

WK Flow Calculations.m

```
% PURPOSE: Use windkessel models to calculate flow waveforms that
%           correspond to pressure waveforms
```

```
%
% VARIABLES:
%     t    = discrete time
%     T    = duration of signal
%     dt   = sampling time of data
%     dtL  = time lag between max press. and flow values
%     Fs   = sampling frequency [Hz]
%     P    = pressure
%     Qwk  = windkessel-calculated flow rate
%     Zwk  = windkessel-calculated impedance
%     L    = inductance windkessel parameter
%     C    = capacitance windkessel parameter
%     R    = resistacne windkessel parameter
```

```
%-----
%                               Written by: Christopher Basciano
%                               March 2010
%                               Mechanical and Aerospace Engineering
%                               North Carolina State University, Raleigh, NC
%-----
```

```
clc
clear all
```

```
%set global variables
global PopMeanQ PopSysQ
global Pcl
```

```
%-----
%                               USER INPUT
%-----
%Specify desired mean and max flow rates in [cm3/s]:
%     Population Tumor Flow Rate: 2.684*Healthy
%         * PopHeathyMean = 2.164
%           PopHealthyMax = 4.205
%         * PopTumorMean = 5.808
%           PopTumorMax = 11.286
%         * PatientTumorMean = 4.6234
%           PatientTumorMax = 9.3777
```

```
PopMeanQ = 5.808
PopSysQ = 11.286
```

```
% END USER INPUT
```

WK Flow Calculations.m [cont.]

```
%-----  
%                               Import clinical pressure and flow data  
%-----  
  
%Import clinical RHA flow rate data  
PIQdata = dlmread('Patient1_RHA_OutFlowRate.dat');  
[rq,cq]=size(PIQdata);  
tndQ = PIQdata(1:rq-1,1);  
Qcl = PIQdata(1:rq-1,2);  
Qexport = [tndQ Qcl];  
Qclmean = mean(Qcl)  
Qclsys = max(Qcl)  
  
%import clinical pressure data  
Pdata = dlmread('Patient1_Down_Pressure.dat');  
[rp,cp]=size(Pdata);  
tndP = Pdata(1:rp-1,1);  
Pcl = Pdata(1:rp-1,2);  
  
%Calculate time-lag from systolic pressure and max flow rate  
[mxQcl,Iqx] = max(Qcl);  
[mxP,Ipx] = max(Pcl);  
dtL = tndP(Ipx) - tndQ(Iqx)  
  
%initialize general frequency parameters  
Fs = 100; %non-dimensional sampling frequency  
N = length(Pcl);  
n1 = [0:N/2]';  
n2 = [-N/2+1:-1]';  
n = [n1; n2];  
nn = 21; %number of modes (frequencies to include in plots)  
j = sqrt(-1);  
w0 = 2*pi; %base frequency  
K = j*n*w0;  
  
%-----  
%                               Clinical Fourier Coefficients of Pressure  
%-----  
  
%Calculate fft of clinical flow values  
FFTqcl = fft(Qcl,N);  
%Calculate flow exponential fourier coefficients  
fqcl = FFTqcl/N;  
  
%Calculate fft of clinical pressure values  
FFTpcl = fft(Pcl,N);  
%Calculate pressure exponential fourier coefficients  
fpcl = FFTpcl/N;
```

WK Flow Calculations.m [cont.]

```
%Calculate impedance modulus and phase
Zc1 = fpcl./fqcl;
Cln_Mod = abs(Zc1);
Cln_Phs = angle(Zc1);

%-----
%                               2-Element Windkessel model (WK2)
%-----

%Run minimization routines on WK2 Flow calculation
w0 = [10; 2];
lb = [1e-6;1e-6];
ub = [inf;100];
options = optimset('Display','iter','TolFun',1e-20,'TolX',1e-10);
[wk2,fval,exitflag,output] =
fmincon(@WK2_Flow,w0,[],[],[],[],lb,ub,[],options)

%WK2 Impedance calculation    ( Zwk2 = R / (j*n*w0*C*R + 1)
R=wk2(1);    %resistance
C=wk2(2);    %compliance
Zwk2 = R./(K*C*R+1);
WK2_Mod = abs(Zwk2);
WK2_Phs = angle(Zwk2);

%Calculate wk2 flow waveform
qwk2f = (1./Zwk2).*fpcl;    %calculate flow fourier coeff
Qwk2 = real(iff(N.*qwk2f));    % use ifft to get Q_wk2(t)
MeanQwk2 = mean(real(Qwk2));
SysQwk2 = max(real(Qwk2));

%-----
%                               3-Element Windkessel model (WK3)
%-----

%Run minimization routines on WK3 Impedance calculation
w0 = [5.0; 14; 0.01];
lb = [1e-6;1;0];
ub = [5.3;inf;0.1];
Aeq = [1 1 0; 0 0 0; 0 0 0];
Beq = [wk2(1); 0; 0];
options = optimset('Display','iter','TolFun',1e-20,'TolX',1e-10);
[wk3,fval,exitflag,output] =
fmincon(@WK3_Flow,w0,[],[],Aeq,Beq,lb,ub,[],options)

%WK3 Impedance calculation:
%    ( Zwk3 = ( j*n*w0*C*Ru*Rd + Rd + Ru ) / ( j*n*w0*C*Rd+1 )
Ru=wk3(1);    %upstream resistance
Rd=wk3(2);    %downstream resistance
C=wk3(3);    %compliance
```

WK Flow Calculations.m [cont.]

```
Zwk3 = (K*C*Ru*Rd + Rd + Ru)./(K*C*Rd+1);
WK3_Mod = abs(Zwk3);
WK3_Phs = angle(Zwk3);

%Calculate wk2 flow waveform
qwk3f = (1./Zwk3).*fpcl;    %calculate flow fourier coeff
Qwk3 = real(iff(N.*qwk3f)); % use ifft to get Q_wk2(t)
MeanQwk3 = mean(real(Qwk3));
SysQwk3 = max(real(Qwk3));

%-----
%                               4-Element Series Windkessel model (WK4s)
%-----

%Run minimization routines on WK4s Impedance calculation
w0 = [12; 15; 0.1; 0.01];
lb = [1e-6;1e-6;0.5*wk2(2);1e-3];
ub = [inf;inf;wk3(3);0.01];
Aeq = [1 1 0 0; 0 0 0 0; 0 0 0 0; 0 0 0 0];
Beq = [wk2(1); 0; 0; 0];
options = optimset('Display','iter','TolFun',1e-20,'TolX',1e-10);
[wk4s,fval,exitflag,output] =
fmincon(@WK4s_Flow,w0,[],[],[],[],lb,ub,[],options)

%WK4s Impedance calculation:
% ( Zwk4s = [L*C*Rd*(j*n*w0)^2 + (C*Ru*Rd+L)*(j*n*w0)*C*Ru*Rd + Rd + Ru] /
%                                               [j*n*w0*C*Rd + 1]
Ru=wk4s(1);    %upstream resistance
Rd=wk4s(2);    %downstream resistance
C=wk4s(3);    %compliance
L=wk4s(4);    %inductance
Zwk4s = ( (K.^2)*L*C*Rd + K*(C*Ru*Rd+L) + Rd + Ru )./( K*C*Rd+1 );
WK4s_Mod = abs(Zwk4s);
WK4s_Phs = angle(Zwk4s);

%Calculate wk4s flow waveform
qwk4sf = (1./Zwk4s).*fpcl;    %calculate flow fourier coeff
Qwk4s = real(iff(N.*qwk4sf)); % use ifft to get Q_wk4s(t)

%-----
%                               4-Element Parallel Windkessel model (WK4p)
%-----

%Run minimization routines on WK4p Impedance calculation
w0 = [53.5; 18; wk3(3); 0.1];
lb = [1e-2;1e-2;0.01*wk2(2);1e-4];
ub = [100*wk2(1); inf; wk3(3); 100*wk3(3)];
Aeq = [0 0 0 0; 0 1 0 0; 0 0 0 0; 0 0 0 0];
```

WK Flow Calculations.m [cont.]

```
Beq = [0; wk2(1); 0; 0];
options = optimset('Display','iter','TolFun',1e-20,'TolX',1e-10);
[wk4p,fval,exitflag,output] =
fmincon(@WK4p_Flow,w0,[],[],[],[],lb,ub,[],options)

%WK4p Impedance calculation:
% ( Zwk4p = [(L*Ru+L*Rd)*(j*n*w0) + Rd*Ru] /
%           [L*C*Rd*(j*n*w0)^2 + (j*n*w0)*(C*Rd*Ru + L) + Ru]
Ru=wk4p(1); %upstream resistance
Rd=wk4p(2); %downstream resistance
C=wk4p(3); %compliance
L=wk4p(4); %inductance
Zwk4p = ( K*(L*Ru+L*Rd) + Rd*Ru )./( (K.^2)*L*C*Rd + K*(C*Ru*Rd+L) + Ru );
WK4p_Mod = abs(Zwk4p);
WK4p_Phs = angle(Zwk4p);

%Calculate wk4p flow waveform
qwk4pf = (1./Zwk4p).*fpcl; %calculate flow fourier coeff
Qwk4p = real(iff(N.*qwk4pf)); % use ifft to get Q_wk4p(t)

%-----
%                               Impedance Modulus and Phase Plots
%-----

%Calculate lag time between WK flow waveforms and clinical pressure
%waveform
[mxQwk2,Iqx2] = max(Qwk2);
dtL2 = tndP(Ipx) - tndQ(Iqx2);
[mxQwk3,Iqx3] = max(Qwk3);
dtL3 = tndP(Ipx) - tndQ(Iqx3);
[mxQwk4s,Iqx4s] = max(Qwk4s);
dtL4s = tndP(Ipx) - tndQ(Iqx4s);
[mxQwk4p,Iqx4p] = max(Qwk4p);
dtL4p = tndP(Ipx) - tndQ(Iqx4p);

DT = [dtL; dtL2; dtL3; dtL4s; dtL4p]

%display windkessel parameters
WK_coeff = zeros(4,4);
WK_coeff(1,1)=wk2(1); WK_coeff(2,1)=wk2(2);
WK_coeff(1,2)=wk3(1); WK_coeff(2,2)=wk3(2); WK_coeff(3,2)=wk3(3);
WK_coeff(1,3)=wk4s(1); WK_coeff(2,3)=wk4s(2); WK_coeff(3,3)=wk4s(3);
WK_coeff(4,3)=wk4s(4);
WK_coeff(1,4)=wk4p(1); WK_coeff(2,4)=wk4p(2); WK_coeff(3,4)=wk4p(3);
WK_coeff(4,4)=wk4p(4);
fprintf('\n The Windkessel coefficients are: \n')
WK_coeff
fprintf('\n')
```

WK Flow Calculations.m [cont.]

```
%Plot the clinical modulus and phase of the impedance calculations
figure
subplot(2,1,1)
hold on
plot(n(1:nn),WK2_Mod(1:nn), 'b')
plot(n(1:nn),WK3_Mod(1:nn), 'c:')
plot(n(1:nn),WK4s_Mod(1:nn), 'r--')
plot(n(1:nn),WK4p_Mod(1:nn), 'g-.')
hold off
xlabel('Frequency [Hz^*]')
ylabel('Impedance Modulus [mmHg*s/cm^3]')
legend('WK2', 'WK3', 'WK4s', 'WK4p')
subplot(2,1,2)
hold on
plot(n(1:nn),WK2_Phs(1:nn).*(180/pi), 'b')
plot(n(1:nn),WK3_Phs(1:nn).*(180/pi), 'c:')
plot(n(1:nn),WK4s_Phs(1:nn).*(180/pi), 'r--')
plot(n(1:nn),WK4p_Phs(1:nn).*(180/pi), 'g-.')
hold off
xlabel('Frequency [Hz^*]')
ylabel('Impedance Phase Angle [deg.]')
legend('WK2', 'WK3', 'WK4s', 'WK4p')

%plot clinical flow and pressure waveforms with accompanying
% WindKessel calculations
figure
subplot(2,1,1)
hold on
plot(tndQ,Qc1, 'ks', 'MarkerSize', 4.0, 'MarkerFaceColor', 'k')
plot(tndQ,Qwk2, 'b')
plot(tndQ,Qwk3, 'c:')
plot(tndQ,Qwk4s, 'r--')
plot(tndQ,Qwk4p, 'g-.')
hold off
xlabel('Time [t/T]')
ylabel('Flow Rate [cm^3/s]')
legend('Clinical', 'WK2', 'WK3', 'WK4s', 'WK4p')
subplot(2,1,2)
hold on
plot(tndP,Pc1, 'ks', 'MarkerSize', 4.0, 'MarkerFaceColor', 'k')
hold off
xlabel('Time [t/T]')
ylabel('Pressure [mmHg]')
legend('Clinical')
```

WK Flow Calculations.m [cont.]

```
%-----  
%Calculate inlet flow waveform by combining flows of all daughter arteries  
%-----  
  
%import patient's clinical-inspired inflow data  
dataIN=dlmread('Patient1_SMA_InFlowRate.dat');  
[lm,ln]=size(dataIN);  
Qcl_in = dataIN(1:lm-1,2);  
  
%computer common hepatic artery waveforms from population avg.  
% left hepatic artery flow data  
Qch_wk2_pa = Qwk2./0.55;  
Qch_wk3_pa = Qwk3./0.55;  
Qch_wk4s_pa = Qwk4s./0.55;  
Qch_wk4p_pa = Qwk4p./0.55;  
  
%compute scaling factor between common hepatic flow and  
% superior mesenteric arterial flow  
xf2_pa = 7.302/mean(Qch_wk2_pa);  
xf3_pa = 7.302/mean(Qch_wk3_pa);  
xf4s_pa = 7.302/mean(Qch_wk4s_pa);  
xf4p_pa = 7.302/mean(Qch_wk4p_pa);  
  
%Calculate flow exiting superior mesenteric artery  
Qsm_out_wk2_pa = xf2_pa.*Qch_wk2_pa;  
Qsm_out_wk3_pa = xf3_pa.*Qch_wk3_pa;  
Qsm_out_wk4s_pa = xf4s_pa.*Qch_wk4s_pa;  
Qsm_out_wk4p_pa = xf4p_pa.*Qch_wk4p_pa;  
  
%Combine common hepatic and superior mesenteric flows to get inflow  
Qin_wk2_pa = Qsm_out_wk2_pa + Qch_wk2_pa;  
Qin_wk3_pa = Qsm_out_wk3_pa + Qch_wk3_pa;  
Qin_wk4s_pa = Qsm_out_wk4s_pa + Qch_wk4s_pa;  
Qin_wk4p_pa = Qsm_out_wk4p_pa + Qch_wk4p_pa;  
  
%plot the different inflow waveforms  
figure  
hold on  
plot(tndQ,Qcl_in,'k:')  
plot(tndQ,Qin_wk2_pa,'b')  
plot(tndQ,Qin_wk3_pa,'c')  
plot(tndQ,Qin_wk4s_pa,'r')  
plot(tndQ,Qin_wk4p_pa,'g')  
hold off  
title('Inflow waveform with population average flow at LHA')  
xlabel('time [t/T]')  
ylabel('Flow Rate [cm^3/s]')  
legend('Patient', 'WK2', 'WK3', 'WK4s', 'WK4p')
```

WK Flow Calculations.m [cont.]

```
%-----  
%                               Export data for additional plotting  
%-----  
  
%Data to export: 1) Patient and windkessel impedance modulus and phase  
data  
%                 2) RHA windkessel flow waveforms  
%                 3) Both sets of calculated inflow waveforms  
%                 4) SMA outflow waveforms for clinical and population avg.  
  
%Assemble matrices of desired data sets  
%patient impedance  
Imp_cln = [n(1:nn) Cln_Mod(1:nn) Cln_Phs(1:nn)];  
%windkessel impedance  
Imp_wk = [n(1:nn) WK2_Mod(1:nn) WK2_Phs(1:nn) WK3_Mod(1:nn)  
WK3_Phs(1:nn) ...  
WK4s_Mod(1:nn) WK4s_Phs(1:nn) WK4p_Mod(1:nn) WK4p_Phs(1:nn)];  
%RHA windkessel flow waveforms  
Q_rha_wk = [tndQ Qwk2 Qwk3 Qwk4s Qwk4p];  
%Inflow waveforms  
Qin_wk_pa = [tndQ Qin_wk2_pa Qin_wk3_pa Qin_wk4s_pa Qin_wk4p_pa];  
%SMA outflow waveforms  
Qsm_pa = [tndQ Qsm_out_wk2_pa Qsm_out_wk3_pa Qsm_out_wk4s_pa ...  
Qsm_out_wk4p_pa];  
  
%Use dlmwrite function to export data to txt files  
dlmwrite('Patient_Impedance.dat', Imp_cln);  
dlmwrite('Windkessel_Impedance.dat', Imp_wk);  
dlmwrite('Windkessel_RHA_Flow.dat', Q_rha_wk);  
dlmwrite('Windkessel_Population_Inflow.dat', Qin_wk_pa);  
dlmwrite('SMA_PopulationAvgOutflow.dat', Qsm_pa);
```

WK2 Flow.m

```
function Err = WK2_Flow(w)

%PURPOSE: Calculate the difference between population averaged values of
%          mean and max flow rates in the hepatic artery with 2-element
%          windkessel flow rate values using windkessel parameters
%          of: R and C

%set global variable of clinical impedance
%set global variables
global PopMeanQ PopSysQ
global Pcl

%initialize general frequency parameters
N = length(Pcl);
n1 = [0:N/2]';
n2 = [-N/2+1:-1]';
n = [n1; n2];
j = sqrt(-1);
w0 = 2*pi; %base frequency
K = j*n*w0;

%WK2 Impedance calculation ( Zwk2 = R / (j*n*w0*C*R + 1)
R=w(1); %resistance
C=w(2); %compliance
Zwk2 = R./(K*C*R+1);

%Calculate fft of clinical pressure values
FFTpcl = fft(Pcl,N);
%Calculate pressure exponential fourier coefficients
fpcl = FFTpcl/N;

%Calculate wk2 flow waveform
qwk2f = (1./Zwk2).*fpcl; %calculate flow fourier coeff
Qwk2 = real(ifft(N.*qwk2f)); % use ifft to get Q_wk2(t)
MeanQwk2 = mean(real(Qwk2));
SysQwk2 = max(real(Qwk2));

%Experimental mean and max flow waveforms and corresponding error
Err = 100*abs(PopMeanQ - MeanQwk2)/(PopMeanQ) + ...
      100*abs(PopSysQ - SysQwk2)/(PopSysQ);

end %end function
```

WK3 Flow.m

```
function Err = WK3_Flow(w)

%PURPOSE: Calculate the difference between population averaged values of
%          mean and max flow rates in the hepatic artery with 3-element
%          windkessel flow rate values using windkessel parameters
%          of: Ru , Rd , and C

%set global variable of clinical impedance
%set global variables
global PopMeanQ PopSysQ
global Pcl

%initialize general frequency parameters
N = length(Pcl);
n1 = [0:N/2]';
n2 = [-N/2+1:-1]';
n = [n1; n2];
j = sqrt(-1);
w0 = 2*pi; %base frequency
K = j*n*w0;

%WK3 Impedance calculation:
%          ( Zwk3 = ( j*n*w0*C*Ru*Rd + Rd + Ru ) / ( j*n*w0*C*Rd+1 )
Ru = w(1); %upstream resistance
Rd = w(2); %downstream resistance
C = w(3); %compliance
Zwk3 = (K*C*Ru*Rd + Rd + Ru)./(K*C*Rd+1);

%Calculate fft of clinical pressure values
FFTpcl = fft(Pcl,N);
%Calculate pressure exponential fourier coefficients
fpcl = FFTpcl/N;

%Calculate wk2 flow waveform
qwk3f = (1./Zwk3).*fpcl; %calculate flow fourier coeff
Qwk3 = real(iff(N.*qwk3f)); % use ifft to get Q_wk2(t)
MeanQwk3 = mean(real(Qwk3));
SysQwk3 = max(real(Qwk3));

%Experimental mean and max flow waveforms and corresponding error
Err = 100*abs(PopMeanQ - MeanQwk3)/(PopMeanQ) + ...
      100*abs(PopSysQ - SysQwk3)/(PopSysQ);

end %end function
```

WK4s_Flow.m

```
function Err = WK4s_Flow(w)

%PURPOSE: Calculate the difference between population averaged values of
%         mean and max flow rates in the hepatic artery with 4-element
%         series windkessel flow rate values using windkessel parameters
%         of: Ru , Rd , C , and L

%set global variable of clinical impedance
%set global variables
global PopMeanQ PopSysQ
global Pcl

%initialize general frequency parameters
N = length(Pcl);
n1 = [0:N/2]';
n2 = [-N/2+1:-1]';
n = [n1; n2];
j = sqrt(-1);
w0 = 2*pi; %base frequency
K = j*n*w0;

%WK4s Impedance calculation:
% ( Zwk4s = [L*C*Rd*(j*n*w0)^2 + (C*Ru*Rd + L)*(j*n*w0)*C*Ru*Rd + Rd + Ru]
/
%                                     [j*n*w0*C*Rd + 1]
Ru = w(1); %upstream resistance
Rd = w(2); %downstream resistance
C = w(3); %compliance
L = w(4); %inductance
Zwk4s = ( (K.^2)*L*C*Rd + K*(C*Ru*Rd+L) + Rd + Ru )./( K*C*Rd+1 );

%Calculate fft of clinical pressure values
FFTpcl = fft(Pcl,N);
%Calculate pressure exponential fourier coefficients
fpcl = FFTpcl/N;

%Calculate wk2 flow waveform
qwk4sf = (1./Zwk4s).*fpcl; %calculate flow fourier coeff
Qwk4s = real(ifft(N.*qwk4sf)); % use ifft to get Q_wk2(t)
MeanQwk4s = mean(real(Qwk4s));
SysQwk4s = max(real(Qwk4s));

%Experimental mean and max flow waveforms and corresponding error
Err = 100*abs(PopMeanQ - MeanQwk4s)/(PopMeanQ) + ...
      100*abs(PopSysQ - SysQwk4s)/(PopSysQ);

end %end function
```

WK4p_Flow.m

```
function Err = WK4p_Flow(w)

%PURPOSE: Calculate the difference between population averaged values of
%         mean and max flow rates in the hepatic artery with 4-element
%         parallel windkessel flow rate values using windkessel parameters
%         of: Ru , Rd , C , and L

%set global variable of clinical impedance
%set global variables
global PopMeanQ PopSysQ
global Pcl

%initialize general frequency parameters
N = length(Pcl);
n1 = [0:N/2]';
n2 = [-N/2+1:-1]';
n = [n1; n2];
j = sqrt(-1);
w0 = 2*pi; %base frequency
K = j*n*w0;

%WK4p Impedance calculation:
% ( Zwk4p = [(L*Ru+L*Rd)*(j*n*w0) + Rd*Ru] /
%           [L*C*Rd*(j*n*w0)^2 + (j*n*w0)*(C*Rd*Ru+L) + Ru]
Ru = w(1); %upstream resistance
Rd = w(2); %downstream resistance
C = w(3); %compliance
L = w(4); %inductance
Zwk4p = ( K*(L*Ru+L*Rd) + Rd*Ru )./( (K.^2)*L*C*Rd + K*(C*Ru*Rd+L) + Ru );

%Calculate fft of clinical pressure values
FFTpcl = fft(Pcl,N);
%Calculate pressure exponential fourier coefficients
fpcl = FFTpcl/N;

%Calculate wk2 flow waveform
qwk4pf = (1./Zwk4p).*fpcl; %calculate flow fourier coeff
Qwk4p = real(ifft(N.*qwk4pf)); % use ifft to get Q_wk2(t)
MeanQwk4p = mean(real(Qwk4p));
SysQwk4p = max(real(Qwk4p));

%Experimental mean and max flow waveforms and corresponding error
Err = 100*abs(PopMeanQ - MeanQwk4p)/(PopMeanQ) + ...
      100*abs(PopSysQ - SysQwk4p)/(PopSysQ);

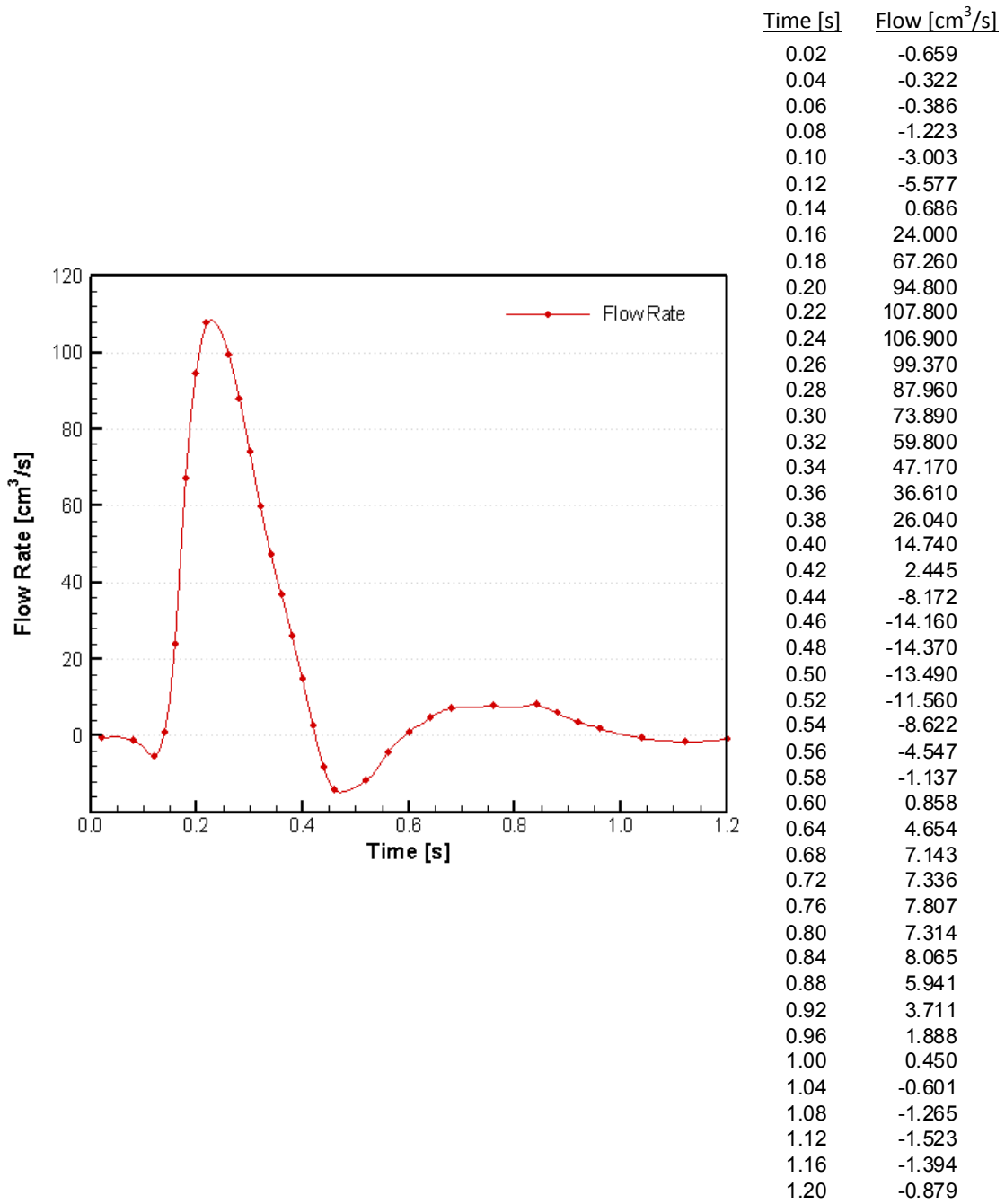
end %end function
```

APPENDIX IV: Discrete Data of Derived Inlet/Outlet Transient Waveforms Based on *in-vivo* Hemodynamics Data

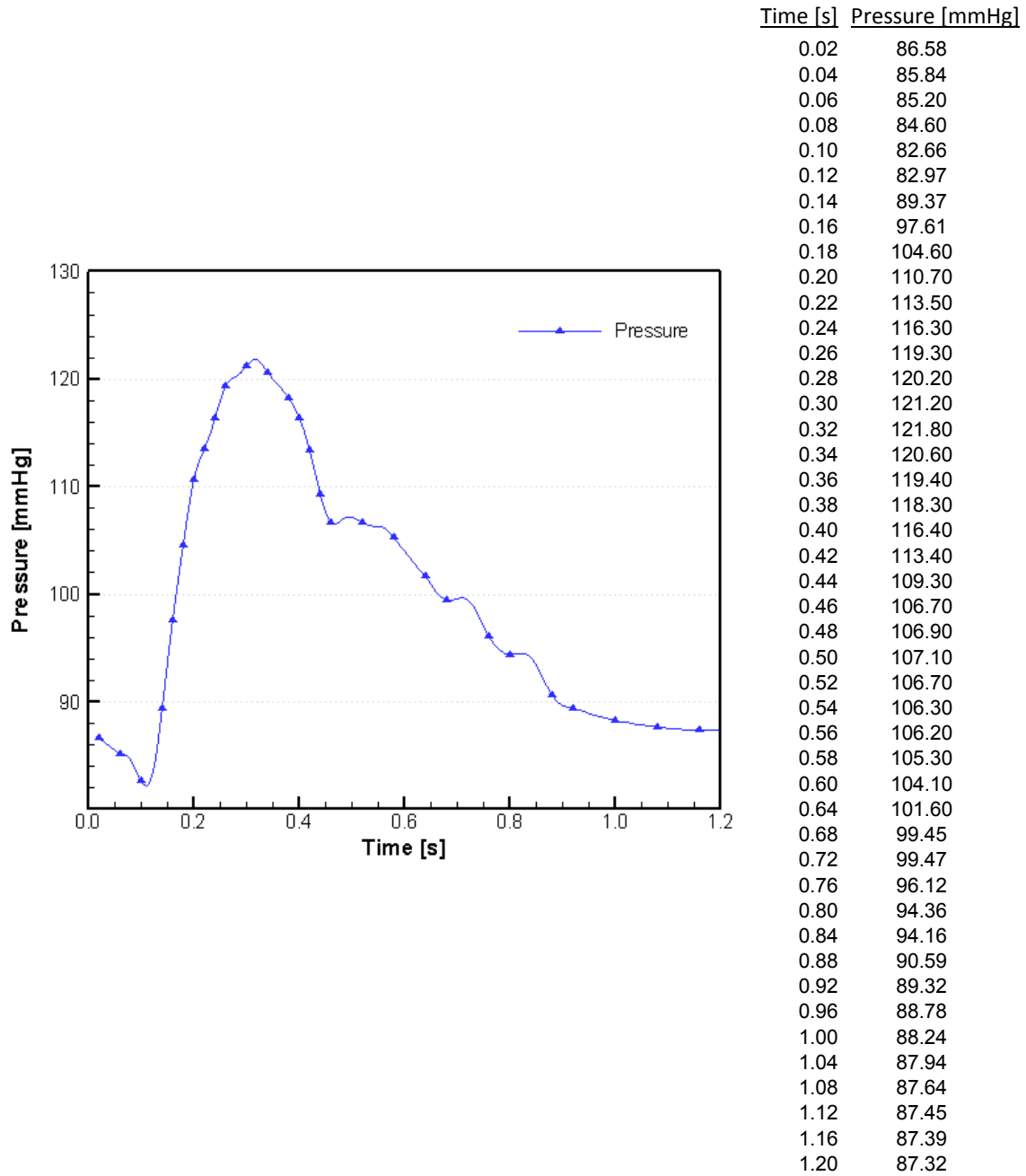
Summary

To enhance the ability of future research to utilize the transient waveforms constructed in the current analysis, the discrete, numerical data of each implemented waveform is included in this appendix. More specifically, a visual plot of each implemented transient waveform is accompanied by a table of nondimensional time and signal magnitude values. The transient waveforms included in this appendix are the AAA infrarenal flow, the AAA common iliac pressure, the SMA inflow and outflow waveforms, the CHA inflow waveform from the WK2 calculation, the LHA outflow waveforms, and the patient's *in-vivo* downstream RHA pressure.

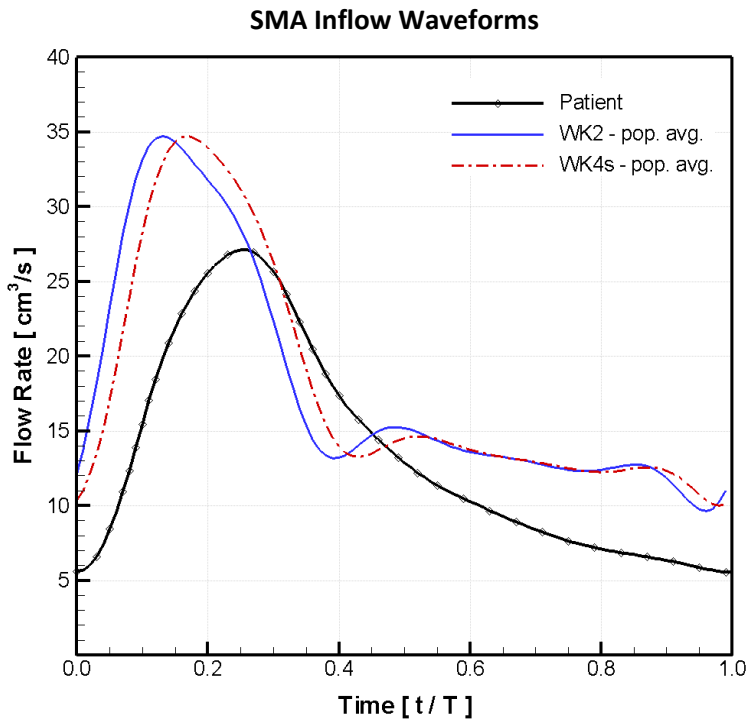
AAA Infrarenal Inflow Waveform



AAA Common Iliac Pressure Waveform

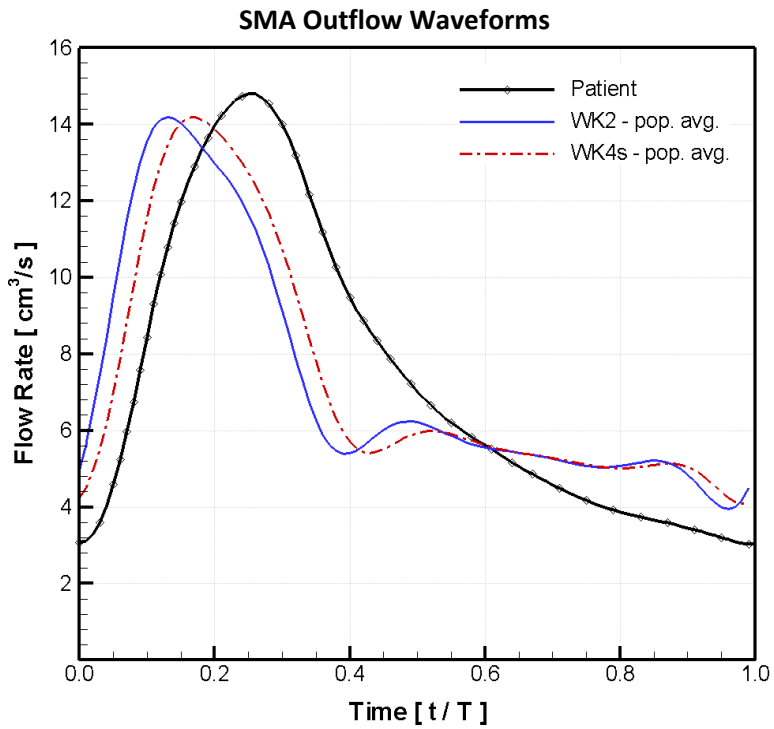


Hepatic SMA Inflow Waveforms



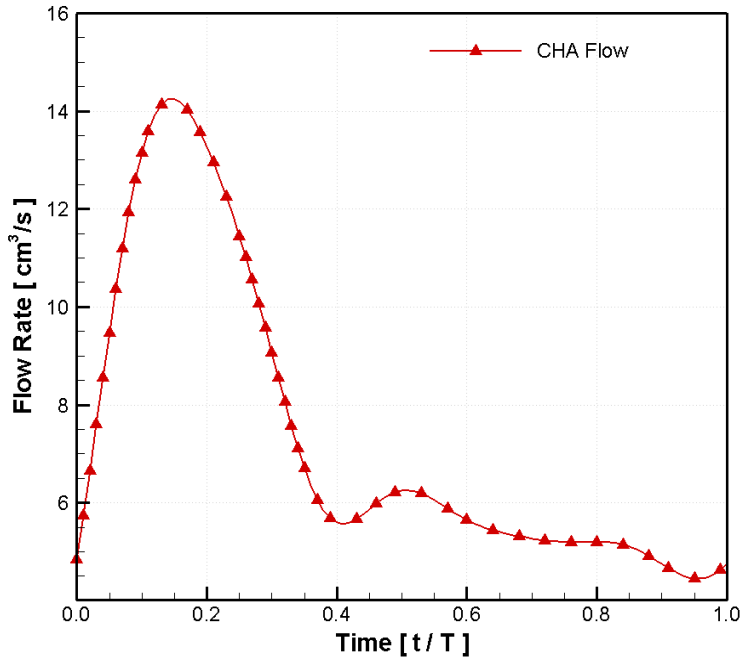
| Time [t/ T] | Flow [cm ³ /s] | | |
|----------------|---------------------------|--------|--------|
| | Patient | WK2 | WK4s |
| 0.00 | 5.542 | 12.249 | 10.429 |
| 0.02 | 6.021 | 15.908 | 12.107 |
| 0.04 | 7.410 | 20.683 | 15.151 |
| 0.06 | 9.602 | 25.765 | 19.305 |
| 0.08 | 12.360 | 30.168 | 23.954 |
| 0.10 | 15.460 | 33.187 | 28.309 |
| 0.12 | 18.460 | 34.542 | 31.701 |
| 0.14 | 20.910 | 34.609 | 33.798 |
| 0.16 | 22.830 | 33.880 | 34.651 |
| 0.18 | 24.360 | 32.825 | 34.573 |
| 0.20 | 25.570 | 31.749 | 33.923 |
| 0.22 | 26.450 | 30.653 | 32.965 |
| 0.24 | 27.000 | 29.307 | 31.808 |
| 0.26 | 27.090 | 27.543 | 30.377 |
| 0.28 | 26.630 | 25.207 | 28.562 |
| 0.30 | 25.650 | 22.330 | 26.247 |
| 0.32 | 24.140 | 19.266 | 23.497 |
| 0.34 | 22.300 | 16.488 | 20.535 |
| 0.36 | 20.480 | 14.426 | 17.720 |
| 0.38 | 18.830 | 13.365 | 15.436 |
| 0.40 | 17.350 | 13.238 | 13.952 |
| 0.42 | 16.240 | 13.700 | 13.302 |
| 0.44 | 15.310 | 14.384 | 13.325 |
| 0.46 | 14.420 | 14.968 | 13.709 |
| 0.48 | 13.610 | 15.235 | 14.182 |
| 0.50 | 12.860 | 15.198 | 14.518 |
| 0.52 | 12.200 | 14.923 | 14.637 |
| 0.54 | 11.600 | 14.528 | 14.544 |
| 0.56 | 11.110 | 14.132 | 14.314 |
| 0.58 | 10.680 | 13.814 | 14.021 |
| 0.60 | 10.280 | 13.584 | 13.740 |
| 0.62 | 9.881 | 13.426 | 13.506 |
| 0.64 | 9.459 | 13.307 | 13.326 |
| 0.66 | 9.086 | 13.188 | 13.185 |
| 0.68 | 8.741 | 13.048 | 13.057 |
| 0.70 | 8.396 | 12.867 | 12.920 |
| 0.72 | 8.068 | 12.668 | 12.762 |
| 0.74 | 7.781 | 12.478 | 12.587 |
| 0.76 | 7.514 | 12.348 | 12.419 |
| 0.78 | 7.284 | 12.312 | 12.294 |
| 0.80 | 7.092 | 12.390 | 12.247 |
| 0.82 | 6.934 | 12.557 | 12.294 |
| 0.84 | 6.791 | 12.717 | 12.414 |
| 0.86 | 6.640 | 12.733 | 12.537 |
| 0.88 | 6.489 | 12.470 | 12.554 |
| 0.90 | 6.334 | 11.852 | 12.350 |
| 0.92 | 6.164 | 10.955 | 11.856 |
| 0.94 | 5.963 | 10.059 | 11.125 |
| 0.96 | 5.765 | 9.634 | 10.377 |
| 0.98 | 5.600 | 10.243 | 9.994 |
| 1.00 | 5.542 | 12.249 | 10.429 |

Hepatic SMA Outflow Waveforms



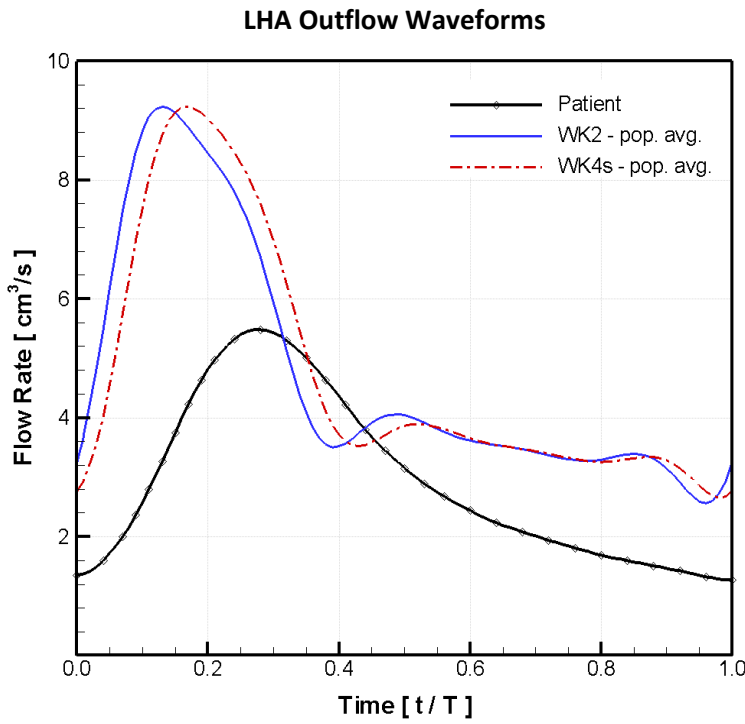
| Time [t/ T] | Flow [cm ³ /s] | | |
|----------------|---------------------------|--------|--------|
| | Patient | WK2 | WK4s |
| 0.00 | 3.025 | 5.007 | 4.264 |
| 0.02 | 3.286 | 6.503 | 4.949 |
| 0.04 | 4.044 | 8.455 | 6.194 |
| 0.06 | 5.241 | 10.533 | 7.892 |
| 0.08 | 6.744 | 12.333 | 9.792 |
| 0.10 | 8.436 | 13.567 | 11.573 |
| 0.12 | 10.080 | 14.121 | 12.959 |
| 0.14 | 11.410 | 14.148 | 13.817 |
| 0.16 | 12.460 | 13.850 | 14.165 |
| 0.18 | 13.290 | 13.419 | 14.133 |
| 0.20 | 13.960 | 12.979 | 13.868 |
| 0.22 | 14.440 | 12.531 | 13.476 |
| 0.24 | 14.740 | 11.981 | 13.003 |
| 0.26 | 14.780 | 11.260 | 12.418 |
| 0.28 | 14.530 | 10.305 | 11.676 |
| 0.30 | 14.000 | 9.128 | 10.730 |
| 0.32 | 13.180 | 7.876 | 9.606 |
| 0.34 | 12.170 | 6.740 | 8.395 |
| 0.36 | 11.180 | 5.897 | 7.244 |
| 0.38 | 10.280 | 5.464 | 6.310 |
| 0.40 | 9.468 | 5.412 | 5.703 |
| 0.42 | 8.863 | 5.601 | 5.438 |
| 0.44 | 8.358 | 5.880 | 5.447 |
| 0.46 | 7.873 | 6.119 | 5.604 |
| 0.48 | 7.429 | 6.228 | 5.798 |
| 0.50 | 7.020 | 6.213 | 5.935 |
| 0.52 | 6.659 | 6.100 | 5.984 |
| 0.54 | 6.334 | 5.939 | 5.946 |
| 0.56 | 6.065 | 5.777 | 5.852 |
| 0.58 | 5.831 | 5.647 | 5.732 |
| 0.60 | 5.613 | 5.553 | 5.617 |
| 0.62 | 5.393 | 5.489 | 5.521 |
| 0.64 | 5.163 | 5.440 | 5.448 |
| 0.66 | 4.959 | 5.391 | 5.390 |
| 0.68 | 4.771 | 5.334 | 5.338 |
| 0.70 | 4.583 | 5.260 | 5.282 |
| 0.72 | 4.403 | 5.179 | 5.217 |
| 0.74 | 4.247 | 5.101 | 5.146 |
| 0.76 | 4.101 | 5.048 | 5.077 |
| 0.78 | 3.975 | 5.033 | 5.026 |
| 0.80 | 3.871 | 5.065 | 5.006 |
| 0.82 | 3.785 | 5.133 | 5.026 |
| 0.84 | 3.706 | 5.199 | 5.075 |
| 0.86 | 3.624 | 5.205 | 5.125 |
| 0.88 | 3.542 | 5.098 | 5.132 |
| 0.90 | 3.457 | 4.845 | 5.049 |
| 0.92 | 3.364 | 4.479 | 4.847 |
| 0.94 | 3.255 | 4.112 | 4.548 |
| 0.96 | 3.146 | 3.938 | 4.242 |
| 0.98 | 3.057 | 4.187 | 4.085 |
| 1.00 | 3.025 | 5.007 | 4.264 |

Hepatic CHA WK2 Inflow Waveform



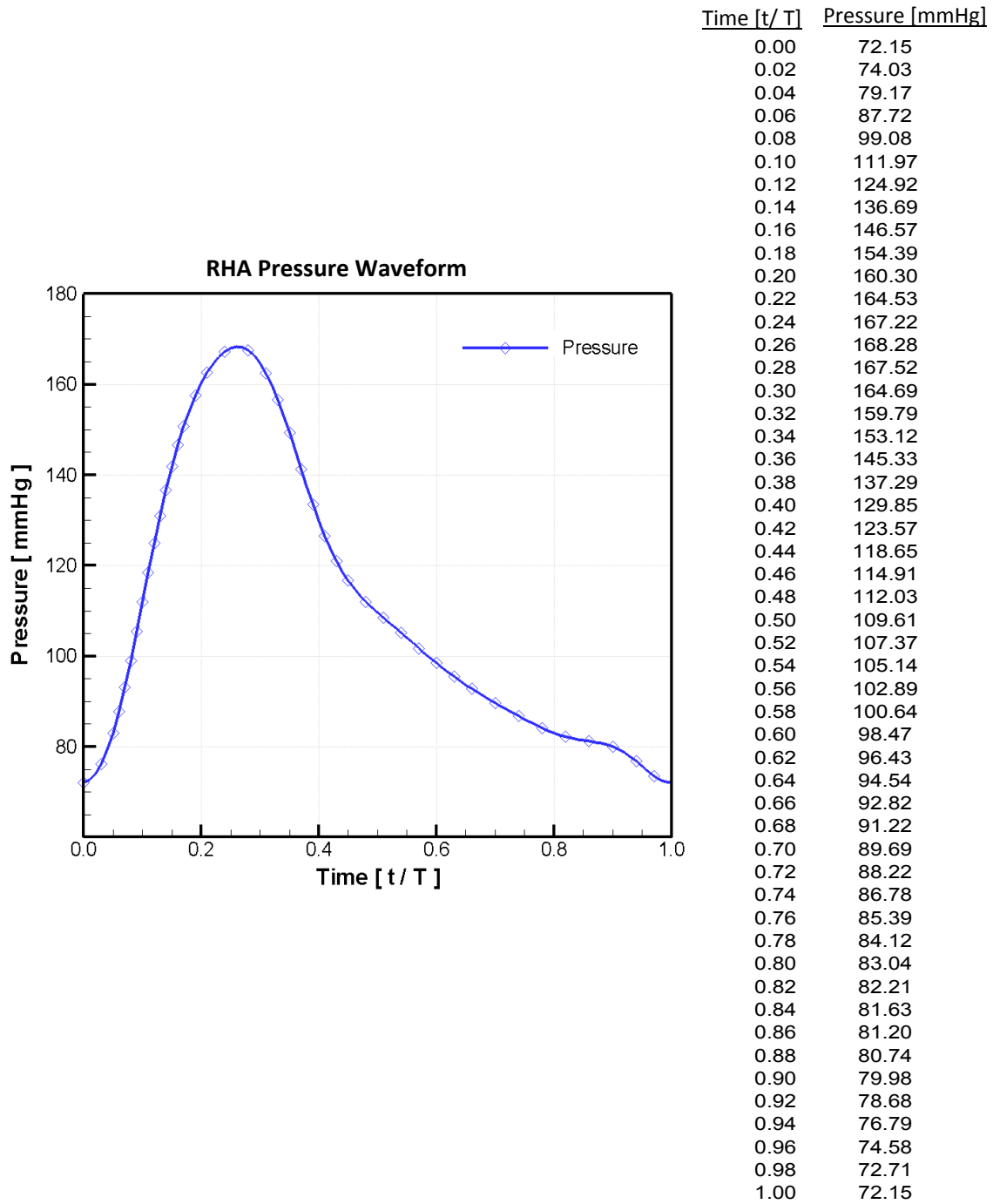
| Time [t/T] | WK2 Flow [cm ³ /s] |
|------------|-------------------------------|
| 0.00 | 4.759 |
| 0.02 | 6.661 |
| 0.04 | 8.550 |
| 0.06 | 10.360 |
| 0.08 | 11.938 |
| 0.10 | 13.150 |
| 0.12 | 13.917 |
| 0.14 | 14.234 |
| 0.16 | 14.166 |
| 0.18 | 13.813 |
| 0.20 | 13.274 |
| 0.22 | 12.613 |
| 0.24 | 11.859 |
| 0.26 | 11.012 |
| 0.28 | 10.076 |
| 0.30 | 9.069 |
| 0.32 | 8.053 |
| 0.34 | 7.115 |
| 0.36 | 6.351 |
| 0.38 | 5.835 |
| 0.40 | 5.595 |
| 0.42 | 5.596 |
| 0.44 | 5.758 |
| 0.46 | 5.977 |
| 0.48 | 6.161 |
| 0.50 | 6.252 |
| 0.52 | 6.234 |
| 0.54 | 6.125 |
| 0.56 | 5.966 |
| 0.58 | 5.795 |
| 0.60 | 5.643 |
| 0.62 | 5.523 |
| 0.64 | 5.435 |
| 0.66 | 5.369 |
| 0.68 | 5.315 |
| 0.70 | 5.268 |
| 0.72 | 5.229 |
| 0.74 | 5.203 |
| 0.76 | 5.192 |
| 0.78 | 5.195 |
| 0.80 | 5.199 |
| 0.82 | 5.187 |
| 0.84 | 5.141 |
| 0.86 | 5.047 |
| 0.88 | 4.909 |
| 0.90 | 4.746 |
| 0.92 | 4.589 |
| 0.94 | 4.478 |
| 0.96 | 4.451 |
| 0.98 | 4.537 |
| 1.00 | 4.759 |

Hepatic LHA Outflow Waveforms



| Time [t / T] | Flow [cm ³ /s] | | |
|-----------------|---------------------------|-------|-------|
| | Patient | WK2 | WK4s |
| 0.00 | 1.276 | 3.259 | 2.775 |
| 0.02 | 1.413 | 4.232 | 3.221 |
| 0.04 | 1.594 | 5.502 | 4.031 |
| 0.06 | 1.859 | 6.855 | 5.136 |
| 0.08 | 2.173 | 8.026 | 6.373 |
| 0.10 | 2.571 | 8.829 | 7.531 |
| 0.12 | 3.026 | 9.190 | 8.434 |
| 0.14 | 3.504 | 9.208 | 8.992 |
| 0.16 | 3.994 | 9.013 | 9.218 |
| 0.18 | 4.439 | 8.732 | 9.198 |
| 0.20 | 4.814 | 8.447 | 9.025 |
| 0.22 | 5.105 | 8.155 | 8.770 |
| 0.24 | 5.326 | 7.797 | 8.462 |
| 0.26 | 5.453 | 7.328 | 8.082 |
| 0.28 | 5.478 | 6.706 | 7.599 |
| 0.30 | 5.424 | 5.941 | 6.983 |
| 0.32 | 5.296 | 5.126 | 6.251 |
| 0.34 | 5.111 | 4.386 | 5.463 |
| 0.36 | 4.890 | 3.838 | 4.714 |
| 0.38 | 4.639 | 3.556 | 4.107 |
| 0.40 | 4.364 | 3.522 | 3.712 |
| 0.42 | 4.073 | 3.645 | 3.539 |
| 0.44 | 3.804 | 3.827 | 3.545 |
| 0.46 | 3.558 | 3.982 | 3.647 |
| 0.48 | 3.346 | 4.053 | 3.773 |
| 0.50 | 3.152 | 4.043 | 3.862 |
| 0.52 | 2.975 | 3.970 | 3.894 |
| 0.54 | 2.816 | 3.865 | 3.869 |
| 0.56 | 2.674 | 3.760 | 3.808 |
| 0.58 | 2.552 | 3.675 | 3.730 |
| 0.60 | 2.439 | 3.614 | 3.655 |
| 0.62 | 2.333 | 3.572 | 3.593 |
| 0.64 | 2.232 | 3.540 | 3.545 |
| 0.66 | 2.151 | 3.509 | 3.508 |
| 0.68 | 2.080 | 3.471 | 3.474 |
| 0.70 | 2.011 | 3.423 | 3.437 |
| 0.72 | 1.941 | 3.370 | 3.395 |
| 0.74 | 1.874 | 3.320 | 3.349 |
| 0.76 | 1.810 | 3.285 | 3.304 |
| 0.78 | 1.748 | 3.276 | 3.271 |
| 0.80 | 1.691 | 3.296 | 3.258 |
| 0.82 | 1.642 | 3.341 | 3.271 |
| 0.84 | 1.598 | 3.383 | 3.303 |
| 0.86 | 1.553 | 3.387 | 3.335 |
| 0.88 | 1.512 | 3.317 | 3.340 |
| 0.90 | 1.469 | 3.153 | 3.285 |
| 0.92 | 1.424 | 2.915 | 3.154 |
| 0.94 | 1.375 | 2.676 | 2.960 |
| 0.96 | 1.327 | 2.563 | 2.761 |
| 0.98 | 1.287 | 2.725 | 2.659 |
| 1.00 | 1.276 | 3.259 | 2.775 |

Hepatic RHA *in-vivo* Pressure Waveform



APPENDIX V: Steady Particle-Hemodynamics of an Abdominal Aortic Aneurysm

Flow Fields and Parameters

Steady simulations were run at Reynolds numbers of 475, 1129, and 1656 using the hydraulic diameter at the domain inlet, the minimum Quemada viscosity, and the constant blood density in the Reynolds formula. A Reynolds number of 475 represents the arithmetic mean value of the inflow waveform. Ten-thousand particles of each blood particle were injected in the domain at the inlet with a zero slip velocity using the cross-sectional spatial distribution described in Section 5.1. Particles were tracked through the domain for a maximum of 10s or until their center of mass crossed one of the domain's boundaries, resulting in a particle's wall deposition or exit. The same convergence criteria listed in Section 5.1 was used in the steady-state simulations.

The steady Reynolds numbers created similar flow patterns with regions of massive flow separation and rotational flow around the axial (longitudinal) direction of the AAA sac. Figure A4.1 plots representative streamlines through the AAA domain for each Reynolds number.

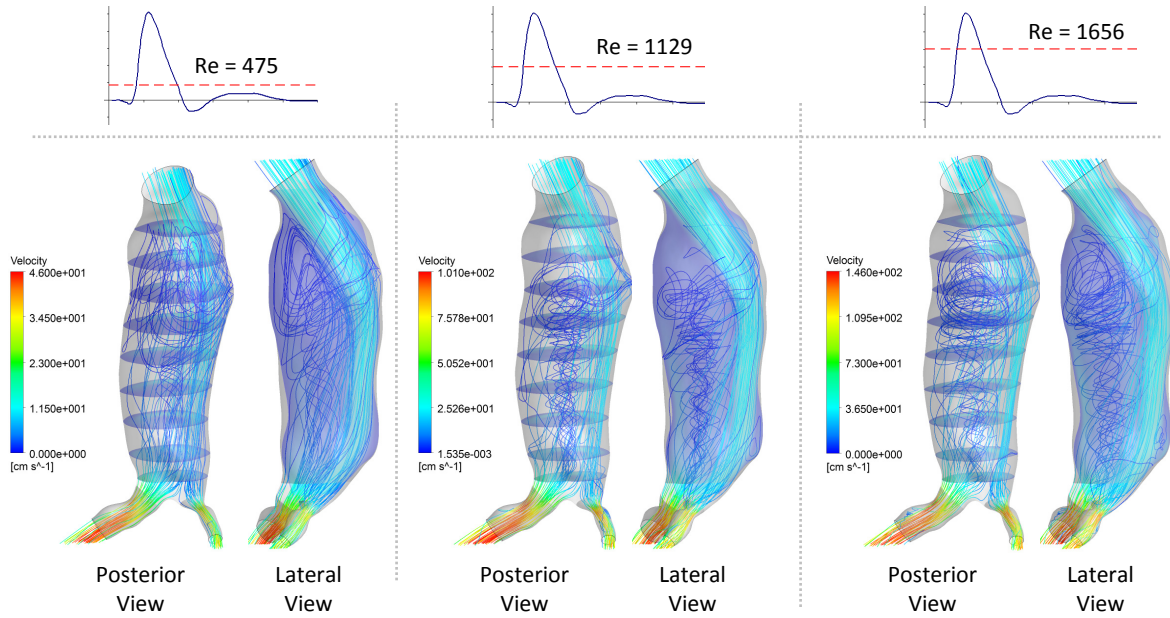


Figure A4.1: Streamline plots of steady flow through an AAA

The neck angle of the analyzed AAA directs incoming blood towards a specific region of the AAA wall, causing flow separation near the posterior wall and at regions of local expansion. Resulting flow recirculation contains three-dimensional features at all Reynolds numbers, with large portions of the circulatory flow moving through multiple two-dimensional planes. Incoming flow at higher magnitudes provide streamlines with increased energy that does not dissipate upon colliding with the AAA wall, increasing the intensity of the circulating flow around the axial direction of the AAA. Such behavior is clearly illustrated in Fig. A4.1 in the Reynolds number plots above 1000, where tightly-wound, rotational streamlines are clearly seen in the general flow separation region near the posterior wall. Figure A4.2 provides additional insight by plotting the in-plane (secondary) velocity vectors in the AAA sac.

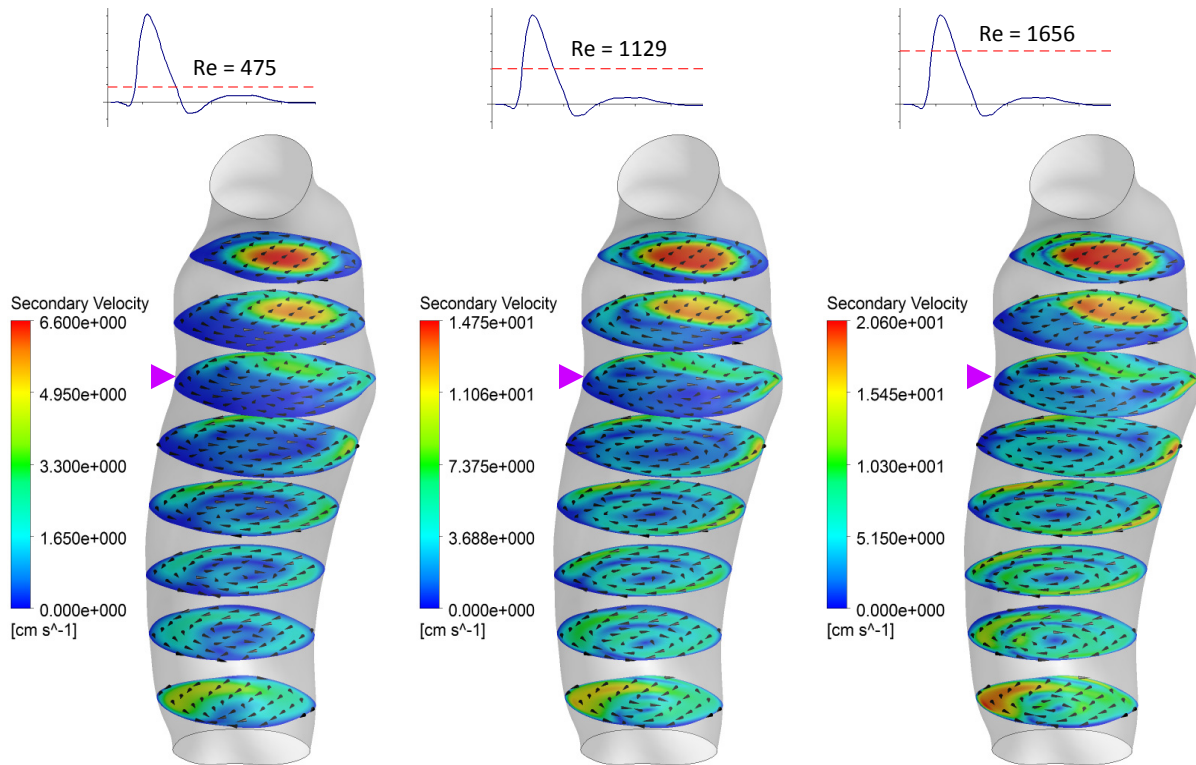


Figure A4.2: Secondary velocity vector plots in the AAA sac

The influence of the local geometry and steady inflow are underscored by similar secondary flow patterns at all inflow Reynolds numbers. However, at Reynolds numbers above 1000, a stronger magnitude of secondary flow exists at every cross sectional plane. Of particular note is the third plane from the most proximal plane in Fig. A4.2 (marked with arrowhead), where incoming flow collides with the anterior AAA wall and moves along the wall towards the posterior AAA lumen. The flow patterns in this plane are heavily dependent on the momentum which the fluid streamlines collide with the AAA wall. Where increased momentum results in multiple regions of rotational flow at elevated magnitudes compared to the single recirculation region with relatively low magnitude at the lowest Reynolds number. The AAA morphology influences on the secondary flow fields are also seen at the proximal

(topmost) and distal (bottommost) planes. Where, at the proximal planes, the secondary velocity is predominantly directed towards the anterior AAA wall due to the upstream neck angle and, at the distal planes, the secondary velocity reveals elevated flow towards the left common iliac artery due to its lower downstream resistance from its larger diameter.

Plots of non-Newtonian viscosity throughout the AAA sac reveal localized regions of elevated viscosity due to flow reattachment and low shear rates. Elevated viscosity is correlated with regions of low spatial changes in the velocity, and if the regions have a low velocity magnitude the fluid has a greater tendency to stagnate in the local region, increasing the potential of ILT formation and/or growth. In particular, the proximal planes in the analyzed AAA contain the max. regions of viscosity in the AAA sac for all simulated Reynolds numbers. However, the ratio of the local viscosity divided by the minimum Quemada viscosity reveals different contour patterns for each Reynolds number. Figure A4.3 plots the viscosity ratio on the cross-sectional planes in the AAA sac and on a surface 0.5mm offset from the outer wall into the AAA lumen for all simulated Reynolds numbers.

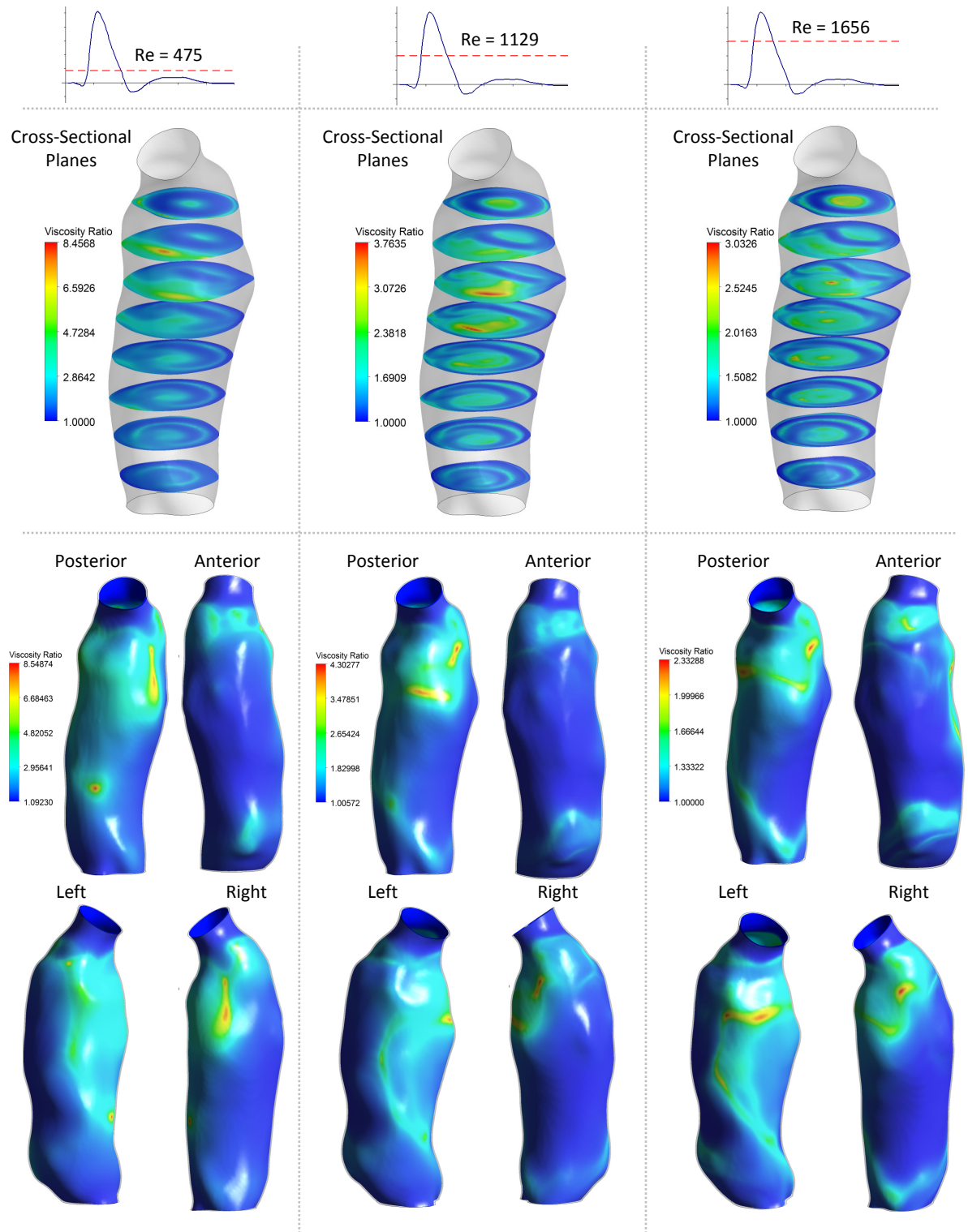


Figure A4.3: Non-Newtonian viscosity ratio contours throughout the AAA

The higher Reynolds numbers were inversely related to the maximum viscosity. While similar patterns are seen in the viscosity contours shown in Fig. A4.3, noticeable differences exist in the location of max. viscosity. Reynolds numbers above 1000 exhibited more horizontal regions of elevated viscosity compared to the vertical regions of the lower Reynolds number. Additionally, the distal, anterior-facing bulge did not exhibit the highest regions of viscosity due to the AAA neck directing flow almost entirely down the anterior wall creating high shear rates across the surface compared to the posterior regions.

Wall shear stress (WSS) contours on the AAA wall reveal areas of increased flow and where potential regions of flow stagnation and/or recirculation occur. Figure A4.4 plots the WSS contours and vector field along the AAA wall for the different inflow Reynolds numbers.

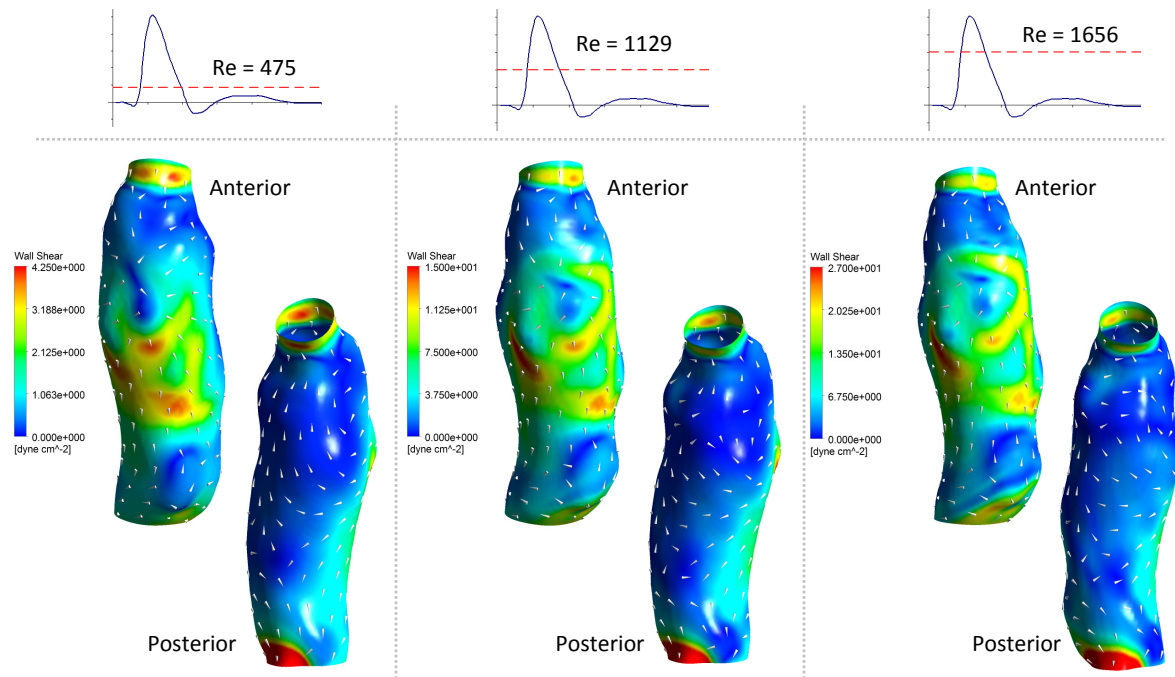


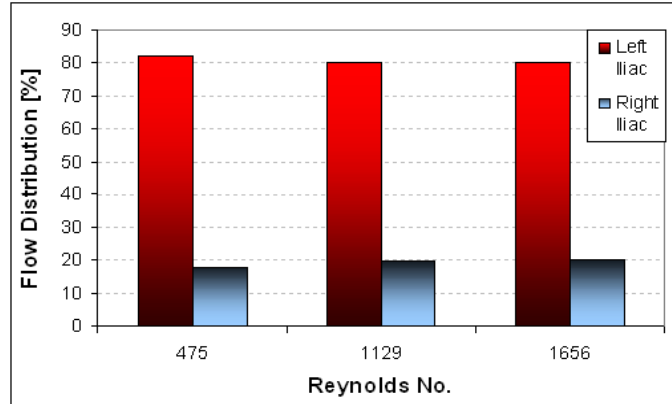
Figure A4.4: WSS contours and vector field on the AAA wall

General shear patterns are similar for all inflow magnitudes, where subtle differences exist in the WSS directions in low shear regions. The recirculation patterns in the posterior region are seen in the upward WSS vectors, and the collision point of the incoming blood flow with the anterior wall is represented by “source-like” pattern WSS vectors. In all three inflow magnitudes, the maximum shear stress is located on the anterior portion of the AAA wall due to the upstream neck angle, which directs more flow closely along the anterior wall and causes massive flow separation with recirculation along the posterior wall.

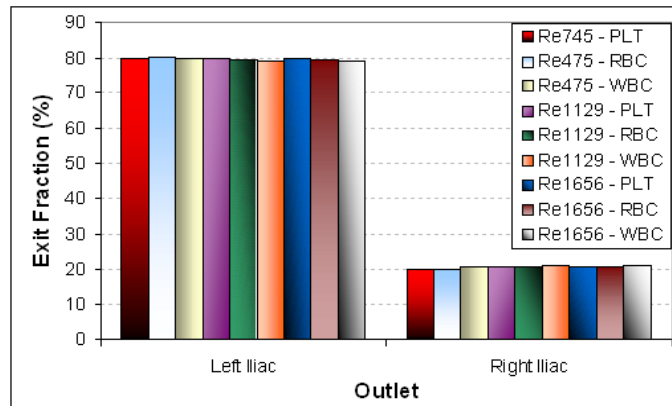
In summary, the local flow fields are predominantly characterized by the AAA morphology and local flow conditions. The AAA neck angle, downstream resistance, and inflow magnitude have been shown to have a quantitative impact on the resulting flow field. Flow recirculation caused by steady inflow has been shown to possess three-dimensional characteristics with secondary flow fields and viscosity contours dependent on the magnitude of the incoming flow. Highly localized regions of elevated viscosity have been shown to exist in near wall regions, where the location and regional distribution is dependent on the inflow magnitude. The elevated regions of viscosity have an increased potential for fluid stagnation and are thus more prone to ILT formation and/or growth.

Particle Transport and Trajectories

The one-way coupled Eulerian-Lagrangian particle transport model calculated particle exit fractions that closely matched the flow distribution through the two iliac outlets, while the particle injection fractions reveal subtle differences between the flow distribution and the particle terminal location percentage. Figure A4.5 plots the various percentages and the equations that define the particle injection and exit fractions.



$$\text{Exit Fraction} = 100\% \cdot \frac{\text{No. of Locally Exited Particles}}{\sum \text{Exited Particles}}$$



$$\text{Injection Fraction} = 100\% \cdot \frac{\text{No. of Locally Exited Particles}}{\sum \text{Injected Particles}}$$

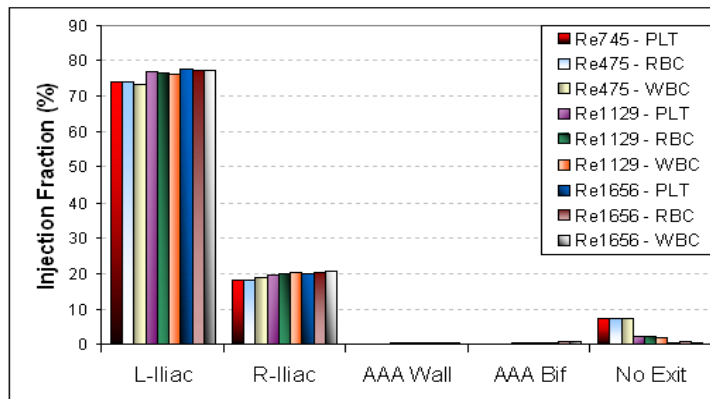


Figure A4.5: Steady flow distribution, particle exit fractions, and particle injection fractions

The particle exit fraction is a quantitative measurement of where particles exit the computational domain, where the particle injection fraction is a quantitative measurement of the terminal locations of all injected particles. Interestingly, the particle exit fractions are very close to the flow distribution percentages for all Reynolds numbers and all particle types. In attempts of relating the particle transport to AAA morphology, the hydraulic diameters and cross-sectional areas of the inlet, left iliac artery outlet, and right iliac artery outlet were calculated and compared. No correlations were observed between the outlet to inlet cross-sectional area or hydraulic diameter ratios and the particle exit fractions. However, the ratio between the left and right iliac arteries' cross-sectional area was 3.253 and the mean ratio of all particle exit fractions through the left and right hepatic arteries was 3.884 ± 0.083 . While the percent difference is approximately 18%, a rough estimate of the particle exit fraction ratio under equal downstream resistance may be possible by comparing the vessel cross-sectional areas. Additional studies are needed to provide more insight on this observation, but the current data provides sufficient physical evidence via equal downstream resistances and similar bifurcation angles that the vessel cross-sectional area would have a prominent influence on flow distribution and thus particle transport.

The injection fraction graph in Fig. A4.5 suggests that the amount of particle deposition in the AAA sac is minimal (almost negligible), but the plot does not provide enough detail to determine if there are preferred particle characteristics that suggest enhanced deposition potential in the domain. Additionally, a noticeable amount of particles remain in the AAA domain after 10s of particle transport. Figure A4.6a graphs the percentage of injected particles deposited along the AAA wall (deposition efficiency) vs. their Stokes number with

a polynomial curve fitted line that has an R^2 value of 0.9212. Additionally, Fig. A4.6b shows the percentage of particles left in the AAA domain after 10s of particle transport with an exponential curve fit that has an R^2 value of 0.9993.

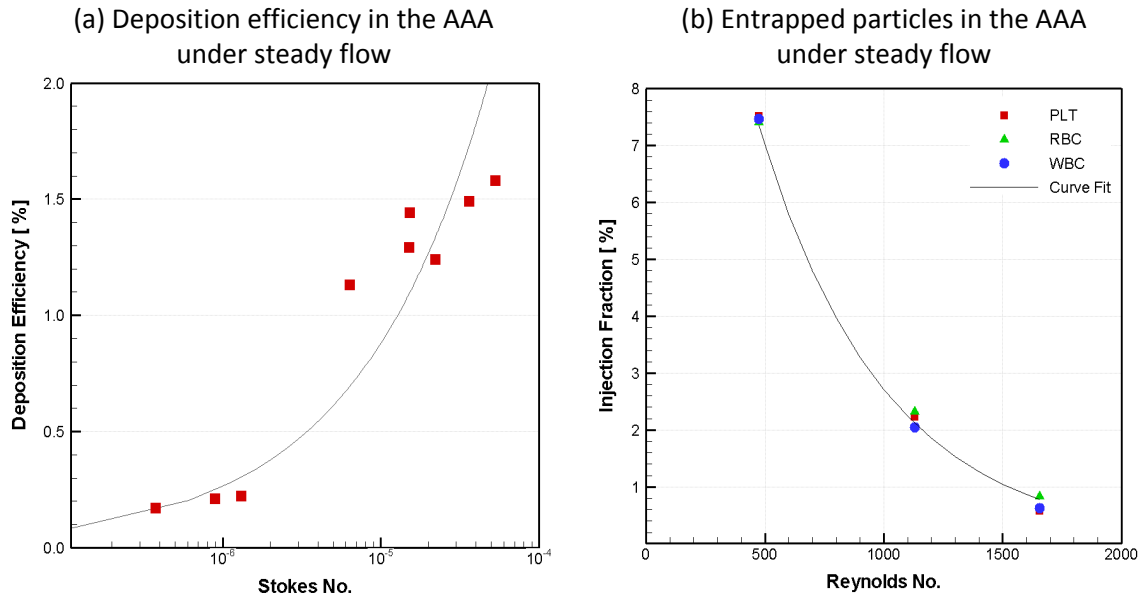


Figure A4.6: (a) Deposition efficiency in the AAA vs. particle Stokes Number and (b) Injection fraction of particles left in AAA domain

Figure A4.6a shows a clear dependence of particle deposition on the Stokes number, which includes both flow and particle characteristics. Conversely, the number of particles remaining in the AAA domain after 10s of particle transport appears to be dependent on the flow field and nearly independent of particle characteristics. The higher Stokes numbers are only seen at Reynolds numbers greater than 1000 and reveal that more particles deposit along the AAA walls at higher flow magnitudes, yet fewer particles remain in the AAA domain at these higher flows. Moreover, the decrease of particles left in the AAA domain is much greater than the increase of particles depositing along the AAA wall at the higher flow magnitudes.

The particle injection fraction graph in Fig. A4.5 reveals that most of the particles that were once entrapped in the AAA domain under lower flow magnitudes, exit the domain through the left or right iliac arterial outlets at higher flow. Such interpretation of the data reveals that the flow field magnitude has a pivotal impact on the particle transport, which suggests that transient particle transport will be heavily dependent on the duration and magnitude of antegrade flow portions of the inflow waveform.

Particle Reynolds numbers in the AAA domain (for all inflow magnitudes) were less than 0.19, 0.59, and 0.86 for the PLTs, RBCs, and WBCs, respectively. Interestingly, the location of the AAA domain's max. particle Reynolds number was outside the AAA sac for all particles and flow conditions. Table A4.1 lists the max. particle Reynolds number of each particle type in each of the three different flow fields.

Table A4.1: Maximum particle Reynolds numbers in the AAA sac

| Inflow Reynolds Number | Particle Reynolds No. | | |
|------------------------|-----------------------|------------|------------|
| | <i>PLT</i> | <i>RBC</i> | <i>WBC</i> |
| 475 | 0.03 | 0.08 | 0.19 |
| 1129 | 0.12 | 0.37 | 0.59 |
| 1656 | 0.16 | 0.54 | 0.86 |

In the AAA sac, the majority of particle Reynolds numbers (Re_p) are three orders of magnitude below unity and satisfy the condition of Stokes Flow with an $Re_p \ll 1$. The dominance of drag forces is thus reinforced and suggests that the particles' velocity and in turn trajectories can be expected to closely follow the general flow field in the AAA sac. Figure A4.7 plots the particle trajectories colored with particle velocity magnitude and reveals a close match to the fluid streamlines shown in Fig A4.1.

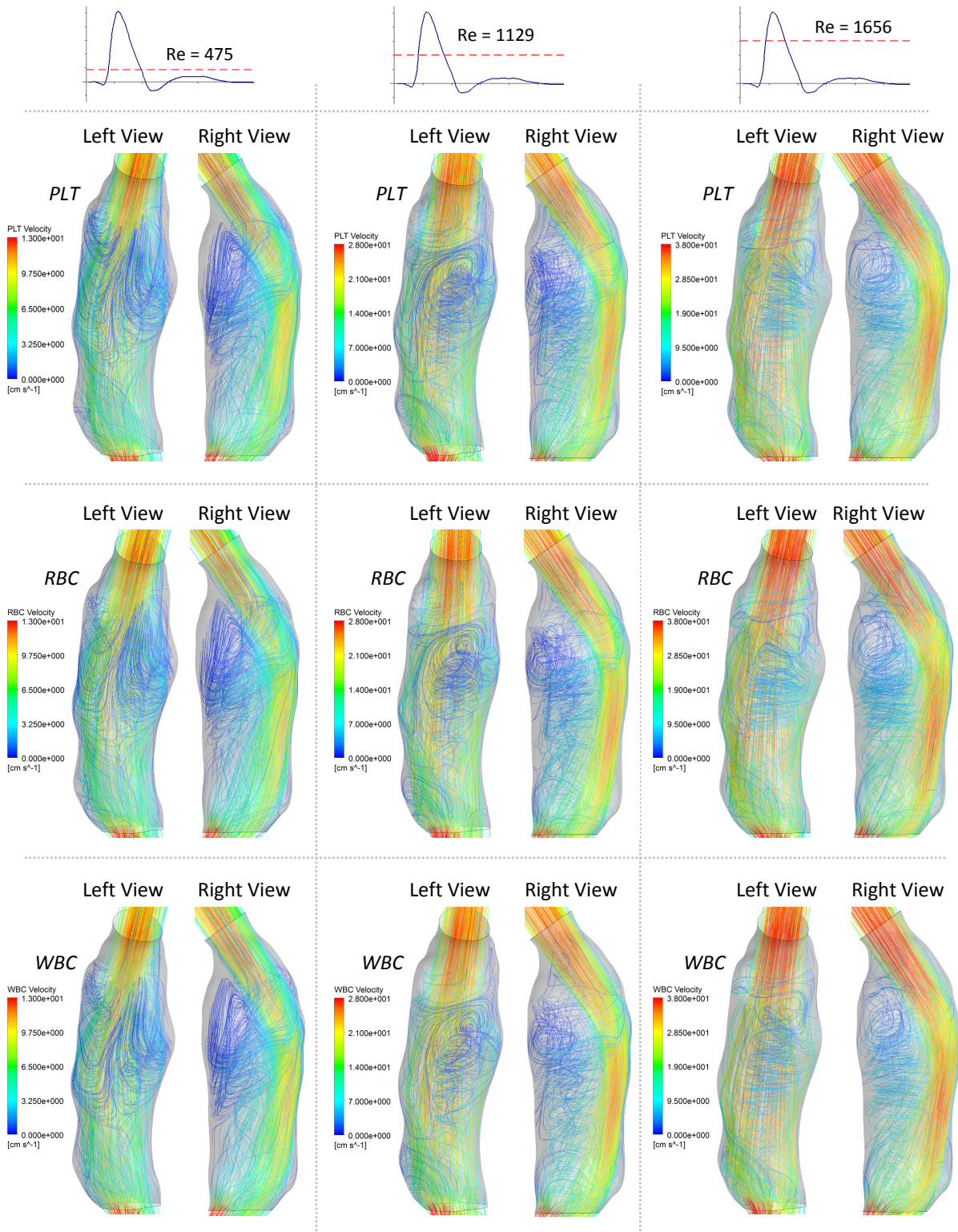


Figure A4.7: Particle trajectories under the different steady flow fields

Interestingly, the individual particle characteristics of the PLTs, RBCs, and WBCs have almost negligible impact on the representative particle trajectories. Particle deposition along the AAA walls was negligible and even the WBCs with the largest diameter and Stokes number primarily deposited at the AAA bifurcation and not in the circulatory flow of the posterior AAA region.

Fluid-Particle Entrapment and Transit Time

Residence time of the Eulerian fluid phase was calculated at each element by integrating Eq. (5.1a,b) and obtaining a spatially varying distribution throughout the AAA domain. The max fluid residence time was inversely related to inflow magnitude and the location of the max values were at near-wall regions of circulating flow particularly at the posterior AAA wall. Figure A4.8 plots the residence time in the AAA sac on cross sectional planes for each inflow Reynolds number with fluid streamlines passing through the planes.

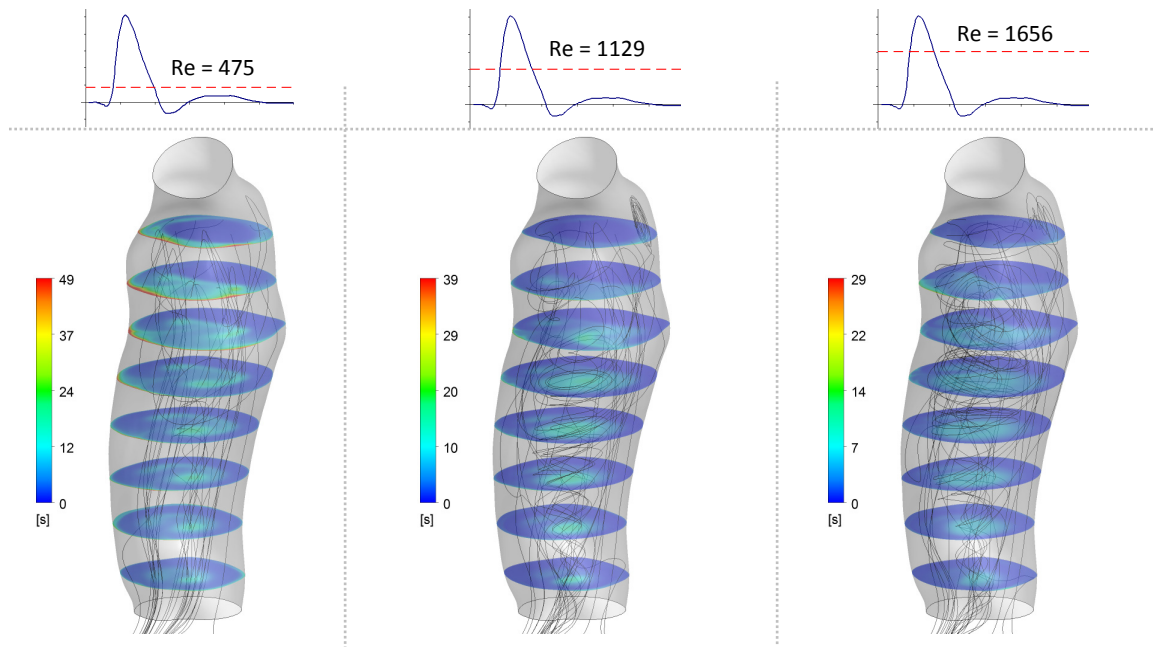


Figure A4.8: Residence time distribution in the AAA sac

Figure A4.8 also reveals a correlation between regions of circulating flow and increased fluid residence time plus a strong dependency on the inflow magnitude. Furthermore, the plots reveal that even constant incoming flow results in regions of elevated fluid residence time due to the AAA domain's vessel expansions causing flow separation and/or recirculation. Figure A4.9 supplements the cross-sectional views by depicting the residence time distribution along the AAA wall revealing specific regions of enhanced fluid residence time along the posterior wall.

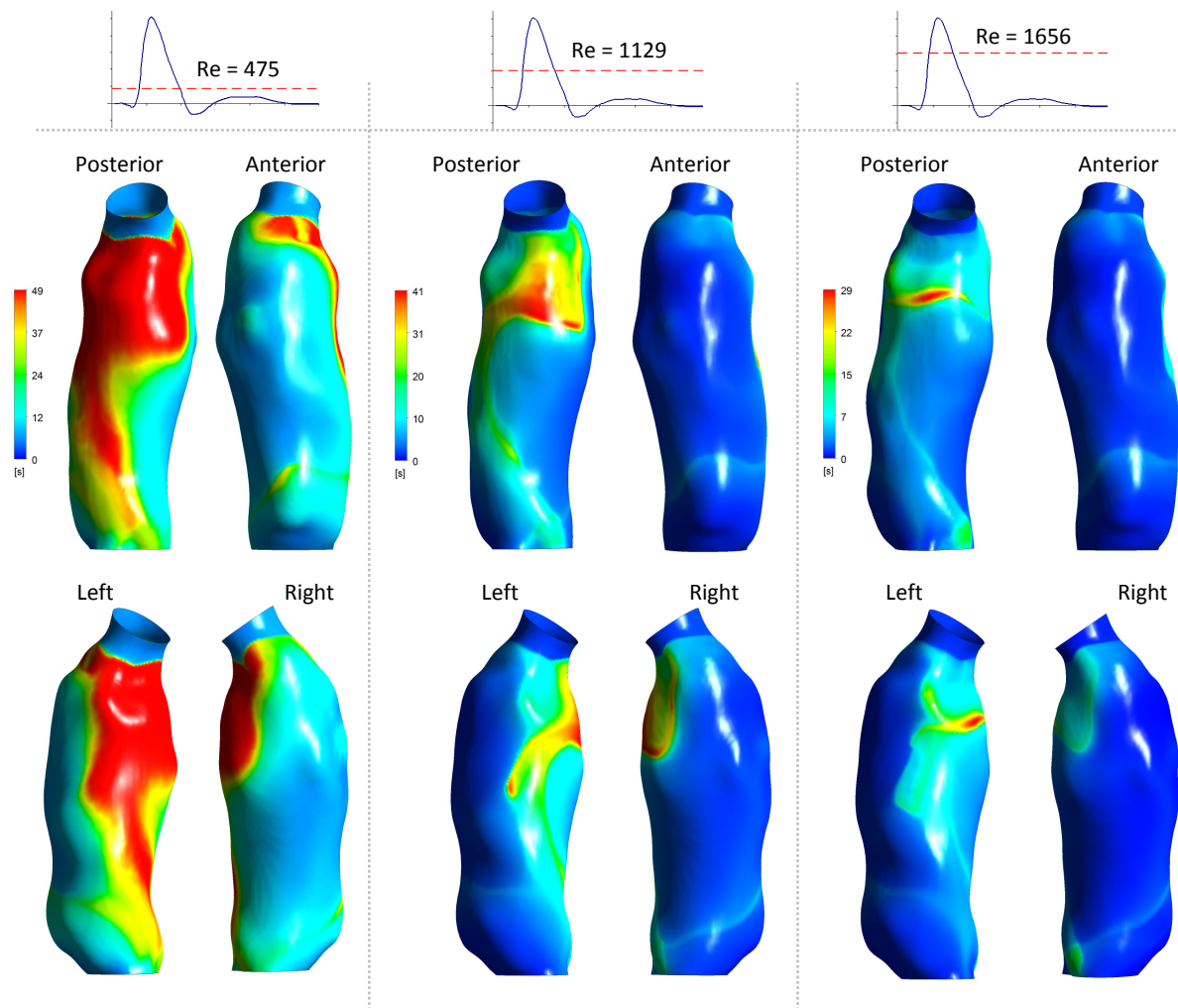


Figure A4.9: Contours of residence time distribution along the AAA wall

Particle entrapment is correlated with the enhanced regions of fluid residence time. Figure A4.10 plots the particle trajectories, where blue, green, and red trajectories represent particles that exit the left iliac artery, exit the right iliac artery, and never leave the system in 10 seconds of continuous inflow, respectively.

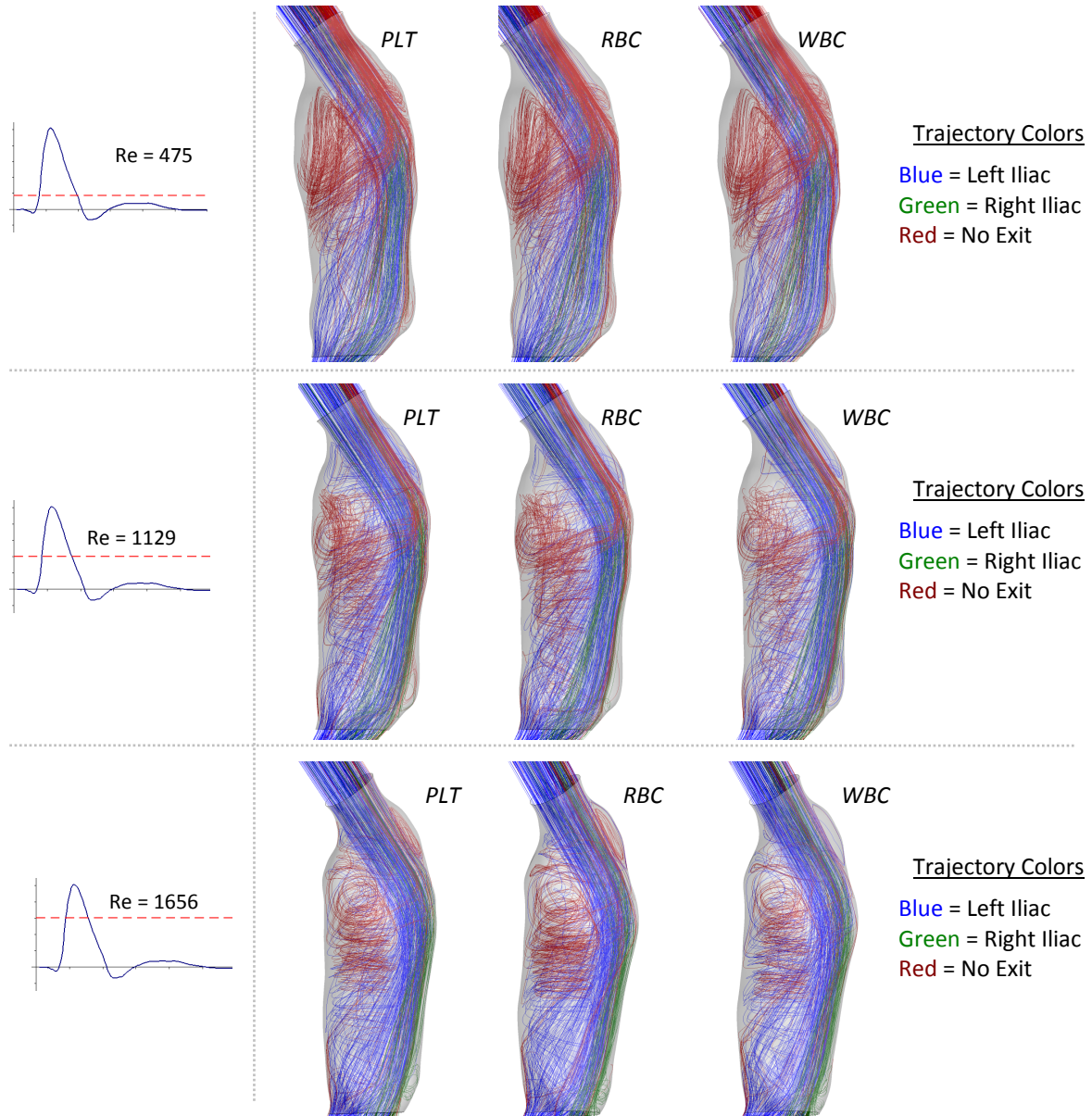


Figure A4.10: Particle trajectory maps in the AAA domain

The spatial location of the entrapped trajectories (red colored) is within regions of circulating flow (see Figs A4.1 and A4.2) and near regions of elevated viscosity and low WSS. While particle recirculation and circulatory trajectories are not unique to particles entrapped in the system, Fig. A4.10 reveals that the overwhelming majority of particles in the recirculation regions do not exit the domain. Again, the same observations hold true that, in general, the results suggest the individual particle characteristics had a lesser importance on particle entrapment than the general AAA morphology and inflow magnitude. The cross-sectional release positions plotted in Fig. A4.11 reinforce this observation by revealing almost negligible differences between the release maps at the particle injection plane of the different particles types with an apparent dependence on the inflow magnitude.

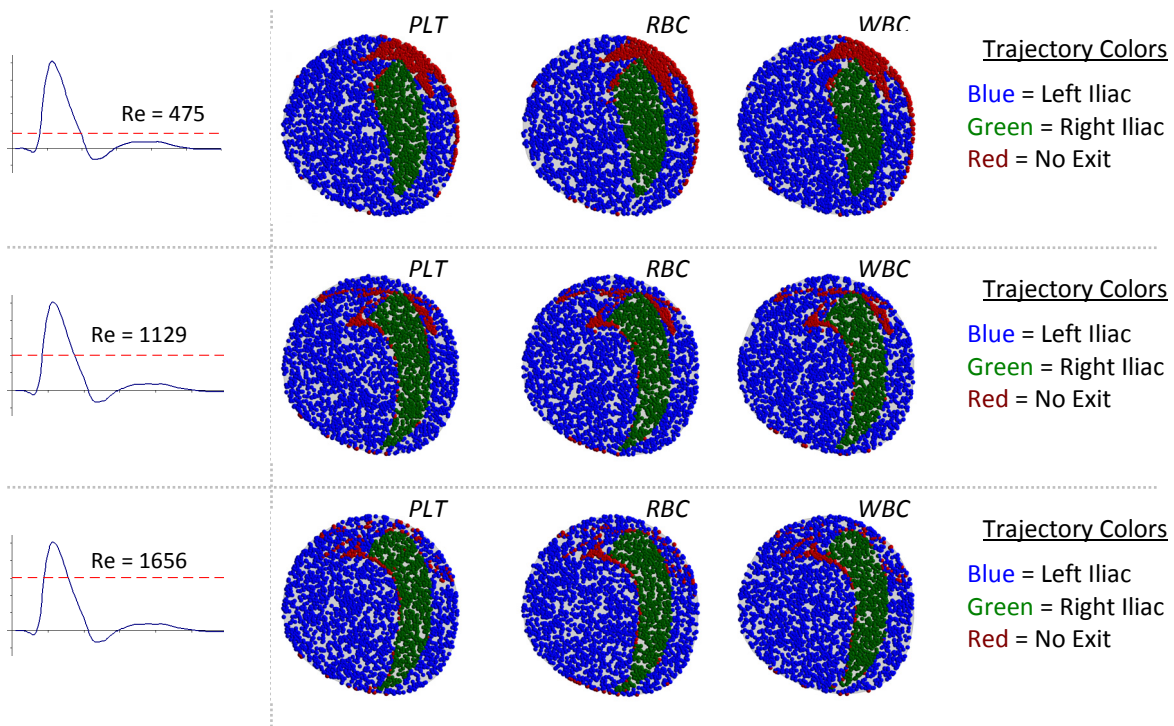


Figure A4.11: Particle release maps at the particle injection plane

An important note is that the spatial area occupied by each zone in Fig A4.11 is directly related to the particle distribution fractions shown in Fig. A4.5. Also of interest is the organization of unique particle release zones in Fig. A4.11, where particles that do not exit the system are actually located towards the anterior surface of the AAA even though the recirculation regions are primarily located in the posterior region of the AAA. The particles are thus transported to the recirculation regions by the incoming flow that collides with the AAA anterior surface and dividing into portions that traverse towards the posterior wall.

While flow in the physiologic AAA system is pulsatile, the steady-state analysis is beneficial as a first test to determine potential dependencies of particle transport on the local hemodynamics. The results suggest that inflow magnitude, inflow duration, and AAA morphology play crucial roles in particle transport throughout the system. Most importantly, the steady flow results support the hypothesis that particles can be entrapped within the AAA domain, where PLTs could become activated due to shear stress exposure and initiate the coagulation/clotting process (see Sect.1.4-1.5) which would lead to ILT formation and/or growth.

APPENDIX VI: Custom ANSYS CFD Post v12.1 Perl Scripts and MATLAB Functions for AAA Particle Post-Processing

Summary

Appendix IV lists the crucial ANSYS CFD Post (Canonsburg, PA) Perl/power syntax scripts and MATLAB particle processing functions that were used for the AAA particle-hemodynamics analysis. The first Perl/power syntax script is an ANSYS CFD Post session file that cycles through all the particles that do not exit the domain and based on their z-coordinate classifies whether the remaining particles are in the region of interest and records the CFX particle identifier number if the particle is in the appropriate region(s). The second Perl/power syntax script is also an ANSYS CFD Post session file that cycles through the particles that deposited along the selected boundary wall(s) and exports the x,y,z locations of the particle deposition location. The MATLAB functions are notably more complex and serve many different purposes. The first function is the PTsegment.m which processes the ANSYS CFD Post particle trajectory output into a Cell data type where each particle is its own Cell index. The second set of code is the script DomainGeometricProcessing.m, which calculates centerline and boundary information of the AAA domain also exported by ANSYS CFD Post. The script also sets up the necessary variables for a local radial coordinate centered at the lumen's approximate centerline. Utilizing the newly created geometric parameters, the next function ParticlePosition.m calculates and plots the transient locations of particles in the different near-wall regions of the current geometry. Subsequently, the

PTrNWRT.m file calculates the near-wall residence times of particles moving through the near-wall regions of interest and the last function PTregShear.m calculates the time-averaged shear stress acting on every particle as it traverses through the near wall region. An important note is that the many of the functions rely on the output of the previous function to correctly operate. Specifically, all MATLAB files require the cell array exported by the file PTsegment.m to run; ParticlePosition.m and PTrNWT.m also require the geometric parameters from DomainGeometricProcessing; and PTregShear requires the regional Cell data type output by the PTrNWT.m function.

ParticleNoExitCounter.cse

```
# Written By: Chris Basciano
# June 2010
# Department of Mechanical and Aerospace Engineering
# North Carolina Sate University, Raleigh, NC

#-----

#PURPOSE: count particles left in AAA domain and record the CFX
#         particle ID numbers of particles in regions of interest

#start timer
! $start = time();

#set total number of injected particles
! $nmax = 10090;

#Create particle tracks of all particles not exiting domain
! $boundaryname = "No Boundary";
! $material = "RBC";

#reset tracklist
! $NBtrackList = ();
! @NBtracks = ();
! @PTnent = ();
! @PTexit = ();
! @PTtrap = ();
! @PTbif = ();

PARTICLE TRACK: Particle Track 1
  Activate Filter = On
  Domain List = All Domains
  Ending Boundary = $boundaryname
  Filter On Track Selection = Off
  Filter On Diameter = Off
  Filter On End = On
  Filter On Start = Off
  Maximum Number of Tracks = $nmax
  Track Material = $material
  Visibility = On
  Option = From Res
END

#get the list of tracks that are displayed and terminate at $boundaryname
! $NBtrackList = getValue( "Particle Track 1", "Tracks Displayed" );
#Tracks Displayed is csv list, need to break it into arry using Perl split
command
! @NBtracks = split(/, /, $NBtrackList );
```

ParticleNoExitCounter.cse [cont]

```
#cylce through tracks and determine if particles enetered or exited 1D
region of interest

#initialize counter variables
! $Knent=0;
! $Kexit=0;
! $Ktrap=0;
! $Kbif=0;

#set uppder and lower region limits
! $Zx = 26;
! $Zn = 17;
! $Znb = 16.5;

! foreach $i ( @NBtracks )
!{
PARTICLE TRACK: Particle Track 2
  Activate Filter = On
  Any All Condition = Match ALL
  Domain List = All Domains
  Ending Boundary = $boundaryname
  Filter On Track Selection = On
  Filter On Diameter = Off
  Filter On End = On
  Filter On Start = Off
  Maximum Number of Tracks = 1
  Track Selection = $i
  Track Material = $material
  Limit Track Option = User Specified
  Track Start Time = 5.5 [s]
  Track End Time = 6.00000 [s]
  Visibility = OFF
  Option = From Res
END

! $minZ = minVal("Z","Particle Track 2");
! $maxZ = maxVal("Z","Particle Track 2");

! if ($maxZ>$Zx)
! {
! @PTnent[$Knent] = $i;
! $Knent = $Knent+1;
! } #end if loop

! if ($minZ<$Znb)
! {
! @PTexit[$Kexit] = $i;
! $Kexit = $Kexit+1;
! } #end if loop
```

ParticleNoExitCounter.cse [cont]

```
! if ($minZ>=$Zn && $maxZ<=$Zx)
! {
! @PTtrap[$Ktrap] = $i;
! $Ktrap = $Ktrap+1;
! } #end if loop

! if ($minZ<$Zn && $minZ>=$Znb)
! {
! @PTbif[$Kbif] = $i;
! $Kbif = $Kbif+1;
! } #end if loop

! } #end foreach loop

! $ptNE = join(", ", @PTnent);
! $ptEX = join(", ", @PTexit);
! $ptE = join(", ", @PTtrap);
! $ptB = join(", ", @PTbif);

# create filenames and open files to export particle track numbers
! @FneA = ($material, "_Particles_NoEnter.txt");
! @FexA = ($material, "_Particles_Exit.txt");
! @FeA = ($material, "_Particles_Trap.txt");
! @FeB = ($material, "_Particles_Bif.txt");

! $FneS = join("", @FneA);
! $FexS = join("", @FexA);
! $FeS = join("", @FeA);
! $FbS = join("", @FeB);

! open OUTne, ">$FneS";
! open OUTex, ">$FexS";
! open OUTe, ">$FeS";
! open OUTb, ">$FbS";

# print data files containing CFX particle track numbers
!print OUTne "## This file contains the CFX particle numbers of
particles\n";
!print OUTne "##          not entering region of interest\n\n";
!print OUTne "$ptNE";

!print OUTex "## This file contains the CFX particle numbers of
particles\n";
!print OUTex "##          exiting region of interest\n\n";
!print OUTex "$ptEX";

!print OUTe "## This file contains the CFX particle numbers of
particles\n";
```

ParticleNoExitCounter.cse [cont]

```
!print OUTe "##          with final position inside AAA sac\n\n";
!print OUTe "$ptE";

!print OUTb "## This file contains the CFX particle numbers of
particles\n";
!print OUTb "##          with final position in bifurcation region\n\n";
!print OUTb "$ptB";

# close export files
! close OUTne;
! close OUTex;
! close OUTe;
! close OUTb;

#end timer
! $end = time();
! $dt = ($end-$start)/60;
! print "\nElapsed time was: ",$dt," [min] \n";

#display ending message
! print "\n          Finito \n";
```

ParticleDepositionPositions.cse

```
# Written By: Chris Basciano
# February 2010
# Department of Mechanical and Aerospace Engineering
# North Carolina Sate University, Raleigh, NC

#-----

# Power syntax / PERL script used for particle post-processing
# Written by: Chris Basciano February 2010

#start timer
! $start = time();

# Set name of material used for particle (specific to .res file)
! $material = "WBC";

# Set name of file for export
! @file = ($material, "_Endpoints.txt");
! $filename = join("",@file);

# Set the name of the boundary on which the tracks terminate
! $boundaryname = "WALL_AAA";

# Set the max. number of tracks to consider
! $nmax = 1000;

# open file for endpoint data
!open OUT, ">$filename";

# print header for data file so it can be read in as a polyline
!print OUT "## This file contains the endpoints of a particle tracking
run.\n";
!print OUT "## X Y Z coordinates are followed by:  particle traveling
distance, particle traveling time, particle speed, and particle
number.\n";
!print OUT "\n[Name]\n";
!print OUT "Polyline 1\n";
!print OUT "\n[Data]\n";
!print OUT "X [ cm ], Y [ cm ], Z [ cm ], Pdistance [ cm ], Ptraveltime [
s ], Pspeed [cm s^-1 ], Pnumber []\n";

#Create particle track for $material whose terminal locations are
$boundaryname

PARTICLE TRACK: Particle Track 1
  Activate Filter = On
  Domain List = All Domains
  Ending Boundary = $boundaryname
  Filter On Track Selection = Off
```

ParticleDepositionPositions.cse [cont]

```
Filter On Diameter = Off
  Filter On End = On
  Filter On Start = Off
  Maximum Number of Tracks = $nmax
  Track Material = $material
  Visibility = On
  Option = From Res
END

#get the list of tracks that are displayed and terminate at $boundaryname
! $trackList = getValue( "Particle Track 1", "Tracks Displayed" );
#Tracks Displayed is csv list, need to break it into array using Perl split
command
!@tracks = split(/, /, $trackList );

#Loop over previous tracks displayed
! foreach $i ( @tracks )
!{
PARTICLE TRACK: Particle Track 2
  Activate Filter = On
  Filter On Track Selection = On
  Maximum Number of Tracks = 1
  Track Material = $material
  Track Selection = $i
  Visibility = Off
  Option = From Res
END

EXPORT:
  Export Connectivity = Off
  Export File = track.dat
  Export Geometry = On
  Export Node Numbers = Off
  Export Null Data = Off
  Export Type = Generic
  Include Header = On
  Location List = Particle Track 2
  Null Token = 0
  Overwrite = On
  Precision = 8
  Separator = ", "
  Spatial Variables = X,Y,Z
  Variable List = $material.Particle Traveling Distance, \
$material.Particle Traveling Time, $material.Velocity
  Vector Brackets = ()
  Vector Display = Scalar
END

>export
```

ParticleDepositionPositions.cse [cont]

```
!open TEMP, "< track.dat";
!$/ = "\n";
!$j = 1;
#determines last line of TEMP file and gives that line value to x and y
!while (defined ($x = <TEMP>))
!{
!$y = $x;
!$j++;
!} #end while loop

!chomp $y; #removes end of line character
#exports final position of particle $i to polyline file
!print OUT "$y, $i\n";

!close TEMP;

!} #end for loop

!close OUT;

#end timer
! $end = time();
! print "\n";
! print "Elapsed time was", ($end-$start),"[s]";
! print "\n";
```

PTsegment.m

```
%Purpose: Function to segment particle track file into a cell array where
%         each cell contains one particle's trajectory data
%
%Input: Requires particle track file with specified arrangement of
%       particle variables:
%       1) Temporal data must be row-based such that each row
%          corresponds to a different point in time
%       2) Column 9 MUST contain either particle traveling
%          distance or particle traveling time
%       3) Total number of particles MUST be less than 5000
%
%Output: 1) Cell array of each particle trajectory,
%        2) Number of particle trajectories,
%        3) Array of each particle's index and range of data
%
%-----
%               Written By: Christopher Basciano
%                   May 2010
%       Department of Mechanical and Aerospace Engineering
%       North Carolina State University, Raleigh, NC
%-----

function [CelllPT,nPT,PTrc] = PTsegment(pt_data)

%get size of dataset
[nR,nC] = size(pt_data);

%initialize counter variable (k) for number of PTs and allocate array that
%records rows of initial and final locations of particle (PTrc)
k=0;
PTrc = zeros(5000,3);

%Loop through array containing particle trajectory data row-by-row
for i=1:nR
    %Determine if current line is initial position of particle by testing
    %if its traveling time or distance is zero
    if pt_data(i,9)==0
        k=k+1; %increment particle counter
        PTrc(k,1)=k; %record particle index
        PTrc(k,2)=i; %record row of initial particle position
        if k>=2
            PTrc(k-1,3)=i-1; %Record row of final particle position
        end
    end
end
%Complete row recording and construct Cell array after last row of
%particle data array
if i==nR
    nPT = k; %record final value of particle counter
    PTrc(nPT,3)=nR; %record last particle's row of final position
    CelllPT = cell(nPT,1); %allocate cell array dimensions
end
```

PTsegment.m [cont]

```
%construct cell array where each cell
% contains one particle's trajectory data
for ii=1:nPT
    r1 = PTrc(ii,2);    %recall row of particle's initial position
    r2 = PTrc(ii,3);    %recall row of particle's final position
    %set array cell to range of particle's data
    CellPT{ii,1} = pt_data(r1:r2,1:nC);
end
end
end
end %end function
```

DomainGeometricProcessing.m

```
%Purpose: MATLAB script to construct geometric parameters that describe
          the AAA lumen and save them with a .mat extension for easy
          future use
%
%Input: Two ASCII data files from CFX Post:
%       File 1) x,y,z centerpoints of AAA cross-sectional planes
%       File 2) x,y,z points of curve surrounding each AAA
%             cross-sectional planes
%
%Output: Figure of constructed near wall region and saved .mat file for
%       future use
%
%-----
%                               Written By: Christopher Basciano
%                               June 2010
%       Department of Mechanical and Aerospace Engineering
%       North Carolina State University, Raleigh, NC
%-----

%AAA geometric Parameter Processing

close all
clear all
clc

%center points of planes in AAA Sac
fpath =
'D:\ChrisBasciano2\ILT_Particle_Hemodynamics2\AAA_Sac_Centerline_Points.csv';
v';
Cpoints = dlmread(fpath, ',', 8, 0);
[npr, npc] = size(Cpoints);
Xd = Cpoints(1:npr, 1);
Yd = Cpoints(1:npr, 2);
Zd = Cpoints(1:npr, 3);

%data file containing wall lines
fpath =
'D:\ChrisBasciano2\ILT_Particle_Hemodynamics2\AAA_Sac_WallPolylines.csv';
Wall = dlmread(fpath, ',', 8, 0);
[wr, wc] = size(Wall);
track = zeros(wr, 2);
track(1, 1) = 1;
k=0;
for i=1:wr-1
    if Wall(i, 3)~=Wall(i+1, 3)
        k=k+1;
        track(k, 2)=i;
        track(k+1, 1)=i+1;
    end
end
if i==wr-1
```

DomainGeometricProcessing.m [cont]

```
nL = k+1;
track(nL,2)=i+1;
cL = cell(nL,1);
RL = zeros(nL,1);
for ii=1:nL
    r1 = track(ii,1);
    r2 = track(ii,2);
    cL{ii}= Wall(r1:r2,1:wc);
    %calculate min. local radial coordiante of AAA wall lines
    xL = cL{ii}(:,1) - Xd(ii); %local x-coord
    yL = cL{ii}(:,2) - Yd(ii); %local y-coord
    rL = sqrt( xL.^2 + yL.^2 ); %local radial coord
    RL(ii) = min(rL);
end
end
end

%Rearrange data so that the minimum z-location is the first entry
Cpoints = [Cpoints(10,1:3); Cpoints(1:9,1:3)];
Xd = Cpoints(1:npr,1);
Yd = Cpoints(1:npr,2);
Zd = Cpoints(1:npr,3);
cL = {cL{10} cL{1:9}};
RL = [RL(10); RL(1:9)];

%Construct circles that are a distance 'dw' from minimum wall radius
dw = 0.1;
nn = 50;
zi = [0:1:9];
xlg = zeros(nn,length(zi));
ylg = zeros(nn,length(zi));
zlg = zeros(nn,length(zi));
for k=1:length(zi)
    r = interp1(Zd,RL,zi(k),'pcubic') - dw;
    [xm,ym,zm] = cylinder(r,nn);
    for j=1:nn
        xlg(j,k) = xm(1,j) + interp1(Zd,Xd,zi(k),'pcubic');
        ylg(j,k) = ym(1,j) + interp1(Zd,Yd,zi(k),'pcubic');
        zlg(j,k) = zm(1,j);
    end
end

%construct spline centerline
zs = [0:0.25:9]';
xs = interp1(Zd,Xd,zs,'pchip');
ys = interp1(Zd,Yd,zs,'pchip');
```

DomainGeometricProcessing.m [cont]

```
%plot reconstructed AAA geometry
figure
axes('YTickLabel',{ '2.5', '2.0', '1.5', '1.0', '0.5', '0.0', '-0.5', '-1.0', '-1.5', '-2.0'},...
     'FontSize',12);
hold on
plot3(Xd,Yd,-1*Zd,'ok')
plot3(xs,ys,-1*zs,'k-','LineWidth',1.0)
for i=1:nL
    plot3(cL{i}(:,1),cL{i}(:,2),-1*cL{i}(:,3),'k','LineWidth',2)
end
for i=1:length(zi)
    plot3(xlg(:,i),ylg(:,i),-1*zlg(:,i),'r:')
end
hold off
xlim([-1.5 2.5])
ylim([-2.5 2])
zlim([-9.5 0.5])
xlabel('Anatomic Y-Coord. [cm]','FontSize',16)
ylabel('Anatomic X-Coord. [cm]','FontSize',16)
zlabel('Anatomic Z-Coord. [cm]','FontSize',16)

save ('AAA_Geometric_Parameters.mat','Cpoints','RL','cL')
```

ParticlePosition.m

```
%Purpose: Function to plot the particles in the near-wall regions
%
%Input: Cell Array where data in Cell elements are temporal row-based with
%       NaN entered at all values not in region of interest
%
%Output: Figure(s) of desired data ranges
%
%-----
%               Written By: Christopher Basciano
%                   June 2010
%       Department of Mechanical and Aerospace Engineering
%       North Carolina State University, Raleigh, NC
%-----

function [Npt]=ParticlePosition(Cell,Time,Cpoints,cL,RL)

%Assumed columns in Cell data are:
%   X, Y, Z, Time-Averaged Pressure Gradient on PT trajectories,
%   Fluid Residence Time Distribution on Trajectories,
%   PT_Reynolds_Number, PT_Slip_Velocity, PT_Time,
%   PT_Travel_Distance, PT_Travel_Time, PT_Velocity Magnitude,

%determine size of cell array
rC = length(Cell);

%create new cell for additional trajectory calculations
Fpos = zeros(rC,3);

%set centerpoint coordinates
Xd = Cpoints(:,1);
Yd = Cpoints(:,2);
Zd = Cpoints(:,3);

%interpolation spline points
zs = [0:0.25:9]';
xs = interp1(Zd,Xd,zs,'pchip');
ys = interp1(Zd,Yd,zs,'pchip');

%plot the AAA geometry with particle locations
figure
hold on
plot3(Xd,Yd,-1*Zd,'ok') %centerpoints
plot3(xs,ys,-1*zs,'k-','LineWidth',2.0) %center spline curve
nL = length(cL);
for i=1:nL
    plot3(cL{i}(:,1),cL{i}(:,2),-1*cL{i}(:,3),'k') %wall splines
end
```

ParticlePosition.m [cont]

```
%loop through local coordinates and plot particle locations
q1u=0; q2u=0; q3u=0; q4u=0;
q1m=0; q2m=0; q3m=0; q4m=0;
q1b=0; q2b=0; q3b=0; q4b=0;
dw = 0.1;
for i=1:rC

    %get size of local array in cell element
    [nr,nc] = size(Cell{i});

    %Get x,y,z points from each trajectory at 'Time'
    Fpos(i,1) =
    interp1(Cell{i}(1:5:nr,8),Cell{i}(1:5:nr,1),Time,'pcubic');
    Fpos(i,2) =
    interp1(Cell{i}(1:5:nr,8),Cell{i}(1:5:nr,2),Time,'pcubic');
    Fpos(i,3) =
    interp1(Cell{i}(1:5:nr,8),Cell{i}(1:5:nr,3),Time,'pcubic');

    %convert particle final position to local coordinates centered at a
    % spline curve approximating lumen centerline and calculate distance
    from
    % minimum radial distance of the local wall
    Lc = zeros(rC,3);
    FposL = zeros(rC,4);
    Lc(:,1) = interp1(Zd,Xd,Fpos(:,3),'pchip');
    Lc(:,2) = interp1(Zd,Yd,Fpos(:,3),'pchip');
    FposL(:,1) = Fpos(:,1) - Lc(:,1); %local x-coord
    FposL(:,2) = Fpos(:,2) - Lc(:,2); %local y-coord
    FposL(:,3) = sqrt( FposL(:,1).^2 + FposL(:,2).^2 ); %local radial
    coord
    FposL(:,4) = interp1(Zd,RL,Fpos(:,3),'pchip') - FposL(:,3);

    %determines what region particle coordinates are in
    if ( Fpos(i,3)>=0 && Fpos(i,3)<3.0 ) %proximal region
        if ( FposL(i,1)>=0 && FposL(i,2)>0 && FposL(i,4)<=dw ) %quadrant
            plot3(Fpos(i,1),Fpos(i,2),-1*Fpos(i,3),'cs','MarkerSize',5)
            q1u = q1u + 1; %counter
        elseif ( FposL(i,1)<0 && FposL(i,2)>=0 && FposL(i,4)<=dw )
            plot3(Fpos(i,1),Fpos(i,2),-1*Fpos(i,3),'gs','MarkerSize',5)
            q2u = q2u + 1;
        elseif ( FposL(i,1)<=0 && FposL(i,2)<0 && FposL(i,4)<=dw )
            plot3(Fpos(i,1),Fpos(i,2),-1*Fpos(i,3),'bs','MarkerSize',5)
            q3u = q3u + 1;
        elseif ( FposL(i,1)>0 && FposL(i,2)<=0 && FposL(i,4)<=dw )
            plot3(Fpos(i,1),Fpos(i,2),-1*Fpos(i,3),'rs','MarkerSize',5)
            q4u = q4u + 1;
        end
    elseif ( Fpos(i,3)>=3.0 && Fpos(i,3)<=6.0 ) %mid region
        if ( FposL(i,1)>=0 && FposL(i,2)>0 && FposL(i,4)<=dw ) %quadrant
```

ParticlePosition.m [cont]

```
    plot3(Fpos(i,1),Fpos(i,2),-1*Fpos(i,3),...
          'c^','MarkerFaceColor','c','MarkerSize',5)
    q1m = q1m + 1; %counter
elseif ( FposL(i,1)<0 && FposL(i,2)>=0 && FposL(i,4)<=dw )
    plot3(Fpos(i,1),Fpos(i,2),-1*Fpos(i,3),...
          'g^','MarkerFaceColor','g','MarkerSize',5)
    q2m = q2m + 1;
elseif ( FposL(i,1)<=0 && FposL(i,2)<0 && FposL(i,4)<=dw )
    plot3(Fpos(i,1),Fpos(i,2),-1*Fpos(i,3),...
          'b^','MarkerFaceColor','b','MarkerSize',5)
    q3m = q3m + 1;
elseif ( FposL(i,1)>0 && FposL(i,2)<=0 && FposL(i,4)<=dw )
    plot3(Fpos(i,1),Fpos(i,2),-1*Fpos(i,3),...
          'r^','MarkerFaceColor','r','MarkerSize',5)
    q4m = q4m + 1;
end
elseif ( Fpos(i,3)>6.0 && Fpos(i,3)<9.0 )
    if ( FposL(i,1)>=0 && FposL(i,2)>0 && FposL(i,4)<=dw ) %quadrant
        plot3(Fpos(i,1),Fpos(i,2),-1*Fpos(i,3),'c+','LineWidth',1)
        q1b = q1b + 1; %counter
    elseif ( FposL(i,1)<0 && FposL(i,2)>=0 && FposL(i,4)<=dw )
        plot3(Fpos(i,1),Fpos(i,2),-1*Fpos(i,3),'g+','LineWidth',1)
        q2b = q2b + 1;
    elseif ( FposL(i,1)<=0 && FposL(i,2)<0 && FposL(i,4)<=dw )
        plot3(Fpos(i,1),Fpos(i,2),-1*Fpos(i,3),'b+','LineWidth',1)
        q3b = q3b + 1;
    elseif ( FposL(i,1)>0 && FposL(i,2)<=0 && FposL(i,4)<=dw )
        plot3(Fpos(i,1),Fpos(i,2),-1*Fpos(i,3),'r+','LineWidth',1)
        q4b = q4b + 1;
    end
end
end
hold off
xlim([-1.5 2.5])
ylim([-2.5 2])
zlim([-9.5 0.5])
xlabel('Anatomic Y-Coord. [cm]')
ylabel('Anatomic X-Coord. [cm]')
zlabel('Anatomic Z-Coord. [cm]')

%Reconstruct the data quadrants into anatomic quadrants
% Anterior Right = data quad 4
% Anterior Left = data quad 1
% Posterior Left = data quad 2
% Posterior Right = data quad 3
Qu = [q4u; q1u; q2u; q3u];
Qm = [q4m; q1m; q2m; q3m];
Qb = [q4b; q1b; q2b; q3b];
Npt = [Qu, Qm, Qb];
```

ParticlePosition.m [cont]

```
%plot number of particles in bar graph
figure
axes('XTick',[1 2 3 4]);
box('on');
bar(Npt,'group')
xlabel('Quadrant Number','FontSize',14)
ylabel('Number of Particles','FontSize',14)
legend('Proximal AAA','Middle AAA','Distal AAA')

end %end function
```

PTrNWRT.m

```
%Purpose: Function to calculate regional distribution of particle near-  
          wall residence time illustrate particle positions close to wall  
          over the data's final cardiac cycle
```

```
%  
%Input: Cell Array where data in Cell elements are temporal row-based  
%  
%Output: Figure(s) of desired data ranges  
%
```

```
-----  
%  
%                Written By: Christopher Basciano  
%                June 2010  
%                Department of Mechanical and Aerospace Engineering  
%                North Carolina State University, Raleigh, NC  
%-----
```

```
function [RegionCells,TransTimes]=PTrNWRT(Cell,Cpoints,RL)
```

```
%Assumed columns of data is:  
%   X, Y, Z, Time-Averaged Pressure Gradient on PT trajectories,  
%   Fluid Residence Time Distribution on Trajectories,  
%   PT_Reynolds_Number, PT_Slip_Velocity, PT_Time,  
%   PT_Travel_Distance, PT_Travel_Time, PT_Velocity Magnitude,
```

```
rC = length(Cell);
```

```
%number of regions where local transit times will be calculated  
nROI = 12;  
%cell that stores particle data in each region  
RegionCells = cell(rC,nROI);  
%Cell which local centerpoint for each particle position  
Lc = cell(rC);  
%Cell which holds particles local coordinates  
PTposL = cell(rC);  
%radial distance from wall to define regions of interest  
dw = 0.1;  
%Array which stores net transit time of each particle through each region  
TransTimes = zeros(rC,nROI);
```

```
%AAA Sac centerline points
```

```
Xd = Cpoints(:,1);
```

```
Yd = Cpoints(:,2);
```

```
Zd = Cpoints(:,3);
```

```
%cycle through each particle's data
```

```
for i=1:rC
```

```
    [nr,nc] = size(Cell{i});
```

```
    for k=1:nROI
```

```
        RegionCells{i,k} = zeros(12,5);
```

PtrNWRT.m [cont]

```
end

%convert particle position to local coordinates centered at a
% spline curve approximating lumen centerline and calculate
% radial distance from minimum local wall radius
%Vessel x,y centroid location at particle's z location
Lc{i}(1:nr,1) = interp1(Zd,Xd,Cell{i}(1:nr,3), 'pchip');
Lc{i}(1:nr,2) = interp1(Zd,Yd,Cell{i}(1:nr,3), 'pchip');
%local x-coord from lumen centroid
PTposL{i}(1:nr,1) = Cell{i}(1:nr,1) - Lc{i}(1:nr,1);
%local y-coord from lumen centroid
PTposL{i}(1:nr,2) = Cell{i}(1:nr,2) - Lc{i}(1:nr,2);
%local z-coord from lumen centroid
PTposL{i}(1:nr,3) = Cell{i}(1:nr,3);
%local radial coord from lumen centroid;
PTposL{i}(1:nr,4) = sqrt( PTposL{i}(1:nr,1).^2 + ...
    PTposL{i}(1:nr,2).^2 );
%radial distance from minimum wall radius;
PTposL{i}(1:nr,5) = interp1(Zd,RL,Cell{i}(1:nr,3), 'pchip') - ...
    PTposL{i}(1:nr,4);

%cycle through each line of particle (i)'s data
ctr1=0; ctr2=0; ctr3=0; ctr4=0;
ctr5=0; ctr6=0; ctr7=0; ctr8=0;
ctr9=0; ctr10=0; ctr11=0; ctr12=0;
for ii=2:nr-1

    %Determine if particle is in ROI 1 (Prox. Anterior Right)
    if ( PTposL{i}(ii,1)>=0 && PTposL{i}(ii,2)<0 && ...
        PTposL{i}(ii,3)>=0 && PTposL{i}(ii,3)<3.0 && ...
        PTposL{i}(ii,5)<=dw )
        %Determine if row is entry point of particle into ROI 1
        if ( PTposL{i}(ii-1,1)<0 || PTposL{i}(ii-1,2)>=0 || ...
            PTposL{i}(ii-1,3)<0 || PTposL{i}(ii-1,3)>=3.0 || ...
            PTposL{i}(ii-1,5)>dw )
            ctr1 = ctr1 + 1;
            RegionCells{i,1}(ctr1,1)= ii;
            RegionCells{i,1}(ctr1,3)= Cell{i}(ii,8);
        end
        %Determine if row is exit point of particle out of ROI 1
        if ( PTposL{i}(ii+1,1)<0 || PTposL{i}(ii+1,2)>=0 || ...
            PTposL{i}(ii+1,3)<0 || PTposL{i}(ii+1,3)>=3.0 || ...
            PTposL{i}(ii+1,5)>dw )
            RegionCells{i,1}(ctr1,2) = ii;
            RegionCells{i,1}(ctr1,4) = Cell{i}(ii,8);
        end
    end
end %End ROI 1 if-statement

%Determine if particle is in ROI 2 (Prox. Anterior Left)
```

PTrNWRT.m [cont]

```
if ( PTposL{i}(ii,1)>=0 && PTposL{i}(ii,2)>=0 && ...
    PTposL{i}(ii,3)>=0 && PTposL{i}(ii,3)<3.0 && ...
    PTposL{i}(ii,5)<=dw )
    %Determine if row is entry point of particle into ROI 2
    if ( PTposL{i}(ii-1,1)<0 || PTposL{i}(ii-1,2)<0 || ...
        PTposL{i}(ii-1,3)<0 || PTposL{i}(ii-1,3)>=3.0 || ...
        PTposL{i}(ii-1,5)>dw )
        ctr2 = ctr2 + 1;
        RegionCells{i,2}(ctr2,1)= ii;
        RegionCells{i,2}(ctr2,3)= Cell{i}(ii,8);
    end
    %Determine if row is exit point of particle out of ROI 2
    if ( PTposL{i}(ii+1,1)<0 || PTposL{i}(ii+1,2)<0 || ...
        PTposL{i}(ii+1,3)<0 || PTposL{i}(ii+1,3)>=3.0 || ...
        PTposL{i}(ii+1,5)>dw )
        RegionCells{i,2}(ctr2,2) = ii;
        RegionCells{i,2}(ctr2,4) = Cell{i}(ii,8);
    end
end %End ROI 2 if-statement

%Determine if particle is in ROI 3 (Prox. Posterior Left)
if ( PTposL{i}(ii,1)<0 && PTposL{i}(ii,2)>=0 && ...
    PTposL{i}(ii,3)>=0 && PTposL{i}(ii,3)<3.0 && ...
    PTposL{i}(ii,5)<=dw )
    %Determine if row is entry point of particle into ROI 3
    if ( PTposL{i}(ii-1,1)>=0 || PTposL{i}(ii-1,2)<0 || ...
        PTposL{i}(ii-1,3)<0 || PTposL{i}(ii-1,3)>=3.0 || ...
        PTposL{i}(ii-1,5)>dw )
        ctr3 = ctr3 + 1;
        RegionCells{i,3}(ctr3,1)= ii;
        RegionCells{i,3}(ctr3,3)= Cell{i}(ii,8);
    end
    %Determine if row is exit point of particle out of ROI 3
    if ( PTposL{i}(ii+1,1)>=0 || PTposL{i}(ii+1,2)<0 || ...
        PTposL{i}(ii+1,3)<0 || PTposL{i}(ii+1,3)>=3.0 || ...
        PTposL{i}(ii+1,5)>dw )
        RegionCells{i,3}(ctr3,2) = ii;
        RegionCells{i,3}(ctr3,4) = Cell{i}(ii,8);
    end
end %End ROI 3 if-statement

%Determine if particle is in ROI 4 (Prox. Posterior Right)
if ( PTposL{i}(ii,1)<0 && PTposL{i}(ii,2)<0 && ...
    PTposL{i}(ii,3)>=0 && PTposL{i}(ii,3)<3.0 && ...
    PTposL{i}(ii,5)<=dw )
    %Determine if row is entry point of particle into ROI 4
    if ( PTposL{i}(ii-1,1)>=0 || PTposL{i}(ii-1,2)>=0 || ...
        PTposL{i}(ii-1,3)<0 || PTposL{i}(ii-1,3)>=3.0 || ...
        PTposL{i}(ii-1,5)>dw )
        ctr4 = ctr4 + 1;
```

PTrNWRT.m [cont]

```
        RegionCells{i,4}(ctr4,1)= ii;
        RegionCells{i,4}(ctr4,3)= Cell{i}(ii,8);
    end
    %Determine if row is exit point of particle out of ROI 4
    if ( PTposL{i}(ii+1,1)>=0 || PTposL{i}(ii+1,2)>=0 || ...
        PTposL{i}(ii+1,3)<0 || PTposL{i}(ii+1,3)>=3.0 || ...
        PTposL{i}(ii+1,5)>dw )
        RegionCells{i,4}(ctr4,2) = ii;
        RegionCells{i,4}(ctr4,4) = Cell{i}(ii,8);
    end
end %End ROI 4 if-statement

%Determine if particle is in ROI 5 (Mid. Ant. Right)
if ( PTposL{i}(ii,1)>=0 && PTposL{i}(ii,2)<0 && ...
    PTposL{i}(ii,3)>=3 && PTposL{i}(ii,3)<=6.0 && ...
    PTposL{i}(ii,5)<=dw )
    %Determine if row is entry point of particle into ROI 5
    if ( PTposL{i}(ii-1,1)<0 || PTposL{i}(ii-1,2)>=0 || ...
        PTposL{i}(ii-1,3)<3.0 || PTposL{i}(ii-1,3)>6.0 || ...
        PTposL{i}(ii-1,5)>dw )
        ctr5 = ctr5 + 1;
        RegionCells{i,5}(ctr5,1)= ii;
        RegionCells{i,5}(ctr5,3)= Cell{i}(ii,8);
    end
    %Determine if row is exit point of particle out of ROI 5
    if ( PTposL{i}(ii+1,1)<0 || PTposL{i}(ii+1,2)>=0 || ...
        PTposL{i}(ii+1,3)<3.0 || PTposL{i}(ii+1,3)>6.0 || ...
        PTposL{i}(ii+1,5)>dw )
        RegionCells{i,5}(ctr5,2) = ii;
        RegionCells{i,5}(ctr5,4) = Cell{i}(ii,8);
    end
end %End ROI 5 if-statement

%Determine if particle is in ROI 6 (Mid. Ant. Left)
if ( PTposL{i}(ii,1)>=0 && PTposL{i}(ii,2)>=0 && ...
    PTposL{i}(ii,3)>=3 && PTposL{i}(ii,3)<=6.0 && ...
    PTposL{i}(ii,5)<=dw )
    %Determine if row is entry point of particle into ROI 6
    if ( PTposL{i}(ii-1,1)<0 || PTposL{i}(ii-1,2)<0 || ...
        PTposL{i}(ii-1,3)<3.0 || PTposL{i}(ii-1,3)>6.0 || ...
        PTposL{i}(ii-1,5)>dw )
        ctr6 = ctr6 + 1;
        RegionCells{i,6}(ctr6,1)= ii;
        RegionCells{i,6}(ctr6,3)= Cell{i}(ii,8);
    end
    %Determine if row is exit point of particle out of ROI 6
    if ( PTposL{i}(ii+1,1)<0 || PTposL{i}(ii+1,2)<0 || ...
        PTposL{i}(ii+1,3)<3.0 || PTposL{i}(ii+1,3)>6.0 || ...
        PTposL{i}(ii+1,5)>dw )
        RegionCells{i,6}(ctr6,2) = ii;
```

PTrNWRT.m [cont]

```
        RegionCells{i,6}(ctr6,4) = Cell{i}(ii,8);
    end
end %End ROI 6 if-statement

%Determine if particle is in ROI 7 (Mid. Post. Left)
if ( PTposL{i}(ii,1)<0 && PTposL{i}(ii,2)>=0 && ...
    PTposL{i}(ii,3)>=3 && PTposL{i}(ii,3)<=6.0 && ...
    PTposL{i}(ii,5)<=dw )
    %Determine if row is entry point of particle into ROI 7
    if ( PTposL{i}(ii-1,1)>=0 || PTposL{i}(ii-1,2)<0 || ...
        PTposL{i}(ii-1,3)<3.0 || PTposL{i}(ii-1,3)>6.0 || ...
        PTposL{i}(ii-1,5)>dw )
        ctr7 = ctr7 + 1;
        RegionCells{i,7}(ctr7,1) = ii;
        RegionCells{i,7}(ctr7,3) = Cell{i}(ii,8);
    end
    %Determine if row is exit point of particle out of ROI 7
    if ( PTposL{i}(ii+1,1)>=0 || PTposL{i}(ii+1,2)<0 || ...
        PTposL{i}(ii+1,3)<3.0 || PTposL{i}(ii+1,3)>6.0 || ...
        PTposL{i}(ii+1,5)>dw )
        RegionCells{i,7}(ctr7,2) = ii;
        RegionCells{i,7}(ctr7,4) = Cell{i}(ii,8);
    end
end %End ROI 7 if-statement

%Determine if particle is in ROI 8 (Mid. Post. Right)
if ( PTposL{i}(ii,1)<0 && PTposL{i}(ii,2)<0 && ...
    PTposL{i}(ii,3)>=3 && PTposL{i}(ii,3)<=6.0 && ...
    PTposL{i}(ii,5)<=dw )
    %Determine if row is entry point of particle into ROI 8
    if ( PTposL{i}(ii-1,1)>=0 || PTposL{i}(ii-1,2)>=0 || ...
        PTposL{i}(ii-1,3)<3.0 || PTposL{i}(ii-1,3)>6.0 || ...
        PTposL{i}(ii-1,5)>dw )
        ctr8 = ctr8 + 1;
        RegionCells{i,8}(ctr8,1) = ii;
        RegionCells{i,8}(ctr8,3) = Cell{i}(ii,8);
    end
    %Determine if row is exit point of particle out of ROI 8
    if ( PTposL{i}(ii+1,1)>=0 || PTposL{i}(ii+1,2)>=0 || ...
        PTposL{i}(ii+1,3)<3.0 || PTposL{i}(ii+1,3)>6.0 || ...
        PTposL{i}(ii+1,5)>dw )
        RegionCells{i,8}(ctr8,2) = ii;
        RegionCells{i,8}(ctr8,4) = Cell{i}(ii,8);
    end
end %End ROI 8 if-statement

%Determine if particle is in ROI 9 (Dist. Ant. Right)
if ( PTposL{i}(ii,1)>=0 && PTposL{i}(ii,2)<0 && ...
    PTposL{i}(ii,3)>6 && PTposL{i}(ii,3)<=9.0 && ...
    PTposL{i}(ii,5)<=dw )
```

PTrNWRT.m [cont]

```
%Determine if row is entry point of particle into ROI 9
if ( PTposL{i}(ii-1,1)<0 || PTposL{i}(ii-1,2)>=0 || ...
    PTposL{i}(ii-1,3)<=6.0 || PTposL{i}(ii-1,3)>9.0 || ...
    PTposL{i}(ii-1,5)>dw )
    ctr9 = ctr9 + 1;
    RegionCells{i,9}(ctr9,1)= ii;
    RegionCells{i,9}(ctr9,3)= Cell{i}(ii,8);
end
%Determine if row is exit point of particle out of ROI 9
if ( PTposL{i}(ii+1,1)<0 || PTposL{i}(ii+1,2)>=0 || ...
    PTposL{i}(ii+1,3)<=6.0 || PTposL{i}(ii+1,3)>9.0 || ...
    PTposL{i}(ii+1,5)>dw )
    RegionCells{i,9}(ctr9,2) = ii;
    RegionCells{i,9}(ctr9,4) = Cell{i}(ii,8);
end
end %End ROI 9 if-statement

%Determine if particle is in ROI 10 (Dist. Ant. Left)
if ( PTposL{i}(ii,1)>=0 && PTposL{i}(ii,2)>=0 && ...
    PTposL{i}(ii,3)>6 && PTposL{i}(ii,3)<=9.0 && ...
    PTposL{i}(ii,5)<=dw )
    %Determine if row is entry point of particle into ROI 10
    if ( PTposL{i}(ii-1,1)<0 || PTposL{i}(ii-1,2)<0 || ...
        PTposL{i}(ii-1,3)<=6.0 || PTposL{i}(ii-1,3)>9.0 || ...
        PTposL{i}(ii-1,5)>dw )
        ctr10 = ctr10 + 1;
        RegionCells{i,10}(ctr10,1)= ii;
        RegionCells{i,10}(ctr10,3)= Cell{i}(ii,8);
    end
    %Determine if row is exit point of particle out of ROI 10
    if ( PTposL{i}(ii+1,1)<0 || PTposL{i}(ii+1,2)<0 || ...
        PTposL{i}(ii+1,3)<=6.0 || PTposL{i}(ii+1,3)>9.0 || ...
        PTposL{i}(ii+1,5)>dw )
        RegionCells{i,10}(ctr10,2) = ii;
        RegionCells{i,10}(ctr10,4) = Cell{i}(ii,8);
    end
end
end %End ROI 10 if-statement

%Determine if particle is in ROI 11 (Dist. Post. Left)
if ( PTposL{i}(ii,1)<0 && PTposL{i}(ii,2)>=0 && ...
    PTposL{i}(ii,3)>6 && PTposL{i}(ii,3)<=9.0 && ...
    PTposL{i}(ii,5)<=dw )
    %Determine if row is entry point of particle into ROI 11
    if ( PTposL{i}(ii-1,1)>=0 || PTposL{i}(ii-1,2)<0 || ...
        PTposL{i}(ii-1,3)<=6.0 || PTposL{i}(ii-1,3)>9.0 || ...
        PTposL{i}(ii-1,5)>dw )
        ctr11 = ctr11 + 1;
        RegionCells{i,11}(ctr11,1)= ii;
        RegionCells{i,11}(ctr11,3)= Cell{i}(ii,8);
    end
end
```

PTrNVRT.m [cont]

```
%Determine if row is exit point of particle out of ROI 11
if ( PTposL{i}(ii+1,1)>=0 || PTposL{i}(ii+1,2)<0 || ...
    PTposL{i}(ii+1,3)<=6.0 || PTposL{i}(ii+1,3)>9.0 || ...
    PTposL{i}(ii+1,5)>dw )
    RegionCells{i,11}(ctr11,2) = ii;
    RegionCells{i,11}(ctr11,4) = Cell{i}(ii,8);
end
end %End ROI 11 if-statement

%Determine if particle is in ROI 12 (Dist. Post Right)
if ( PTposL{i}(ii,1)<0 && PTposL{i}(ii,2)<0 && ...
    PTposL{i}(ii,3)>6 && PTposL{i}(ii,3)<=9.0 && ...
    PTposL{i}(ii,5)<=dw )
    %Determine if row is entry point of particle into ROI 12
    if ( PTposL{i}(ii-1,1)>=0 || PTposL{i}(ii-1,2)>=0 || ...
        PTposL{i}(ii-1,3)<=6.0 || PTposL{i}(ii-1,3)>9.0 || ...
        PTposL{i}(ii-1,5)>dw )
        ctr12 = ctr12 + 1;
        RegionCells{i,12}(ctr12,1)= ii;
        RegionCells{i,12}(ctr12,3)= Cell{i}(ii,8);
    end
    %Determine if row is exit point of particle out of ROI 12
    if ( PTposL{i}(ii+1,1)>=0 || PTposL{i}(ii+1,2)>=0 || ...
        PTposL{i}(ii+1,3)<=6.0 || PTposL{i}(ii+1,3)>9.0 || ...
        PTposL{i}(ii+1,5)>dw )
        RegionCells{i,12}(ctr12,2) = ii;
        RegionCells{i,12}(ctr12,4) = Cell{i}(ii,8);
    end
end
end %End ROI 12 if-statement

%Calculate transit times on last iteration and record last
%point if in region of interest
if ii==nr-1
    %ROI 1 testing (Prox. Ant. Right)
    if ( PTposL{i}(ii+1,1)>=0 && PTposL{i}(ii+1,2)<0 && ...
        PTposL{i}(ii,3)>=0 && PTposL{i}(ii,3)<3.0 && ...
        PTposL{i}(ii,5)<=dw && ctr1>0 )
        RegionCells{i,1}(ctr1,2) = ii+1;
        RegionCells{i,1}(ctr1,4) = Cell{i}(ii+1,8);
    end
    % ROI 2 testing (Prox. Ant. Left)
    if ( PTposL{i}(ii+1,1)>=0 && PTposL{i}(ii+1,2)>=0 && ...
        PTposL{i}(ii,3)>=0 && PTposL{i}(ii,3)<3.0 && ...
        PTposL{i}(ii,5)<=dw && ctr2>0 )
        RegionCells{i,2}(ctr2,2) = ii+1;
        RegionCells{i,2}(ctr2,4) = Cell{i}(ii+1,8);
    end
    %ROI 3 testing (Prox. Post. Left)
    if ( PTposL{i}(ii+1,1)<0 && PTposL{i}(ii+1,2)>=0 && ...
        PTposL{i}(ii,3)>=0 && PTposL{i}(ii,3)<3.0 && ...
```

PTrNVRT.m [cont]

```
PTposL{i}(ii,5)<=dw && ctr3>0 )
    RegionCells{i,3}(ctr3,2) = ii+1;
    RegionCells{i,3}(ctr3,4) = Cell{i}(ii+1,8);
end
%ROI 4 testing (Prox. Post. Right)
if ( PTposL{i}(ii+1,1)<0 && PTposL{i}(ii+1,2)<0 && ...
    PTposL{i}(ii,3)>=0 && PTposL{i}(ii,3)<3.0 && ...
    PTposL{i}(ii,5)<=dw && ctr4>0 )
    RegionCells{i,4}(ctr4,2) = ii+1;
    RegionCells{i,4}(ctr4,4) = Cell{i}(ii+1,8);
end

% ROI 5 testing (Mid. Ant. Right)
if ( PTposL{i}(ii+1,1)>=0 && PTposL{i}(ii+1,2)<0 && ...
    PTposL{i}(ii,3)>=3 && PTposL{i}(ii,3)<=6.0 && ...
    PTposL{i}(ii,5)<=dw && ctr5>0 )
    RegionCells{i,5}(ctr5,2) = ii+1;
    RegionCells{i,5}(ctr5,4) = Cell{i}(ii+1,8);
end

%ROI 6 testing (Mid. Ant. Left)
if ( PTposL{i}(ii+1,1)>=0 && PTposL{i}(ii+1,2)>=0 && ...
    PTposL{i}(ii,3)>=3 && PTposL{i}(ii,3)<=6.0 && ...
    PTposL{i}(ii,5)<=dw && ctr6>0 )
    RegionCells{i,6}(ctr6,2) = ii+1;
    RegionCells{i,6}(ctr6,4) = Cell{i}(ii+1,8);
end

%ROI 7 testing (Mid. Post. Left)
if ( PTposL{i}(ii+1,1)<0 && PTposL{i}(ii+1,2)>=0 && ...
    PTposL{i}(ii,3)>=3 && PTposL{i}(ii,3)<=6.0 && ...
    PTposL{i}(ii,5)<=dw && ctr7>0 )
    RegionCells{i,7}(ctr7,2) = ii+1;
    RegionCells{i,7}(ctr7,4) = Cell{i}(ii+1,8);
end

%ROI 8 testing (Mid. Post. Left)
if ( PTposL{i}(ii+1,1)<0 && PTposL{i}(ii+1,2)<0 && ...
    PTposL{i}(ii,3)>=3 && PTposL{i}(ii,3)<=6.0 && ...
    PTposL{i}(ii,5)<=dw && ctr8>0 )
    RegionCells{i,8}(ctr8,2) = ii+1;
    RegionCells{i,8}(ctr8,4) = Cell{i}(ii+1,8);
end

%ROI 9 testing (Dist. Ant. Right)
if ( PTposL{i}(ii+1,1)>=0 && PTposL{i}(ii+1,2)<0 && ...
    PTposL{i}(ii,3)>6 && PTposL{i}(ii,3)<=9.0 && ...
    PTposL{i}(ii,5)<=dw && ctr9>0 )
    RegionCells{i,9}(ctr9,2) = ii+1;
    RegionCells{i,9}(ctr9,4) = Cell{i}(ii+1,8);
end

%ROI 10 testing (Dist. Ant. Left)
if ( PTposL{i}(ii+1,1)>=0 && PTposL{i}(ii+1,2)>=0 && ...
    PTposL{i}(ii,3)>6 && PTposL{i}(ii,3)<=9.0 && ...
```

PTrNVRT.m [cont]

```
PTposL{i}(ii,5)<=dw && ctr10>0 )
    RegionCells{i,10}(ctr10,2) = ii+1;
    RegionCells{i,10}(ctr10,4) = Cell{i}(ii+1,8);
end
%ROI 11 testing (Dist. Post. Left)
if ( PTposL{i}(ii+1,1)<0 && PTposL{i}(ii+1,2)>=0 && ...
    PTposL{i}(ii,3)>6 && PTposL{i}(ii,3)<=9.0 && ...
    PTposL{i}(ii,5)<=dw && ctr11>0 )
    RegionCells{i,11}(ctr11,2) = ii+1;
    RegionCells{i,11}(ctr11,4) = Cell{i}(ii+1,8);
end
%ROI 12 testing (Dist. Post. Left)
if ( PTposL{i}(ii+1,1)<0 && PTposL{i}(ii+1,2)<0 && ...
    PTposL{i}(ii,3)>6 && PTposL{i}(ii,3)<=9.0 && ...
    PTposL{i}(ii,5)<=dw && ctr12>0 )
    RegionCells{i,12}(ctr12,2) = ii+1;
    RegionCells{i,12}(ctr12,4) = Cell{i}(ii+1,8);
end
end
end

%Calculate net particle transit time near wall in each region
% rows = particle net transit time ; columns = 12 regions
for k=1:nROI
    RegionCells{i,k}(1:12,5) = RegionCells{i,k}(1:12,4) - ...
        RegionCells{i,k}(1:12,3);
    TransTimes(i,k) = sum( RegionCells{i,k}(1:12,5) );
    if TransTimes(i,k)==0
        TransTimes(i,k)=NaN;
    end
end
end

figure
boxplot(TransTimes,'notch','on')
xlabel('AAA Near-Wall Region','FontSize',16)
ylabel('Net Particle Transit Time [s]','FontSize',16)

end %end function
```

PTregShear.m

```
%Purpose: Function to calculate regional time-averaged shear stress acting
%         on the particles
%
%Input: Cell Array where data in Cell elements are temporal row-based
%       Cell array that is exported from PTrNWRT function
%       Note: the
%
%Output: Figure(s) of desired data ranges
%
%-----
%               Written By: Christopher Basciano
%                   June 2010
%       Department of Mechanical and Aerospace Engineering
%       North Carolina State University, Raleigh, NC
%-----

function [RegShearPT] = PTregShear(PTcell,PTregCell,PTdiam)

%Assumed columns of PTcell data is:
%   X, Y, Z, Time-Averaged Pressure Gradient on PT trajectories,
%   Fluid Residence Time Distribution on Trajectories,
%   PT_Reynolds_Number, PT_Slip_Velocity, PT_Time,
%   PT_Travel_Distance, PT_Travel_Time, PT_Velocity Magnitude,

%Assumed columns of PTregCell is:
%   Row of PTcell when particle enters ROI,
%   Row of PTcell when particle exits ROI,
%   time at particle entry, time at particle exit, transit time

%ensure the raw pt data has same number of particles as regional data
rC = length(PTcell);
[nn,nROI] = size(PTregCell);
if rC~=nn
    error('number of particle mismatch of data files')
end

ShearPT = cell(rC,nROI);
RegShearPT = NaN(rC,nROI);

%loop through the ROI
for i=1:nROI

    %loop through the particles
    for j=1:rC

        %get dimensions of particle region cell data
        [nr,nc] = size(PTregCell{j,i});
        %reset data row index
        g=0;
```

PTregShear.m [cont]

```
%loop through the PTregCell contents
for k=1:nr

    %Begin calculation only if cell element holds data
    if ( PTregCell{j,i}(k,1)>0 )
        %get particle "j" data from PTcell{j} only where
        %   particle "j" is in ROI "i"
        r1 = PTregCell{j,i}(k,1);
        r2 = PTregCell{j,i}(k,2);
        %calculate shear stress only from r1:r2
        for ii=r1:r2
            %iterate number of data rows in ROI
            g=g+1;
            %calculate drag coefficient
            ShearPT{j,i}(g,1) = (24./PTcell{j}(ii,6)).*...
                (1+0.15.*(PTcell{j}(ii,6)).^0.687);
            %calculate shear stress on particle
            ShearPT{j,i}(g,2) = (1/8).*ShearPT{j,i}(g,1).* ...
                1.06.*PTcell{j}(ii,7).^2 - ...
                0.25*PTcell{j}(ii,4).*PTdiam;
        end
    end

end

if ShearPT{j,i}>0
    %calculate time-average shear stress on particle for time
    %   while in ROI number i
    RegShearPT(j,i) = mean( ShearPT{j,i}(1:g,2) );
end

end

end

figure
boxplot(RegShearPT,'notch','on')
xlabel('AAA Near-Wall Region','FontSize',16)
ylabel('Time-Averaged Particle Shear Stress [dyne/cm^2]','FontSize',16)

end %end function
```

APPENDIX VII: Custom ANSYS CFD Post v12.1 Perl Scripts for Hepatic Post-Processing

Summary

Appendix VII lists the crucial ANSYS CFD Post (Canonsburg, PA) Perl/power syntax scripts that were used for the hepatic particle-hemodynamics analysis. The first Perl/power syntax script is an ANSYS CFD Post session file that calculates the number of particles that exit the symmetric representative CHA domain (see Sect. 6.3) and exports the calculations in a text file easy plotting. The second Perl/power syntax script is also an ANSYS CFD Post session file that cycles creates the particle release map at the injection location of the particles. There is no output from this session file, the user must then save the resulting figure that is displayed in the CFD Post window.

ParticleExitQuantities.cse

```
# Purpose: ANSYS CFX Post v12.1 power syntax / PERL script used to
#           calculate number of particles exiting each domain outlet or
#           remain in the hepatic artery computational domain with
#           implanted SMC geometry

# Written by: Chris Basciano, May 2010
#             Department of Mechanical and Aerospace Engineering
#             North Carolina State University, Raleigh, NC

#-----#
#-----#
#           Create particle tracks that calculate
#           the number of particles exiting each outlet
#-----#

# Set names of files for exporting the particle exit data
! $filename1 = "SIR-Sphere_Exit_Data.txt";
! $filename2 = "THERA-Sphere_Exit_Data.txt";

# open file for recording particle exit data
! open OUT1, ">$filename1";
! open OUT2, ">$filename2";

# print file information and column labels to data files
! print OUT1 "### This file contains the number of SIR-Spheres exiting each
domain outlet.\n";
! print OUT1 "### Domain Outlet      Number of SIR-Spheres\n";
! print OUT2 "### This file contains the number of THERA-Spheres exiting
each domain outlet.\n";
! print OUT2 "### Domain Outlet      Number of THERA-Spheres\n";

#Create Perl string arrays containing boundary and particle track names

! @BOUNDARIES [0] = "OUTLET1,OUTLET1 2";
! @BOUNDARIES [1] = "OUTLET2,OUTLET2 2";
! @BOUNDARIES [2] = "OUTLET3,OUTLET3 2";
! @BOUNDARIES [3] = "OUTLET4,OUTLET4 2";
! @BOUNDARIES [4] = "OUTLET_GDA,OUTLET_GDA 2";
! @BOUNDARIES [5] = "No Boundary";

! @COLORS [0] = "0.666667, 0, 0";           #deep red
! @COLORS [1] = "0, 0, 1";                 #blue
! @COLORS [2] = "0.666667, 0, 1";         #purple
! @COLORS [3] = "0.968627, 0.647059, 0";  #orange
! @COLORS [4] = "0.666667, 0.666667, 0";  #tan
! @COLORS [5] = "0.866667, 0.866667, 0.866667"; #light grey
```

ParticleExitQuantities.cse - [cont]

```
! @SRtracks[0] = "Particle Track SR1";
! @SRtracks[1] = "Particle Track SR2";
! @SRtracks[2] = "Particle Track SR3";
! @SRtracks[3] = "Particle Track SR4";
! @SRtracks[4] = "Particle Track SR GDA";
! @SRtracks[5] = "Particle Track SR NoExit";

! @THtracks[0] = "Particle Track TH1";
! @THtracks[1] = "Particle Track TH2";
! @THtracks[2] = "Particle Track TH3";
! @THtracks[3] = "Particle Track TH4";
! @THtracks[4] = "Particle Track TH GDA";
! @THtracks[5] = "Particle Track TH NoExit";

#use for loop to cycle through each of the Perl array elements

! for ($i=0; $i<=5; $i++) {

!   $boundaryname = @BOUNDARIES[$i];
!   $trackcolor = @COLORS[$i];
!   $sirtrack = @SRtracks[$i];
!   $theratrack = @THtracks[$i];

PARTICLE TRACK: $sirtrack
  Activate Filter = On
  Any All Condition = Match ALL
  Colour = $trackcolor
  Colour Map = Default Colour Map
  Colour Mode = Constant
  Colour Scale = Linear
  Culling Mode = No Culling
  Domain List = All Domains
  Draw Faces = On
  Draw Lines = Off
  Draw Symbols = Off
  Draw Tracks = On
  Ending Boundary = $boundaryname
  Filter On Diameter = Off
  Filter On End = On
  Filter On Start = Off
  Filter On Track Selection = Off
  Limit Track Option = Up To Current Timestep
  Reduction Factor = 1.0
  Reduction or Max Tracks = Reduction
  Show Track Labels = Off
  Option = From Res
  Track Material = SIRsphere
  Visibility = Off
END
```

ParticleExitQuantities.cse - [cont]

```
#Record number of SIRspheres exiting $boundaryname

! $srtrknums = getValue( $sirtrack, "Tracks Displayed" );
! @srtrks = split(/, /, $srtrknums );
! $exitsum1 = $#srtrks + 1;
! print OUT1 "$boundaryname:      $exitsum1\n";

PARTICLE TRACK: $theratrack
  Activate Filter = On
  Any All Condition = Match ALL
  Colour = $trackcolor
  Colour Map = Default Colour Map
  Colour Mode = Constant
  Colour Scale = Linear
  Culling Mode = No Culling
  Domain List = All Domains
  Draw Faces = On
  Draw Lines = Off
  Draw Symbols = Off
  Draw Tracks = On
  Ending Boundary = $boundaryname
  Filter On Diameter = Off
  Filter On End = On
  Filter On Start = Off
  Filter On Track Selection = Off
  Limit Track Option = Up To Current Timestep
  Reduction Factor = 1.0
  Reduction or Max Tracks = Reduction
  Show Track Labels = Off
  Option = From Res
  Track Material = THERAsphere
  Visibility = Off
END

! $thtrknums = getValue( $theratrack, "Tracks Displayed" );
! @thtrks = split(/, /, $thtrknums );
! $exitsum2 = $#thtrks + 1;
! print OUT2 "$boundaryname:      $exitsum2\n";

! }      # end for loop

! close OUT1;
! close OUT2;
```

ParticleReleaseMap.cse

```
# Purpose: ANSYS CFX Post v12.1 power syntax / PERL script used to
#          construct particle release maps at particle injection plane
#          of the hepatic artery geometry with implanted SMC geometry

# Written by: Chris Basciano, May 2010
#            Department of Mechanical and Aerospace Engineering
#            North Carolina State University, Raleigh, NC

#-----#

#-----#
#          Create particle release maps of particle exit locations
#          at particle injection plane
#-----#

#Create Perl string arrays containing boundary and particle track names

! @BOUNDARIES [0] = "OUTLET1,OUTLET1 2";
! @BOUNDARIES [1] = "OUTLET2,OUTLET2 2";
! @BOUNDARIES [2] = "OUTLET3,OUTLET3 2";
! @BOUNDARIES [3] = "OUTLET4,OUTLET4 2";
! @BOUNDARIES [4] = "OUTLET_GDA,OUTLET_GDA 2";
! @BOUNDARIES [5] = "No Boundary";

! @COLORS [0] = "0.666667, 0, 0";           #deep red
! @COLORS [1] = "0, 0, 1";               #blue
! @COLORS [2] = "0.666667, 0, 1";       #purple
! @COLORS [3] = "0.968627, 0.647059, 0"; #orange
! @COLORS [4] = "0.666667, 0.666667, 0"; #tan
! @COLORS [5] = "0.866667, 0.866667, 0.866667"; #light grey

! @SRmaps [0] = "Particle Map SR1";
! @SRmaps [1] = "Particle Map SR2";
! @SRmaps [2] = "Particle Map SR3";
! @SRmaps [3] = "Particle Map SR4";
! @SRmaps [4] = "Particle Map SR GDA";
! @SRmaps [5] = "Particle Map SR NoExit";

! @THmaps [0] = "Particle Map TH1";
! @THmaps [1] = "Particle Map TH2";
! @THmaps [2] = "Particle Map TH3";
! @THmaps [3] = "Particle Map TH4";
! @THmaps [4] = "Particle Map TH GDA";
! @THmaps [5] = "Particle Map TH NoExit";
```

ParticleReleaseMap.cse – [cont]

#use for loop to cycle through each of the Perl array elements

```
! for ($i=0; $i<=5; $i++) {  
  
!   $boundaryname = @BOUNDARIES[$i];  
!   $mapcolor = @COLORS[$i];  
!   $sirmap = @SRmaps[$i];  
!   $theramap = @THmaps[$i];  
  
PARTICLE TRACK: $sirmap  
  Activate Filter = On  
  Any All Condition = Match ALL  
  Colour = $mapcolor  
  Colour Map = Default Colour Map  
  Colour Mode = Constant  
  Colour Scale = Linear  
  Culling Mode = No Culling  
  Domain List = All Domains  
  Draw Faces = On  
  Draw Lines = Off  
  Draw Symbols = On  
  Draw Tracks = Off  
  Ending Boundary = $boundaryname  
  Filter On Diameter = Off  
  Filter On End = On  
  Filter On Start = Off  
  Filter On Track Selection = Off  
  Limit Track Option = User Specified  
  Surface Drawing = Smooth Shading  
  Symbol Max Time Selection = Current Time  
  Symbol Scale Type = Relative  
  Symbol Size = 0.1  
  Symbol Start Time = 10 [s]  
  Symbol Stop Time = 0 [s]  
  Symbol Size Option = Constant  
  Symbol Stop Time = 0 [s]  
  Symbol Time Interval = 0.0001 [s]  
  Track End Distance = 60 [micron]  
  Track End Time = 0.0 [s]  
  Track Limit Type = Distance  
  Track Start Distance = 0.0 [cm]  
  Track Start Time = 0.0 [s]  
  Track Symbol = Ball  
  Transparency = 0.0  
  Reduction Factor = 1.0  
  Reduction or Max Tracks = Reduction  
  Show Track Labels = Off  
  Option = From Res
```

ParticleReleaseMap.cse – [cont]

```
Track Material = SIRsphere  
Visibility = On  
END
```

```
PARTICLE TRACK: $theramap  
Activate Filter = On  
Any All Condition = Match ALL  
Colour = $mapcolor  
Colour Map = Default Colour Map  
Colour Mode = Constant  
Colour Scale = Linear  
Culling Mode = No Culling  
Domain List = All Domains  
Draw Faces = On  
Draw Lines = Off  
Draw Symbols = On  
Draw Tracks = Off  
Ending Boundary = $boundaryname  
Filter On Diameter = Off  
Filter On End = On  
Filter On Start = Off  
Filter On Track Selection = Off  
Limit Track Option = User Specified  
Surface Drawing = Smooth Shading  
Symbol Max Time Selection = Current Time  
Symbol Scale Type = Relative  
Symbol Size = 0.1  
Symbol Start Time = 10 [s]  
Symbol Stop Time = 0 [s]  
Symbol Size Option = Constant  
Symbol Stop Time = 0 [s]  
Symbol Time Interval = 0.0001 [s]  
Track End Distance = 60 [micron]  
Track End Time = 0.0 [s]  
Track Limit Type = Distance  
Track Start Distance = 0.0 [cm]  
Track Start Time = 0.0 [s]  
Track Symbol = Ball  
Transparency = 0.0  
Reduction Factor = 1.0  
Reduction or Max Tracks = Reduction  
Show Track Labels = Off  
Option = From Res  
Track Material = THERAsphere  
Visibility = Off  
END
```

```
! } # end for loop
```

ParticleReleaseMap.cse – [cont]

#Set view to the particle release plane

VIEW:View 1

Camera Mode = User Specified

CAMERA:

Option = Pivot Point and Quaternion

Pivot Point = 0, -0.000125811, -0.661924

Scale = 1.94663

Pan = -0.204466, -0.0171701

Rotation Quaternion = 0, 1, 0, 6.12323e-017

END

END

#Set wireframe to outline appropriate region

WIREFRAME:Wireframe

Apply Instancing Transform = On

Colour = 0, 0, 0

Domain List = SMC_CHA,SMC2,SMC_Lumen

Edge Angle = 30 [degree]

Line Colour Mode = User Specified

Line Width = 3

Show Surface Mesh = Off

END

APPENDIX VIII: Copyright Permissions

Summary

Appendix VIII lists the copyright permissions associated with the figures used from other copyrighted sources. The first is from ASME regarding the ILT figure from Wang et al. (2001), the second is from SpringerLink for using Koops et al. (2004) anatomical diagrams of the hepatic artery, and the third is from Wake Radiology Oncology Services for graciously allowing the use of their medical illustrations and images.

ASME Copyright Permissions

Dear Mr. Basciano,

It is our pleasure to grant you permission to publish the ASME Figure 2 from "Mechanical properties and microstructure of intraluminal thrombus from abdominal aortic aneurysm," by David H.J. Wang , Michel Makaroun , Marshall W. Webster , David A. Vorp, ASME Journal of Biomechanical Engineering, Vol. 123, 20001, cited in your letter for inclusion in a Doctoral Thesis entitled Computational Particle-Hemodynamics Analysis Applied to an Abdominal Aortic Aneurysm with Thrombus and Microsphere-Targeting of Liver Tumors to be published by North Carolina State University and ProQuest. As is customary, we request that you ensure proper acknowledgment of the exact sources of this material, the authors, and ASME as original publisher.

In accordance with ASME policy, this permission is contingent upon payment of a royalty fee of **US\$20 for 1 figure** (\$20.00 for the first figure/table, \$10 thereafter). This is solely charged to non-authors of the requested ASME papers. We accept payments on all major credit cards such as: Visa, MasterCard, American Express, Discover, and Diners Club, or by check payable to ASME. Please send payment to the attention Michelle DeBlasi, ASME Accounting, 22 Law Drive, Fairfield, NJ 07007, and indicate A/C# 1-1150-0000-4303. Should you have any questions regarding payment form or transfer, please contact Ms. DeBlasi; P: 973-244-2268, F: 973-882-4924; E:deblasim@asme.org.

Many thanks for your interest in ASME publications.

Sincerely,
Beth Darchi
Copyrights & Permissions
ASME International
Three Park Avenue
New York, NY 10016
P: 212-591-7700
F: 212-591-7292
E: darchib@asme.org

SpringerLink Copyright Permissions

Rightslink Printable License

https://s100.copyright.com/App/PrintableLicenseFrame.jsp?publi...

SPRINGER LICENSE TERMS AND CONDITIONS

Jun 15, 2010

This is a License Agreement between Chris Basciano ("You") and Springer ("Springer") provided by Copyright Clearance Center ("CCC"). The license consists of your order details, the terms and conditions provided by Springer, and the payment terms and conditions.

All payments must be made in full to CCC. For payment instructions, please see information listed at the bottom of this form.

| | |
|-------------------------------------|--|
| License Number | 2450310683956 |
| License date | Jun 15, 2010 |
| Licensed content publisher | Springer |
| Licensed content publication | Surgical and Radiologic Anatomy |
| Licensed content title | Anatomic variations of the hepatic arteries in 604 selective celiac and superior mesenteric angiographies |
| Licensed content author | A. Koops |
| Licensed content date | Jun 1, 2004 |
| Volume number | 26 |
| Issue number | 3 |
| Type of Use | Thesis/Dissertation |
| Portion | Figures |
| Author of this Springer article | No |
| Order reference number | |
| Title of your thesis / dissertation | Computational Particle-Hemodynamics Analysis Applied to an Abdominal Aortic Aneurysm with Thrombus and Microsphere-Targeting of Liver Tumors |
| Expected completion date | Dec 2010 |
| Estimated size(pages) | 350 |
| Total | 0.00 USD |
| Terms and Conditions | |

Introduction

The publisher for this copyrighted material is Springer Science + Business Media. By clicking "accept" in connection with completing this licensing transaction, you agree that the following terms and conditions apply to this transaction (along with the Billing and Payment terms and conditions established by Copyright Clearance Center, Inc. ("CCC"), at the time that you opened your Rightslink account and that are available at any time at <http://myaccount.copyright.com>).

Limited License

With reference to your request to reprint in your thesis material on which Springer Science and Business Media control the copyright, permission is granted, free of charge, for the use indicated in your enquiry. Licenses are for one-time use only with a maximum distribution equal to the number that you identified in the licensing process.

SpringerLink Copyright Permissions – [cont]

Rightslink Printable License

<https://s100.copyright.com/App/PrintableLicenseFrame.jsp?publi...>

This License includes use in an electronic form, provided it is password protected or on the university's intranet, destined to microfilming by UMI and University repository. For any other electronic use, please contact Springer at (permissions.dordrecht@springer.com or permissions.heidelberg@springer.com)

The material can only be used for the purpose of defending your thesis, and with a maximum of 100 extra copies in paper.

Although Springer holds copyright to the material and is entitled to negotiate on rights, this license is only valid, provided permission is also obtained from the (co) author (address is given with the article/chapter) and provided it concerns original material which does not carry references to other sources (if material in question appears with credit to another source, authorization from that source is required as well). Permission free of charge on this occasion does not prejudice any rights we might have to charge for reproduction of our copyrighted material in the future.

Altering/Modifying Material: Not Permitted

However figures and illustrations may be altered minimally to serve your work. Any other abbreviations, additions, deletions and/or any other alterations shall be made only with prior written authorization of the author(s) and/or Springer Science + Business Media. (Please contact Springer at permissions.dordrecht@springer.com or permissions.heidelberg@springer.com)

Reservation of Rights

Springer Science + Business Media reserves all rights not specifically granted in the combination of (i) the license details provided by you and accepted in the course of this licensing transaction, (ii) these terms and conditions and (iii) CCC's Billing and Payment terms and conditions.

Copyright Notice:

Please include the following copyright citation referencing the publication in which the material was originally published. Where wording is within brackets, please include verbatim.

"With kind permission from Springer Science+Business Media: <book/journal title, chapter/article title, volume, year of publication, page, name(s) of author(s), figure number(s), and any original (first) copyright notice displayed with material>."

Warranties: Springer Science + Business Media makes no representations or warranties with respect to the licensed material.

Indemnity

You hereby indemnify and agree to hold harmless Springer Science + Business Media and CCC, and their respective officers, directors, employees and agents, from and against any and all claims arising out of your use of the licensed material other than as specifically authorized pursuant to this license.

No Transfer of License

This license is personal to you and may not be sublicensed, assigned, or transferred by you to any other person without Springer Science + Business Media's written permission.

No Amendment Except in Writing

This license may not be amended except in a writing signed by both parties (or, in the case of Springer Science + Business Media, by CCC on Springer Science +

SpringerLink Copyright Permissions – [cont]

Rightslink Printable License

<https://s100.copyright.com/App/PrintableLicenseFrame.jsp?publi...>

Business Media's behalf).

Objection to Contrary Terms

Springer Science + Business Media hereby objects to any terms contained in any purchase order, acknowledgment, check endorsement or other writing prepared by you, which terms are inconsistent with these terms and conditions or CCC's Billing and Payment terms and conditions. These terms and conditions, together with CCC's Billing and Payment terms and conditions (which are incorporated herein), comprise the entire agreement between you and Springer Science + Business Media (and CCC) concerning this licensing transaction. In the event of any conflict between your obligations established by these terms and conditions and those established by CCC's Billing and Payment terms and conditions, these terms and conditions shall control.

Jurisdiction

All disputes that may arise in connection with this present License, or the breach thereof, shall be settled exclusively by the country's law in which the work was originally published.

Other terms and conditions:

v1.2

Gratis licenses (referencing \$0 in the Total field) are free. Please retain this printable license for your reference. No payment is required.

If you would like to pay for this license now, please remit this license along with your payment made payable to "COPYRIGHT CLEARANCE CENTER" otherwise you will be invoiced within 48 hours of the license date. Payment should be in the form of a check or money order referencing your account number and this invoice number RLNK10800001.

Once you receive your invoice for this order, you may pay your invoice by credit card. Please follow instructions provided at that time.

**Make Payment To:
Copyright Clearance Center
Dept 001
P.O. Box 843006
Boston, MA 02284-3006**

If you find copyrighted material related to this license will not be used and wish to cancel, please contact us referencing this license number 2450310683956 and noting the reason for cancellation.

Questions? customercare@copyright.com or +1-877-622-5543 (toll free in the US) or +1-978-646-2777.

Wake Radiology Oncology Services Copyright Permissions



February 1, 2010

To : whom it may concern

RE: Permission to use illustrations

Chris Basciano has my permission to use my illustrations for his research, writings, presentations and dissertation.

Respectfully submitted,
Andrew Kennedy, MD, FACRO
Co-Medical Director

Andrew S. Kennedy, MD, FACRO · Scott L. Sailer, MD · William A. Dezarn, PhD, DAER
300 Ashville Ave., Suite 110, Cary, NC 27518, USA